

Electrical Losses Mitigation in Silicon Heterojunction Solar Cells

Présentée le 29 septembre 2021

Faculté des sciences et techniques de l'ingénieur
Laboratoire de photovoltaïque et couches minces électroniques
Programme doctoral en photonique

pour l'obtention du grade de Docteur ès Sciences

par

Laurie-Lou SENAUD

Acceptée sur proposition du jury

Prof. N. Grandjean, président du jury
Prof. C. Ballif, Dr B. Y. P. Paviet-Salomon, directeurs de thèse
Dr D. Lachenal, rapporteur
Prof. O. Isabella, rapporteur
Prof. A. Fontcuberta, rapporteuse

[We] don't care what anything was designed to do.

We care about what it can do.

— Apollo 13

To all of you, with warm thanks.

Résumé

Pour relever les défis mondiaux visant à atténuer le changement climatique, l'énergie photovoltaïque est appelée à jouer un rôle important dans la production mondiale d'électricité. De nos jours, les cellules solaires à base de silicium cristallin (c-Si) à jonction unique détiennent la plus grande part du marché photovoltaïque. Pour atteindre l'efficacité maximale de conversion énergétique de ces dispositifs, il a été démontré que les contacts passivants et sélectifs de charges sont les technologies les plus prometteuses. Parmi elles, les cellules solaires à hétérojonction de silicium (SHJ) devraient donner un avantage concurrentiel à l'Union européenne et réduire encore plus le coût de l'énergie solaire photovoltaïque. En effet, les cellules solaires SHJ ont atteint une efficacité record grâce à la haute qualité du matériau c-Si couplée à une excellente passivation de surface. Cependant, malgré des performances remarquables, les différentes couches de matériaux utilisées pour construire les cellules SHJ sont à l'origine de compromis importants entre les propriétés électriques et optiques. En particulier, lorsque le couplage des propriétés des différentes couches de matériaux n'est pas correctement optimisé, d'importantes pertes de transport électrique se produisent, limitant fortement les performances de la cellule SHJ. L'objectif de cette thèse est de décrire, quantifier et atténuer les pertes électriques survenant dans les cellules solaires SHJ actuelles au moyen de méthodologies et de méthodes de caractérisation avancées.

Les principaux résultats de ce travail se déclinent en quatre parties. Premièrement, les ambiguïtés du terme *contact*, tel qu'il est actuellement employé dans la littérature relative aux cellules solaires, sont mises en évidence. Dans ce contexte, nous introduisons une nouvelle description généralisée et sans ambiguïté du concept de *contact* en utilisant la terminologie de la *shell*. Il a été démontré que ce concept permet d'étudier avec précision et de réduire les pertes électriques et optiques affectant les cellules solaires. Ensuite, nous proposons une méthodologie de caractérisation utilisant deux nouvelles approches nommées *top-down* et *bottom-up*. Ces approches sont conçues pour étudier indépendamment les propriétés des couches de matériaux utilisées pour construire les shells, ainsi que les performances des cellules solaires incorporant ces shells au cours des différentes étapes de fabrication. Dans l'ensemble, cette méthodologie s'est révélée être un moyen très efficace de relier les propriétés des shells aux performances finales des cellules solaires. Deuxièmement, nous présentons les mesures de la méthode de longueur de transfert (TLM) sous illumination variable comme une nouvelle méthode de caractérisation avancée pour étudier plus en détail les pertes de transport électrique dans les cellules SHJ. Grâce à cette méthode de caractérisation avancée, nous avons démontré (i) que l'illumination, et donc la densité de porteurs injectés dans

le volume du c-Si, a un impact important sur la valeur de la résistivité de contact (ρ_c), (ii) l'importance de mesurer ρ_c dans des conditions de point de puissance maximale pour une caractérisation pertinente des pertes de transport des cellules solaires, et (iii) comment la dépendance de ρ_c par rapport à un changement de la densité de porteurs injectés dans la masse de c-Si permet de comparer la réponse à l'illumination de différentes shells SHJ. De plus, il a été démontré que l'impact sur les valeurs de ρ_c induit par différentes injections était significativement différent de celui induit par la densité de dopage du c-Si. Finalement, nous avons mené des investigations et des discussions préliminaires sur l'applicabilité des mesures TLM sous illumination pour mesurer les parties de la shell de type p sur les wafers de c-Si de type n. Troisièmement, nous avons développé différentes couches de matériaux et étudié le couplage de leurs propriétés à différents niveaux à l'intérieur des shells dans le but de déterminer leur impact sur les performances finales du dispositif une fois intégré dans des cellules solaires SHJ fonctionnelles. La combinaison en multicouche appliquée aux couches minces hydrogénées de silicium et aux oxydes transparents conducteurs (TCOs) a démontré un fort potentiel de réduction des pertes électriques en (i) améliorant les propriétés de la shell à différents niveaux, (ii) en répondant aux différentes contraintes induites par l'architecture de la cellule, et (iii) en atténuant efficacement les différents compromis impactant les performances de la cellule solaire. Finalement, le quatrième résultat de ce travail est l'intégration des shells les plus prometteuses dans les meilleures cellules solaires de notre laboratoire. Cela a permis d'atteindre des facteurs de forme allant jusqu'à 83.2%, dans le cas de cellules solaires SHJ bifaces de taille 6 pouces, et d'obtenir des cellules IBC SHJ d'une taille de 5 cm \times 5 cm présentant des efficacités allant jusqu'à 25.45%. Finalement, l'optimisation des propriétés optiques des shells nous a permis d'atteindre un J_{SC} élevé de 40.81 mA cm⁻² pour des cellules solaires 2 cm \times 2 cm SHJ monofaces sérigraphiées et, en combinant des propriétés électriques et optiques élevées des shells, une efficacité impressionnante de 24.24% a été atteinte en utilisant une couche d'oxyde de zinc dopées à l'aluminium comme TCO arrière. Comme perspectives d'avenir, les méthodologies et les méthodes de caractérisation avancées et présentées dans ce travail sont appelées à favoriser la compréhension et l'optimisation d'autres technologies de cellules solaires telles que, par exemple, les cellules solaires TOPCon ou tandem.

Mots clefs: cellule solaire en silicium, haute efficacité, contact passivant et sélectif de charges, shell, hétérojonction silicium, pertes électriques, transport des porteurs de charge, méthodes de caractérisation améliorées et avancées, résistivité de contact, niveau d'injection, multicouches, couche mince hydrogénée de silicium amorphe et nanocristalline, oxyde conducteur et transparent.

Abstract

To overcome the worldwide challenges of climate change mitigation, photovoltaic (solar PV) is foreseen to play a significant role in the world electricity production. Nowadays, single junction crystalline silicon (c-Si) based solar cells hold the largest share of the global photovoltaic market. To achieve the maximum energy conversion efficiency of these devices, carrier-selective passivating contacts have been demonstrated to be the most promising technologies. Among them, silicon heterojunction (SHJ) solar cells are expected to give a competitive edge to the European Union and to further reduce the cost of solar PV. Indeed, SHJ solar cells have achieved record efficiency thanks to high c-Si bulk quality coupled with excellent full area surface passivation. However, despite remarkable performance, the different material layers used to build SHJ cells are at the origin of significant trade-offs between electrical and optical properties. In particular, when the properties coupling arising between the different material layers is not properly optimized, significant electrical transport losses occur, strongly capping the SHJ device performance. The aim of this thesis is to accurately describe, quantify, and mitigate the electrical losses occurring in state-of-the-art SHJ solar cells by means of advanced methodologies and characterization methods.

Key outcomes of this work are fourfold. First, the ambiguities of the term *contact* as currently employed in the literature of solar cells are pinpointed. Following this, we introduce a novel generalized and unambiguous description of the so-called contacts using the terminology of *shell*. This concept was demonstrated to allow one to accurately investigate and eventually mitigate the electrical as well as the optical losses affecting state-of-the-art solar cells. Then, we propose a characterization methodology using two new approaches named *top-down* and *bottom-up*. These approaches are designed to independently track the properties of the material layers used to build the shells, as well as the performance of the solar cells incorporating these shells along the different process steps. Overall, this methodology was demonstrated to provide an effective mean to link the resulting properties of the shells to the final performance of the solar cells. Secondly, we present transfer length method (TLM) measurements under variable illumination as a novel advanced characterization method to further study the electrical transport losses in SHJ devices. Using this improved characterization method, we demonstrated (i) that illumination, and thus the injected carrier density inside the c-Si bulk, has a strong impact on the contact resistivity (ρ_c) value, (ii) the importance of measuring ρ_c under maximum power point conditions for a relevant characterization of solar cell transport losses, and (iii) how the dependence of the ρ_c on a change of the injected carrier density within the c-Si bulk makes it possible to compare the illumination response of different SHJ shells.

Abstract

Then, the impact on the ρ_c values induced by different illuminations was demonstrated to be significantly different than the one induced by the doping density of the c-Si bulk. Finally, we conducted preliminary investigations and discussions of the applicability of TLM measurements under illumination to measure p-type shell parts on n-type c-Si wafers. Thirdly, we engineered various material layers and investigated their resulting properties coupling at different levels inside the shells with the aim to relate their impact on the final device performance once integrated in actual SHJ solar cells. Multilayering the thin hydrogenated silicon and the TCO layers demonstrated a high potential for electrical losses mitigation by (i) improving the properties coupling at different levels inside the shell, (ii) addressing the constraints induced by the device architecture, and (iii) effectively mitigating the trade-offs impacting solar cell performance. Finally, the fourth outcome of this work is the integration of the most promising shells in our actual baseline solar cells. This made it possible to reach fill-factors up to 83.2%, in the case of full area 6-inch SHJ solar cells, and to reach SHJ IBC cells with a size of 5 cm \times 5 cm featuring efficiencies up to 25.45%. Finally, optimizations of the optical properties of shells allowed us to reach a high J_{SC} of 40.81 mA cm⁻² for 2 cm \times 2 cm screen-printed SHJ monofacial solar cells and, combining optimal electrical and optical shell properties, an impressive efficiency of 24.24% was achieved using an aluminium-doped zinc oxide layer as rear TCO. As future prospects, the advanced methodologies and characterization methods presented in this work are foreseen to be effectively applied to drive the understanding and optimization of other solar cell technologies such as, e.g. TOPCon or tandem solar cells.

Key words: silicon solar cells, high efficiency, carrier selective passivating contact, shell, silicon heterojunction, electrical losses, charge carrier transport, improved and advanced characterization methods, contact resistivity, injection level, multilayers, amorphous and nanocrystalline thin hydrogenated silicon layer, transparent conductive oxide.

Contents

Abstract (Français/English)	i
List of acronyms and symbols	ix
1 Introduction	1
1.1 Photovoltaics - General context	1
1.1.1 Electricity production and environmental issues – The role of solar energy	1
1.1.2 Cost decrease and competitiveness	3
1.1.3 Photovoltaics technologies and current market status	4
1.2 Motivation	9
1.3 Objectives and structure	10
1.3.1 Objectives	10
1.3.2 Structure of the thesis	11
1.4 Contribution to the research field	12
2 Contacts in Solar Cells	15
2.1 Generalized operating principle of solar cells	15
2.1.1 Current ambiguities in the description of solar cell contacts	17
2.1.2 Shell of solar cells	20
2.2 Physics of semiconductor-based solar cells	25
2.2.1 Generation	25
2.2.2 Recombination losses and passivation mechanisms	28
2.2.3 Selectivity	38
2.2.4 Resistive losses	43
2.2.5 Transport in solar cells	45
2.3 Methodology	48
2.3.1 Top-down and bottom-up approaches	49
2.4 Conclusion	52
3 Experimental processes and characterization systems	53
3.1 Experimental processes	53
3.1.1 Silicon heterojunction solar cells baseline process flow	53
3.1.2 Silicon heterojunction solar cell manufacturing systems	56
3.2 Characterization systems	62

Contents

3.2.1	Layer characterization	62
3.2.2	Cell characterization	91
3.3	Conclusion	108
4	Advanced methods for the electrical characterization of solar cell shells using transfer length method Measurements under variable illumination	111
4.1	Introduction	112
4.2	Experimental details	114
4.2.1	TLM samples and case studies	114
4.2.2	Finite Element Simulations for TLM	117
4.3	TLM measurement under variable illumination - impact on ρ_c and suspected limitations	118
4.3.1	Introduction	118
4.3.2	Illumination and non-ohmic behaviour	118
4.3.3	Illumination and its impact on ρ_c : simulation and experiment	124
4.3.4	Edge recombination and its impact on contact resistivity measurement	130
4.3.5	Conclusion	134
4.4	Doping carrier density and its impact on ρ_c - Comparison with injected carrier density	135
4.4.1	Introduction	135
4.4.2	Results and discussion	135
4.4.3	Conclusion	142
4.5	Hole-selective shell parts on c-Si(p) and c-Si(n) wafers	142
4.5.1	Introduction	142
4.5.2	Results and discussion	143
4.5.3	Conclusion	151
4.6	Practical implications for the design and operation of solar cells	152
4.7	Conclusion	154
5	Top-down and bottom-up approaches to overcome electrical limitations	157
5.1	Introduction	158
5.2	Rationale and experimental details	158
5.3	Cases A & B: Doped thin hydrogenated silicon and TCO layers coupling investigation	162
5.3.1	Introduction	162
5.3.2	Case A.1: n-type thin silicon multilayers development	162
5.3.3	Case A.2: TCO and passivation quality	169
5.3.4	Case A.3: Aluminium-doped zinc oxide development	172
5.3.5	Case B: Indium tin oxide development	178
5.3.6	Conclusion	179
5.4	Case C: Intrinsic and doped thin silicon layers coupling investigation	181
5.4.1	Introduction	181

5.4.2	a-Si:H(i) layer thickness and microdoped multilayer	181
5.4.3	Microdoped multilayer - boron quantity	183
5.4.4	Microdoped multilayer - thickness	185
5.4.5	Microdoped multilayer - boron quantity and thickness	187
5.4.6	Conclusion	189
5.5	Conclusion	189
6	Integration in solar cells	191
6.1	Introduction	191
6.2	R_S breakdown integrating MPP and dark ρ_c values	192
6.3	High quality SHJ shells for high performance solar cells	194
6.3.1	Indium tin oxide optimization for 6-inch solar cells	194
6.3.2	n-type thin silicon multilayer optimization for 2cm x 2cm monofacial solar cells	195
6.3.3	Top-down and bottom-up approaches for IBC optimization	196
6.4	SHJ shells - optical properties optimization	198
6.4.1	Introduction	198
6.4.2	Results and discussion	199
6.5	Conclusion	204
7	Conclusion and prospects	207
7.1	Conclusion	207
7.2	Prospects	211
A	Appendix	215
A.1	TLM under variable illumination and non-ohmic behavior	215
A.2	TLM under variable illumination - injected carrier density computation	218
A.3	Transparent conductive oxide and thickness properties	221
	Bibliography	223
	Remerciements	239
	CV	243
	List of scientific contributions	245

List of acronyms and symbols

Semiconductor Basics

E_g	Band gap energy
E_c	Conduction band energy
E_v	Valence band energy
E_F	Fermi level
E_{Fn}	Electron quasi-Fermi level
E_{Fp}	Hole quasi-Fermi level
FCA	Free carrier absorption
J_n	Electron current density
J_p	Hole current density
n_i	Intrinsic carrier density
n	Total electron density
n_0	Equilibrium electron density
Δn	Excess electron density
p	Total hole density
p_0	Equilibrium hole density
Δp	Excess hole density
SCR	Space charge region
S_{eff}	Effective surface recombination velocity
τ	carrier lifetime
U	recombination rate
WF	Work function

Materials

a-Si:H	Hydrogenated amorphous silicon
a-Si:H(i)	Intrinsic hydrogenated amorphous silicon
a-Si:H(n)	n-doped hydrogenated amorphous silicon
a-Si:H(p)	p-doped hydrogenated amorphous silicon
c-Si	Crystalline silicon

Chapter 0. List of acronyms and symbols

c-Si(n)	n-doped crystalline silicon
c-Si(p)	p-doped crystalline silicon
Cz	Czochralski
FZ	Float-Zone
nc-Si:H	Hydrogenated nanocrystalline silicon
nc-Si:H(n)	p-type hydrogenated nanocrystalline silicon
nc-Si:H(p)	n-type hydrogenated nanocrystalline silicon

Ag	Silver
Al	Aluminum
AZO	Aluminum-doped zinc oxide
ITO	Indium tin oxide
SiN _x	Silicon nitride
SiO _x	Silicon oxide
TCO	Transparent conductive oxide

ARC	Anti-reflective coating
DARC	Double anti-reflective coating

Deposition Processes

PECVD	Plasma enhanced chemical vapor deposition
PVD	Physical vapor deposition
DC	Direct current
RF	Radio frequency

CO ₂	Carbon dioxide
CH ₄	Methane
H ₂	Hydrogen
NH ₃	Ammonia
PH ₃	Phosphine
SiH ₄	Silane
TMB	Trimethylborane

Characterizations

η	Energy conversion efficiency
FF	Fill factor
J_{sc}	Short-circuit current density
V_{oc}	Open-circuit voltage

I	Current
J	Current density
V	Voltage
I - V	Current-voltage
J - V	Current density-voltage
iJ	Implied-current density
iV	Implied-voltage
iV_{OC}	Implied-open-circuit voltage
pJ	Pseudo-current density
pV	Pseudo-voltage
pFF	Pseudo-fill factor
FF_0	Fill factor zero
MPP	Maximum power point
R_S	Series resistance
E_a	Activation energy
Φ_c	Crystallinity factor
ρ_c	Contact resistivity
σ_d	Dark coplanar conductivity
μ	Mobility
R_{sh}	Sheet resistance
EQE	External quantum efficiency
IQE	Internal quantum efficiency
PL	Photoluminescence imaging
RS	Raman spectroscopy
SE	Spectroscopic ellipsometry
TLM	Transfer length method
Solar Cell Technologies	
IBC	Interdigitated back-contact
PERC	Passivated emitter and rear cell
PERL	Passivated emitter and rear locally diffused cell
Poly-Si	Polycrystalline silicon
POLO	Polycrystalline silicon on oxide
SHJ	Silicon heterojunction
TOPCon	Tunnel oxide passivated contact

1 Introduction

1.1 Photovoltaics - General context

1.1.1 Electricity production and environmental issues – The role of solar energy

To fight the perpetual energy consumption growth and greenhouse gas emissions, accelerating the deployment of renewable energies has become more than necessary and is now one of the main challenges of our society. In 2018, the total final energy consumption of the world reached 116 PWh compared to 54 PWh in 1973 and will continue to grow significantly [IEA 2020a]. Currently, 19.3 % of this energy is consumed as electricity [IEA 2020a] and the International Energy Agency (IEA) forecasts a rise of about 60% in the world's electricity demand between 2016 and 2040 in its New Policies Scenario [IEA 2017], which will require to significantly increase the electricity production capacity. However, non-renewable energy sources such as coal, natural gas, nuclear and oil are still mostly used today to generate this electricity. Among these, coal represents the most important part in the total world electricity generation with 38.2 % in 2018 [IEA 2020a].

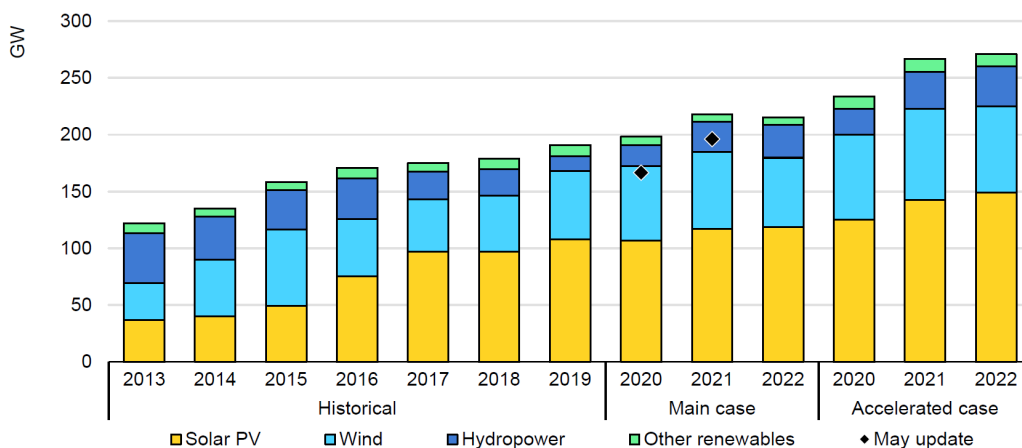
The use of these non-renewable sources releases large amounts of greenhouse gases, such as carbon dioxide, methane and nitrous oxide into the atmosphere, resulting in climate change and global warming. In 2017, the average global temperature has surged about 1.0 °C (likely between 0.8°C and 1.2°C) compared to the 1850s [IPCC 2018], the oceans warming rate was about 0.11 °C per decade over the period 1971 to 2010, and the global sea level has risen by about 19 cm over the period 1901 to 2010 [IPCC 2013, WorldBank 2012]. Climate change is also causing drastic changes in the earth environmental balance. Glacier size in many mountainous domains has dramatically decreased and food harvests are increasingly affected by droughts becoming more important in some parts of the world [IPCC 2014]. To limit climate change and reduce greenhouse gas emissions into the atmosphere, actions have to be taken now to change the global energy policy and to support the use of renewable energy sources.

To address this concern, the 2015 United Nations Climate Change Conference (COP 21) negotiated the Paris Agreement which is a legally binding international treaty on climate change.

Chapter 1. Introduction

This agreement was adopted by 196 Parties that officially recognized the need for a global response to climate change and committed to limit it. The objective of the Paris Agreement is to stabilize the rise in the global temperature. It intends to keep the increase to less than 2 °C above pre-industrial levels, with strong efforts put in place to limit the increase to 1.5 °C. In addition, this agreement forces each party to determine, plan and regularly report on its contribution to the mitigation of global warming. These decisions and objectives promote the transition towards a low-carbon society, thus enhancing the need of clean energy production. This provided substantial opportunities for renewable energy research, development and industrialisation.

Ensuring a sustainable and environmentally friendly society definitely is a tough challenge and, as mentioned above, requires among other changes a radical modification of our energy sources, more specifically making a more intense use of renewable sources such as wind, hydro or solar technologies. Figure 1.1 presents the world renewable electricity net capacity growth for the different renewable technologies over the year 2013-2019 as well as two scenarios (main and accelerated) for the years 2020-2022. Over the past years, the increase of renewable technologies as electricity sources has been substantial and among them, photovoltaic (Solar PV) is foreseen to play a significant role in the world electricity production, thus helping to mitigate climate change [IEA 2014]. Photovoltaic energy indeed features numerous assets as solar radiation is abundant, free, natural and unlimited. Impressively, the amount of energy coming from the sun and reaching the earth in one year corresponds to more than 7'500 times the yearly primary energy consumption of humanity [World Energy Council 2010]. Thus, this energy source has a great potential to fulfill large-scale energy demands all over the world.



IEA. All rights reserved.

Figure 1.1 – World renewable electricity net capacity growth by technology 2013-22 with two scenarios, main and accelerated. The black dot points are the data of May 2020. Image taken from [IEA 2020b].

1.1.2 Cost decrease and competitiveness

Overcoming such worldwide challenges requires new energy strategies, thus fostering the creation of important photovoltaic businesses and competitive technologies. To compete with non-renewable electricity sources, a low levelized cost of electricity (LCOE) of Solar PV energy is required. This was achieved in 2013, when it fell below the LCOE of coal. Since then, the LCOE of Solar PV has continued to show a significant decrease to the present day, demonstrating an impressive overall reduction of 90% since 2009 and becoming the cheapest electricity source in history (see Figure 1.2). In this context, Solar PV was crowned “king of the world’s electricity markets” in IEA report 2020 [IEA 2020c]. This impressive reduction of LCOE was made possible thanks to continuous research and development efforts to improve the energy conversion efficiency and to political incentives, such as feed-in tariffs, in addition to efforts at many different stages along the value chain (raw materials, devices manufacturing, PV modules installation, economy of scale). In the highly competitive PV market, manufacturing companies are always seeking a competitive edge to offer the lowest energy price. In this regard, one of the most direct approach, which is still relevant today, is to further decrease the LCOE of Solar PV energy by improving the PV modules energy conversion efficiency, ideally at fixed or even reduced cost per module [Wang 2011]. Nowadays, as the cost of the PV modules contributes to about 39% of the total expense, whereas the other 61% stand for the balance of system (BOS) [ITRPV 2020, Fraunhofer ISE 2020], it is also relevant to improve the module efficiency at a constant module cost per Wp. As a PV module is made up of several individual solar cells, improving the energy conversion efficiency of these cells is a direct way to improve the module efficiency. While simple to state, actually achieving this goal requires intense research efforts, and different solar cell technologies are competing on the market and at academic level to demonstrate solar devices with increased efficiency but still based on cost-effective manufacturing processes and materials.

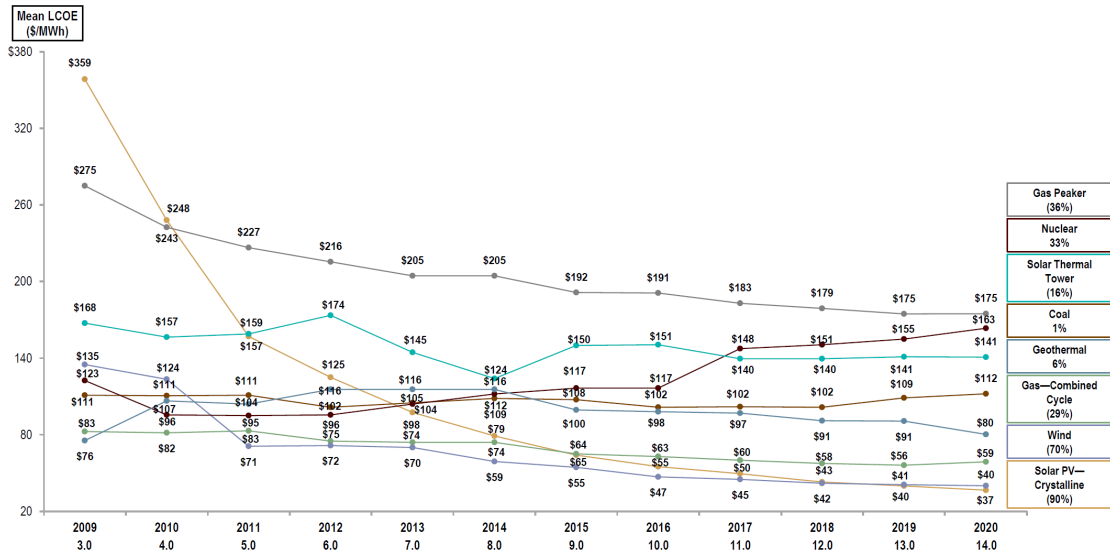


Figure 1.2 – Levelized Cost of Electricity Comparison — Historical Utility-Scale Generation Comparison. Taken from [Lazard 2020].

1.1.3 Photovoltaics technologies and current market status

Currently, about 95% of the global photovoltaic modules production is based on crystalline silicon (c-Si) wafer solar cells [ITRPV 2020]. Various c-Si based technologies have been and are currently developed aiming at continuously increasing the solar cells energy conversion efficiency. The first standard c-Si-based solar cell technology which emerged on the market and in production lines is based on a diffused homojunction with a fired-through metal grid at the front and a full-area aluminium metal contact at the rear, providing back surface field (BSF), hence the name “Al-BSF” referring to such devices (see Figure 1.3a). This architecture features direct metal-silicon contacts which are highly recombinative, i.e., where both electrons and holes recombine at a rate only limited by their thermal velocity, thus limiting the efficiency of such devices to about 20 % in production with the best-in-class Al-BSF device featuring 20.29 % efficiency [Kim 2017].

To achieve a trade-off between the passivated and the contacted areas of the solar cell, different architectures such as the Passivated Emitter and Rear Cell (PERC) [Blakers 1989] and the Passivated Emitter and Rear Locally Diffused Cell (PERL) [Zhao 1999] were developed. Such devices demonstrated improved efficiencies over the standard Al-BSF devices, with up to 23.45 % efficiency for the PERC architecture at industrial scale [JinkoSolar 2017]. A schematic cross section of the PERC technology is given in Figure 1.3b. Going even further, carrier selective passivating contacts (CSPCs) nowadays make it possible to overcome the trade-off between passivation and contact area by enabling a full area passivation while still ensuring an efficient carrier extraction, hence leading to an important efficiency increase. Prominent examples of CSPCs are (i) the doped polysilicon on oxide junction technology, with chemical

passivation done by thin tunnelling oxide layers, referred to as POLO [Römer 2014] or TOPCon [Feldmann 2014] (see Figure 1.3c) and (ii) the amorphous/crystalline silicon heterojunction (SHJ) technology, based on amorphous silicon layers for chemical passivation [Tanaka 1992] (see Figure 1.3d). Remarkably, these two technologies demonstrated over 25% efficiency for both side-contacted devices at research level [Adachi 2015, Richter 2021] and recently, Hanergy demonstrated SHJ solar cells featuring 25.11% efficiency in pilot line production [Ru 2020]. Note that most of the aforementioned technologies and materials can be integrated into an interdigitated back-contact (IBC) design, where the contacts are placed at the back of the device. Such IBC architectures permit the reduction of optical losses occurring at the front side of the solar cell (hence a higher generated current), but usually lead to a more complex process flow, and thus to higher costs. IBC solar cells have however demonstrated up to 26.7 % efficiency [Yoshikawa 2017] using SHJ passivating contacts at research level, and 25 % in mass production, most probably using poly-Si-based contacts [Smith 2014]. Four schematic cross sections of typical monofacial Al-BSE, PERC, TOPCon and SHJ solar cells are given in Figure 1.3 and a selective overview of the efficiencies of some of the solar cell technologies discussed above is given in Table 1.1. Note that these four technologies can feature a bifacial configuration.

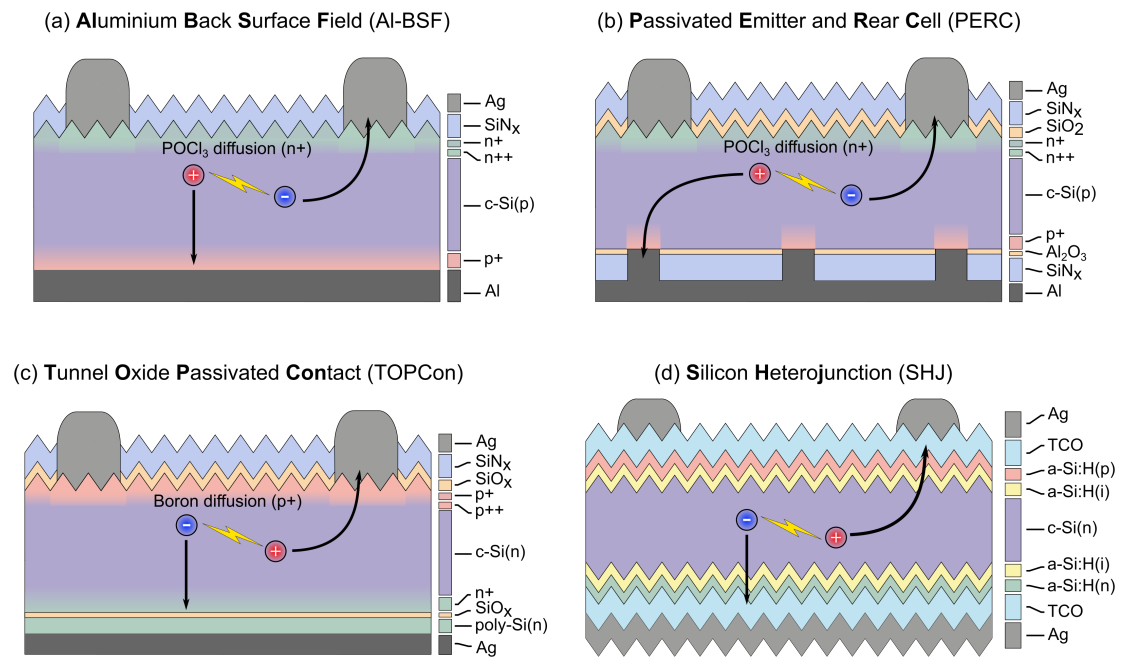


Figure 1.3 – Schematic cross section of typical monofacial (a) Al-BSE, (b) PERC, (c) TOPCon and (d) SHJ solar cells.

Technology	Type	Area (cm ²)	J_{SC} (mA/cm ²)	V_{OC} (mV)	FF (%)	Eff. (%)	Reference
Al-BSF	Prod.	245.7 (ta)	38.76	647	80.92	20.29	[Kim 2017]
PERC	Prod.	245.7 (ta)	*	*	*	23.45	[JinkoSolar 2017]
PERC	Prod.	261.4 (ta)	41.14	693.2	82.63	23.56	QCells Europe
TOPCon	Lab-scale	4.0 (da)	42.05	732.3	84.3	26.0	[Richter 2021]
SHJ	Lab-scale	151.9 (ap)	40.80	738	83.5	25.10	[Adachi 2015]
SHJ	Pilot	244.45 (ta)	39.55	747	85.0	25.11	[Ru 2020]
IBC-POLO	Lab-scale	4.0 (da)	42.62	726.6	84.3	26.1	[Green 2021]
IBC-SHJ	Lab-scale	79.0 (da)	42.65	738	84.9	26.7	[Yoshikawa 2017]

Table 1.1 – Overview of the performance of some selected best-in class single junction c-Si based solar cells featuring various technologies.

Nowadays, the photovoltaics (PV) world market is composed of 20% of Al-BSF cells and up to 72% of the so-called "PERx" family, namely PERC, PERL, and PERT solar cells in addition to the TOPCon solar cells. The last 8 % is shared by the emerging PV technologies which are the SHJ (referred in Figure 1.4 to as HJT, "HeteroJunction Technology") and the back-contact cells (see Figure 1.4). For the reasons outlined above in section 1.1.3, the highly competitive PV market is driven by the continuous improvement of the PV modules energy conversion efficiency. Consequently, technologies unable to maintain a steep improvement of their efficiency are expected to quickly disappear from the market. This is illustrated in Figure 1.4 where it is observed that the Al-BSF technology is expected to be totally wiped out off the market by 2027. Even the current workhorse of the PV industry, namely the PERx family, having reached its maximum achievable energy conversion efficiency, is expected to see fierce competition from alternative single-junction concepts with higher efficiency as early as 2022, which are the carrier-selective passivating contacts solar cells, such as SHJ and TOPCon technologies, as well as back-contacted solar cells. Overall, CSPC-based technologies are expected to take significant world market shares in the coming years.

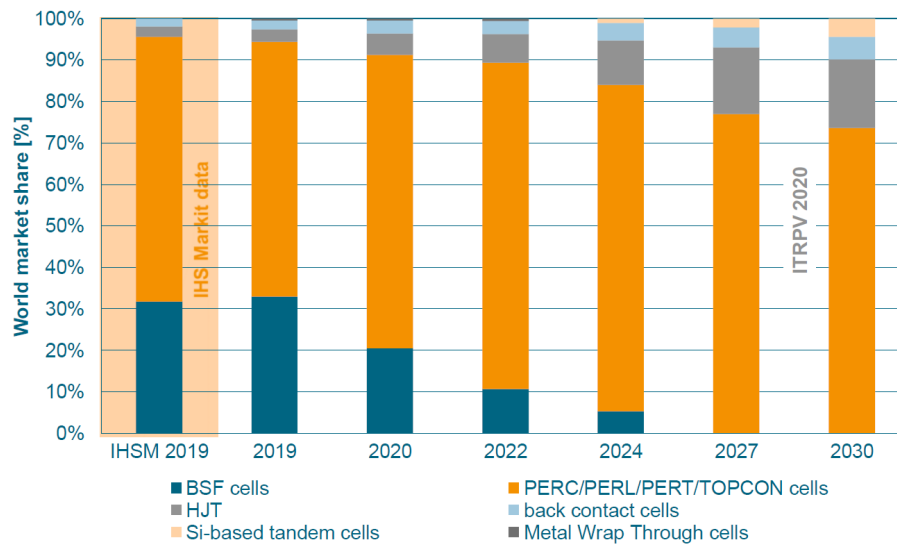


Figure 1.4 – World market share of the different cell technologies. Taken from [ITRPV 2020].

Figure 1.5 presents the breakdown of PV module production by region over the years 1997 to 2019. Until 2008, Europe was representing an important part with more than 25%, completed mainly by Japan, US, and the rest of the world (ROW). Since 2005, China (including Taiwan here) started to drastically increase its PV module production capacity and reached an impressive 67% of the world’s PV production in 2019 from about 6% in 2005. Thus, China is nowadays leading the Solar PV module production over the world.

Recently, European politicians and private investors have pledged to rebuild the European technological leadership in the PV sector. This results mainly from the European Green Deal which is the European Commission’s new growth strategy for the European Union’s (EU) economy, people and planet, aiming to complete the Paris Agreement’s objectives [European Commission 2019]. The Green Deal commits to achieving climate neutrality by 2050 and paves the way for an energy and economic transition that is fair and socially just. To achieve these goals, the deal presents a series of actions to be taken by the EU in the coming years across all sectors such as energy, transport, industry, finance and trade, in order to reach climate neutrality. This deal is a potential game-changer for Europe. Indeed, moving towards a carbon-neutral economy is a unique opportunity to create new, skilled and local jobs, support the competitiveness of EU businesses and accelerate investment in innovation and clean energy technologies to ensure Europe’s industrial leadership. The European Green Deal and the upcoming legislation on Sustainable Finance will therefore play a critical role in establishing the required funds and ensuring that future investments are directed towards renewable energy sources, such as solar PV, and assets that will support the large-scale industrial deployment of existing innovative European renewable technologies. In particular, a recent report from SolarPower Europe and LUT University [SolarPower Europe & LUT University 2020] states that, considering the leadership scenario to achieve the ambitious 1.5°C Paris Agreement

target, a massive electrification of energy will be necessary and, among electricity sources, Solar PV is expected to represent above 7 TW in Europe. To fulfill these expectations, solar PV manufacturing must therefore be strengthened as a key element of the European green economy and must be a major element of Europe’s industrial strategy. The solar sector must be established as a strategic value chain to ensure Europe’s security of supply and industrial leadership in clean energy technologies.

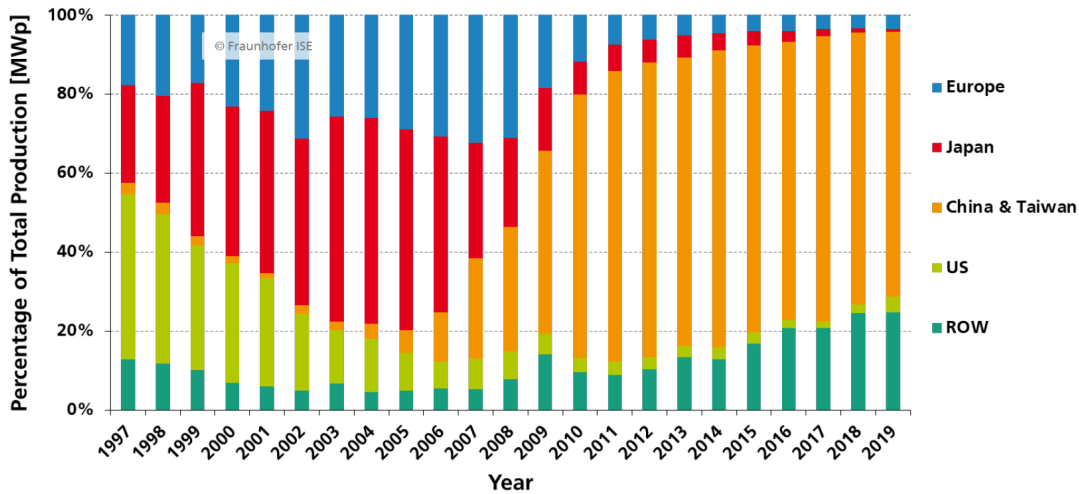


Figure 1.5 – PV module production by region over the years 1997 to 2019 given in percentage of Total MWp produced. Taken from [Fraunhofer ISE 2020].

Achieving these goals calls for major technological breakthroughs to increase the PV modules’ energy conversion efficiency by at least 35% and reduce the turn-key system costs by at least 50% by 2030 compared to 2015 [TWG 2017]. High efficiency is crucial for EU Solar industries to compete with Chinese prices and to contribute to the EU’s energy independence. In this context, as presented above, CSPC-based solar cell technologies are expected to bring a competitive edge to Solar PV companies by further reducing the cost of PV and enabling a strong development of solar cell manufacturing in EU. In particular, among CSPC-based solar cells, the SHJ technology has a clear potential to enter the world market with competitive prices in addition to setting itself apart from competing technologies (see Figure 1.4). The Technology Readiness Level of the SHJ technology is currently between applied research and industrial deployment, and efforts are ongoing to reach its efficiency limit in the coming years. Historically, SHJ solar cells were first industrialised by Panasonic/Sanyo in Japan and the PV-Lab, CSEM, Meyer-Burger, and Indeotec in Switzerland played a significant role in developing simple approaches to industrialization. Nowadays in Europe, the ENEL Group in Italy leads the way for SHJ industrialisation, followed by EcoSolifer in Hungary. In addition, HEVEL in Russia is an important partner for Europe in the deployment of SHJ devices. Recently, the Meyer Burger Group joined the race and is preparing for large-scale SHJ module manufacturing in Germany. Finally, the SHJ technology is foreseen to experience a large industrial deployment in other countries, especially in China.

1.2 Motivation

The use of carrier-selective passivating contacts (CSPCs) has been theoretically identified [Cuevas 2015] and experimentally demonstrated [Yoshikawa 2017, Haase 2018] to be the most promising way to reach the practical energy conversion efficiency limit of single junction, crystalline silicon (c-Si) based solar cells. In particular, as presented in Table 1.1, among the CSPC technologies, SHJ solar cells demonstrated high efficiency up to 25.1% in double side configuration and up to 26.7% with IBC configuration. However, comparing the final performances of [Adachi 2015] and [Ru 2020], it is observed that to achieve similar efficiency, different trade-offs are present between the cell parameters, i.e., between high passivation quality (V_{OC} and V_{MPP}), low resistive effect (R_s), and efficient light collection (J_{SC}). Indeed, nowadays, one important efficiency limitation of c-Si solar cells using CSPCs remains optimizing these different trade-offs to allow for high transport quality together with efficient light collection, resulting eventually in high device efficiency. These trade-offs are due to a challenging optimization of the different components building CSPC-based solar cells. More precisely, carrier-selective passivating contacts are composed of layers of different materials featuring various properties, and the resulting coupling of their physical properties shapes the overall device performance. The understanding of CSPCs is then an important lever to appreciate the different trade-offs and to mitigate the electrical and optical losses together.

In particular, CSPCs determine the electrical properties of a solar cell by defining its (i) passivation ability, (ii) selectivity ability, and (iii) terminal electrodes. These are the electrical functions required to extract efficiently the photogenerated carriers from the silicon bulk and to inject them into an external load. In this regard, one way to overcome the remaining efficiency losses is to mitigate the transport losses affecting the extraction of photogenerated carriers [Procel 2018] by improving the passivation quality and by reducing the resistive losses, both resulting in an improvement in the overall selectivity of the CSPCs of solar cells. However, the conceptually simple CSPCs are in practice difficult to manufacture, and only approximate concepts have been developed so far. Particularly, the properties of interest of the individual components constituting CSPCs are still not clearly identified, and their potential experimental characterizations remain arduous. Therefore, predicting how good or adapted a component will be for a CSPC and how it will influence the global solar cell performance is challenging. Moreover, the three required electrical functions are generally intertwined, making it even more difficult to change only a component of the CSPC without affecting its global properties and thus the whole solar cell properties. As a consequence, a trial-and-error method is often used to optimize CSPCs. There is then a lack of general understanding and no clear methodology exists today to predict whether a component with given properties will act as an efficient part of CSPCs or not and how it is linked to the whole solar cell properties. This thesis aims at bridging this comprehension gap, as will be detailed below.

1.3 Objectives and structure

1.3.1 Objectives

This thesis aims at accurately describing, quantifying, and mitigating the electrical transport losses occurring in state-of-the-art SHJ solar cells, with a particular focus on the CSPCs part of these cells, as well as providing technological means to mitigate these losses. As mentioned above, the SHJ technology demonstrated up to 26.7% efficiency. However, when the CSPCs of SHJ solar cells are not properly optimized, important electrical transport losses occur, strongly capping the solar cell performance [Chavali 2018]. Previous investigations reported that the TCO/metal interface within the CSPCs of SHJ solar cells is not the limiting factor for the electrical losses [Lee 2014, Gogolin 2014]. Therefore, the work of this thesis focuses on investigating the thin hydrogenated silicon layers and TCO layers, which constitute together the major part of the CSPCs of SHJ solar cells, aiming at eventually decreasing the electrical transport losses occurring in the whole device.

First, it will be demonstrated that the term *contact* has long been used in the literature of solar cells with varying meanings, often mixing different electrical functions. To address this ambiguity, this thesis aims to provide a generalized and unambiguous description of contacts in solar cells, allowing one to accurately investigate – and eventually mitigate – the electrical as well as optical losses affecting state-of-the-art SHJ solar cells. This revised theoretical framework is intended to make it possible to study the entanglement of the different components of CSPCs.

Secondly, this thesis aims to define and develop a careful methodology to experimentally characterize the properties of the CSPCs, their components as well as the potential of each component to act efficiently as part of CSPCs. Physical key parameters as well as their adapted characterization methods will be sought to unveil the links between the final solar cell performance and the resulting electrical transport quality. Advanced characterization methods will be developed and applied to the different components of solar cells. Eventually, this novel methodology and these novel descriptions and characterization methods will make it possible to engineer layers allowing one to build high-quality CSPCs where transport losses are efficiently mitigated by targeting high selectivity and passivation quality, while still enabling high light collection. The best CSPC schemes will then be implemented into complete SHJ solar cells to fully validate their electrical transport properties. Their ability to adapt to different architecture constraints (monofaciality, bifaciality and IBC) will also be investigated.

The overarching objective of this thesis is to bridge the gap between theory and experiment by bringing new, advanced and improved developments, methodologies, characterization methods, and information about the electrical characteristics of SHJ solar cells thanks to measurable parameters, as well as identifying suitable materials and processing for achieving this goal. New material layers will eventually be integrated into best-in-class SHJ devices, to demonstrate reduced transport losses, evidenced by the achievement of high *FF*. This work

will hence contribute to spread the SHJ and CSPC knowledge required to reach high efficiency solar cells while keeping simple process steps allowing for a low fabrication cost. As a future outlook, this approach will be generalized to other solar cell technologies.

1.3.2 Structure of the thesis

After a general introduction to the photovoltaics technologies presented in the current chapter, the different topics addressed in this thesis are structured as follows:

- **Chapter 2** discusses the concept of *contact* in solar cells in detail along with the fundamental operating principles of solar cells. A generalized and unambiguous description of contacts is presented by introducing the new terminology of *shell* and a novel characterization methodology using two new approaches, named *top-down* and *bottom-up*, is presented.
- **Chapter 3** presents the main processes and systems used during this thesis for the fabrication and characterization of SHJ devices. Particular emphasis is put on various layer and cell characterization techniques, which encompass a significant and in-depth work of development, understanding, and optimisation.
- **Chapter 4** presents a novel characterization method based on an upgraded theoretical framework of transfer length method (TLM) measurements. TLM measurements under variable illumination are performed to further study the electrical losses induced by resistive effect in SHJ solar cells.
- **Chapter 5** presents an in-depth experimental study to accurately investigate and characterize the electrical losses affecting the collection of photogenerated carriers in SHJ solar cells. In particular, the development of multilayers is conducted to allow for electrical transport losses mitigation by tuning the shell properties at different levels. This study combines the methodologies presented in chapter 2, the characterization methods presented in chapter 3, as well as the advanced TLM measurements presented in chapter 4.
- **Chapter 6** presents the integration of the most promising shells featuring the different layers developed and presented in chapter 5 inside the best baseline solar cells which are processed during this work.
- **Chapter 7** summarizes the main results obtained in the scope of this thesis, presents a general conclusion on the outcomes of this work as well as possible future developments, and finally discusses the prospects of this work.

1.4 Contribution to the research field

This work contributes to the field of research in silicon-based photovoltaic devices as well as in thin-film and semiconductor technologies in many ways which are presented in this section.

First, we pinpointed the ambiguities of the term *contact* as currently employed in the literature of solar cells, and we proposed a new generalized and unambiguous description of the so-called *contacts* using the terminology of *shell*. This was demonstrated to allow one to accurately investigate and eventually mitigate the electrical as well as the optical losses affecting state-of-the-art solar cells. Then, we proposed a novel characterization methodology using two new approaches named the *top-down* and the *bottom-up* approaches. These define a characterization procedure designed to independently track the properties of the material layers used to build the shells, as well as the performance of the solar cells incorporating the shell along the different process steps. Significantly, this was demonstrated to provide an efficient way to link the resulting properties of the shells to the final performance of the solar cells. Overall, our work brings new perspectives and descriptions of the term *contact* and how to identify and address the electrical as well as the optical losses of solar cells which may complement the global understanding in the photovoltaics community.

Secondly, we developed a new and advanced method to characterize the electrical transport quality of solar cells based on an upgraded theoretical framework of transfer length method (TLM) measurements. We performed TLM measurements under variable illumination to further study specific SHJ shells including different electron and hole-selective components. Using this improved characterization method, we demonstrated that ρ_c increases with the illumination augmentation, i.e., with the rise of the injected carrier density. Our results pinpointed the importance of considering the MPP injection level to measure the ρ_c in order to accurately study the transport losses and their impact on the *FF* of solar cells. In addition, this method showed that different shell parts featuring various thin silicon layers are impacted differently by illumination. Furthermore, we evidenced that the impacts on the ρ_c values induced by different illuminations or by different c-Si bulk doping densities were significantly different. Finally, we demonstrated that in addition to the wafer doping density, its polarity (p or n-type) plays also a major role for the determination of the value of ρ_c . Consequently, we investigated the applicability of TLM measurements under variable illumination to measure p-type shell parts on n-type c-Si wafers. Comparing the ρ_c values at high illumination of similar p-type shell parts deposited either on c-Si(n) or on c-Si(p) wafers, we observed that these values are of the same order of magnitude. However, two major observations put in evidence that the relevance of TLM under variable illumination to measure the value of ρ_c for the case of p-type shell parts deposited on c-Si(n) wafers is still questionable. Additional studies are required to complete the validity of this method and to complete the global description and understanding of the physical phenomena which are involved when performing such characterizations. Overall, our results build the basis for further investigation towards accurate ρ_c measurement which is a prerequisite for building precise R_S breakdowns of solar cells.

Thirdly, we demonstrated that the combination of the *top-down* and the *bottom-up* approaches is a relevant methodology to develop different material layers, investigate their resulting properties as well as the physical properties coupling arising at different levels inside the shells, and finally relate it to the final performance once integrated in actual solar cells. Our study demonstrated how combining both methods allows one to unveil the resulting transport quality by first investigating selected physical key parameters of given material layers with the *top-down* approach and, secondly, to study how they impact the final solar cell performance by analysing the shell properties obtained with the *bottom-up* approach. In addition, this was demonstrated to make it possible to optimize the resulting shell performance according to the different architectures the shell must fit in. In particular, the development of multilayers was proven to allow for electrical transport losses mitigation by decoupling the different material contributions and by tuning the material properties coupling arising at different levels inside the shell. In addition, we demonstrated the potential of multilayers to release the different electrical trade-offs the shell has to deal with.

Finally, we demonstrated that combining the shell concept with both the *top-down* and the *bottom-up* approaches allows us to improve our solar cell baseline by focusing on electrical and optical losses mitigation. Thanks to this methodology, the final shell characteristics obtained and their integration in actual devices made it possible to reach FF up to 83.2%, in the case of full area 6-inch solar cells, and efficiency up to 25.45% for SHJ IBC cells with a size of 5 cm \times 5 cm. In addition, we conducted further optimizations of the optical properties of shells along the electrical ones. From this optimization, a high J_{SC} of 40.81 mA cm⁻² was obtained for 2 cm \times 2 cm screen-printed SHJ monofacial solar cells and, combining high electrical and optical properties, an impressive efficiency of 24.24% was demonstrated using AZO layers, which is an indium-free TCO.

Our findings open new perspectives for SHJ solar cells by bringing novel methodologies as well as improved and advanced characterization methods which provide additional understanding of SHJ electrical losses. In particular, this work contributes to bridge the gap between theory and experiment by bringing new, advanced and improved developments, methodologies, characterization, and information about the electrical properties of SHJ solar cells. Overall, this work contributes to spread the SHJ and CSPCs knowledge required to reach high solar cell efficiencies. This work was carried out in the framework of the european projects NextBase and AMPERE. Finally, part of the work presented in this thesis was performed in collaboration with various colleagues inside the PV-Center (CSEM) and at PV-Lab (EPFL) as well as with members of Meyer Burger Research AG, Delft University of Technology (TU Delft) and CEA-INES. The publications in peer-reviewed journals and conference presentations related to this thesis work are given in Appendix.

2 Contacts in Solar Cells

Summary

In this chapter, the concept of *contact* in solar cells is discussed in details along with the fundamental operating principles of solar cells. First, the role of the contact and its definition are detailed, synthesized and put into perspective with different solar cell technologies. Secondly, a generalized and unambiguous description of contacts in solar cells is presented by introducing the new terminology of *shell*. This terminology aims to accurately investigate – and eventually mitigate – the electrical as well as the optical losses affecting state-of-the-art solar cells. Then, an overview of the fundamental physics of semiconductor-based solar cells is given, including the electron and hole generation mechanisms and the different physical phenomena impacting the carrier transport in silicon solar cells. These phenomena are bulk and surface recombination, passivation, selectivity, and resistive effects. Furthermore, a description of the carrier transport in the specific case of the silicon heterojunction technology and its impact on the efficiency of such devices is given. Finally, a novel characterization methodology using two new approaches named *top-down* and *bottom-up* is presented.

2.1 Generalized operating principle of solar cells

In the approach proposed by [Cuevas 2015], a solar cell can be seen as a balloon inflated with light-generated carriers. This “balloon” corresponds to the solar cell absorber where electron-hole pairs are generated by converting the energy of the incoming light and is illustrated in Figure 2.1a. In general, reaching the maximal power conversion efficiency limit of a given absorber requires to extract these photogenerated carriers from the absorber bulk with as few opto-electrical losses as possible. To do so, one optical and three electrical functions must be fulfilled:

- (i) To maximise the electron-hole pairs photogeneration inside the absorber bulk. This calls for a smart optical design of the solar cell so as not to hinder the light absorption in the absorber, namely by minimizing the reflection and the parasitic absorption losses (Figure 2.1b).
- (ii) To avoid recombination, i.e. loss of carriers, in the bulk and at the surface of the absorber, therefore maintaining the electron and hole excess concentrations at their highest. This is called *passivation* and is introduced in details along with recombination mechanisms in section 2.2.2 (Figure 2.1c).
- (iii) To spatially separate the holes and the electrons at different absorber locations in order to create a current flow inside the device. This process is called *selectivity* and is described in more details in section 2.2.3 (Figure 2.1d).
- (iv) To provide terminal electrodes to eventually extract the carriers from the absorber and to inject them into an external load. This defines the way out for the photogenerated carriers and sets the total current flow direction (Figure 2.1e).

These individual functions required to design an efficient solar cell are illustrated in Figure 2.1. Note that the coupling of the aforementioned electrical functions ((ii), (iii), and (iv)) will directly define the *electrical transport* quality of the solar cell, where electrical transport denotes the flow of both carrier types from the absorber to the external load (see section 2.2.5).

In practice, it is so far not possible to use a unique material to perfectly achieve all these functions simultaneously. To circumvent this issue, both sides of the absorber are completed with either materials with locally changing properties or stacks of several thin layers made from different materials, or combinations of these two, depending on the solar cell technology. These will fulfill the optical requirement for efficient light collection and absorption inside the absorber while providing local or global passivation as well as the so-called *contacts* to efficiently extract the photogenerated carriers. However, as various solar cell technologies were developed (as introduced in chapter 1), the distinction between these different functions and notions began to mix as synergies appeared between them and new physical descriptions were established, leading to misleading uses of the term *contact*. Providing a clearer explanation is an important topic of this PhD work, and is done in sections 2.1.1 and 2.1.2 below.

2.1. Generalized operating principle of solar cells

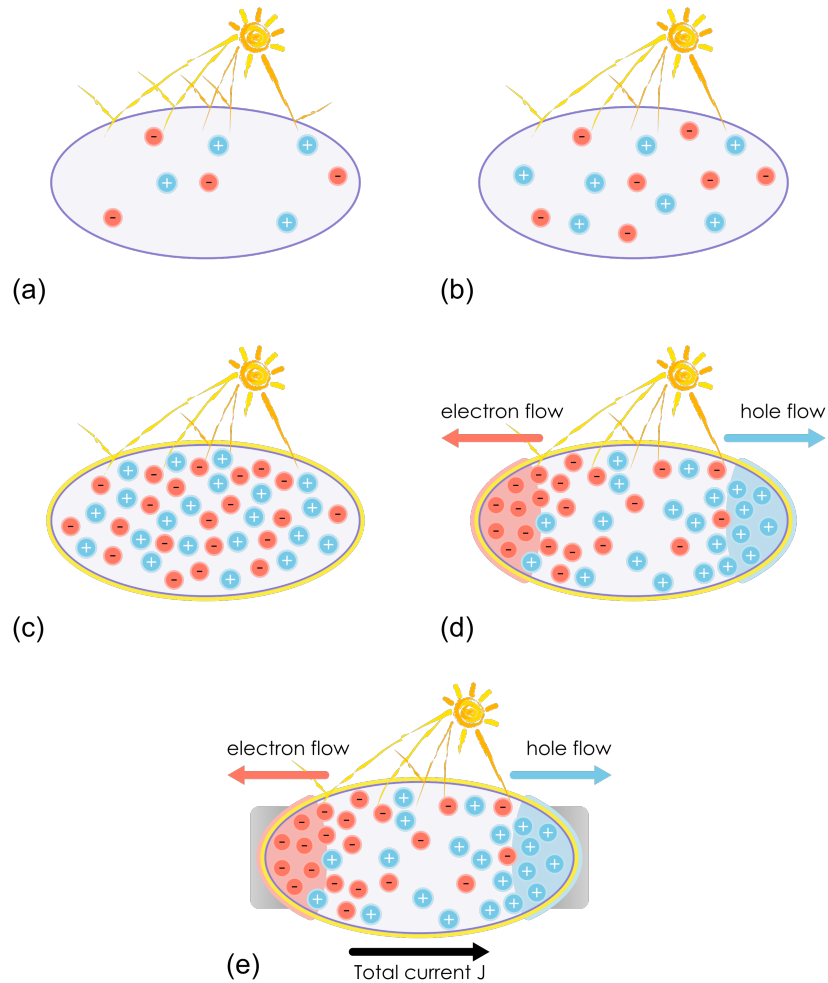


Figure 2.1 – Schematic description of the operating principle of a solar cell illustrated using the "balloon" approach with (a) electron-hole pairs generation inside the absorber, (b) minimization of the reflection and the parasitic absorption losses, (c) surface passivation, (d) carrier selectivity and (e) terminal electrodes.

2.1.1 Current ambiguities in the description of solar cell contacts

The term *contact* has long been used in the literature of solar cells with varying meanings and electrical functions, but always involves the extraction of photogenerated carriers. Going back to its general and fundamental definitions, the term contact can be employed for (i) a connection between two points in an electrical circuit, (ii) a common area with two conductive parts touching or coupled, (iii) a conductive element of a component that touches or is coupled with another conductive element to ensure the passage of current, or (iv) simply each part that ensures electrical contact. In the case of solar cells, the commonly employed contact schemes consist of several stacked materials and/or a single material with locally changing properties. As prime examples, the PERC and the SHJ technologies which were introduced in chapter 1

are depicted in Figure 2.2 with the complete description of the different involved materials.

In PERC devices, the term *contact* is usually meant to describe the areas where metallic materials directly touch the silicon wafer. More precisely, for the PERC device depicted here (Figure 2.2a), the front contact is composed of a silver grid locally fired-through the passivating silicon nitride (SiN_x) and silicon oxide (SiO_2) layers, therefore *contacting* the selective n-type POCl_3 diffusion doping (n^{++}) at the front surface of the c-Si(p) wafer. Interestingly, note however that to create a *good* contact - i.e. a contact with low electrical losses - the POCl_3 front diffusion usually features higher doping (n^{++}) below the silver contacts than between them (so-called *selective emitter* [Hahn 2010, Weber 2018]). At the rear, the contact is composed of aluminium (Al) dots obtained by locally opening the rear passivating aluminium oxide Al_2O_3 and SiN_x layers. Importantly here, besides *contacting* the silicon bulk, the PERC rear Al contact also creates selective p-type doped regions (p^+) at the contact dots, owing to the formation of an Al-Si eutectic during the curing of the Al paste. Therefore, the Al paste must be designed to provide sufficient selectivity while ensuring optimal contact. Thus, in contrast to the PERC front contact, its rear contact features an additional functionality, as it fosters carrier selectivity (here towards holes) in addition to fulfilling its role of terminal electrode. Moreover, the front contacting and passivating layers must be optimized together to ensure high passivation and the possibility to fire-through the silver grid while neither damaging the selective diffusion nor creating a shunt. Finally, the SiN_x layers and doped regions inside the c-Si bulk must be optimized to enable optimal light collection and minimal parasitic absorption. Moreover, in this design, a critical trade-off between passivating areas and recombinative metal areas is present. Indeed, the areas below the metallized regions (Al and Ag) are highly recombinative, whereas the passivation is present only below the two passivating layers. Overall, it is of prime importance to understand that the design of the PERC contacts directly results from acknowledging that fulfilling all the opto-electrical functions required for efficient solar cells at the same time is challenging, and that trade-offs consequently have to be made most of the time. Hence, the localization of the front and rear contacts in PERC solar cells appeared as the best option to balance recombination and optical losses with proper passivation, carrier selectivity, and extraction.

The case of contacts in SHJ devices (Figure 2.2b) is completely different. Here, the term *contact* refers to the front and back stacks of materials composed of thin layers of four different materials which are intrinsic hydrogenated amorphous silicon (a-Si:H(*i*)), doped hydrogenated thin silicon layers (here in amorphous phase, a-Si:H(*n*) and a-Si:H(*p*)), transparent conductive oxide (TCO), and silver (Ag). In contrast to PERC ones, SHJ contacts do not need to be localized to mitigate recombination losses, as they are purposely designed to provide surface passivation. In that case the whole stack of layers features a global material properties coupling which defines the final passivation, selectivity and electrodes abilities, in addition to ensuring proper light collection and absorption within the silicon wafer. More precisely, the a-Si:H(*i*) layers provide chemical passivation whereas the doped thin silicon layers maintain and complete this passivation while providing selectivity. The TCO layers ensure the contact between the passivating selective layers and the silver grid at the front, and the silver blanket layer at the

2.1. Generalized operating principle of solar cells

back. The front TCO also provides lateral conductivity, acting as a lateral *contact* to the silver grid. Moreover, it optimizes the photogeneration by providing minimal light reflection and low parasitic absorption. Finally, note that the TCO coupled with the thin silicon layers define together the final passivation and selectivity ability of SHJ solar cells. Here again, we see that for SHJ devices, the *contacts* do not only act as terminal electrodes, but also efficiently provide the passivation and selectivity functions while fulfilling the optical requirements.

Thus, in both the PERC and SHJ cases, all these different layers complement each other to overcome the different trade-offs required to reach the optimal opto-electrical solar cell performance. To do so, the *contacts* take different shapes, materials and roles in addition to their initial function as terminal electrodes.

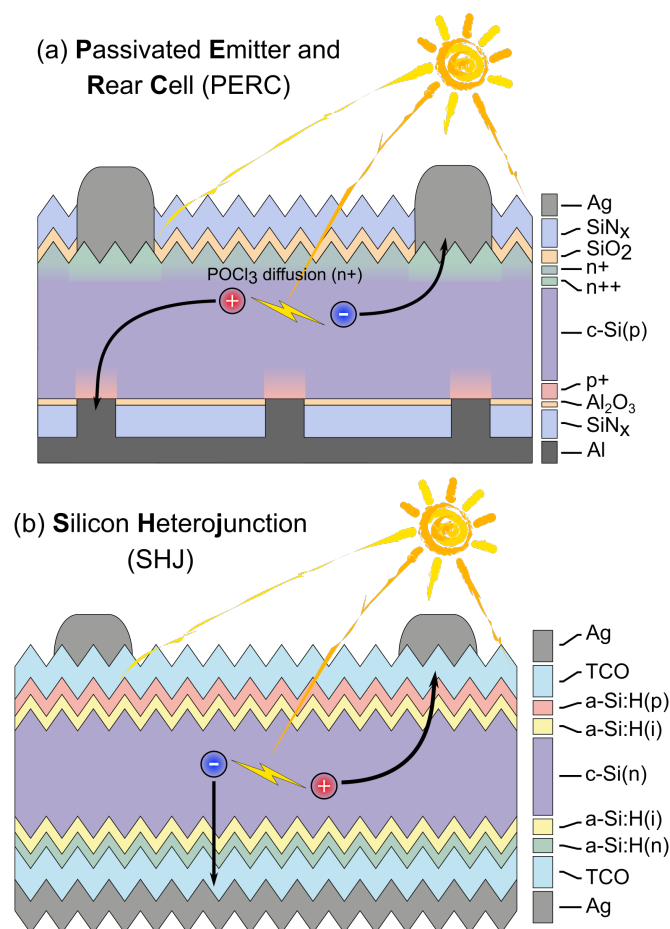


Figure 2.2 – Schematic cross section of a typical monofacial (a) PERC and (b) SHJ solar cell.

These examples evidence that the term *contact* in its common use for solar cells is rather confusing, as it encompasses many different materials, often providing multiple roles in addition to terminal electrode. Another limitation is that the term *contact* is generally limited to electrical concerns, neglecting the optical requirements for optimal light collection, which

bring significant constraints defining its final shape and properties. Therefore, different terminologies were previously introduced to describe in more details distinct parts of solar cell contacts. The terms *passivating contact* and *carrier-selective contact (CSC)* are used to refer to a material or a stack of materials providing passivation or selectivity, respectively, in addition to carrier extraction. Leaving aside the function of terminal electrode, the term *membrane* was introduced by [Würfel 2005] to describe materials providing selectivity, and similarly the term *skin* was proposed by [Cuevas 2015, Fell 2017] to describe passivation in addition to selectivity. Finally, following the pioneering work of [Yablonovitch 1985], the ability to provide selectivity and passivation in addition to carrier extraction has been recently defined as a *carrier-selective passivating contact (CSPC)*, i.e. a contact which passivates the surface of the absorber, and which blocks one type of carrier from escaping the absorber while allowing the other one to be extracted. Prime examples of CSPCs are the SHJ technology [Tanaka 1992], as well as various approaches based on a thin tunnelling oxide capped with polycrystalline silicon, such as TopCON [Feldmann 2014] and POLO [Römer 2014] mentioned in chapter 1. However, even with these new definitions, the term contact stays ambiguous as it can equally refer to many of its constituting sub-components [Koswatta 2015]. Indeed, the contact of solar cells is composed by various sub-contacts created between the different components, resulting in a misleading understanding and ambiguities when talking about the contacts present inside the contact of solar cell. In addition, importantly, when two or more components of a solar cell contact are stacked in thin layers, the resulting properties of the whole contact stack differ from the sum of the individual components properties, since a coupling of their properties appears. This is a major feature to take into account and will be detailed more precisely in section 2.1.2 below.

2.1.2 Shell of solar cells

Taking notice of the ambiguous use of the term contact, this thesis aims at providing a generalized and unambiguous description of contacts in solar cells, allowing one to accurately investigate – and eventually mitigate – the electrical as well as the optical losses affecting state-of-the-art solar cells: the terminology of *shell* [Senaud 2019].

As defined in the frame of this thesis, the shell must fulfil the three electrical functions required for efficient carrier extraction mentioned above, i.e., passivation, selectivity, as well as providing terminal electrodes. In addition, the shell must comply with optical requirements so as not to hinder light absorption in the absorber. More specifically, at the front side of solar cells, the shell must be highly transparent to minimize the parasitic absorption losses. At the rear side, depending on the solar cell architecture, the shell might be required to be highly transparent as well (e.g., to ensure a high bifaciality), but also to provide a high internal reflection to increase the photons' optical path in the absorber bulk. As a result, the most important challenge of a given shell is to fulfil all these electrical and optical functions simultaneously with as few losses as possible, to reach high quality light collection and carrier extraction, thus eventually allowing for high conversion efficiency once integrated in a solar cell. Depending on the solar

2.1. Generalized operating principle of solar cells

cell technology, the shell may consist of unique materials with locally changing properties, and/or in a stack of several thin layers made of different materials. As depicted in Figure 2.2, the doping gradient in the silicon absorber used in the PERC technology is a typical example of the former, whereas the intrinsic and doped hydrogenated amorphous silicon, transparent conductive oxide (TCO), and metal layer stacks in the SHJ technology is a perfect example of the latter. Generalizing, it thus means that the shell includes all parts of the solar cell located at both sides of the absorber from its near-surface modified region to the last terminal electrodes included, before the external load. Importantly, the global shell characteristics and its ability to provide the required electrical and optical functions, are eventually defined by the global properties coupling of all its different components and of the absorber bulk. In the specific case of the electrical properties, this coupling is evidenced by the energy band bending arising when the different elements constituting the shell are deposited on the absorber. This makes it possible to pinpoint the changes in the interfaces and material properties along the transversal direction of the carriers flow¹. Note that due to this coupling, the “influence” of the shell might also extend into a part of the absorber bulk close to its surface, such as a space charge region (SCR) induced via the energy band bending.

To illustrate the shell concept, its application to the PERC and SHJ technologies is now detailed. In the case of the PERC technology, the shell is composed of the selective diffused POCl_3 at the front (with n^+ and n^{++} regions), the localized Al diffusion at the rear, the front and the back metal electrodes (back Al and front Ag), as well as the different passivating layers which are the SiO_2 and the SiN_x deposited at the front side and the Al_2O_3 and the SiN_x deposited at the back side of the $c\text{-Si}(p)$ bulk. Such a PERC shell is illustrated in Figure 2.3(a) and its corresponding energy band diagram below the contacted areas is illustrated in Figure 2.3(b). In the specific case of the SHJ technology, the shell is composed of the two stacks of the standard SHJ thin layers deposited at both side of the $c\text{-Si}(n)$ bulk. These are made out of thin intrinsic and doped hydrogenated silicon, TCO, and metal layers. Such an SHJ shell is illustrated in Figure 2.4(a)² and its corresponding energy band diagram below the contacted areas in Figure 2.4(b). In both cases, it appears clearly that the shell is then composed of several interfaces and sub-contacts defined by the coupling of the different material layers and the silicon bulk. These are highlighted as orange-hatched areas in Figures 2.3(a) and 2.4(a). In general, the coupling of the physical properties of the different shell material layers and those of the absorber bulk defines the overall opto-electrical properties of the solar cell and thus determines the final device performance. As a prime example, the front TCO of two side-contacted SHJ devices must be designed to provide minimal parasitic light absorption and optimal anti-reflection properties to foster photogeneration, as well as efficient lateral transport up to the metal grid, which depends on the finger spacing and on the TCO conductivity, while providing at the same time sufficient surface passivation and low resistive effect when combined with the thin silicon

¹Note that energy band diagrams do not reveal the lateral transport of carriers occurring inside the silicon bulk and the TCO in the case of the SHJ technology, and inside the doped emitter in the case of the PERC technology.

²Note that in back-contacted solar cells, the purposes of the front part of the shell are only passivation and optical losses minimization, since the carrier-selective and electrode aspects are performed by the rear part of the shell in addition to passivation.

layers. This results in complex top-down and bottom-up sequential optimizations (see section 2.3.1). Moreover, the SCR resulting from the silicon bulk properties coupling with the shell components determines the extent and the "range of influence" of the carrier-selective contact (CSC) in the case of PERC solar cells and the carrier-selective-passivating contact (CSPC) in the case of SHJ solar cells. These are illustrated in the orange and light-orange dashed areas in Figures 2.3(a) and 2.4(a). Overall, it is thus challenging to optimize only one part of a shell without affecting its global opto-electrical properties, as a single sub-component directly influences its final optical and electrical characteristics. Most importantly, the global resulting solar cell electrical properties are eventually shaped by the coupling of the physical properties of all the different material layers, including the silicon bulk, which defines the overall energy band diagram, presented in the space domain in Figure 2.3(b) for the PERC case and in Figure 2.4(b) for the SHJ case. In the case of the PERC band diagram, the SiN_x and the SiO₂ layers are not depicted as they are not involved directly in the vertical carrier transport. Their signature on the energy diagram is visible in the electron and hole quasi-Fermi levels (E_{Fn} and E_{Fp} , respectively). Indeed, their passivation ability, balanced by the recombination present below the metal contacting areas, defines the resulting quasi-Fermi level splitting, and thus the final energy band arrangement. In contrast, for the SHJ case, the thin silicon, TCO, and metal layers are all involved in the energy band diagram as they are all present in the vertical way of the carrier transport. In that case, the quasi-Fermi level splitting is defined by the coupling of the properties of all these involved layers. Thus, overall, due to these global material properties couplings, the addition, removal, or change of a single shell sub-component or of the c-Si bulk directly affects the global energy band arrangement, making it difficult to predict precisely *a priori*. Each component of the shell must then be developed considering its resulting coupling with all the other sub-components and the c-Si bulk. Closing this comprehension gap requires to take a closer look at the way the photogenerated carriers move within the energy band structure; this is the topic of section 2.2.5.

2.1. Generalized operating principle of solar cells

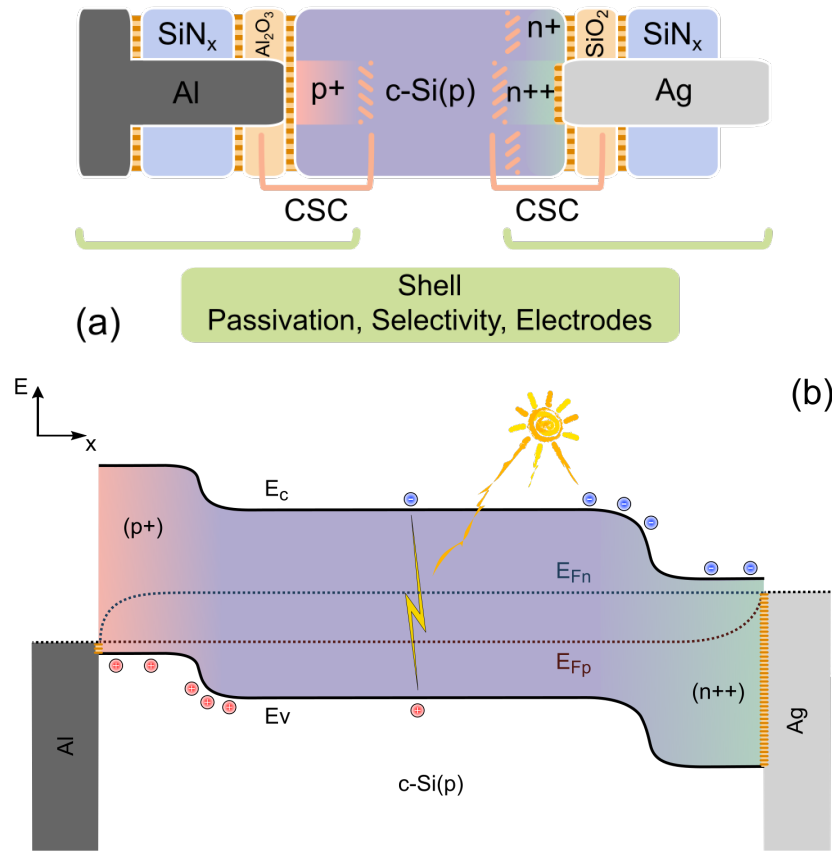


Figure 2.3 – (a) Sketch of a PERC shell. The p-type c-Si bulk coupled with the front and the rear parts of the shell and their different material layers are represented. These are the selective front POCl_3 diffusion ($n+$ and $n++$) and the back Al diffusion ($p+$), the thin silicon oxide (SiO_2) and silicon nitride (SiN_x) layers deposited at the front sides and the aluminium oxide Al_2O_3 and the SiN_x layers deposited at the back side of the c-Si(p) bulk, as well as the front and the back metal layers (Ag and Al layers, respectively). All these sub-layers coupled together eventually define the characteristics of the three different electrical functions (passivation, selectivity and terminal electrode), which are partly revealed in the energy band diagram in (b). The different interfaces and sub-contacts defined by these different sub-layers are represented in orange-dashed areas. Finally, the carrier-selective contact (CSC) influence range extending from the end of the diffused doped region to farther inside the c-Si bulk is also represented in orange-dashed areas. (b) Corresponding schematic energy band diagram below the front and the rear contacting areas in the space domain in open-circuit condition and under injection. The conduction and the valence band energies (E_c and E_v , respectively), as well as the band bending (spatial evolution of the energy states) are represented spatially for the different material properties and layers. The electron and hole quasi-Fermi levels (E_{Fn} and E_{Fp} , respectively) are also depicted spatially through the c-Si(p) bulk and through the shell parts building the contacting area.

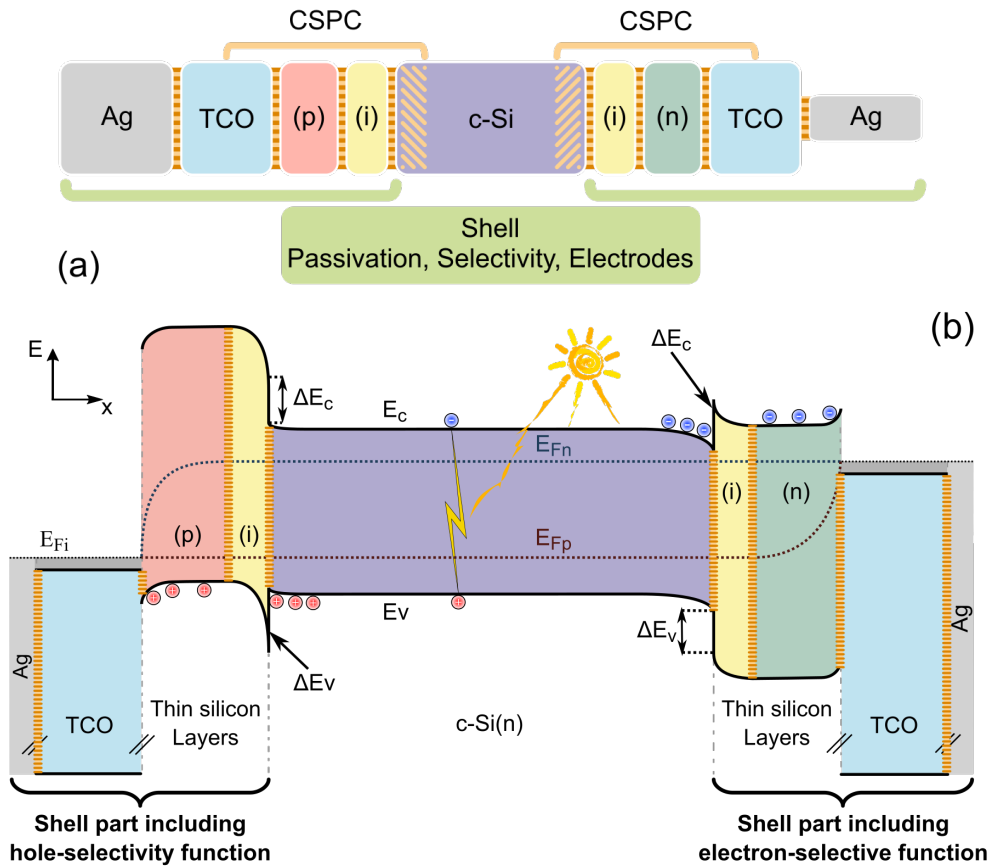


Figure 2.4 – (a) Sketch of a SHJ shell. The n -type $c\text{-Si}$ bulk coupled with the two parts of the shell which encompass the different material layers are represented. These are the intrinsic hydrogenated amorphous silicon layer (i), p and n -type thin silicon layers, (p) and (n) respectively, as well as TCO and Ag layers. All these sub-layers coupled together define the characteristics of the three different electrical functions (passivation, selectivity and terminal electrode), which are partly revealed in the energy band diagram in (b). The numerous interfaces and sub-contacts defined by the different sub-layers are represented in orange-hatched areas. Finally, the CSPC influence range extending from the TCO to inside the n -type $c\text{-Si}$ bulk is also represented in light-orange dashed areas. (b) Corresponding schematic energy band diagram below the front and the rear contacting areas in the space domain in open-circuit condition and under injection. The conduction and the valence band energies (E_c and E_v , respectively), as well as the band bending (spatial evolution of the energy states) are represented spatially for the different SHJ materials layers. The electron and hole quasi-Fermi levels (E_{Fn} and E_{Fp} respectively) are also depicted spatially through the $c\text{-Si}(n)$ bulk and the shell. The conduction and the valence band offsets with their respective energies (ΔE_c and ΔE_v , respectively) are also depicted. These band offsets define different energy barriers affecting the transport of the photogenerated carriers.

Going back to the definition of the term *contact* introduced in section 2.1.1, the shell as a

whole corresponds then to the broadest possible definition of the contact of solar cells as it allows one to optimize the extraction of the current out of the silicon bulk. Yet, we pinpointed that contacts are also present between the different components of the shell. A shell is then a stack of different coupled contacts, this stack being again coupled to the silicon bulk in order to form the eventual contact of the solar cell.

2.2 Physics of semiconductor-based solar cells

This section details the main semiconductor physics relevant for the understanding of the operation of a solar cell. It covers the fundamental operating principles of solar cells from generation to extraction of charge carriers. To this end, the fundamental concepts of generation, recombination losses, passivation, selectivity, and resistive effects as well as transport of charge carriers are detailed. All along this section, these different principles are detailed and related to the different aspects that the shells in general have to fulfil in order to provide high efficiency solar cells.

2.2.1 Generation

In semiconductors, electron-hole pairs can be generated thanks to the energy of incoming light. This generation depends on the energy of the incoming photons (E_{ph}) and the forbidden bandgap (E_g) of the semiconductor. E_g corresponds to the energy range where no available energy states are present in the semiconductor and is defined as the difference between the lowest energy level of the conduction band (E_c) and the highest energy level of the valence band (E_v). The solar spectrum contains photons of different energies covering a wide energy range from the ultraviolet (UV) to infrared (IR). When the energy of the incoming photon is higher than or equal to E_g , the photon can be absorbed by the semiconductor. In this case, an electron from the occupied low energy states of the valence band gains energy and is released to reach an unoccupied higher energy state within the conduction band, leaving behind a hole (which is a positive charge) in the valence band. These electrons and holes are then free to move inside the semiconductor within their respective bands, and contribute to the electric current. In the case of $E_{ph} > E_g$, the energy difference between E_{ph} and E_g is dissipated inside the semiconductor lattice as heat. This phenomenon is referred to as *thermalization*. In contrast, for photons with $E_{ph} < E_g$, the semiconductor is transparent³ and these photons cannot be absorbed to generate electron-hole pairs. Note that conversely to generation, under specific conditions, electrons and holes may annihilate each others in many different *recombination* processes, which will be described in more detail in section 2.2.2.

³Transparent for electron-hole pairs generation but photons with energy smaller than E_g can be absorbed by free-carriers absorption (FCA) in the case of doped semiconductor or by defects present inside the bandgap.

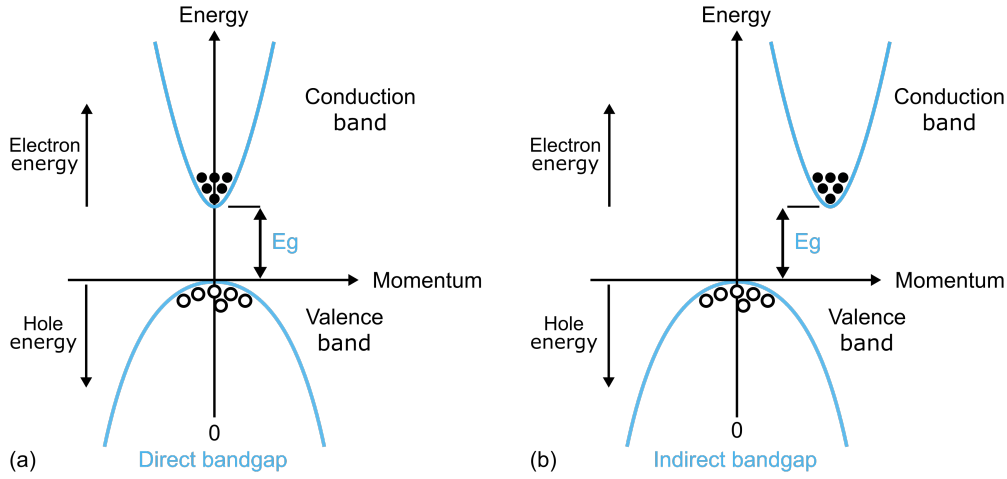


Figure 2.5 – Schematic energy-momentum diagrams representing (a) a direct semiconductor band gap and (b) an indirect semiconductor band gap. The electron and hole energies as well as the conduction and valence bands are depicted. Empty circles indicate holes in the valence band and dots indicate electrons in the conduction bands. Figures inspired by [Sze 2012].

The magnitude of photon absorption in semiconductors is defined by the wavelength-dependent absorption coefficient according to Lambert-Beer’s law [Green 2008]. Absorption is extremely efficient in direct bandgap semiconductors, such as gallium arsenide or indium phosphide, whose highest energy state of E_v is directly aligned with the lowest energy state of E_c in the momentum space of the electronic dispersion diagram (see Figure 2.5a). In contrast, for semiconductors with an indirect bandgap, such as silicon, absorption requires both the energy provided by a photon and an additional momentum provided by a lattice vibration, called phonon. Indeed, for such indirect bandgap semiconductors, the E_v maximum and the E_c minimum are not located at the same momentum in the electronic dispersion diagram, see Figure 2.5b).

In the absence of any external excitation such as light (dark condition), pressure, or electric field and at thermal equilibrium, i.e., at a given temperature and in steady state, continuous and spontaneous thermal agitation occurs (thanks to the thermal energy) which results in the excitation of electrons from the valence band to the conduction band, leaving an equal number of holes in the valence band. The equilibrium electron and hole densities are denoted as n_0 and p_0 , respectively, and are described by Boltzmann approximation as follows [Green 1982]:

$$n = n_0 = N_c \exp\left(\frac{E_F - E_c}{k_B T}\right) \quad (2.1)$$

$$p = p_0 = N_v \exp\left(\frac{E_v - E_F}{k_B T}\right) \quad (2.2)$$

where n and p are the total density of electrons and holes (here equal to n_0 and p_0), N_v and

N_c are the effective densities of states in the valence and in the conduction band, respectively, k_B is the Boltzmann constant, T is the temperature of the semiconductor and E_F is the Fermi energy level. The Fermi energy level represents the electrochemical potential of a carrier type in the semiconductor, describing the occupation of states in the conduction and valence bands. In the dark, electrons and holes have the same electrochemical potential, thus a single E_F describes both carrier types and is located inside the bandgap, its position depending on the doping of the semiconductor. In addition, the carrier concentration in thermal equilibrium conditions, called the intrinsic carrier density (n_i), is defined as [Green 1982, Sze 2012]:

$$n_i^2 = np = n_0 p_0 \quad (2.3)$$

$$n_i = \sqrt{n_0 p_0} = \sqrt{N_c N_v} \exp\left(\frac{E_v - E_c}{2k_B T}\right) \quad (2.4)$$

In particular, for silicon, n_i is equal to $9.65 \times 10^9 \text{ cm}^{-3}$ at 300 K [Sze 2012].

Under illumination, due to the photogeneration, an equal amount of electrons and holes, called the excess carrier concentration (Δn and Δp , respectively) is added to the dark equilibrium densities. The following relations give the thermal equilibrium of electron and hole densities under illumination [Sze 2012]:

$$n = n_0 + \Delta n = N_c \exp\left(\frac{E_{Fn} - E_c}{k_B T}\right) \quad (2.5)$$

$$p = p_0 + \Delta p = N_v \exp\left(\frac{E_v - E_{Fp}}{k_B T}\right) \quad (2.6)$$

where $\Delta n = \Delta p$ and E_{Fn} and E_{Fp} are the *quasi-Fermi levels* which are the electrochemical potentials describing the occupation of energy states of electrons in the conduction band and of holes in the valence band, respectively. As the illumination case represents a non-equilibrium state of the semiconductor, the densities of electrons and holes differ from their respective values in dark equilibrium.

In addition, in the illuminated case the product np becomes [Sze 2012]:

$$np = n_i^2 \exp\left(\frac{E_{Fn} - E_{Fp}}{k_B T}\right) \quad (2.7)$$

This equation shows that an increase of electron and hole densities due to illumination increases the energy difference between both quasi-Fermi levels logarithmically. This is called the quasi-Fermi level splitting. Importantly, the quasi-Fermi level splitting defines the free

energy of the system and corresponds to the maximum voltage which can be built up by the semiconductor material and thus which can be obtained from a solar cell. This maximum voltage is also called the implied voltage (iV) and is defined as:

$$iV = \frac{E_{Fn} - E_{Fp}}{q} = \frac{k_B T}{q} \ln \left(\frac{np}{n_i^2} \right) \quad (2.8)$$

with q equal to the elementary charge. In actual devices, the implied voltage is impacted by the recombination mechanisms which induce a loss of electron and hole densities, leading to a decrease in the maximum implied voltage available. Recombination mechanisms are detailed in the following section 2.2.2.

2.2.2 Recombination losses and passivation mechanisms

Recombination is the opposite process to electron-hole pair generation, occurring when an electron loses energy and stabilizes back to the valence band, annihilating with a hole. The average time span between generation and recombination is determined by the minority carrier lifetime. This characterizes the amount of time an electron stays in the conduction band before recombining with a hole. This process hence requires the presence of both photo-generated carrier types at the recombination sites. The recombination processes occurring in semiconductors can be separated in two different categories, namely, bulk recombination and surface recombination. In solar cells, the detrimental effect of recombination processes is to produce a direct loss of carriers which induces a voltage drop reducing the maximum voltage available for a constant generation rate, hence limiting the device performance. Achieving the lowest possible recombination rate is thus crucial to reach high solar cell efficiency. In the following paragraphs, a quantitative description of the global recombination rate occurring inside the absorber, and more precisely inside the silicon absorber, as a function of the dopant density and carrier injection level is given. In addition, insights into how to mitigate recombination are also discussed with a particular focus on the first important role of the shell, namely, providing passivation to minimize surface recombination.

Bulk recombination

Three different fundamental recombination mechanisms occur in the bulk of semiconductors, impacting the carrier lifetime. These are: radiative band-to-band recombination, Auger recombination, and Shockley-Read-Hall (SRH) recombination [Sze 2006]. These mechanisms are depicted in Figure 2.6. Among these mechanisms, radiative band-to-band and Auger are intrinsic phenomena directly linked to the material properties, whereas SRH is an extrinsic phenomenon as it is related to the presence of defect states in the forbidden gap stemming from contaminants such as impurities or doping, or caused by lattice defects. In the following

paragraphs, the recombination rates per unit area and time U ($\text{cm}^{-3} \text{s}^{-1}$) for each mechanism are detailed and associated to their corresponding carrier lifetimes τ , expressed per unit of time (s^{-1}). The lifetime and the recombination rates are associated to each other using the relation: $U = \frac{\Delta n}{\tau_n}$ or $U = \frac{\Delta p}{\tau_p}$, with τ_n and τ_p the lifetimes of electron and hole, respectively, and Δn and Δp the disturbances of the respective carriers from their equilibrium values n_0 and p_0 .

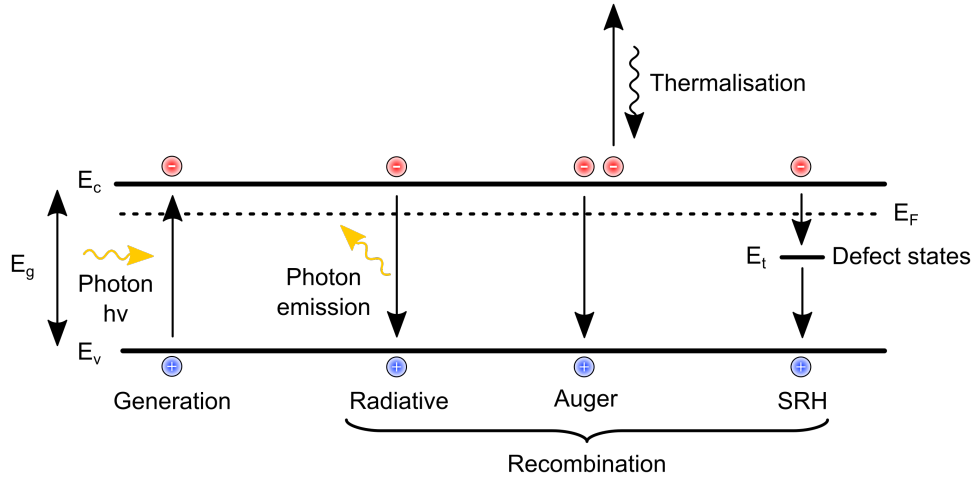


Figure 2.6 – The generation and the three bulk recombination mechanisms occurring in semiconductors. The conduction band (E_c) and valence band (E_v) energies as well as the Fermi energy (E_F) and the defect states energy (E_t) are depicted to illustrate the semiconductor energy states.

Radiative band-to-band recombination In radiative recombination, an excited electron recombines directly with a hole, losing its energy and falling from the conduction band to the valence band. During this process, the excess energy is released by the emission of a photon. The radiative recombination rate (U_{rad}) is given by [Green 1982]:

$$U_{Rad} = B(np - n_0 p_0) = B(np - n_i^2) \quad (2.9)$$

With $n = \Delta n + n_0$ and $p = \Delta p + p_0$ the electron and hole concentrations, n_0 and p_0 the equilibrium electron and hole doping concentration and B the radiative recombination coefficient which depends on the material. The key driver for radiative recombination is thus the imbalance between the actual carrier density (n and p) and the equilibrium carrier density (n_0 and p_0). Accordingly, assuming charge neutrality ($\Delta n = \Delta p$), the radiative lifetime is given by:

$$\tau_{Rad} = \frac{1}{B(n_0 + p_0) + B\Delta n} \quad (2.10)$$

It is then determined that in low injection conditions ($\Delta n = \Delta p \ll p_0 + n_0$), the radiative lifetime is determined by the doping density such that the higher $p_0 + n_0$ is, the lower τ_{Rad} . On the contrary, in high injection conditions ($\Delta n = \Delta p \gg p_0 + n_0$), the radiative lifetime is determined by the excess-carrier density, such that the higher Δn is, the lower τ_{Rad} .

In particular, in the case of silicon, which is an indirect bandgap semiconductor, the creation or annihilation of a phonon is required for radiative recombination in order to conserve the momentum, as for the generation mechanism. Radiative recombination rate is then several orders of magnitude lower for silicon than for direct bandgap semiconductors. This is reflected by the small B value close to $2.0 \times 10^{-15} \text{ cm}^3 \text{ s}^{-1}$ for silicon [Green 1982], compared to $1.3 \times 10^{-10} \text{ cm}^3 \text{ s}^{-1}$ for gallium arsenide, which is a direct bandgap semiconductor [T Hooft 1981]. As a consequence, radiative recombination is not the dominant recombination process in silicon solar cells. This is illustrated in Figure 2.7 for three different silicon bulks.

Auger recombination Auger recombination is a three-body process where the excess energy produced by the recombination is transferred to a third free carrier (hole or electron) located close to the recombination location. This carrier is excited to a higher energy level without moving to another energy band, then loses its excess energy by thermalization, and eventually by emitting phonons. The Auger recombination rate is given by [Vossier 2010]:

$$U_{Auger} = C_n(n^2 p - n_0^2 p_0) + C_p(np^2 - n_0 p_0^2) \quad (2.11)$$

With $n = \Delta n + n_0$ and $p = \Delta p + p_0$ the electron and hole concentrations, n_0 and p_0 the equilibrium electron and hole concentrations and C_n and C_p the Auger coefficients for electrons and holes, respectively.

A recent derivation of this empirical equation 2.11 is given in [Richter 2012] which presents the Auger lifetimes at high and low injection for the case of an n-type silicon bulk:

$$\tau_{Auger,low} = \frac{1}{C_n N_D^2} \quad (2.12)$$

$$\tau_{Auger,high} = \frac{1}{(C_n + C_p) \Delta n^2} \quad (2.13)$$

with N_D the donor concentration of the n-type silicon bulk. In both cases, the lifetime is inversely proportional to the square of the carrier concentration and thus at high carrier concentrations, induced e.g., by heavy doping (equation 2.12) or high injection level (equation 2.13), Auger recombination becomes the predominant recombination mechanism. This effect

is illustrated in Figure 2.7: the higher the excess carrier density, the lower the Auger lifetime. Therefore, Auger recombination dictates the performance of high-voltage solar cells as they feature high injection levels, i.e. high $\Delta n = \Delta p$ values.

Shockley-Read-Hall recombination SRH recombination occurs via defect states within the bandgap, i.e., the forbidden energy gap of the semiconductor. The defect states might be induced by impurities, doping, or lattice defects such as dislocations or vacancies. These defect states in semiconductors can give rise to allowed energy levels within the forbidden gap. These defect levels then create an efficient two-step recombination process where electrons fall from the conduction band to the defect level before eventually falling to the valence band to recombine with holes. The excess energy from this recombination mechanism can be emitted as a photon or phonon. The defect states have given capture cross-sections and emission rates for both electrons and holes depending mostly on the defect energy level (E_t). Two categories of defects may be present. The first one is named "trap states". These states have an energy close to the conduction (resp. valence) band edge and they can capture an electron (resp. hole) but with a high probability that the captured charge will be thermally emitted back to its initial energy band, rather than being annihilated by recombination with the opposite charge. The second category encompasses the defect states with energy close to the middle of the band gap. In that case, the occupation probabilities that a defect state can trap an electron and a hole become similar. Thus, the closer the defect energy (E_t) is to mid-gap, the more likely an electron and a hole can be trapped simultaneously and then recombine. Such states then behave as important recombination centres which are detrimental to solar cell performance. The SRH recombination rate induced by a single defect level was determined by the statistical model presented by Shockley and Read [Shockley 1952] and by Hall [Hall 1952]:

$$U_{SRH} = \frac{v_{th} N_t (np - n_i^2)}{\frac{1}{\sigma_p} (n + n_1) + \frac{1}{\sigma_n} (p + p_1)} \quad (2.14)$$

with $n_1 = n_i e^{\frac{E_t - E_i}{k_B T}}$ and $p_1 = n_i e^{\frac{E_i - E_t}{k_B T}}$

and where v_{th} is the thermal velocity of the charge carriers, N_t is the trap density, n and p are the electron and hole densities, respectively, n_i is the intrinsic carrier density, σ_n and σ_p are the capture cross-sections corresponding to the probability that the defect state captures an electron or a hole, respectively, E_i is the intrinsic energy level, E_t is the energy level of the defect state, k_B is the Boltzmann constant and T is the absolute temperature. From the recombination rate and assuming charge neutrality ($\Delta n = \Delta p$), the associated SRH lifetime is

expressed as follows:

$$\tau_{SRH} = \frac{\frac{1}{\sigma_p}(n_0 + \Delta n + n_1) + \frac{1}{\sigma_n}(p_0 + \Delta p + p_1)}{v_{th}N_t(p_0 + n_0 + \Delta n)} \quad (2.15)$$

At low injection level ($\Delta n = \Delta p \ll p_0 + n_0$) and for an n-type semiconductor with $n \sim N_D$, the SRH lifetime can be expressed as follows:

$$\tau_{SRH,low} = \frac{1}{\sigma_p v_{th} N_t} \left(1 + \frac{n_1}{N_D} \right) + \frac{1}{\sigma_n v_{th} N_t} \left(\frac{p_1}{N_D} \right) \quad (2.16)$$

In that case, the lifetime depends on the doping concentration and the trap density as well as on the properties of defect states such as the energy level and the capture cross-section. In contrast, at high injection level ($\Delta n = \Delta p \gg p_0 + n_0$), the SRH lifetime does not depend on the energy level nor on the doping concentration and is expressed as follows:

$$\tau_{SRH,high} = \frac{1}{\sigma_p v_{th} N_t} + \frac{1}{\sigma_n v_{th} N_t} \quad (2.17)$$

depending then only on the capture cross-section of the defect state in addition to the trap density.

SRH recombination was the dominant bulk recombination mechanism for solar cells produced from defective silicon wafers, which was previously the case for multicrystalline silicon wafers and, to a lesser extent for Czochralski-grown ones. However, in contrast to the intrinsic radiative and Auger recombination mechanisms, SRH recombination is an extrinsic mechanism and can thus be mitigated by improving the quality and purity of the silicon wafers. In this regard, float-zone monocrystalline silicon wafers have demonstrated superior quality, but recent improvements in Czochralski growth [Wang 2018] and the development of high-performance multicrystalline materials [Altermatt 2018] partially bridged this quality gap. The behaviour of the SRH lifetime as a function of the injection level is plotted in Figures 2.7 for (a) low, (b) medium, and (c) high-quality bulk material corresponding to currently commercially available silicon wafers, along with the radiative and Auger lifetimes as well as the effective bulk lifetime. It is observed that the SRH recombination is dominant at low injection for the three cases, but its impact decreases with the increase of the silicon bulk quality.

Effective bulk lifetime The overall effective bulk lifetime (τ_{bulk}) is then a combination of the three lifetimes described above. Thus, the inverse τ_{bulk} can be written as the sum of all inverse lifetimes as follows [Würfel 2005]:

$$\frac{1}{\tau_{bulk}} = \frac{1}{\tau_{Rad}} + \frac{1}{\tau_{Auger}} + \frac{1}{\tau_{SRH}} \quad (2.18)$$

Hence, as illustrated in Figure 2.7, the overall recombination rate at a given injection level is dominated by the smallest lifetime value, i.e., by the highest recombination rate. In general, under high injection, the silicon bulk is limited by Auger recombination, whereas SRH recombination usually dominates at lower injection conditions. However, in current crystalline silicon solar cells, the bulk defect density is well controlled as high quality bulk material is industrially available. The SRH lifetime of a good Czochralski n-type silicon wafer (Cz-Si(n)) is nowadays close to 10 ms at an injection level of $5 \times 10^{14} \text{ cm}^{-3}$, see Figure 2.7(c), compared to below 100 μs for multicrystalline p-type material (mc-Si(p)) [Fell 2015], see Figure 2.7(a).

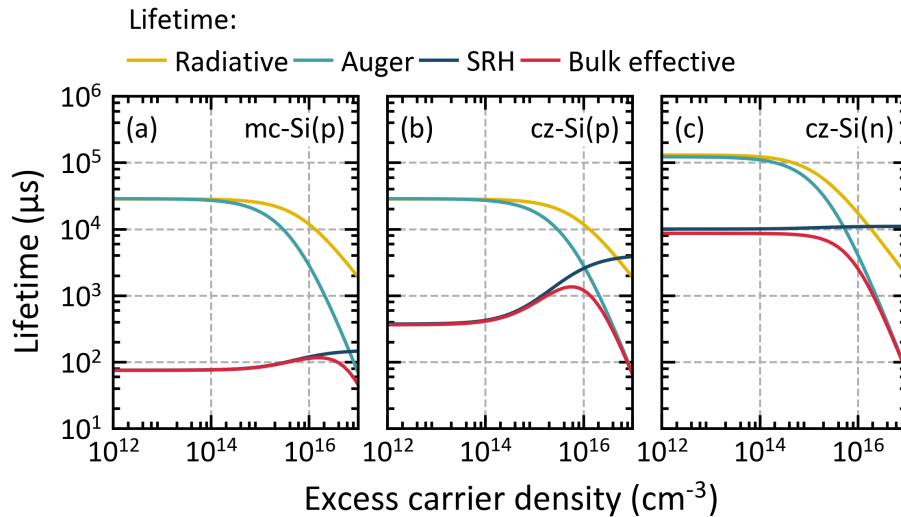


Figure 2.7 – Simulated bulk lifetimes as a function of the excess carrier density for a (a) multicrystalline p-type wafer (mc-Si(p)) featuring a bulk resistivity of $2 \Omega \text{ cm}$ with high SRH recombination, (b) a Czochralski p-type wafer (Cz-Si(p)) featuring a bulk resistivity of $2 \Omega \text{ cm}$ with medium SRH recombination and (c) a Czochralski n-type wafer (Cz-Si(n)) featuring a bulk resistivity of $3 \Omega \text{ cm}$ with low SRH recombination. The three bulk recombination mechanisms, which are radiative, Auger and SRH, as well as the effective bulk lifetime are plotted. The SRH curves were calculated for the case of a deep defect ($E_t = E_i$). Simulated data from PVLighthouse [McIntosh 2011].

Surface recombination

In addition to the recombination taking place inside the bulk of the semiconductor, recombination also happens at its surfaces. Indeed, the surfaces of a crystalline semiconductor feature interruptions of the crystal lattice periodicity, named *dangling bonds* which are induced by unpaired outer-shell electrons. These dangling bonds cause localized electronic defect states within the bandgap. These states, also referred to as *interface defect states*, act as recombination centres at the surface of the semiconductor, trapping both electrons and holes when they are present at the surface. Since the surface recombination mechanism occurs via defect states, it is described by the SRH theory in analogy to defect recombination in the bulk of a semiconductor [Shockley 1952, Aberle 2000]. However, contrary to SRH bulk, the surface defects states are not localized at a single energy level but rather form a group of defect states distributed across the bandgap. The surface recombination rate per unit area and time, U_s ($\text{cm}^{-3} \text{s}^{-1}$), is defined as:

$$U_s = \frac{n_s p_s - n_i^2}{\frac{n_s + n_1}{S_p} + \frac{p_s + p_1}{S_n}} \quad (2.19)$$

with $S_p = \sigma_p v_{th} N_{it}$ and $S_n = \sigma_n v_{th} N_{it}$.

Here n_s and p_s are the surface concentrations of electrons and holes respectively, S_n and S_p are the surface recombination velocities of electrons and holes, N_{it} is the surface defect density and n_1 and p_1 were defined previously by the SRH model in equation 2.14. In addition, as the surface of the semiconductor presents a large number of defect states at various energy levels in the bandgap, N_{it} can be expressed by an energy-dependent interface defect density (D_{it}) such as $N_{it} = \int_{E_v}^{E_c} D_{it}(E) dE$. Thus, the capture cross-sections become energy-dependent as well, leading to a surface recombination rate expressed as follows:

$$U_s = v_{th} (n_s p_s - n_i^2) \int_{E_v}^{E_c} \frac{D_{it}(E) dE}{\frac{n_s + n_1(E)}{\sigma_p(E)} + \frac{p_s + p_1(E)}{\sigma_n(E)}} \quad (2.20)$$

Especially, the surface recombination rate is related to the surface recombination velocity (S) by:

$$U_s \equiv S \Delta n_s |_{surface} \quad (2.21)$$

with Δn_s the excess minority carrier density at the surface itself.

In particular, when an overlying layer or when a doping region within the silicon bulk is present at the surface, band alignment requirements involve an electric charge at the silicon surface (see section 2.2.2). A potential is then present, inducing a band bending at the silicon absorber surface, and hence a space charge region of a certain width d exists. In this case, in order to account for this band bending in the vicinity of the semiconductor surface, an effective surface recombination velocity (S_{eff}) is defined as the ratio of the values of U_s and Δn_s which are taken at the edge of the space charge region inside the c-Si bulk, i.e, at a distance d from the surface where the bands are still flat [Aberle 2000]:

$$S_{eff} = \frac{U_{s,x=d}}{\Delta n_{s,x=d}} \quad (2.22)$$

S_{eff} typically ranges between 10^7 cm s^{-1} for a direct metal/semiconductor contact to below 10 cm s^{-1} for a well-passivated surface (see section 2.2.2) [Cuevas 1996, Olibet 2007b].

As the annihilation of excess carriers by surface recombination is very efficient in semiconductors, due to significant D_{it} , it has been and still is one of the most critical recombination mechanisms for crystalline silicon solar cells. Therefore, it is crucial to mitigate its contribution. To that end, different approaches are used and are presented in section 2.2.2.

Effective recombination

The effective recombination, i.e., the total recombination occurring in a semiconductor wafer, is the result of the recombinations occurring in the bulk and at both surfaces. Thus, by summing all the recombination rates presented above and in the case of a sufficiently small S_{eff} ⁴, the effective carrier lifetime for a symmetric structure can be expressed as follows [Schroder 2006]:

$$\frac{1}{\tau_{eff}} = \frac{1}{\tau_{bulk}} + \frac{2S_{eff}}{w} \quad (2.23)$$

where w is the wafer thickness. The factor 2 multiplying the surface recombination part S_{eff} stems from the symmetric structure hypothesis.

As mentioned in section 2.2.2, well-optimized bulk materials are nowadays industrially available for crystalline silicon solar cells, therefore bulk recombination is usually less severe than

⁴Considering a typical n-type silicon wafer with a resistivity of $3 \Omega \text{ cm}$ and an effective carrier lifetime of 5 ms, the condition gives $S_{eff} < 260 \text{ cm s}^{-1}$ at high injection and $S_{eff} < 570 \text{ cm s}^{-1}$ at low injection [McIntosh 2011]. Nowadays, these constraints are always achieved in practice due to high passivation qualities [Olibet 2007b, Olibet 2007a, Cuevas 2018].

surface recombination. In addition to this, the current trend towards the use of thinner silicon wafers to save costs [ITRPV 2020] makes the mitigation of surface recombination the primary concern of current crystalline silicon solar cells. To illustrate this point, Figure 2.8 plots the simulated effective lifetime curves as a function of the wafer thickness for two effective surface recombination values of (a) 50 cm s^{-1} and (b) 5 cm s^{-1} and for three bulk quality levels (low, medium and high corresponding to the ones presented in Figure 2.7). First, it is observed that the thinner the wafer is, the lower the effective lifetime, owing to an increased contribution of surface recombination (see equation 2.23). Secondly, the higher the bulk quality is, the more significant the decrease of the effective lifetime becomes as a function of the wafer thickness, i.e. the more limited by surface recombination. Thirdly, regardless of the wafer thickness, a lower effective surface recombination allows for higher effective lifetime; this is especially true for high bulk quality material. Consequently, surface passivation is one of the most important levers for solar cell performances improvement. Two passivation approaches to maximize τ_{eff} by lowering the surface recombination are presented in section 2.2.2.

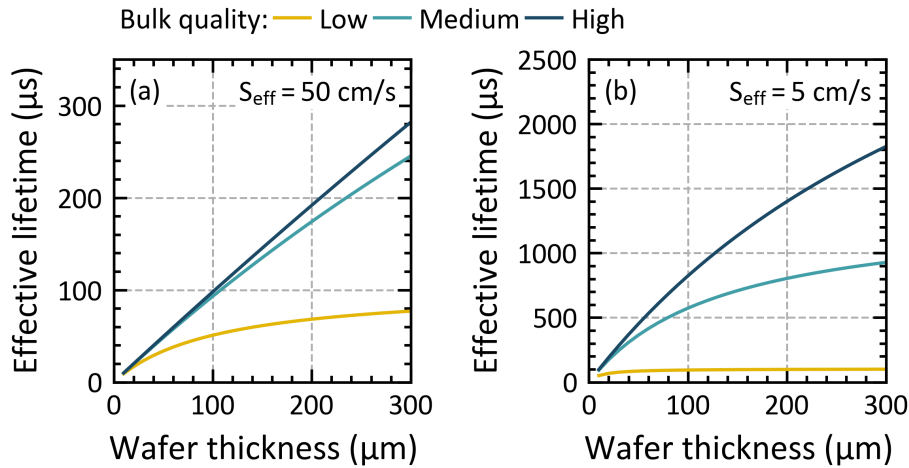


Figure 2.8 – Simulated effective lifetimes as a function of the wafer thickness for two different effective surface recombinations (a) of 50 cm s^{-1} and (b) of 5 cm s^{-1} . In both cases, the three bulk quality levels presented in Figure 2.7 are considered. These bulk quality levels correspond to a bulk lifetime of $104 \mu\text{s}$ (low), $1343 \mu\text{s}$ (medium) and of $4661 \mu\text{s}$ (high) considering an injection level of $5 \times 10^{15} \text{ cm}^{-3}$.

Passivation mechanisms

In order to reach good electrical transport in solar cells, one important role of the shell is to minimize, and even to avoid in the ideal case, the recombination of photogenerated carriers at the surface of the absorber. Decreasing the surface recombination allows for higher quasi-Fermi levels splitting inside the absorber (see section 2.2.1, equation 2.8), leading to a higher maximal available voltage, and therefore to a higher final solar cell performance. The process of decreasing surface recombination is called passivation. A contact fulfilling this goal is

accordingly defined as a *passivating contact*, as introduced in section 2.1.1. Since both carrier types exist at the absorber surface, recombination centres have to be avoided by the mean of passivation. Two pathways for surface passivation exist: chemical and field-effect passivation, and are presented below and illustrated in Figure 2.9. Both passivation mechanisms are generally provided by additional material layers, individually or combined in a stack, which constitute then part of the shell of the solar cell.

Chemical passivation Chemical passivation reduces the number of interface defect states, and therefore of recombination sites, by saturating the dangling bonds present at the absorber surface [Yablonoitch 1986, Higashi 1990]. In the case of crystalline silicon, the surface dangling bonds can be efficiently saturated by growing or depositing a dielectric layer such as silicon dioxide (SiO_2) or hydrogenated amorphous silicon (a-Si:H) at the crystalline silicon surface [Jin 2007, Pankove 1979]. Such passivating layers strongly reduce the interface defect density, leading to an important recombination reduction. In addition, dangling bonds can be bounded to hydrogen atoms as well, originating either from the passivating overlayer itself or from an annealing inside an external hydrogen-containing ambient. As introduced above in section 2.2.2, the surface recombination rate is directly proportional to the interface defect density which is approximately of the order of 10^{13} cm^{-2} for non-passivated crystalline silicon [Aberle 2000]. With the growth of a high-quality thermal SiO_2 layer completed by a consecutive annealing in a hydrogen atmosphere, it is possible to obtain an interface defect density of about 10^9 cm^{-2} [Jin 2007]. Even more efficient, covering the silicon surface with low-temperature-grown intrinsic a-Si:H, a quasi-perfect passivation can be reached with a defect density reported to be as low as 10^7 cm^{-2} [Pankove 1979]. An illustration of chemical passivation is given in Figure 2.9.

Field-effect passivation Field-effect passivation reduces the recombination rate by repelling one type of carriers from the surface while keeping the defect density constant. In this case, the lack of one charge carrier (n_s or p_s) at the surface limits the recombination probability of the electron-hole pairs [Cuevas 2018]. This mechanism can be achieved by creating a band bending variation, and thus an electric field, underneath the surface. The band bending can either be created by a doping profile below the interface, by the presence of fixed electrical charges at the surface, by the introduction of a doped material, or by using materials with different work functions [Cuevas 1996, Cuevas 2018, Olibet 2007b, Olibet 2007a]. To produce field-effect passivation, one method is to use a thin material layer featuring a net positive or negative charge and to deposit it on the c-Si surface. This has the consequence of attracting carriers having the opposite charge, which will then accumulate at the interface between the charged layer and the semiconductor. Common examples of such layers are silicon oxide (SiOx) [Kerr 2002] or silicon nitride (SiNx) [Hezel 1981] whose positive charge creates a very thin layer inside the c-Si semiconductor and close to its surface where the concentration of electrons is consequently larger than that of holes. Thus, they can be employed to passivate n-type surfaces by repelling the minority carriers, which are in this case holes, away from the interface. In the

same way, aluminium oxide (Al_2O_3) owns negative fixed charges which will attract, this time, holes close to the c-Si surface when deposited as an overlayer on a p-type surface [Hoex 2008]. In addition, doped c-Si regions and doped layers also produce field-effect passivation, owing to an induced band bending at the surface of the c-Si semiconductor. The band bending will produce either accumulation or inversion conditions at the surface which create then a region near the surface with high electron or hole concentration. Prime examples of field-effect passivation using doped layers are the n-type and p-type hydrogenated amorphous (a-Si:H(*n*) and a-Si:H(*p*) respectively) used in the silicon heterojunction technology introduced in section 2.1.2 [Olibet 2007a]. Furthermore, field-effect passivation is achieved with the use of highly n-type and p-type doped regions inside the c-Si bulk underneath the metal layers as employed in the Al-BSF, PERC and TOPCon technologies. As a last example, materials featuring a sufficiently high or low work function can also provide either accumulation or inversion conditions, thus creating regions near the surface with high electron or hole concentration. One common material featuring a high work function (of about 6 eV) is molybdenum oxide (MoOx) which produces an accumulation layer on p-type silicon and an inversion layer on n-type silicon [Cuevas 2018].

An illustration of field-effect passivation is given in Figure 2.9 along with chemical passivation. Importantly, note that field-effect passivation is part of the selectivity process since one carrier type is preferred to the other. More details are given in section 2.2.3.

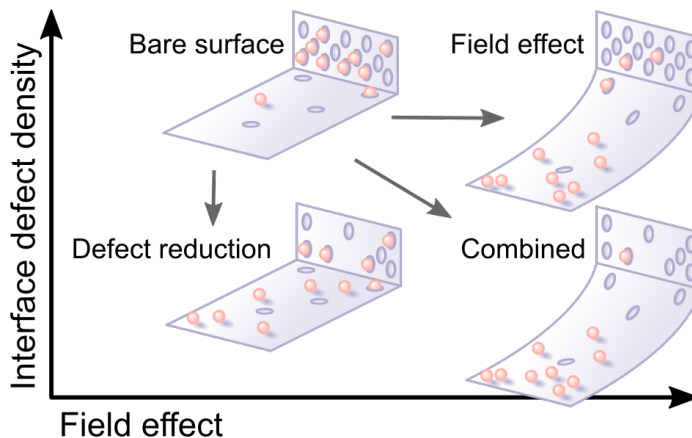


Figure 2.9 – Illustration of chemical and field-effect surface passivations. Figure reproduced from [Hofmann 2008].

2.2.3 Selectivity

After passivation, the second role of the shell is to foster an electrical current in the device. To do so, the shell has to separate the electrons and holes by creating a flow of each carrier type towards different absorber locations. Indeed, to deliver energy to an external circuit, a solar

cell needs to have distinct regions that selectively conduct either electrons or holes towards two different metallic terminal electrodes. This is called *selectivity* and as introduced in section 2.1.1, a contact fulfilling this goal is commonly defined as a *carrier-selective contact*. As at the metallic terminal electrodes a recombination-active interface is present, it is necessary to prevent at least one type of photogenerated carriers from reaching this interface, since, as detailed in section 2.2.2, any recombination mechanism requires the presence of both carrier types at the recombination sites. A barrier to the flow of one carrier type is then required to extract the other carrier type with as few recombination losses as possible at the terminal electrodes. The effect of this barrier on electrons or holes can be physically interpreted as a resistance, or conversely, as a reduced conductivity for one carrier type. Physically, to separate and extract the photogenerated carriers, a driving force that separately propels electrons and holes to their respective terminal electrodes is necessary. This separation of carriers is induced by the driving forces taking place in the semiconductor absorber, resulting in the current density of electrons (J_n) and holes (J_p) which define together the charge-carrier transport. Two charge-carrier transport mechanisms are present in semiconductors: diffusion and drift. Diffusion transport results from chemical forces, whereas drift transport results from electrical forces. Both forces then define the current density of carriers and thus the resulting global charge-carrier transport. If both forces are present in a semiconductor, they contribute simultaneously to the current densities of both carrier types, which are given in one dimension and in steady state as follows [Wurfel 2015]:

$$J_n = +qD_n \frac{dn}{dx} - q\mu_n n \frac{d\phi}{dx} = \frac{\sigma_n}{q} \frac{dE_{Fn}}{dx} = \mu_n n \frac{dE_{Fn}}{dx} \quad (2.24)$$

$$J_p = -qD_p \frac{dp}{dx} - q\mu_p p \frac{d\phi}{dx} = \frac{\sigma_p}{q} \frac{dE_{Fp}}{dx} = \mu_p p \frac{dE_{Fp}}{dx} \quad (2.25)$$

with D_n and D_p the diffusion constants for electrons and holes respectively, μ_n and μ_p their respective mobilities, q the elementary charge, ϕ the electrical potential, n and p the electron and hole densities, E_{Fn} and E_{Fp} the electron and hole quasi-Fermi levels and σ_n and σ_p the electron and hole conductivities. The unity of the current density is generally given in (mAcm^{-2}).

In the semiconductor, the overall current density is equal to the sum of J_n and J_p :

$$J_{\text{total}} = J_n + J_p = \frac{\sigma_n}{q} \frac{dE_{Fn}}{dx} + \frac{\sigma_p}{q} \frac{dE_{Fp}}{dx} \quad (2.26)$$

It is observed from equations 2.24 and 2.25 that the combination of the chemical and electrical potential gradients generates the net force necessary to obtain a current flow. This global

force depends on the gradient of the electrochemical potentials, i.e., E_{Fn} and E_{Fp} , as well as the carrier conductivities and defines the real charge currents of electrons and holes in semiconductors. In particular, it is important to notice that this charge current is then present whether there is an electric field or not, or a concentration gradient or not [Wurfel 2015].

More specifically, the driving forces for charge-carrier transport in a semiconductor are thus the gradient of the quasi-Fermi potentials and the carrier conductivity. However, the quasi-Fermi potential gradients alone are generally not sufficient to enable selective transport, but they are giving the direction of the flow of carriers. First and foremost, an efficient selectivity requires to establish a conductivity asymmetry, i.e., providing different conductivities for the two carrier types at different locations in the device [Wurfel 2015, Cuevas 2015, Onno 2019]. Therefore, region(s) featuring high electron conductivity but low hole conductivity must be created, as well as region(s) featuring the opposite properties. Carriers will then preferentially flow towards the region featuring the highest conductivity for them. The conductivity must then be large for electrons and small for holes at the electron contact, which is the negative terminal, and conversely at the hole contact, which is the positive terminal.

In short, an ideal carrier-selective contact must fulfil the two following criteria:

- The electron (resp. hole) flow towards the negative (resp. positive) contact must not encounter a voltage drop (see section 2.2.4) in order not to affect the electrical transport;
- Any hole (resp. electron) flow towards the negative (resp. positive) contact must be avoided.

The selectivity in terms of electron and hole conductivities is illustrated in Figure 2.10 for the ideal and non-ideal case.

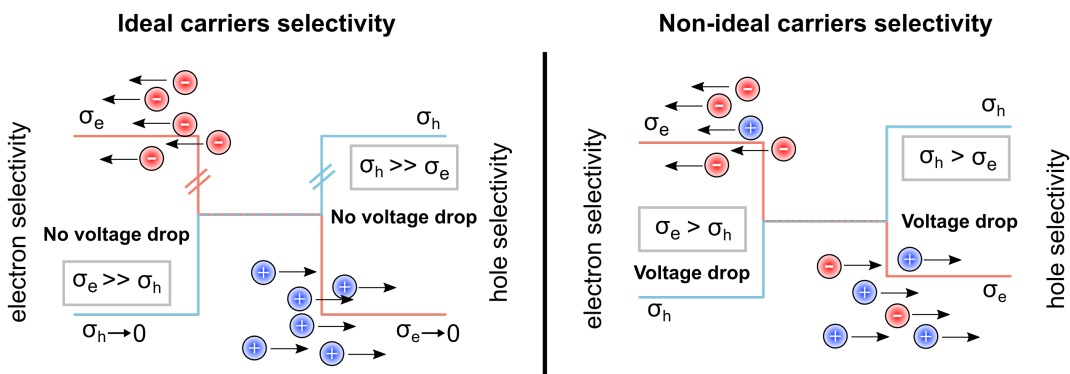


Figure 2.10 – Illustration of ideal and non-ideal selectivity with electron and hole conductivities.

In homojunction crystalline silicon solar cells (such as Al-BSF and PERC technologies introduced in chapter 1), selectivity is usually obtained by highly counterdoping the surface of the

silicon absorber. This allows for blocking one type of carrier while providing at the same time a high conductivity to transport the other carrier type to its terminal electrodes: the so-called n-type emitter acts as a selective conductor for electrons whereas the p-type base selectively conducts holes [Brendel 2016, DeWolf 2012]. In the same way, efficient selectivity is achieved in SHJ solar cells by using doped hydrogenated amorphous silicon layers coupled with thin intrinsic ones, which induce a band bending repelling one carrier type while attracting the other. In addition, it was demonstrated by [Wurfel 2015] that asymmetries in mobility, in addition to carrier density, can be exploited to separate charge carriers, and, in a hypothetical case where the asymmetry in mobility is high enough, showed that selective transport can be achieved without any doping at all. In actual solar cells, the challenge for the shells is to provide carrier selectivity while ensuring surface passivation. Since selectivity influences the conductivity of carriers with the repulsion of one carrier type and the selection of the other, it can then be seen as an important factor of field-effect passivation. However, the main difference between a passivating and carrier-selective contact is that the latter needs to use conductive materials. Single carrier conduction then goes along with passivation [Cuevas 2015], thus consequently, all field-effect passivated contacts are selective, and selectivity necessarily encompasses a degree of passivation.

A method to quantify the selectivity is based on the comparison between the internal open circuit voltage of the absorber bulk, which is the implied open-circuit voltage iV_{OC} (introduced in more detail in section 3.2.2), and the external V_{OC} (introduced in more detail in section 3.2.2) which is measured between the end of the two terminal electrodes, for a given shell (see Figure 2.11). Open-circuit condition indicates that zero current is extracted outside the device and no net current flows under steady-state conditions. As already introduced in section 2.2.1 with equation 2.8, the value of iV_{OC} is directly linked to the bulk and surface recombination mechanisms and for a given bulk recombination, it gives information on the surface passivation quality. For a given bulk recombination, a high value of iV_{OC} indicates a good surface passivation, thus iV_{OC} is the ability of the solar cell to get high quasi-Fermi levels splitting within the absorber. On the other hand, V_{OC} is a measure of the external voltage and represents the ability of the solar cell to maintain the quasi-Fermi levels splitting through the shell, and then at the terminal electrodes [Bivour 2014a]. Consequently, the V_{OC} of the device is limited by the surface passivation if $V_{OC} \approx iV_{OC}$ or by selectivity if $V_{OC} < iV_{OC}$. A perfect selectivity is then achieved when the external V_{OC} equals the internal iV_{OC} . The voltage difference between iV_{OC} and V_{OC} corresponds then to the total electrical voltage drop, induced by the whole shells, at open-circuit condition. From this definition, to quantitatively assess the selectivity, the ratio V_{OC}/iV_{OC} is used [Onno 2019]. This way, the closer the ratio gets to 1, the higher the selectivity is. In addition, it is important to notice that this induced voltage drop at open-circuit condition may be different from the one at other applied voltages, such as the one at the maximum power point of a complete device since for other operating voltages than V_{OC} , current is extracted outside the cell and series resistance effects are involved. This implies different electron and hole currents and thus different voltage drops. However, it is possible to compare the pseudo-IV curve, free from series resistance, and the implied I - V curve to extract

information on selectivity at different injection levels (see section 3.2.2).

Figure 2.11 presents a schematic description of the spatial evolution of the quasi-Fermi level splitting from the bulk to the metallic terminal electrodes. For the sake of example, in this particular case, a shell with an ideal hole selectivity on the left and a non-ideal electron selectivity on the right is depicted. At open-circuit condition, the recombination currents of holes and electrons present in the selective part of the shell are equal ($J_0 = J_{0e} = J_{0h}$), however, their respective quasi-Fermi level drops ΔE_{Fp} and ΔE_{Fn} can be different. For the non-ideal electron selectivity part of the shell presented here, electron and hole quasi-Fermi level drops occur between the bulk and the electrodes and in the specific case of open-circuit condition, these drops can be related to the recombination current by the notion of resistance, namely R_e for electron and R_h for hole. These electron and hole resistances are directly linked to their respective conductivities σ_e and σ_h [Onno 2019]. For an electron-selective contact, ΔE_{Fn} must be smaller than ΔE_{Fp} and inversely for the hole-selective contact. Note that for an effective selectivity, this must be fulfilled for a wide voltage range, including the voltage at the operating point of solar cells, not only at V_{OC} . Moreover, the higher the difference between the quasi-Fermi level drop of holes and electrons within the selective shell part, the more important the selectivity.

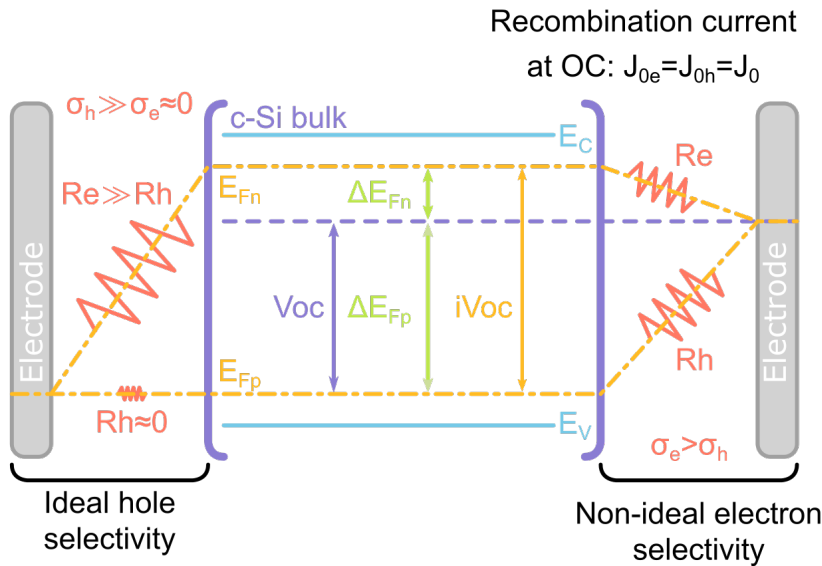


Figure 2.11 – Schematic description of the spatial evolution of the quasi-Fermi levels splitting from the bulk to the terminal electrodes. The c-Si bulk is represented in the centre with a shell featuring an ideal hole selectivity on the left and a non-ideal electron selectivity on the right. E_{Fn} and E_{Fp} are the energy of the electron and hole quasi-Fermi levels, respectively. The ideal left part of the shell presents zero hole quasi-Fermi level voltage drop with a negligible hole associated resistance and an electron associated resistance approaching infinity. For the non-ideal shell part on the right, R_e and R_h are the associated resistances to the quasi-Fermi level voltage drops for the electron (ΔE_{Fn}) and hole (ΔE_{Fp}), respectively.

In this particular case, presenting an ideal hole selectivity on the left, the ratio of the electron quasi-Fermi level drop (ΔE_{Fn}) to the hole quasi-Fermi level drop (ΔE_{Fp}) induced by non-ideal electron selective shell part is given by:

$$\frac{\Delta E_{Fn}}{\Delta E_{Fp}} = \frac{R_e}{R_h} = \frac{iV_{OC} - V_{OC}}{V_{OC}} \quad (2.27)$$

This ratio gives then an information on the selectivity. The smaller the ratio, the higher the electron selectivity, and thus the smaller the electron quasi-Fermi level voltage drop (compared to the hole quasi-Fermi level voltage drop). A complete description of the selectivity defined by the voltage drop is given in [Onno 2019].

Finally, note that this simple calculation is close to another proposition given by [Brendel 2016] which quantifies the selectivity as:

$$S = \frac{\rho_m}{\rho_M} \quad (2.28)$$

where ρ_m is the resistivity of the minority carriers and ρ_M is the resistivity of the majority carriers. With this definition, it is easily understood that to have a high selectivity, as many majority carriers and as few minority carriers must be obtained at each contact, corresponding to a low ρ_M and a high ρ_m , respectively. Consistently with what was derived following the aforementioned approach of [Wurfel 2015], an asymmetric resistance, i.e., conductivity, for holes and electrons at the contacts is necessary to obtain a high value of S .

2.2.4 Resistive losses

As presented previously, the shell of solar cells must fulfil the roles of passivation, selectivity, and terminal electrodes together. In addition, it has to allow for efficient light collection (e.g., to be highly transparent). However, the different components constituting the shell may lead to additional resistive and recombination losses induced by different physical phenomena. These can cause important electrical transport losses in the solar cell, leading to a decrease of its fill factor (FF) (introduced in section 3.2.2). In the following, the notion of resistance is detailed. The aim is to complete the basis to understand how electrical transport losses are related to voltage drops, for the two kinds of electrical losses which are (i) recombination (loss of carriers, which consequently leads to a loss of chemical potential, as introduced in section 2.2.2) and (ii) resistive effect (loss of carrier energy inducing an electrical voltage drop, as detailed in this section 2.2.4).

During their displacement, which is defined by the current density (introduced in section

2.2.3), the movement of carriers can be hindered by other material particles or physical effects present in the medium under study. Electrical resistance is the property of a material to oppose the passage of an electric current. In other words, it is a measure of the difficulty to pass an electric current through a given medium. The resistance is liable for the dissipation of energy in the form of heat when the current is flowing through a medium, a physical phenomenon called the *Joule effect*. When a continuous potential difference, expressed in volt (V), is applied to a medium, an electric charge displacement is created which can be quantified by the intensity of the current, expressed in ampere (A). Indeed, the electrical voltage drop, which is the difference between the voltages on one side of the medium and the other, not the voltage itself, provides the driving force which pushes the current through it, and represents the ease with which a current can pass through this medium. It is then an information on how the carriers lose energy in a medium, eventually inducing electrical transport losses. The medium properties in terms of resistive losses are fully stated by the relationship linking the voltage between its terminals and the current flowing through it:

$$I = f(U) \tag{2.29}$$

with U the applied voltage and I the resulting current.

The electrical resistance (R) of a material is defined as the ratio of the applied voltage U to the current I flowing through it:

$$R = \frac{U}{I} \tag{2.30}$$

For a large variety of materials and conditions, the voltage and current are directly proportional to each other and the resistance R is then constant at a given temperature or strain. This proportionality is called Ohm's law and materials satisfying this law are called *ohmic* materials. The current-voltage curve (I - V curve) of an ohmic device is hence a straight line passing through the origin with a positive slope. However, in many practical cases, materials and components used in electronics such as solar cells, diodes, batteries or transformers, don't obey Ohm's law: U and I are not linearly proportional, thus the resistance varies with the voltage and current. These are called *non-linear* or *non-ohmic* materials. For these materials, the $\frac{U}{I}$ ratio can still be of interest and is referred to as the *static resistance*; in addition, the derivative of the I - V curve $\frac{dU}{dI}$, called the *differential resistance*, can also prove more insightful depending on the study. The current-voltage relation of a non-ohmic device can, e.g., follow an exponential trend, as in the case of a $p - n$ diode. In solar cells contacts, different physical phenomena leading to electrical voltage drops are caused by resistive effects, in addition to chemical potential drops caused by recombination. Moreover, depending on the solar cell

architecture, charge carriers can flow along multi-dimensional paths, leading to lateral and transversal transports⁵. As the lateral and transversal resistivities might be very different depending on the material properties, different resistive effects can potentially occur.

2.2.5 Transport in solar cells

Transport is defined in this thesis as every single displacement of photogenerated carriers from their generation location until their extraction location at the terminal electrodes of the shell. The transport is thus the flow of both carrier types from the absorber through the shell, on their way to their selective areas and final respective electrodes. The quality of the carrier transport is impacted by two physical phenomena, namely, recombination and resistive effects, both resulting in electrical losses. Recombination is the result of a loss of carriers which induces a *chemical potential* drop; its magnitude is defined by the absorber bulk quality and the shell passivation ability. In contrast, resistive effects are the result of drift-diffusion and interface's phenomena which induce an *electrical potential* drop when both carrier types flow from their generation location inside the absorber to the terminal electrodes, passing through the shell. Both electrical losses impact the final device performances, with the pV reflecting the recombination losses, and the R_s reflecting the resistive losses [Cuevas 2015, Würfel 2005]. In order to reach high FF and eventually high conversion efficiency, pV must be maximized while R_s must be minimized (see section 3.2). Thus, one way to overcome the efficiency losses is to mitigate the transport losses affecting the extraction of photogenerated carriers [Procel 2018, Onno 2019] by improving the passivation quality and by reducing the resistive losses, both resulting in an improvement of the overall selectivity of the shell of solar cells [Würfel 2015]. Nowadays, in state-of-the-art single junction crystalline silicon-based solar cells, the contribution of the crystalline silicon bulk to the electrical losses is not limiting the solar cell performances anymore, as it operates close to its Auger limit and features a suitable conductivity [Richter 2019]. Rather, the main contributions to the electrical losses are dictated by the shell itself, therefore best-in-class c-Si solar cells are nowadays considered to be *shell-limited* devices [Roe 2019, Onno 2019]. It turns out from this electrical transport analysis that improving the c-Si solar cell conversion efficiency requires to mitigate the recombination losses and the resistive effects induced by the shell. To do so, the shell must support a large quasi-Fermi levels splitting inside the bulk in addition to a minimal chemical drop until the terminal electrodes, together with providing minimal supplemental resistive effects in addition to the absorber own resistance. To illustrate the resistive electrical losses induced by the transport of carriers, the case of SHJ solar cell is detailed. In the particular case of SHJ solar cells, the shells aim at meeting the requirements mentioned previously by combining thin layers of different materials (see section 2.1.2). However, these layers involve additional bulk resistivities and several energy barriers stemming from discontinuities in the energy band structure, arising at the hetero-interfaces created between the different materials constituting

⁵This is e.g. the case in the front hole or electron-selective passivating contact of SHJ devices, where the holes or electrons are thought to travel transversally across the a-Si:H(i)/a-Si:H(p) stack, then laterally within the TCO layer in parallel with the c-Si wafer [Bivour 2014c, Haschke 2020] until they reach the metallic fingers.

the SHJ shell, both leading to additional resistive losses [Procel 2019]. Such differences in the resistivity and energy barriers are clearly visible on the energy band diagram of the SHJ shell sketched in Figures 2.4(b) and 2.12 below. The different interfaces are built between the c-Si bulk and the intrinsic amorphous silicon layers, between the intrinsic amorphous silicon layers and the doped thin silicon layers, as well as between the doped thin silicon layers and the TCOs. The overall energy band bending and alignment, including the characteristics of the different energy barriers (such as their height and width), are governed by the coupling of the physical properties of the different materials constituting the shell as well as by the absorber bulk properties. In particular, the requirement for a unique Fermi energy among the device, from the c-Si bulk to the last material layers, defines the resulting band bending. In addition, the Fermi and quasi-Fermi levels are determined by the c-Si absorber carrier density, the thickness, the activation energy, and the defect density of the thin silicon layers, as well as the work function and the carrier concentration of the TCO layer, among others [Procel 2018, Varache 2012]. These key parameters define the energy position of the conduction and the valence bands with respect to the Fermi level for each thin materials layer and thus define the resulting transport quality. Carrier transport through the hetero-interfaces located along the energy-band diagram occurs by two different general mechanisms, namely *thermionic emission* and *tunnelling*. In the specific case of SHJ shells, several tunnelling processes have been identified [Schulze 2010] and thoroughly described, these are: direct tunneling (DT) [Jeong 1998], band-to-band tunneling (B2BT) [Kane 1961] and trap-assisted tunneling (TAT) [Jiménez-Molinos 2002]. These processes are illustrated in Figure 2.12. These mechanisms are difficult to observe, measure, and quantify in practice since they are entangled and do not contribute with the same weight to the total electrical transport. An example highlighting the complexity of the different transport mechanisms is given by [Schulze 2010] in which an overview of transport in the particular case of SHJ shells is presented, and more precisely for the c-Si/a-Si:H stack. In such heterojunction stacks, band offsets may act as barriers and the bulk properties may be discontinuous as important defects (i.e., gap states or traps) are present in the amorphous layer as well as possible interface states at the interface [Varache 2012]. These can further complicate the achievement of good transport properties, as the different transport mechanisms are expected to compete against one another. In particular, bulk defect energy states (E_t) in the band gap of one or several materials constituting part of the shell (a SHJ shell in the present case) may give rise to trapping of charge carriers from the bands, leading to recombination or TAT. Transport can also occur via B2BT or by TAT before a re-emission occurs or that the opposite carrier type is also captured resulting in recombination. In addition, an important density of electronic states is present in the band gap of amorphous layers, resulting in important band tails and numerous dangling bond states situated deep in the gap. This is why this material is especially prone to such TAT transport mechanisms.

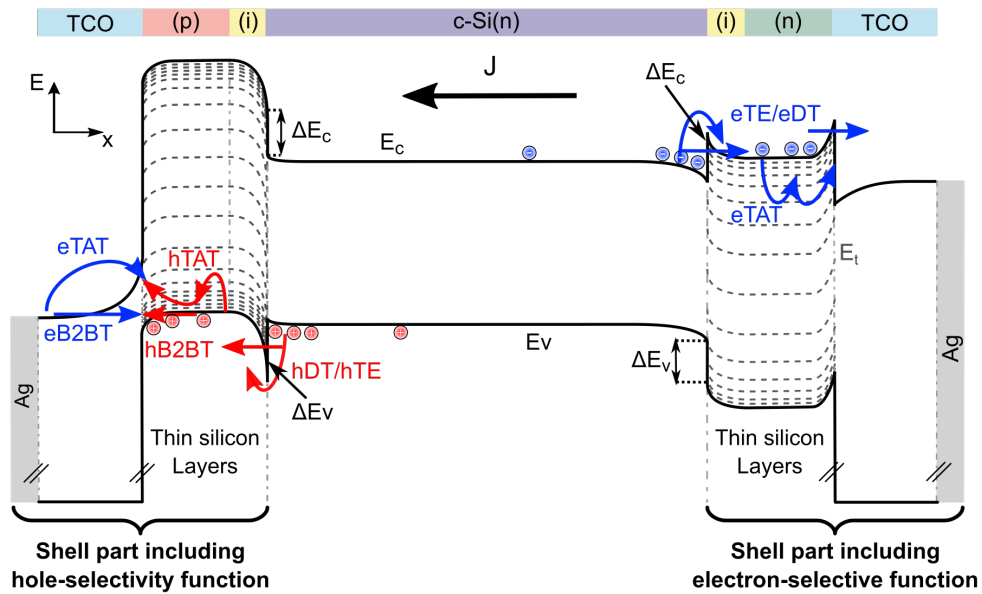


Figure 2.12 – Schematic band diagram of SHJ structure with a c-Si(n) bulk coupled with the two parts of the shell which encompass the different material layers including the hole-collecting function on the left and electron-collecting function on the right (see Figure 2.4). The different transport mechanisms are represented for electrons (e) and holes (h). These mechanisms are thermionic emission (TE), direct tunnelling (DT), band-to-band tunnelling (B2BT) and trap-assisted tunnelling (TAT). Inspired from [Procel 2020].

In particular, due to this complex structure, the optimization of a-Si:H layer properties by means of deposition parameters variation is hindered by several trade-offs. For example, when aiming at reducing the interface defect density, the band gap may change, leading to different band offset values, thus completely reshuffling the energy band arrangement, eventually changing the passivation and selectivity ability, impacting then the overall transport properties. Similarly, when the thickness of the intrinsic amorphous layer is increased, the passivation is improved, however the transport quality is degraded owing to an increase of resistivity induced by this highly resistive intrinsic layer in addition to a reduced band bending inside the c-Si close to its surface. Moreover, amorphous layers have a very low doping efficiency, which makes it impossible to reach high doping without increasing the defect density [Shah 2010]; yet, achieving high net doping of silicon thin films is known to play a major role in the performance of SHJ solar cells [Bivour 2014b]. Furthermore, the addition of a TCO layer on the thin doped hydrogenated silicon layers results in a coupling of their properties which depends on the aforementioned thin silicon layer parameters (doping, defect density, etc.) as well as on the TCO parameters such as its band gap, electron affinity, and carrier density. The carrier density relates to the Fermi level position of the TCO, which is however most frequently described using the TCO *work function* [Klein 2010]: the lower the TCO doping, the higher the work function [Klein 2009]. In short, as the different transport mechanisms are depending on many different material and stack properties, as well as the

resulting coupling properties, it is difficult to predict if these changes will be beneficial or detrimental to the global transport properties *a priori*. In addition, a complete theoretical description of the transport mechanisms in SHJ shells seems extremely difficult, and a single analytical model accounting for all possible transport mechanisms which can be directly linked to material properties does not exist yet [Schulze 2010].

One way to quantify the resistive losses induced by the electrical transport of carrier extraction through solar cell shells is to measure the contact resistivity value (ρ_c). This parameter allows one to assess the carrier transport quality through the interfaces and materials composing the shells. Any change to the energy barriers or to the bulk properties of the materials constituting the shell and of the absorber bulk will directly affect the ρ_c value [Procel 2019]. The parameter ρ_c reflects then the resistive losses of the carrier transport induced by the global band bending resulting from the coupling of the different material properties and is therefore a relevant parameter to investigate different interfaces and coupling within and induced by the shells in general. More detail on ρ_c measurement is given in section 3.2.1.

2.3 Methodology

As introduced in chapter 1, the use of carrier-selective passivating contacts has been theoretically identified [Cuevas 2015] and experimentally demonstrated [Yoshikawa 2017, Haase 2018] to be the most promising way to reach the practical efficiency limit of single junction, crystalline silicon (c-Si) based solar cells. Yet, electrical transport losses affecting the collection of photogenerated carriers as well as optical losses remain to be addressed and, to this aim, different methodologies and characterization methods are currently used. In the first section 2.1.2 of this chapter, a generalized and unambiguous description of contacts in solar cells was presented by introducing the terminology of *shell*. This concept aims to accurately investigate – and eventually mitigate – the electrical as well as the optical losses affecting state-of-the-art solar cells. Importantly, this terminology makes it possible to go beyond the limitations of the term of *contact*, which is indifferently used to refer to any part of the solar cell where the generated carriers are extracted, and therefore to precisely consider the interfaces and the physical properties coupling present between the different materials in solar cells. Indeed, as detailed all along this chapter 2, contact schemes for solar cells actually consist of several stacked materials, materials with locally changing properties, or combinations of both.

In this section, a novel characterization methodology using two approaches named the *top-down* and the *bottom-up* approaches is presented. These define a characterization procedure designed to independently track the properties of the materials used to build the whole shell as well as the performance of the solar cell incorporating the shell along its different process steps. The aim is to be able to link the properties of the shell to the final performance of the solar cell. As stated in chapter 1, one major objective of this thesis is to unveil some key parameters controlling the transport losses in SHJ shells with the aim to find practical levers which can be linked to the relevant transport mechanisms and which can give experimental information and

guidelines to improve the shell. To do so, the so-called *top-down* and *bottom-up* approaches were designed and are introduced in the following section 2.3.1.

2.3.1 Top-down and bottom-up approaches

As described in the previous section 2.2.5, electrical transport losses defined by the shells of solar cells are difficult to identify and to control since multiple material layers and several entangled physical phenomena are involved. In this thesis, one major objective is to understand and improve the electrical transport of the shells of silicon heterojunction solar cells with a particular focus on the carrier-selective and passivating functions. To this end, to study and mitigate the electrical transport losses, two approaches were used. The first one is called the *bottom-up* approach and consists in monitoring the shell properties along its different process steps, as illustrated in Figure 2.13 for the case of a SHJ shell. The parameters typically monitored in this approach are the passivation, the selectivity as well as the final solar cell parameters such as the open-circuit voltage (V_{OC}), fill factor (FF) and series resistance (R_S). The second approach is named *top-down*. In that case, each individual shell sub-component is characterized independently, providing physical key parameters which give insights into the electrical properties of the shell under study. Typical physical parameters characterized during this work are the thickness, activation energy, crystallinity, conductivity, contact resistivity, carrier density and sheet resistance of thin layers made of various materials. These physical parameters are foreseen to unveil the link between the final shell properties and the resulting electrical transport quality of solar cells. In addition, these would be parameters giving particularly valuable information on the ability of a material, or a material stack, to make an efficient carrier-selective passivating contact and be part of the shell.

Combining these two approaches therefore gives relevant information on the global electrical transport. This permits the control and improvement of the transport quality of the shells, first by investigating the physical parameters of shell components with the *top-down* approach and, secondly, to study how they impact the final cell performance by analysing the shell parameters obtained from the *bottom-up* approach. The different characterization methods used in both the *top-down* and *bottom-up* approaches are detailed in section 3.2. Finally, once the transport quality of a promising shell has been established, its optical properties and its potential to satisfy different solar cell architecture constraints can also be assessed using both approaches. A major outcome of this novel characterization methodology is thus to bridge the gap between theory and experiment by bringing new insights about the electrical quality of the shell thanks to measurable parameters, as well as identifying suitable materials for achieving high electrical solar cell performance.

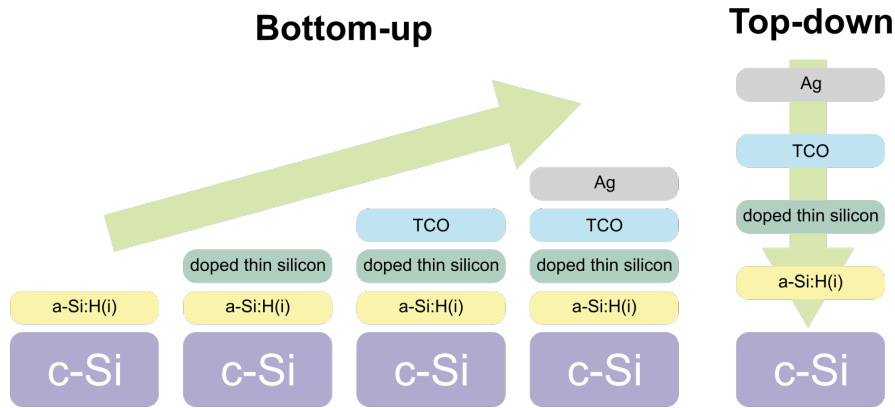


Figure 2.13 – Description of the bottom-up and top-down approaches in the case of a SHJ shell.

The measurements of the different material and shell parameters mentioned previously were selectively performed at three different levels: on each shell component layer taken separately, on chosen stacks of layers of the shell, and on the whole shell. There are two important points to keep in mind, to get relevant information on the electrical transport. First, the level at which the physical parameters are measured must be well understood because the shell characteristics are not simply the sum of the properties of its component layers, but their properties are coupled together. Secondly, the substrate (e.g., glass sample or c-Si wafer) on which the layer, the stack, or the shell is deposited affects the layer growth and hence the measured parameters [Cruz 2020] (see next paragraph and Figure 2.14). Thus, a careful analysis has to be conducted to study the material layer as a function of the substrate properties. In addition, such an approach allows for the characterization of the different electrical functions and of the shell without requiring each time the fabrication of a complete solar cell. Eventually, combining these measurements makes it possible to predict how efficient a solar cell can be made with a given shell.

As introduced above, when two or more contact materials are coupled, the resulting transport quality differs from the sum of the individual component properties, since a coupling of the material properties appears. Short examples of material properties coupling evidenced by the *bottom-up* and the *top-down* approaches are given in Figure 2.14. First, comparing the contact resistivity (ρ_c) values of the a-Si:H(i)/ITO (abbreviated i/ITO here) stack with the a-Si:H(n)/ITO and a-Si:H(i)/a-Si:H(n)/ITO (abbreviated n/ITO and in/ITO respectively here) it is observed that ρ_c of the in/ITO stack is lower than the ones of the i/ITO and of the n/ITO stack. This illustrates well that the overall contact resistivity of the in/ITO stack is not equal to the simple "mathematical" sum of the contact resistivities of its sub-layers i and n measured individually. Moreover, the implied V_{OC} (iV_{OC}) values measured after the intrinsic and doped thin silicon layers (abbreviated ip and in here) deposition at both sides of the c-Si wafer may be different than the one measured after the final step of TCO deposition (on top of the thin silicon layers) completed with annealing. Here, the iV_{OC} values obtained after TCO deposition

and annealing are higher than after the first step of ip/in deposition. Such coupling effects are also well illustrated with the crystallinity factor (Φ_c). Indeed, the surface Φ_c value obtained for the p-type thin nanocrystalline silicon layers (ncP) deposited on a-Si:H(i) layer (incP) is lower than the surface Φ_c value obtained for this same layer deposited on the a-Si:H(i) and n-type nanocrystalline thin silicon layer stack (incNncP) (see Figure 2.14c). In addition, this Φ_c value is lower than the one of the single incn layer. One last example to illustrate the importance of the coupling of the layer properties to the final shell properties can be given by looking at the TCO carrier concentration (N) obtained when measured either on a bare glass substrate or on a glass substrate covered with an a-Si:H(i) and n-type thin silicon layer stack (i/n). The values obtained on the i/n layer-coated glass are generally higher than when the same TCO is directly deposited on a bare glass sample. The different parameters and characterization methods used to illustrate these examples are detailed in chapter 3.⁶ Importantly, this methodology combining the *top-down* and *bottom-up* approaches was introduced in this section with specific examples of SHJ shells but can be generalized to any solar cell technology.

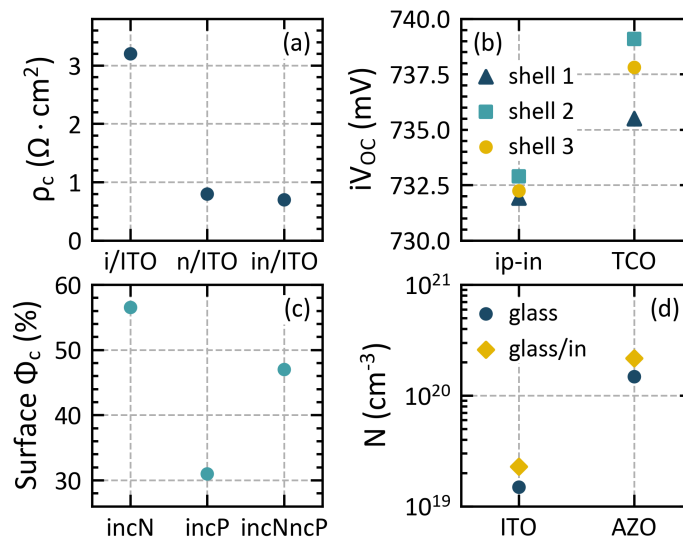


Figure 2.14 – Illustrative examples of the relevance of the bottom-up and the top-down approaches to fully characterize a shell. (a) contact resistivity ρ_c values for different stacks of layers. (b) iV_{OC} values for three different shells after deposition of front and back thin silicon layers ip-in and after the deposition and the annealing of the front and back TCOs. (c) surface Raman crystallinity factor (Φ_c) values of different thin silicon layer stacks. (d) Carrier concentration of two different TCOs (indium-tin oxide (ITO) and aluminium-doped zinc oxide (AZO)) deposited either on bare glass samples or on glass samples coated with thin i/n silicon layers.

⁶Note that all the physical parameters and layers presented here, namely, ρ_c , iV_{OC} , Φ_c , and carrier concentration as well as in-ip and TCO are introduced in more detail in chapter 3.

2.4 Conclusion

In this chapter, we presented and discussed the concept of *contact* in solar cells in detail along with the fundamental operating principles of solar cells. In particular, we presented a generalized and unambiguous description of contacts in solar cells by introducing the new terminology of *shell*. Then, we gave an overview of the fundamental physics of semiconductor-based solar cells, including the electron and hole generation mechanisms and the different physical phenomena impacting the carrier transport in silicon solar cells which are bulk and surface recombination, passivation, selectivity, and resistive effects. Furthermore, a description of the carrier transport in the specific case of silicon heterojunction solar cells and its impact on the efficiency of such devices was given. Finally, we presented a novel characterization methodology using two new approaches named *top-down* and *bottom-up* which were established to accurately study, investigate and mitigate the electrical transport losses.

In the following chapters, the concepts introduced here will be applied to various case studies. First, in chapter 3, different characterization techniques used to characterize the different shell sub-layers individually or in various stacks (*top-down*) and to characterize the evolution of the shell properties along the different process steps as well as the final solar cell performance (*bottom-up*) will be presented. Secondly, in chapters 4, 5 and 6, the shell concept and both the *top-down* and the *bottom-up* approaches will be rigorously applied to experimental SHJ materials and solar cells, with the aim to accurately investigate and eventually mitigate the electrical as well as the optical losses affecting actual SHJ solar cells.

3 Experimental processes and characterization systems

Summary

This chapter presents the main processes and equipment used during this thesis for the fabrication and the characterization of silicon heterojunction (SHJ) solar cells. In a first part, an overview of the process flow used for the fabrication of the three different SHJ device architectures studied in this thesis is presented. These architectures are the monofacial, the bifacial, and the interdigitated back-contact (IBC). Then, a detailed presentation of the different processing equipment and tools is given. In the second part, the layer and cell characterization techniques and systems used and developed along this work are described. Significant emphasis is put on this part, which presents an important work of development, understanding and optimisation performed on several characterization methods and systems. In particular, the transfer length method, the Raman spectra measurement, the dark conductivity measurement, the photoconductance decay computations, as well as the pJ - pV curves extraction method are presented in detail.

3.1 Experimental processes

3.1.1 Silicon heterojunction solar cells baseline process flow

The process flows used to manufacture the three different SHJ device architectures studied in this work, namely the monofacial, bifacial, and IBC configurations, are depicted in Figure 3.1. In all cases, n-type monocrystalline silicon (c-Si(n)) wafers featuring a resistivity between 1.8 to 3 Ω cm, a thickness between 150 to 240 μ m, and grown either by the Czochralski (Cz) or the float-zone (Fz) technique, are used (unless mentioned otherwise). First, the wafer is textured on both sides in an alkaline solution to create random pyramids and then wet chemically-cleaned using different chemical baths. Then, before the deposition of the different layers, the native silicon oxide present on both sides of the c-Si wafer is removed in a diluted hydrofluoric acid solution. Promptly after this step, a thin blanket hydrogenated intrinsic amorphous silicon (a-Si:H(i)) film is deposited on both sides of the wafer for surface

passivation by plasma-enhanced chemical vapour deposition (PECVD), using an Indeotec Octopus II system. Then the n-type and the p-type hydrogenated thin silicon layers are immediately deposited, with the same deposition system, on top of the a-Si:H(i) layers. These layers are in amorphous (a-Si:H(n/p)) or nanocrystalline (nc-Si:H(n/p)) phase depending on the device architecture. For the monofacial configuration, generally a full blanket a-Si:H(p) layer is deposited on the top and a full blanket a-Si:H(n) layer is deposited at the back side of the wafer and conversely for the bifacial configuration (a-Si:H(n) on top and a-Si:H(p) at the back side) [Descoedres 2011, Descoedres 2017]. For the IBC configuration, the nc-Si:H(n) layer is deposited in situ through a shadow mask to define the electron-collecting area of this architecture, then the mask is removed and a full blanket nc-Si:H(p) layer is deposited on top of the a-Si:H(i) and nc-Si:H(n) layers, covering the entire back surface. Then, at the front side, the thin a-Si:H(i) passivating film is covered by a silicon nitride (SiN_x) antireflecting coating (ARC) deposited at low temperature (200 °C), providing additional surface passivation, high transparency and good light coupling [Tomasi 2017]. After the PECVD steps, transparent conductive oxide (TCO) and silver layers are deposited using sputtering techniques. For monofacial and bifacial devices, indium tin oxide (ITO) or aluminium-doped zinc oxide (AZO) films are deposited at the front and at the back sides of the wafer. ITO layers are deposited using DC magnetron sputtering with the Indeotec Octopus II PVD tool, and AZO layers are deposited by RF magnetron sputtering with an Oerlikon Clusterline tool. The front TCO thickness is adapted to act as an efficient ARC. Then, for monofacial devices, a 200-nm-thick silver rear blanket layer is sputtered over the whole back TCO layer. In the case of IBC devices, a full blanket AZO layer is deposited at the back side onto the nc-Si:H(p) layer. Finally, the metallic grids are applied by screen-printing a low-temperature silver paste at the front side of monofacial and bifacial solar cells, as well as at the back side of bifacial and IBC solar cells. An annealing at 210 °C during 10 to 30 minutes is also applied to cure the paste. As a last step for the IBC devices, the AZO layer parts present between the silver grids are etched away in a light acidic solution.

3.1. Experimental processes

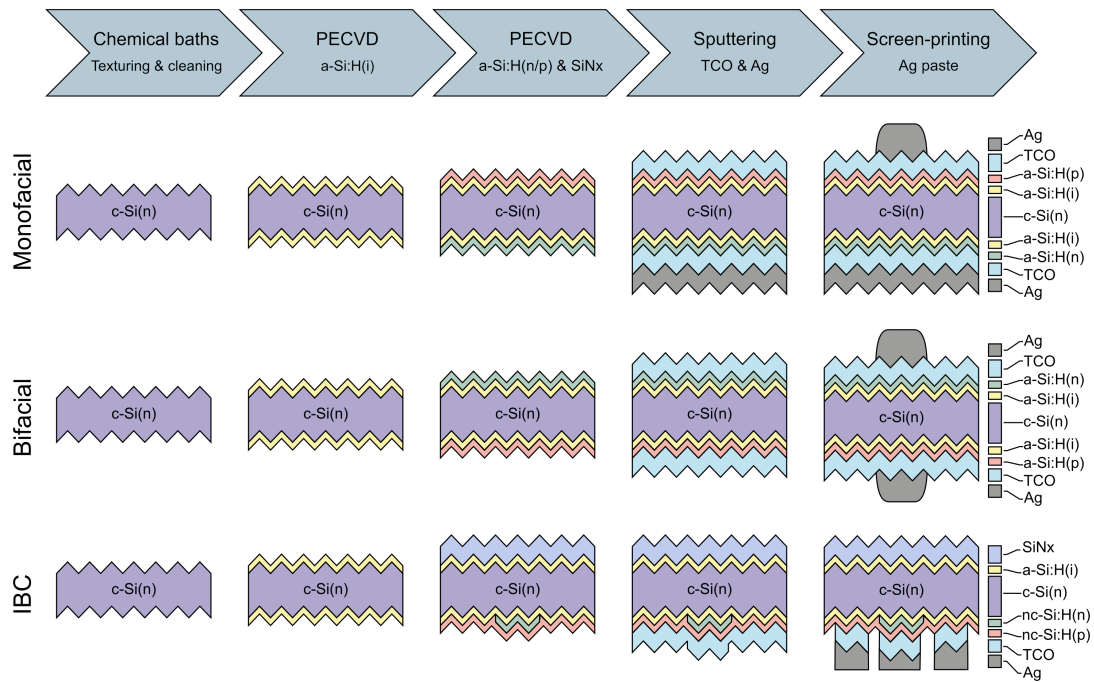


Figure 3.1 – Overview of the process flows of the three SHJ architectures processed in this work, which are the monofacial (top), the bifacial (middle), and the IBC (bottom).

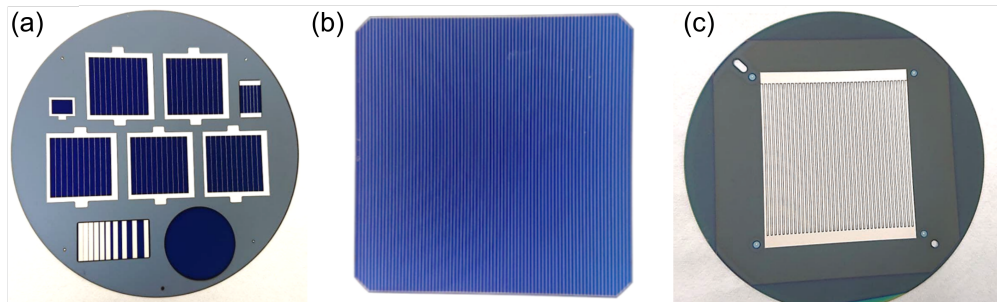


Figure 3.2 – Pictures of the three SHJ architectures processed in this work, which are (a) the monofacial, (b) the bifacial, and (c) the IBC.

During this work, the monofacial solar cells were generally processed on 4-inch FZ silicon wafers. A metallic shadow mask was used during the front TCO deposition to define five $2\text{ cm} \times 2\text{ cm}$ solar cells per wafer. In contrast, the bifacial solar cells were processed on full 6-inch Cz silicon wafers, while the IBC devices had a size of $5\text{ cm} \times 5\text{ cm}$ and were fabricated on 4-inch FZ or Cz silicon wafers.

3.1.2 Silicon heterojunction solar cell manufacturing systems

Wafer texturing and cleaning

The monocrystalline silicon wafers used to fabricate solar cells feature an $\langle 100 \rangle$ orientation and are obtained by slicing high-purity silicon ingots using arrays of wires. After wire sawing, the wafer surface is highly defective and rough, presenting microcracks and dislocations. Thus, as a first step, these saw damages are removed in a concentrated potassium hydroxide (KOH) bath to obtain a favourable electronic quality. Then, as the reflectivity of a flat silicon surface, even when coated with a well optimised antireflecting coating, is quite high (up to 13 % in the visible spectrum) [Sobkowicz 2014], the light trapping properties of the silicon surface has to be enhanced. To do so, micro-scale random pyramids are patterned on the surface using a second KOH bath in which the temperature, the KOH and the surfactant concentrations are optimized to promote the pyramids' formation. This process is named texturization. The KOH solution etches the crystalline planes present on the surface of the wafer at different rates and reveals the $\langle 111 \rangle$ -oriented faces [Madou 2002] while patterning the random pyramids, resulting in an increase of the surface area by a factor of ~ 1.73 . This factor is found by trigonometric calculations considering the angle of 54.7° between the (100) and (111) planes of a pyramid on a textured c-Si wafer [Seidel 1990]. The resulting pyramids range between 1 to $5\ \mu\text{m}$ and result in multiple light reflections, each contributing to the enhancement of the light absorption inside the wafer. Finally, the texturization process is followed by a cleaning sequence using acid baths to remove the metallic and the organic contaminants [Papet 2006]. In this way, a highly pure silicon wafer surface is obtained and a practically perfect optical structure is achieved without the need for complex and expensive patterning techniques [DeWolf 2012]. Finally, before cell processing, the surface native oxide is removed by dipping the wafer in a 5 % diluted hydrofluoric acid (HF) solution for 60 s.

Plasma-enhanced chemical vapour deposition (PECVD)

The thin hydrogenated silicon and the SiN_x layers illustrated in Figure 3.1 are deposited by plasma-enhanced chemical vapour deposition (PECVD). This technique is based on the dissociation of gas precursor molecules in a plasma. By definition, a plasma is an ionized gas that includes a mixture of electrons and neutral atoms, ions, free radicals, and molecules at different levels of excitation. The energy transfer from electrons to gas precursor molecules occurs via collisions, inducing a radiation in the visible part of the spectrum [Lieberman 1994]. To ignite and maintain a plasma, the reactor chamber is filled with a precursor gas at low pressure which is then ionized by means of an electric field which can be generated with different sources. These sources can be radio-frequency, microwave or a continuous electrical discharge between two electrodes, depending on the gas constituents. In these conditions, the plasma features free electrons which present a higher temperature than the gas. Thus, under this non-equilibrium state, chemical reactions are initiated by collisions of highly energetic electrons and gas molecules which facilitates the deposition even at low temperatures

(~200 °C) [Smith 1995].

The PECVD system used in this thesis is the Octopus II system from Indeotec, depicted in Figure 3.3b. This system is composed of a cluster of different PECVD chambers (as well as a PVD one which is described in more details in section 3.1.2). To deposit a layer, first, after the HF dip for native oxide removal, the silicon wafers are put on a metal plate and introduced in the processing chamber. Before injecting the gases, the chamber is brought to high vacuum to remove the unwanted components and impurities (e.g., possibly remaining from previous depositions) and to reach the adequate pressure for plasma ignition. Then, the chosen mix of gas precursors is introduced homogeneously in the chamber through a shower head and the desired mixing of gases is achieved with mass flow controller (MFC) valves. A schematic description of the PECVD reactor is given in Figure 3.3a. These MFC valves regulate the amount of each chosen gas precursor allowing for a large variety of gas compositions. The unit used to measure the gas flow is the standard cubic centimeters per minute (sccm). One sccm represents $1 \text{ cm}^3 \text{ min}^{-1}$ of gas flow at standard conditions which is defined by a pressure of 1.013 bar and a temperature of 273.15 K. During the process, the chamber pressure is automatically regulated by a butterfly valve placed between the process pumping unit and the chamber. The main gases used in this thesis for the thin hydrogenated silicon and SiNx layers deposition are the following:

- Silane (SiH_4) which is the main precursor for silicon-based layers.
- Trimethylborane ($\text{B}(\text{CH}_3)_3$), called TMB, which is diluted in 98 % of H_2 and used to provide boron (B) species for p-type doping.
- Phosphine (PH_3) which is also diluted in 98 % of H_2 and used to provide phosphorus (P) species for n-type doping.
- Hydrogen (H_2) which is used to increase the hydrogen content of a layer and to promote crystallinity if introduced in large amount inside the gas mix.
- Carbon dioxide (CO_2) which is used for plasma treatment and to vary the transparency and the crystallinity of thin hydrogenated silicon layers.
- Ammonia (NH_3) which is used to provide nitrogen (N) species for SiNx layers.

The PECVD reactor contains two parallel electrodes 15 mm apart between which the plasma is created. Both electrodes are metal plates connected to a RF power generator. One electrode is the RF powered metal plate which contains the gas shower head and the second one is the grounded metal plate which holds the substrate. In addition, the two parallel plates are sealed in a hermetic box, in which the plasma is confined, defining the so-called *plasma box*. This box is placed in a main chamber in order to reach a high primary vacuum and allows one to keep a differential pressure with the main vacuum chamber to prevent impurities coming from the cold walls of the main chamber from being introduced inside the plasma. In addition,

Chapter 3. Experimental processes and characterization systems

the differential pressure can be used to vary the final layer properties. The chamber and the substrate are heated up and maintained at a given temperature (generally 200 °C). Once the pressure and thermal equilibrium of the gas mix in the chamber are reached, the power supply is switched on at an excitation frequency of 13.56 MHz or 40.68 MHz. This energy source provides the required kinetic energy for electrons contained in the gas to dissociate the gas molecules. Thus, the ions and radicals diffuse towards the edges of the reactor where they react with each other to form a material film. The plasma characteristics and hence the growth of the material film and its resulting properties are determined by many different process parameters. These are the gas mixture, flow and pressure, temperature, RF power density, excitation frequency, deposition time, reactor conditioning as well as substrate (here silicon wafers) properties. In addition, the reactor geometry as well as the distance between both electrodes play also an important role. Thus, controlling these parameters allows for a good control of the layer microstructure and the possibility to alloy the layer composition in a wide range as well as to vary the layer properties such as doping concentration, crystallinity, bandgap, hydrogen content, etc.

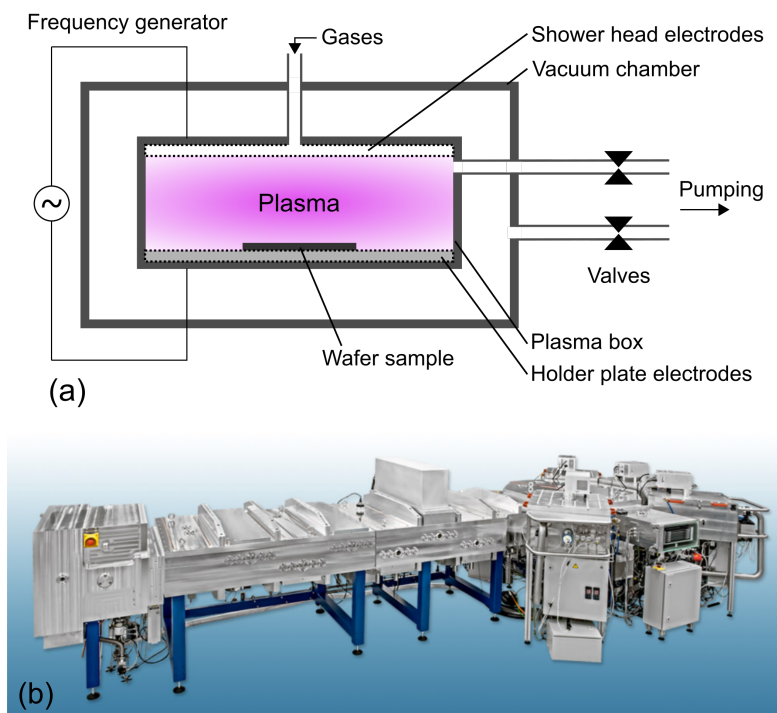


Figure 3.3 – (a) Schematic description of a PECVD reactor with the plasma box design. (b) Picture of an R&D Octopus II from Indeotec (Copyright Indeotec SA).

Magnetron sputtering deposition

Magnetron sputtering is a physical vapour deposition (PVD) technique used along this work to deposit TCO and silver layers. This technique is based on a kinetic process where energetic ions, generally argon (Ar) ions, are thrown towards a target, made of the materials to be deposited, to extract atoms from the surface and deposit them on a substrate, such as silicon wafers. First, the Ar ions are created with a plasma ignited and maintained in a chamber at low pressure by radio-frequency (RF) or direct current (DC) excitation depending on the material to be deposited. RF excitation can be used for both conductive and non-conductive targets, whereas DC excitation can be used only for conductive targets. To separate the atoms from the target surface, the Ar ions are accelerated towards the target by means of an electric field and concentrated on the target with a magnetic field. Secondly, electrons are also emitted from the target surface due to the ions bombardment. These electrons are important to maintain the plasma discharge and the sputtering yield. After ejection of atoms from the target, formation of layers on the substrate surface occurs by clustering of sputtered atoms. During TCO sputtering deposition, alloying gases such as hydrogen (H₂) or oxygen (O₂) can be added to the Ar gas to vary the TCO final properties. In particular, the electrical properties of a given TCO films, such as its carrier density, mobility and conductivity, depend on the oxygen vacancies present inside its structure [Lewis 2000, Barraud 2013] and this vacancies can be modified by varying the O₂ partial pressure during the deposition [Ellmer 2001]. The deposition rate decreases with the rise of the pressure and increases with the rise of the power, as a higher pressure reduces the maximal kinetic energy of the Ar ions while the power increases it. These parameters have to be optimised carefully to ensure high quality layer properties as well as to minimise the sputtering damages caused by ions and radicals bombardment as well as UV irradiation, eventually detrimentally impacting the underlying thin silicon layer properties [Demaurex 2012].

Throughout this work, ITO layers were deposited using DC magnetron sputtering with an In₂O₃:SnO₂ target with the Indeotec Octopus II PVD tool (see Figure 3.3b), and AZO layers were deposited by RF magnetron sputtering with an ZnO:Al₂O₃ target, containing 2 % of Al₂O₃, using an Oerlikon Clusterline tool. During deposition, the sample is placed on a holder which either translates at a constant speed in front of the target (as in the Octopus II) or rotates at a constant speed (as in the Oerlikon Clusterline) to obtain a homogeneous film thickness. A pre-sputtering treatment is generally applied before the actual deposition to have a constant target surface state for each deposition.

For 2 cm × 2 cm monofacial solar cells the front TCO is masked to define the final active cell area. This masking is required to avoid leakage of current through TCO parts at the edges of the active cell area which are not exposed to light. In addition to the requirement of masking the front TCO, in general, the TCO deposited over the hole-collecting shell part must always be masked. Indeed, in the case of full blanket TCO layer deposited on p-type thin silicon layer, if not masked to define the different cells, the TCO will extend the effective area of the p-n junction diode while keeping the illuminated zone constant, resulting in a dark

diode in parallel with the illuminated one, leading to the introduction of artefacts in the IV measurements. For full 6-inch bifacial solar cells, the back TCO is masked at the wafer edges to avoid shunting between the front and the back side of the solar cell. Finally, for IBC solar cells, the full AZO layer is deposited as a blanket layer over the nc-Si:H(p) layer and then selectively etched away to define the hole and electron electrodes after the screen-printing process.

Screen-printing metallization

Silver paste screen-printing metallization is used to deposit the front and back metal grid of solar cells. The grid must be as conductive as possible while minimising the light shadowing. In the screen-printing technique, the silver paste is applied on top of TCO layers by means of a screen. This screen is a mask consisting of a metallic mesh covered by a resist with local openings defining the required pattern. For SHJ solar cells, dedicated silver pastes (so-called low temperature pastes) are used to comply with the maximal curing temperature of 210 °C of such devices. This limited temperature is needed to preserve the high passivation quality provided by the amorphous layers. Silver pastes are made of silver particles (>70 % solid content) and organic-based ligands. In this work, the silver paste screen-printing was performed in an automated screen-printer, the XH STS from EKRA. It enables to control accurately the wafer alignment and the pressure applied to the squeegee. After undergoing the screen-printing, the low-temperature silver paste has to be cured at a temperature of 150 to 210 °C depending on the paste properties, to evaporate the ligands. This step is usually performed in a belt furnace.

In this work, the front grid pattern, which is used for the 2 cm × 2 cm cells, consists of ten fingers spaced 1.85 mm apart, featuring a width of 35 μm each and connected to each other with an all-around busbar. For the bifacial cells, the pattern is busbar-less and constituted of 81 fingers with a pitch of 1.93 mm at the front side and 259 fingers with a pitch of 0.60 mm at the back side. The fingers have a width of 30 μm. Finally, the IBC grid features 20 n-type fingers with a width of 800 μm and 19 p-type fingers with a width of 1400 μm.

Selective material etching

Selective material etching is performed using wet chemical baths and a protective material. During this work, the sputtered ITO, AZO, and silver (Ag) layers underwent etching processes to define different patterns, such as the TLM pads as well as the IBC electron and hole electrodes designs. First, the desired pattern is applied with the use of a resist mask or another material resistant to the chemical bath. The mask is generally made of screen-printed silver paste or hotmelt resist. The hotmelt resist is applied with the inkjet printing method, which creates a given pattern by printing the hotmelt resist on the sample. This resist protects the masked areas while performing the wet etching on the unmasked areas. The inkjet printer used in this work is the PiXDRO LP50. To selectively etch the materials under investigation, the samples were immersed in chemical baths containing various acidic solutions. The different solutions

and etching times used to etch AZO, Ag and ITO layers are given in table 3.1.

Material	Solution	Etching time (s)
AZO	HCl 0.1%	45-60
Ag	HNO ₃ 26%	20-45
ITO	HCl 37%	~ 240

Table 3.1 – Chemical solutions and etching time used to etch AZO, Ag and ITO layers.

Thermal evaporation

Thermal evaporation is a deposition method in which the material to be deposited is heated up in a high vacuum chamber (below 1×10^{-5} mbar) to its evaporation point. Contrary to PECVD and PVD techniques, a specific material can be deposited without the use of additional gas flow. Small pieces of the material to be deposited are placed in a resistive crucible made of tungsten or molybdenum. A high electric current is then applied to the crucible, inducing Joule effect which heats up both the crucible and the material it contains. In the case of material presenting a high boiling point, an electron beam focused on the crucible can be used as heat source. However, a significant disadvantage of using electron beam is the intense X-ray emission due to the electron Bremsstrahlung which may damage the thin silicon layers of SHJ solar cells. The substrates are placed on the top of the chamber and mounted on a rotary holder to ensure a good deposition homogeneity. To control the thickness of the deposited layer, a piezoelectric micro-balance monitors during the deposition the amount of deposited material. This deposition method was used in this project to deposit magnesium fluoride (MgF₂) as well as aluminium (Al) layers.

Optimal monofacialization of bifacial solar cells

Bifacial solar cells can undergo three additional process steps to transform their architecture in an optimized monofacial configuration featuring improved rear carrier extraction and light-collection. To do this, MgF₂ layers are first deposited by thermal evaporation both at the front and at the back sides, over the full ITO layers and silver grids. Then, a full blanket silver layer is deposited by PVD over the rear MgF₂ layer. The additional front MgF₂ layer coupled with the front ITO layer is optimized to provide an effective double antireflective coating (DARC) thanks to its smaller refractive index than ITO, which increases the J_{SC} of the cell [Lee 2000, Bouhafs 1998, Zhao 1996]. The contact between the rear full area silver layer and the silver grid is made possible thanks to the porosity of the silver grid and to its thickness which is between one and two orders of magnitude thicker than the MgF₂ layer. Thus, the additional full rear silver layer allows for a reduction of the resistive losses by providing a high conductive path for the carrier extraction. In addition, the rear MgF₂ layer provides an improved back reflector by minimizing parasitic IR light losses. Indeed, it has been demonstrated that dielectrics serve as efficient optical buffer layers when inserted between

the TCO and metal layers, increasing the total rear internal reflectance, which yields to an increase of the IR spectral response of the cell. This is made possible thanks to a low refractive index provided by the dielectric layer (here about 1.37 at IR wavelengths for MgF₂) which improves the rear reflectance by both reducing the penetration depth and field strength of evanescent waves and by suppressing the plasmonic absorption in the rear silver layer by pushing it away enough to not being within the penetration depth of the resulting evanescent wave [Holman 2013b, Holman 2013c].

3.2 Characterization systems

As presented in chapter 2, to study and to gain a better understanding of the optical and electrical losses in solar cells and to mitigate their impact on the final device performance, the *top-down* and the *bottom-up* approaches were applied. Different techniques exist to characterize the different shell sublayers individually or in various stacks (*top-down*) and to characterize the evolution of the shell properties along the different process steps as well as the final solar cell performance (*bottom-up*). This section aims at giving the required information and details among all characterization techniques which were used during this work. A particular focus is put on the contact resistivity measurement with the transfer length method, on the Raman measurement for crystallinity and thickness assessments, on the dark conductivity measurement for the activation energy evaluation, on the photoconductance decay measurement for passivation quality tracking along the different shell process steps as well as on the *pJ-pV* curves extraction for pseudo-fill factor assessment. These techniques are the ones which were mainly explored for implementation and improvement in our lab during this work. The physical parameters obtained with the different techniques are presented to give insights on the information they provide in order to unveil the link between the final shell properties and the resulting optical and electrical performances of solar cells.

3.2.1 Layer characterization

The different methods and systems used to characterize the different shell sublayers individually or in various stacks presenting different layer combinations (*top-down*) are presented in this section.

Profilometer

One method to measure the thickness of thin layers is to use a one-dimensional height scanning profilometer. The setup used during this work is the KLA-Tencor P-15 Profiler which is a highly sensitive contact surface profiler which measures step height on sample surfaces. It is composed by a diamond stylus which probes the surface of a sample while moving laterally during a specified distance and with a specified applied contact force. This allows for measuring small surface variations in function of the position by means of the vertical stylus

displacement. The height position of the diamond stylus generates an analogue signal which is converted into a digital one which is analysed and displayed by a computer. Thus, scanning the surface of a substrate and comparing the step height between two surface locations allows the thickness measurement of layers as thin as 10 nm (lower limit) with an error of ± 3 nm. The substrate on which the layer is deposited must be flat, such as glass or polished c-Si wafer. To illustrate the profilometer measurement, a typical thickness series of AZO layer is depicted in Figure 3.4. In this work, two process flows were used to prepare layers for profiling:

- For thickness measurements of thin silicon layers deposited on glass substrates, a step between the bare glass and the deposited layer is formed by exploiting the selective etching of silicon over glass, which e.g. may be accomplished by reactive ion etching (RIE) using a plasma of SF_6/O_2 . First, the targeted area is protected applying a PLASTIK-70 resin and the surrounding layer is etched away by the SF_6/O_2 plasma attack. Afterwards, the resin is dissolved in acetone and the sample is cleaned using isopropanol. This method was used for the investigation of the mixed-phase thin silicon layers developed in this work, as a precise ellipsometer model is challenging to set up in this case.
- For thickness measurement of contact layers such as TCO or metals, the substrate (generally a glass sample) is protected over an area using a marker (generally a black pen) before the layer deposition. After the deposition, this protective mark is dissolved in acetone leaving a bare glass stripe creating a step between the glass and the layer.

From the thickness value obtained on flat substrates, it is possible to estimate the thickness of the same layer deposited on c-Si wafers featuring a textured surface by dividing the thickness obtained on glass samples by a conversion factor. This conversion factor is equal to about 1.73 which is found by trigonometric calculations considering the angle of 54.7° between the (100) and (111) planes of a pyramid on textured c-Si wafer [Seidel 1990]. Note that thinner layer thicknesses (i.e. below 10 nm) can be accurately measured by ellipsometry, and that the thickness of layers deposited on textured c-Si substrates can be directly measured using Raman spectroscopy.

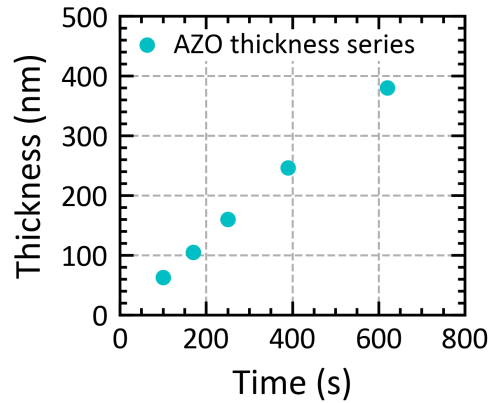


Figure 3.4 – AZO layer thickness as a function of the deposition time. The AZO thickness is measured by profilometer on glass sample for a variation of the deposition time in the Clusterline PVD tool.

Hall effect measurement

To assess the majority charge-carrier resistivity (ρ), concentration (N) and electrical mobility (μ) of thin doped layers, a characterization system combining the van der Pauw method and the Hall effect measurement is used. The sample under study is a square-cut glass with a dimension of 1.5 cm x 1.5 cm coated with the layer under investigation, which is connected with four contacts placed at each edge of its four corners as illustrated in Figure 3.5a.

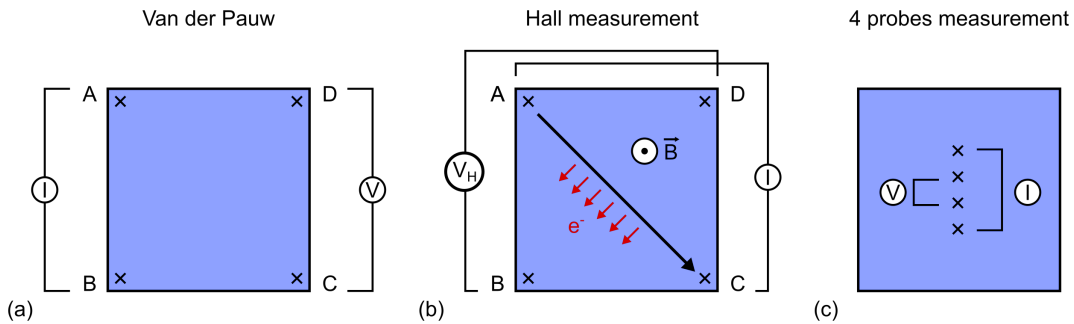


Figure 3.5 – Schematic description of (a) the Van der Pauw configuration, (b) the Hall measurement configuration with the electron flow deflected by the Lorentz force and (c) the four-point probes configuration.

First, the measurement starts by using the van der Pauw method to determine the sheet resistance (R_{sh}) of the layer under investigation. To do this, a series of voltage measurements between the different pairs of contacts is performed. A constant current (I) is forced through opposite pairs of contacts such as A-B or A-D while the voltage (V) is measured across the

other pair of contacts D-C or B-C respectively (see Figure 3.5(a)). From these two values, a resistance is found using Ohm's law: $R_{AB,CD} = V_{CD}/I_{AB}$ and $R_{DC,AB} = V_{AB}/I_{DC}$ which are equivalent by reciprocity theorem leading to $R_{vertical} = (R_{AB,CD} + R_{CD,AB})/2$. The same measurement is performed along AD and BC direction to find the $R_{horizontal} = (R_{AD,BC} + R_{BC,AD})/2$ [Ashcroft 1976, Ginley 2011]. Then, from these two resistances the sheet resistance (R_{sh}) is calculated with the van der Pauw equation:

$$\exp\left(\frac{-\pi \cdot R_{vertical}}{R_{sh}}\right) + \exp\left(\frac{-\pi \cdot R_{horizontal}}{R_{sh}}\right) = 1 \quad (3.1)$$

Then assuming that $R_{vertical} = R_{horizontal} = R$ (i.e., in the case of a perfectly symmetric square sample), the R_{sh} becomes: $R_{sh} = \pi R \cdot \frac{1}{\ln 2}$ and by knowing the thickness of the layer under investigation (t), the resistivity can be finally calculated with:

$$\rho = R_{sh} \cdot t \quad (3.2)$$

Secondly, the Hall measurement is performed to determine the Hall voltage (V_H), which is directly linked to the majority carrier concentration of the layer. To this aim, V_H is created by forcing a current to flow through the diagonal pair of contacts A-C while measuring the voltage across D-B and by applying a constant magnetic field ($B=0.55$ (T) for the setup used in this work) in a direction perpendicular to the current flow, i.e., perpendicular to the sample plane (see Figure 3.5b). In this configuration, the charge carriers are deflected by the resulting Lorentz force leading to the accumulation of electrons at one side of the sample and of holes at the opposite side. This results in a potential drop across the two oppositely charged sides of the sample, which corresponds to the Hall voltage. Then, the measurement is repeated by switching the contact pair and by inverting the magnetic field polarity in order to measure an average value of V_H . Once the value of V_H is acquired, the sheet carrier density (N_s) can be calculated as follows:

$$V_H = \frac{I \cdot B}{q \cdot N_s} \quad (3.3)$$

where q is the charge of the carrier. With these considerations, V_H is negative when electrons are the majority carriers and positive when holes are the majority carrier inside the layers. Then, knowing t and assuming homogeneous and isotropic layer properties, N_s is used to

obtain the majority carrier concentration with:

$$N = \frac{N_s}{t} \quad (3.4)$$

Finally, combining the resistivity obtained with equation 3.2 and the carrier concentration obtained with equation 3.4 the mobility can be computed:

$$\mu = \frac{1}{q \cdot \rho \cdot N} \quad (3.5)$$

Note that these calculations are valid if the following assumptions are fulfilled: the layer thickness must be significantly smaller than the width and length of the sample and the sample must be square and homogeneous in plan. In addition, N and μ are correctly determined with equations 3.4 and 3.5, respectively, as the parameters within the grains for highly doped or degenerate TCO providing the grain size is large enough (typically > 20-50 nm).

This characterization method is generally performed for layers deposited on glass samples. In the case of Hall measurement performed on TCO layers, the glass sample might be coated with a thin silicon layer stack, such as a-Si:H(i)/a-Si:H(n or p). Indeed, as observed in Figure 3.6, the properties of the same TCO layer directly deposited on glass are different than the properties measured on glass coated with thin silicon layer stack used in SHJ solar cells. This is due the TCO growth properties which differ depending on the substrate surface properties, resulting in a coupling between the thin silicon layer and the TCO different than the one between the TCO and the glass substrate [Cruz 2020]. This is important to take into account when studying the final shell properties. In addition, in light of these results, it is important to keep in mind that in actual solar cells the shell components are deposited on a textured c-Si substrate. This will lead to different final shell properties than measured on glass sample. However, the relative trends when comparing different layers on a given substrate are still relevant for our investigation.

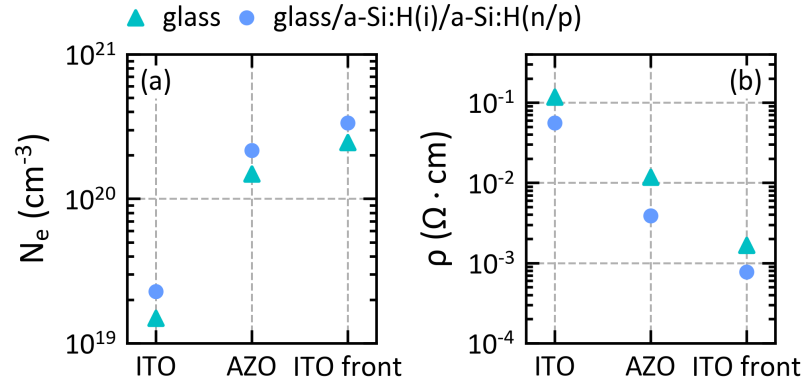


Figure 3.6 – (a) Carrier concentration and (b) resistivity of three different TCO layers (back ITO and AZO layers as well as front ITO layer) measured with the deposition performed directly on glass samples (turquoise points) or on glass samples coated with a-Si:H(i)/a-Si:H(n/p) stack (blue points).

Four-point probes measurement

In addition to the van der Pauw method presented above, the sheet resistance (R_{sh}) of doped thin layers can be determined by a second method which is the four-point probes measurement. This method uses four equidistant in-line contacts which are operated by a sourcemeter (here a Keithley). During the measurement, the four probes are placed on the surface of the layer under investigation deposited on a substrate. This substrate can be a flat glass sample and a flat or textured c-Si wafer. In the case of c-Si wafer, thin insulating layers such as silicon oxide or thin doped hydrogenated silicon layers (p-type on c-Si(n) and n-type on c-Si(p)) are required underneath to prevent the current to flow inside the c-Si bulk. Then a constant current (I) is applied through the outer pair of contacts and the voltage (V) is measured between the inner two contacts as illustrated in Figure 3.5c. As a result of the measurement of these two values, the sheet resistance (measured in Ω/\square) can be calculated as follows:

$$R_{\text{sh}} = \frac{\pi}{\ln 2} \cdot \frac{V}{I} \cong 4.5324 \cdot \frac{V}{I} \quad (3.6)$$

Using the derivation presented in [Valdes 1954] and numerically calculated in [Smits 1958] and [Boussey 1998] which consider the correction factor taking into account a sample of infinite dimension in the plan and accounting for the spacing between the contacts. In the case of a thin material layer of uniform resistivity ρ and of thickness t , the sheet resistance is given by: $R_{\text{sh}} = \frac{\rho}{t}$.

Dark conductivity measurement

The dark conductivity measurement is a characterisation method used to measure the coplanar conductivity and the relative doping level of thin silicon layers. The required sample for the characterization process is a glass substrate coated with the layer under investigation on which two identical 100-nm-thick aluminium contact pads are deposited by thermal evaporation¹. The evaporation occurs through a shadow mask featuring openings with the appropriate pad dimensions. The spacing between the two pads is generally designed to be 0.5 or 1 mm wide, depending on the thin silicon layer resistivity. Two different designs were used during this work: the first one presented in Figure 3.7a, used mainly for full blanket layers and the one presented in Figure 3.7b used to perform the measurement on finger-shaped IBC layers. To ensure a good ohmic contact of the aluminium pads, an annealing of one hour at 180°C is required after the deposition [Shah 2010]. In this configuration, and by assuming homogeneous layers, when the probes are contacted, a one-dimensional and homogeneous current flow is established between the two pads. During the measurement, the two pads are connected in a two-points probe configuration to probe the current (I) and the voltage (V), and the coplanar conductivity (σ (Ωcm)⁻¹) is calculated as follows:

$$\sigma = \frac{I}{V} \cdot \frac{d}{t \cdot l} = \frac{1}{R} \cdot \frac{d}{t \cdot l} \quad (3.7)$$

with l the pad length, d the distance between the two pads and t the layer thickness (see Figure 3.7) as well as R the resulting resistance measured between the two pads.

Depending on the layer resistivity, to measure the resistance (R), the system used during this work can operate either in current source mode or in voltage source mode. The current source mode works by applying a constant current (I) and measuring the resulting voltage (V). This mode is generally suitable for doped thin silicon layers and is called the "doped mode". Inversely, the voltage source mode works by applying a given voltage and by measuring the resulting current, and it is generally applied to lowly doped and intrinsic thin silicon layers and is called the "intrinsic mode". In both cases, the voltage and current are monitored by Keithley 617 electrometers in order to deal with layers presenting very high resistance. For this particular system, the electrometers present an operating range of current between 2×10^{-12} to 2×10^{-3} A. The applied voltage used in the "intrinsic mode" must then be adapted to keep the current in the electrometer range while providing stable measures. Generally, the "doped mode" is used for layer presenting a resistance below $1 \times 10^{10} \Omega$ and the "intrinsic mode" is used for layer with resistance in the range of 1×10^{10} to $1 \times 10^{16} \Omega$. It is possible to perform an "ohmic test" of the layer under investigation by simply performing an I - V curve measurement. This will allow for the choice of the correct mode and to adapt the voltage used in the "intrinsic mode" accordingly. In addition, a Keithley 705 scanner is used to allow for the measurement of

¹Note that it is also possible to perform dark conductivity measurement on c-Si textured wafer using a thin isolating layer, such as silicon nitride, between the c-Si and the layer under investigation.

up to four samples simultaneously in the "doped mode" and up to two samples simultaneously in the "intrinsic mode".

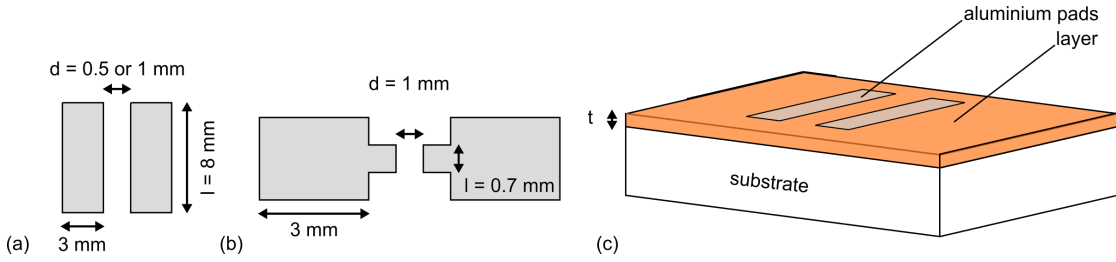


Figure 3.7 – Pads designs for (a) full blanket layers and (b) for finger-shaped IBC layers. (c) Schematic description of a dark conductivity measurement sample with t the thickness of the layer deposited on a given substrate and the aluminium pads deposited on top.

In the particular case of dark equilibrium, the dark coplanar conductivity (σ_d) is known to follow an exponential increase with temperature (T (K)) such as [Shah 2010]:

$$\sigma_d(T) = \sigma_0 \cdot \exp\left(\frac{-E_a}{kT}\right) \quad (3.8)$$

with $k = \frac{k_B}{q}$ and where q is equal to the elementary charge, k_B is the Boltzmann constant, σ_0 is the conductivity prefactor which is assumed, in this simple model, to be a material constant that does not depend on temperature and E_a is the activation energy which is related to the energy difference from the Fermi level (E_F) to the current transporting energy band (conduction band (E_c) for the case of electron and valence band (E_v) for the case of hole). Thus, the value of E_a can be used as a relative measure to evaluate the efficiency of doping in shifting the E_F close to the valence or close to the conduction band. E_a is equal to $E_c - E_F$ for the case of electron majority carrier and to $E_F - E_v$ for the case of hole majority carrier. Thus the lower the E_a the higher the doping of the layer under investigation.

To determine σ_0 and E_a values from equation 3.8, dark coplanar conductivity measurement is performed as a function of the temperature (T). To do this, the sample is positioned in a dark vacuum chamber at a pressure of 1 mbar in an inert nitrogen atmosphere, to avoid air impurity to affect the band bending at the surface of the thin film, and placed on a heating table allowing one to sweep the temperature. The sweep starts first with a linear heating ramp which brings the sample to 180°C within 15 min, then this temperature is kept for 1h30 (annealing and stabilisation of the aluminium contact pads) before cooling gently and linearly to nominal 25°C within 5h30². This slow cooling allows for stabilisation of the material properties between each measurement. Thus, the linear relation of $\ln(\sigma_d(T))$ as a function of $1000/T$ is considered

²In practice, after 5h20 the system is at 33 °C and after 8h of measurement the system stops taking values and is at about 26.8 °C

in the cooling ramp and is given by:

$$\ln(\sigma_d(T)) = \frac{-E_a}{k \cdot 1000} \cdot \frac{1000}{T} + \ln(\sigma_0) \quad (3.9)$$

The factor $\frac{1000}{T}$ is used to obtain E_a in meV. Then, by plotting $\ln(\sigma_d(T))$ as a function of $\frac{1000}{T}$ in an Arrhenius plot, it is possible to apply a linear fit on a given temperature range (inside the cooling ramp) in order to extract, in addition to σ_d at room temperature, both E_a , from the slope, and σ_0 from the y-intercept. To do so, a Python script was created and optimised to make the data treatment. It is important to notice that similarly to the case of Hall measurement, these parameters are extracted assuming homogeneous layers. The temperature range in which E_a and σ_0 are calculated is generally chosen between 100 to 26 °C within the temperature ramp down. As an illustrative example, Figure 3.8 depicts the measurement of $\sigma_d(T)$ for three nc-aSi:H(n) layers featuring three different E_a of 17, 48 and 173 meV and a dark conductivity at room temperature ($\sigma_d(RT)$) of 21.3, 0.92 and 0.02 $\Omega^{-1} \text{cm}^{-1}$. The temperature ramp up is illustrated by a light dashed line and the temperature ramp down by a full light line. In addition, the temperature range considered for the extraction of both parameters is represented by a dark line.

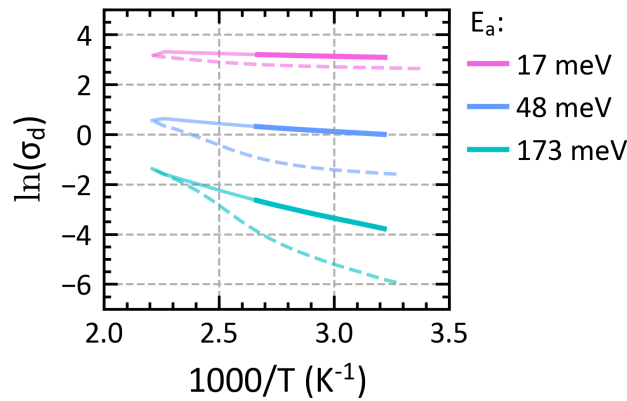


Figure 3.8 – Arrhenius plot of typical $\sigma_{dark}(T)$ measurements for three nc-Si:H(n) layers featuring three different E_a of 17, 48 and 173 meV. The light dashed lines represent the temperature ramp up and the full light lines the temperature ramp down. The dark lines represent the temperature range in which the linear fit is considered for the extraction of both E_a and σ_0 .

Spectroscopic ellipsometry

Spectroscopic ellipsometry (SE) is a quick and non-destructive characterization technique to assess several properties of thin films such as their thickness, bandgap, crystallinity, composition, roughness, refractive index and extinction/absorption coefficient as a function of

wavelength, as well as their optical and dielectric constants. To measure the optical parameters from which the layer properties mentioned above are calculated, SE is based on measuring the polarization state of light which changes after reflection on a sample surface. The system used in this work is the J. A. Woollam Co. Inc α -SE which features an unpolarized white light source produced by a xenon arc lamp. This white light is first transformed into a collimated beam then linearly polarized using appropriate collimators and polarizers. This light beam is then sent to the surface of a sample with a dedicated angle and upon reflection, both p- (parallel to plane of incidence) and s- (perpendicular to plane of incidence) polarizations change in amplitude and in phase. According to the material reflection, the parallel and perpendicular polarisation components are reflected differently, resulting in an elliptically polarized reflected beam. From the resulting reflection, the SE measures the two parameters Psi (Ψ) and Delta (Δ) which are the amplitude ratio and the phase difference between p- and s-polarizations respectively. During a measurement, these two parameters are evaluated as a function of the light energy. The system includes ultraviolet/visible and infrared monochromators allowing one to cover a wide range of the energy spectrum with wavelengths from 380 to 900 nm. For each light energy, the change in polarization state (ζ), which is identified in terms of Δ and Ψ is measured. Then, ζ is directly related to the ratio of the Fresnel reflection coefficients r_p and r_s standing for p- and s-polarized light, respectively, as follows:

$$\zeta = \frac{r_p}{r_s} = \frac{|r_p|}{|r_s|} \cdot e^{i(\delta_p - \delta_s)} = \tan(\Psi)e^{i\Delta} \quad (3.10)$$

with the amplitude $\tan(\Psi) = \frac{|r_p|}{|r_s|}$ ($0^\circ \leq \Psi \leq 90^\circ$) and the phase shift difference $\Delta = \delta_p - \delta_s$ ($0^\circ \leq \Delta \leq 360^\circ$).

Extracting the different layer properties from these measured values requires appropriate fitting of the Ψ and Δ spectra as well as appropriate modelling of the dielectric function leading to the construction of an optical model for data analysis. Different dielectric function models for fitting these spectra exist and an adequate model must be chosen according to the optical properties of the sample. In this work, SE measurements were mainly performed to assess the thickness and bandgap of thin silicon layers. For thin silicon layers, the data were fitted using a Tauc-Lorenz model [Jellison 1996]. In the case of transparent layers, i.e., layers featuring an extinction coefficient close to 0, a Cauchy or Sellmeier model is generally used, and in the presence of free carrier absorption, as is the case for TCO layers, the Drude model is preferentially used. More details and information about the SE technique and fitting models can be found in [Fujiwara 2007].

The sample used for SE measurements must fulfil certain constraints. The layer under investigation must be deposited on a flat substrate, which is generally a planar c-Si wafer or glass. The surface roughness should be minimum since rough surfaces reduce the reflected light intensity leading to noisy measurements. In this work, the thin silicon layers were mainly char-

acterized by SE measurement when deposited on glass substrates. From the substrate choice, the incidence angle, equals to the reflection angle, must also be adapted as it directly depends on the Brewster angle. Indeed, SE measurements are most sensitive to material properties when the difference between r_p and r_s is large, the largest being at the Brewster angle. For the air/c-Si interface, the Brewster angle is close to 74° and for air/glass interface it is around 56° , with respect to the surface normal. Hence, a measurement angle of 70° or 60° is generally suitable for these two substrates, respectively. To increase the fitting accuracy, multiple angles of incidence (65° , 70° and 75°) can be used [Stückelberger 2014]. As an illustration, Figure 3.9 plots the thickness and the gap energy (E_g) obtained with SE measurement of an a-Si:H(i) layer as a function of the deposition time .

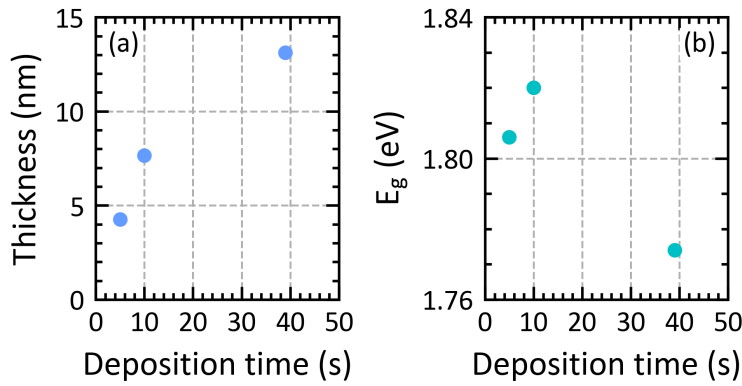


Figure 3.9 – (a) Thickness and (b) bandgap energy (E_g) measured by SE of an a-Si:H(i) layer deposited on glass substrate as a function of the deposition time.

Spectrophotometer

To study the optical properties of a given material layer, one common method is to measure its total transmittance (TT) and reflectance (TR) as a function of the wavelength (λ). These two parameters are given in (%) and allow one to obtain the total absorptance (A) of the material under investigation as a function of λ with:

$$A(\lambda) = 100\% - TT(\lambda) - TR(\lambda) \tag{3.11}$$

with A given in (%) and assuming that all light that is neither transmitted nor reflected is absorbed.

TT and TR were measured using a dual-beam UV-vis-NIR spectrophotometer (Perkin Elmer, lambda 900), equipped with an integrating sphere. The wavelength range of this system is generally between 320 to 2000 nm and can be extended to 250 nm thanks to a deuterium

lamp. The layer under investigation is deposited on an AF32 glass and the sample is measured with the layer surface directed towards the incoming light beam. As an illustration of this characterization method, Figure 3.10 shows the typical optical total transmittance, total reflectance, and absorptance measurement for aluminium-doped zinc oxide (AZO) layers presenting varying oxygen (O_2) content in the deposition gas flow.

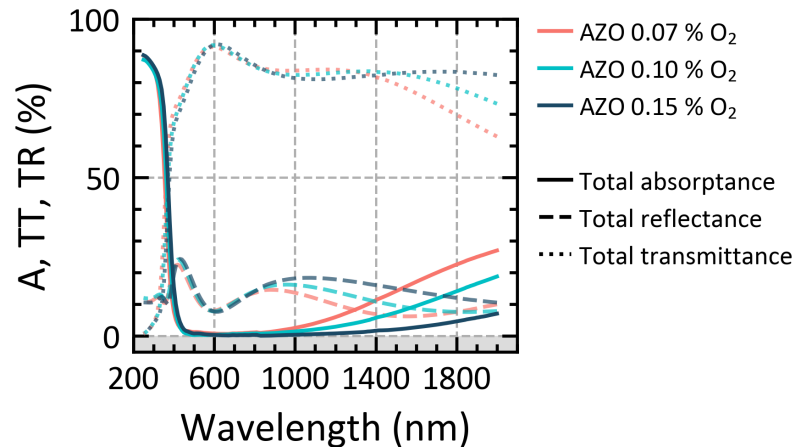


Figure 3.10 – Total transmittance, total reflectance and absorptance of three AZO layers presenting three different oxygen content of 0.07, 0.10 and 0.15% in the deposition gas flow.

Raman Spectroscopy

Raman spectroscopy (RS) is a measurement technique giving indirect information on the structure of a medium such as its elemental composition, thickness or crystallinity ratio. In this work, RS was mainly used to define the crystallinity ratio and the thickness of several material layers developed for the shells of SHJ solar cells. Raman spectroscopy relies on the phenomenon of light-matter interaction and, more specifically, on inelastic scattering of light, also called Raman scattering effect, discovered by C.V. Raman in 1928 [Raman 1928]. It is an analytical technique based on the evaluation of the frequency shift of photons after inelastic interactions with vibration modes (molecular vibrations or phonons in solids) inside the material under study. This method can be applied to the three material states which are gas, liquid, or solid state.

A Raman spectrum describes the intensity of the scattered light as a function of the shift in frequency (i.e., in energy) from the initial excitation light frequency. This resulting frequency shift is called the Raman shift ($\Delta\nu$) and is directly related to the vibrational energy of the bonds between the atoms within the investigated material. The analysis of the scattered frequencies provides information about the structure of the medium. In general, the scattering of light can be of two types called *elastic scattering* and *inelastic scattering*. In the first one, the scattered photons have the same frequency (ν) as the incident ones. In that case the

interaction process is then elastic and is called Rayleigh scattering ($\Delta\nu = 0$). This scattering mode is the predominant one. In the second case, the scattered photons have a different frequency (energy) than the incident ones and the process is then inelastic. This inelastic scattering is called the Raman scattering and is only experienced by a small fraction of photons, about 10^{-6} of the total scattered light. In the case of solid material, the incident photons gain or lose energy in the interaction by absorbing or emitting phonons, respectively. When incident photons gain energy, the frequency of scattered photons shifts up and this process is called the anti-Stokes scattering ($\Delta\nu < 0$). Inversely, when photons lose energy, the frequency of scattered photons shifts down and this process is called the Stokes scattering ($\Delta\nu > 0$). Generally, the anti-Stokes scattering is less probable than the Stokes scattering. When a monochromatic excitation light is used, generally a laser with a given frequency, these two Raman scattering phenomena are shifted symmetrically with respect to the Rayleigh scattering at $\Delta\nu = 0 \text{ cm}^{-1}$.

The Raman spectrum is represented by the plot of the intensity of the Raman scattered light as a function of the Raman shift expressed in absolute wavenumber shift (cm^{-1}). The absolute wavenumber is directly proportional to the photon frequency and is expressed as follow:

$$\bar{\nu} = \frac{\nu}{c} = \frac{1}{\lambda} \quad (3.12)$$

with c the velocity of light in (cm s^{-1}) and λ the light wavelength related to the light frequency ν . Thus, the Raman shift ($\Delta\bar{\nu}$) is calculated as follows:

$$\Delta\bar{\nu} = \bar{\nu}_{\text{laser}} - \bar{\nu}_{\text{Raman}} \quad (3.13)$$

where $\bar{\nu}_{\text{Raman}}$ corresponds to the scattered light absolute wavenumber and $\bar{\nu}_{\text{laser}}$ is the initial absolute wavenumber of the incoming light which is known and constant and depends on the laser used. Importantly, the position of a peak in a Raman spectrum is independent of the laser frequency used. Indeed, as prime example, the Raman shift for crystalline silicon is always equal to 520 cm^{-1} and the position of the Rayleigh scattering is always at $\Delta\bar{\nu} = 0$ regardless of the laser frequency. More details can be found in [Weber 2000].

Raman spectroscopy is a very specialized optical microscopy technique. The measurement system used during this work is a MonoVista CRS+ confocal Raman microscope from S&I. To acquire a Raman spectrum, the sample under study is illuminated with a laser beam focused with an optical microscope. The sample usually consists of a glass substrate or of a flat or textured c-Si wafer, with the material layer under study deposited on it. Using a laser allows one to obtain an excitation light source which provides a powerful beam of monochromatic radiation at a given and stable frequency. This ensures that enough inelastic scattered light is present for it to be detected. The light which is back-scattered by the material under study is

measured by the Raman spectrometer which is coupled to a microscope. More details about Raman spectroscopy systems can be found in [Weber 2000, Turrell 1996]. As prime examples, the main parameters which must be carefully adapted when acquiring Raman spectra are (i) the laser excitation light frequency, which depends on the probed material depth targeted (in this work, a blue (442 nm) and UV (325 nm) lasers were mainly used), (ii) the laser light power to avoid altering the layer properties during measurement, (iii) the microscope objective, (iv) the central position of the Raman spectra, as well as (v) the exposure time and the number of accumulation which are important to enhance the signal-to-noise ratio. The final Raman spectrum, which is analysed and given by this system, contains the Stokes peaks only. In addition, the intensity of the Raman scattered light is expressed in “counts” which is unitless but corresponds to an intensity proportional to the number of incoming photons on the Raman detector. Importantly, the resulting intensity of a Raman spectra depends on the nature of the material, the possible texture of the sample, the volume of the layer investigated, as well as the five parameters mentioned above. These globally determine the number of photons generated, collected, and converted to signals. Therefore, the intensity of a Raman spectrum cannot be used as an absolute value of any material feature. Only the relative intensity or area of different peaks present on the same Raman spectrum can be compared and used as qualitative or quantitative information.

In the specific case of thin hydrogenated silicon layers, Raman spectroscopy can be used to measure their crystallinity ratio. Indeed, mixed-phase thin silicon layers, generally called nanocrystalline silicon layers (nc-Si:H), are composed of conglomerates of nanocrystals incorporated in an amorphous tissue [Vallat-Sauvain 2000]. These different phases (amorphous or crystalline) present in nc-Si:H layers result in different peaks on the Raman spectrum. Raman spectroscopy is then particularly well adapted to discriminate between the amorphous phase and the crystalline phase of thin silicon layers. As presented in Figures 3.12 and 3.13, this Raman spectrum can be deconvoluted into three Gaussian peaks, in which the integrated peak areas are proportional to a specific phase concentration. The first peak is a broad peak centered at 480 cm^{-1} which is characteristic of the transverse optical (TO) mode in amorphous silicon (a-Si:H) and is thus attributed to the amorphous silicon phase. The second peak is centered at about 510 cm^{-1} (or more generally presents in the range of 495 to 515 cm^{-1}) and represents the defective part of the crystalline phase. This peak is still not fully explained and difficult to analyze but it can be associated to different physical phenomena such as crystallites of diameters lower than 10 nm [Islam 2001, Xia 1995], small-sized grains or grain boundaries [Seif 2015], to silicon Wurzite phase [Kobliska 1973] or simply to an artificial way to explain the asymmetry of the crystalline peak [Ledinský 2008], to mention a few. The third and last peak is a narrow peak centered at 520 cm^{-1} which corresponds to the position of the TO mode in crystalline silicon and which is then attributed to silicon crystallites.

Figure 3.11 shows typical Raman spectra of (a) a crystalline silicon (c-Si) wafer and (b) to (d) of various thin silicon layers. The contributions of the three different peaks are easily observed

for the different cases. The Raman spectrum of c-Si ($\Phi_c = 100\%^3$) depicted in (a) exhibits a single narrow peak centered at 520 cm^{-1} , while for mixed-phase nc-Si:H layers (b) and (c), the amorphous and the crystalline phases contribute together to the final Raman spectra. For the highly crystalline nc-Si:H ($\Phi_c = 62\%$) presented in (b), the width of the 520 cm^{-1} peak is slightly larger than the one of c-Si and is not symmetric, presenting a tail towards smaller wavenumbers resulting from the contribution of the defective crystalline and the amorphous phases. The Raman spectrum of the a-Si:H layer ($\Phi_c = 0\%$) shown in (d) exhibits a broad peak centered at 480 cm^{-1} . Finally, the lowly crystalline nc-Si:H layer ($\Phi_c = 31\%$) presented in (c) for its part presents a mixture of the Raman spectra of the highly crystalline (b) and the amorphous layer (d).

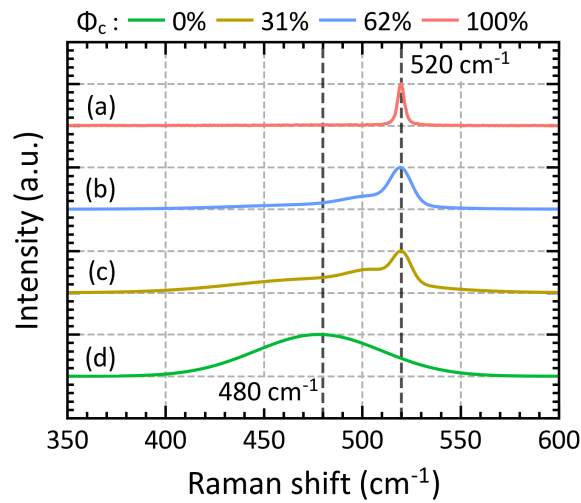


Figure 3.11 – Typical normalized Raman spectra for (a) a c-Si wafer with $\Phi_c = 100\%$, (b) a highly crystalline nc-Si:H layer with $\Phi_c = 62\%$, (c) a lowly crystalline nc-Si:H layer with $\Phi_c = 31\%$, and (d) an a-Si:H layer with $\Phi_c = 0\%$.

Comparing directly different Raman spectra provides a qualitative way to compare the degree of crystallinity of different layers by looking at the relative heights and widths of the amorphous and the crystalline peaks (see Figure 3.14). One step further, it is possible to extract a quantitative value of the crystallinity from the Raman spectra, as the peak areas are proportional to the corresponding phase concentration. To do this, an adapted deconvolution (or curve fitting) procedure is applied to calculate the Raman crystallinity factor Φ_c from given Raman spectra. This crystallinity factor is obtained by dividing the integrated intensity associated to the crystalline phase by the total integrated intensity associated to the crystalline and the amorphous phases. The deconvolution aims to fit Raman spectra by considering the three peaks at 480 , 510 , and 520 cm^{-1} as Gaussian distributions to which a physical meaning can be attributed, as well as to fit an additional continuous background. Then, comparing the

³ Φ_c is the Raman crystallinity factor which reflects the crystallinity of the layer under study and is introduced later in this section.

area of these three fitted peaks allow one to extract the contribution of the different phases present in the material under study. Previous work [Droz 2003] and experimental tests have shown that Gaussian line shapes are more adapted than Lorentzian ones for fitting the three main peaks of interest. Therefore, in this work, Gaussian profiles are used to fit the three peak contributions (amorphous phase, defective crystalline phase, and crystalline phase) present in the Raman spectra of our thin silicon layers. To get meaningful Raman spectra and to perform a precise deconvolution, several parameters must be considered and fixed. First, the silicon-related peaks must be dissociated from the background noise. Secondly, the wavenumber ranges on which the background fit and the fit of the three main peaks will be performed must be established. Then, the background signal must be fitted using different functions (used independently or in combination) to isolate the Raman peaks of interest. Finally, the three main Gaussian parameters such as the frequency position, width, and height must be adapted for each Raman peak.

While performing RS measurements on thin silicon layers, a wide variety of spectra presenting different background signals were obtained. To systematically deconvolute these spectra, the fit of the background signal must be adapted for each case. In particular, the choice of the ranges in which the background signal and the three main Gaussians are fitted is important. If the ranges are not properly chosen, the background signal will not be well fitted and a part of the spectrum of the three main Gaussian signals of the material layer under study will be cut off. In general, the background signal can either be fitted by a linear function, by increasing or decreasing exponential functions, by Gaussian functions, or by a combination of those. More precisely, in this work, two techniques were used to fit the background signal. The first one uses two different steps as illustrated in Figure 3.12. The first step separates the range considered to fit the background signal and the one to fit the three main peaks (Figure 3.12 top). Here, the range of the three main peaks is set between 350 and 600 cm^{-1} whereas the range for the background signal is set between 150 to 350 cm^{-1} combined with 600 to 1200 cm^{-1} . Then the background signal is fitted using in that case a combination of both decreasing and increasing exponential functions completed with a linear function. Finally, the background signal is subtracted to the total Raman spectrum and the three main peaks are fitted in the selected range with their adapted Gaussian functions (Figure 3.12 bottom). In the second technique, the background signal and the three main peaks are fitted at the same time directly to the entire Raman spectrum within the specified ranges. Figure 3.13 shows an example of such fitting method. Here the background signal consists of two Gaussian functions located on the right and on the left sides of the spectrum.

For the three main Gaussian peaks, lower and upper limit values as well as fixed values must be adapted in function of the Raman spectrum for their position (frequency), their width (standard deviation), and their height (amplitude). In general, the frequency and standard deviation of the 520 cm^{-1} peak is not critical as it is generally clearly defined on the spectrum of thin silicon layers. In contrast, a competition between the 480 cm^{-1} and the 510 cm^{-1} peaks can arise leading to fits without physical meaning [Droz 2003]. Therefore, for the deconvolution, the position of the 480 cm^{-1} peak has been restrained in the range 479 to

Chapter 3. Experimental processes and characterization systems

481 cm^{-1} and its standard deviation between 20 and 50 cm^{-1} and the position of the 510 cm^{-1} peak has been restrained in the range between 505 to 510 cm^{-1} , with a peak generally situated at 507 cm^{-1} for our layers under investigation, and its standard deviation between 7 and 15 cm^{-1} . Note that these different choices and parameter values are based on a large number of experimental tests, and not on theoretical considerations.

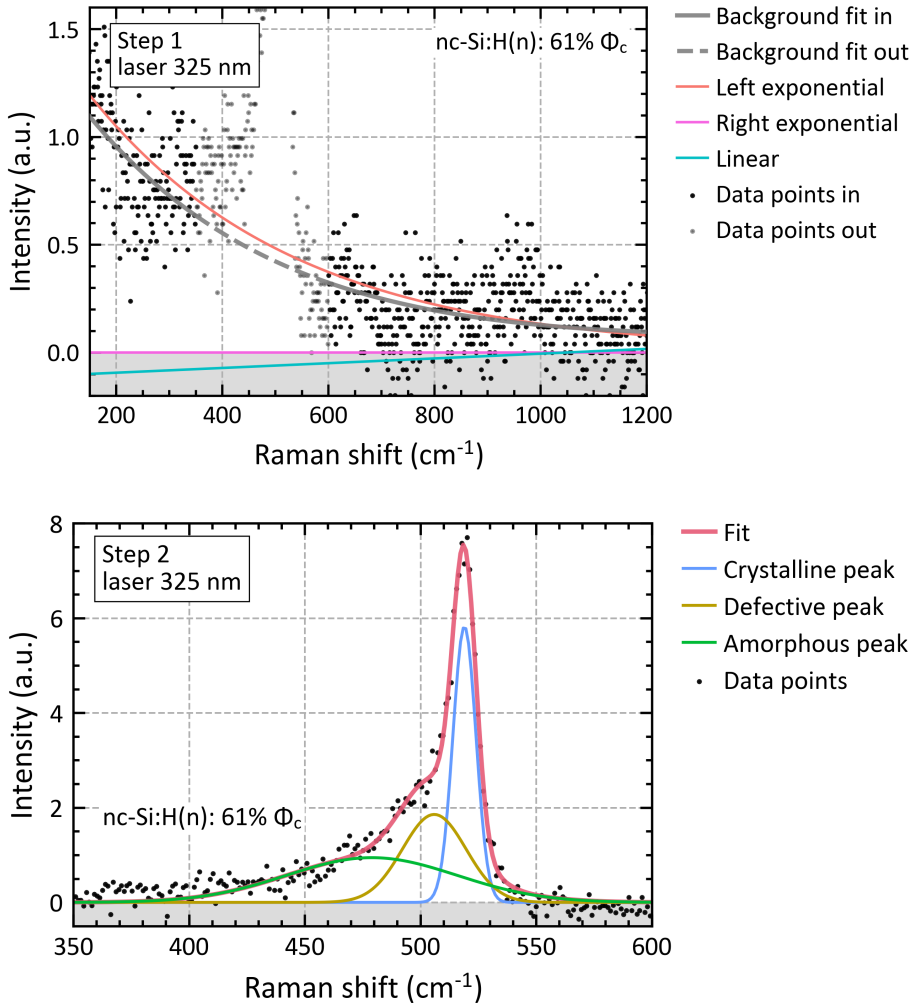


Figure 3.12 – Raman spectrum of an $nc\text{-Si:H}(n)$ layer obtained with the UV laser at 325 nm and its deconvolution in two steps. Top: background signal fitting outside the range of interest of the three main Gaussian peaks. The background is fitted with a left decreasing exponential combined with a right increasing exponential and a linear function. Bottom: main peaks fitting on the data, with removed background, using the three Gaussians for the amorphous, defective and crystalline phases. The range of the background signal is denoted "in" whereas the range of the three main peaks is denoted "out". The $nc\text{-Si:H}(n)$ layer features a Raman crystallinity factor of 61%.

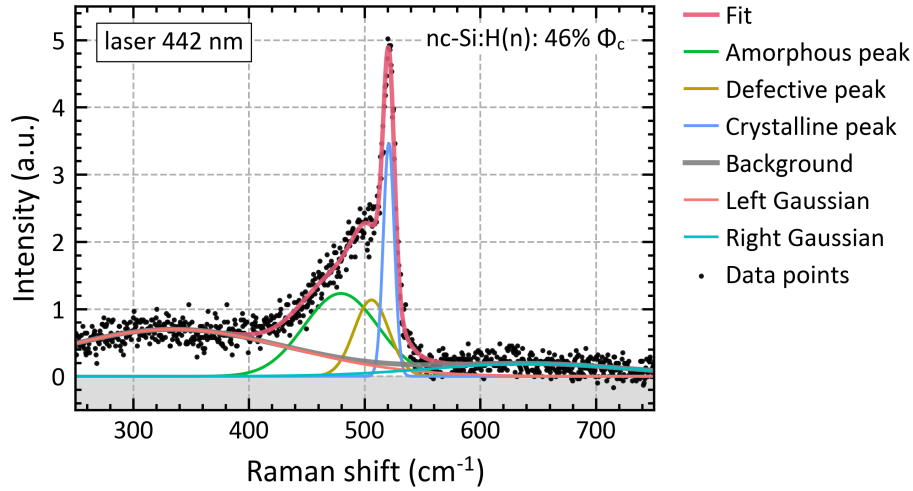


Figure 3.13 – Raman spectrum of an nc-Si:H(n) layer obtained with the blue laser at 442 nm and its deconvolution in one step. The background signal and the three main peaks are fitted at the same time. The background signal is fitted with one left and one right Gaussian function, and the main peak is fitted using the three Gaussian functions for the amorphous, defective and crystalline phases. The nc-Si:H(n) layer features a Raman crystallinity factor of 46%.

From Raman spectroscopy, it is possible to extract the crystalline volume fraction (X_c) of a material which can be expressed as [Droz 2003]:

$$X_c = \frac{V_c}{V_{\text{exp}}} = \frac{I_c}{I_c + \gamma \cdot I_a} \quad (3.14)$$

where V_c is the crystalline volume, V_{exp} the total scattering volume of the Raman measurement, which is equal to $V_a + V_c$ for the case of mixed-phase materials with V_a the amorphous volume, and I_c and I_a the integrated Raman scattered intensities of the amorphous and crystalline phase, respectively. Finally, γ is defined as the ratio of the integrated Raman cross-sections [Tsu 1982].

Whereas I_c and I_a can be directly measured from the Raman spectra, the value of γ is still a subject of debate and obtaining a precise value for the material under study remains challenging. Indeed, values of γ between 0.8 [Ledinský 2006], 0.88 [Tsu 1982, Ledinský 2008], 0.9 [Han 2003] down to 0.1 [Brodsky 1977] have been published. In addition, γ may depend strongly on the size of the crystallites and on the excitation wavelength [Bustarret 1988]. Due to this uncertainty related to the value of γ , the use of the Raman crystallinity factor Φ_c for which $\gamma = 1$ becomes more relevant. This parameter does not reflect the actual crystalline volume fraction, but is a ratio of Raman intensities expressed as [Droz 2004, Droz 2003]:

$$\Phi_c = \frac{I_c}{I_c + I_a} = \frac{I_{520} + I_{510}}{I_{520} + I_{510} + I_{480}} \quad (3.15)$$

where I_i (with $i = \{480, 510, 520\}$) is the area under the Gaussian centred at 480, 510 and 520 cm^{-1} and $I_{520} + I_{510} + I_{480}$ is the total integrated intensity.

In this regard, the simplified Raman crystallinity factor is a suitable parameter to monitor the crystallinity of materials such as c-Si or mixed-phase nc-Si:H layers. However, it is important to keep in mind when comparing such values with the ones given in the literature that the value of Φ_c is not only dependent of the choice $\gamma = 1$, but also on how it is measured (i.e., excitation wavelength, thickness of the material, etc.) and how it is deconvolved (Gaussian contributions, background signal, integrated intensities, amplitude of the peaks, etc.). In addition, it was demonstrated in [Droz 2003] that Φ_c generally slightly overestimates the real crystalline volume fraction X_c .

To study more deeply the crystallinity of a given material layer, Raman spectroscopy can in addition provide a means to probe different depths inside the material by using lasers with different wavelengths (i.e. frequencies). Indeed, for specific layers such as thin silicon ones, the laser wavelength determines the penetration depth of the Raman signal as the higher the photons energy, the more they are absorbed by the medium. This provides a means to probe the material at different depths and thus to study the crystallinity inhomogeneity along the thickness of the material. In particular, for the case of mixed-phase layers such as nc-Si:H, where the microstructure evolves while growth proceeds, multiwavelength Raman measurement may reveal different features as a function of the penetration depth. In this work two laser wavelengths were used, the UV 325 nm and the blue 442 nm. The UV laser light is usually strongly absorbed in the materials under investigation and probes the first nanometers close to the surface of these materials, whereas the 442 nm light is weakly absorbed and probes a deeper volume of the material. The penetration depth d_p represents the depth at which the incident light intensity drops to $\frac{1}{e} = 37\%$ of its initial value. Typical value of d_p for c-Si, a-Si:H and nc-Si:H are depicted in Table 3.2. It is observed that for the 325 nm laser, d_p is similar for the three materials leading to similar probed volumes however, for the 442 nm laser, the d_p values are significantly different. Indeed, d_p at 442 nm is of the order of 23 nm for a-Si:H, of 38 nm for nc-Si:H and up to 426 nm for c-Si. Importantly, the penetration depth is not identical to the depth from which Raman signal is collected. The latter is defined by the Raman collection depth (RCD) which is a function of d_p and depends on the material under investigation. For each material a precise determination of the RCD can be performed [Carpenter 2017]. In addition, it is important to keep in mind that the volume probed with the 442 nm laser includes the volume probed with the 325 nm laser as well as an additional deeper volume. In that case, the Raman crystallinity factor expresses an averaged crystallinity value of the surface volume combined with the deeper volume. Thus, by using these two different excitation wavelengths, it is possible to obtain depth-dependent information on the crystallinity. Figure 3.14a shows

the Raman spectra of nc-Si:H(n) layers deposited on glass substrates and measured either with the 325 nm (orange curve) or the 442 nm (dark blue curve) laser. It is observed that the crystallinity is higher at the surface of the layer than inside its bulk, with values of 52.4% and 24.6% respectively. In addition, Figure 3.14b shows the surface Raman crystallinity factor of a given nc-Si:H(n) layer as a function of its thickness. It is observed that the thicker the layer, the higher the crystallinity probed at the surface. This thickness dependence is also well observed in Figure 3.14a where the nc-Si:H(n) layer measured with the UV laser on a glass substrate (orange curve) presents a Φ_c of 52.4% whereas a Φ_c of only 18.1% is measured when deposited on a textured c-Si wafer (turquoise curve). This is mainly due to the thinner layer obtained on textured c-Si wafers compared to glass for a same deposition recipe (in addition to different growth properties). Both observations illustrate then the high crystallinity dependence with the thickness of nc-Si:H layers. Another important aspect when measuring the crystallinity of material layers is to consider the substrate on which the layer grows. Indeed, as well known, the growth and then the final properties of nc-Si:H layers are highly substrate-dependent [Kondo 1996, Vallat-Sauvain 2005]. For instance, as already presented in section 2.3.1 Figure 2.14, the p-type hydrogenated nanocrystalline thin silicon layer (ncP) presents a Φ_c of 31% when deposited on intrinsic amorphous layers (incP) while presenting a Φ_c of 47% when deposited on the stack composed by intrinsic amorphous combined with an n-type hydrogenated nanocrystalline thin silicon layer (incNncP) for the same deposition parameters. Note that the crystallinity measurement with the blue laser of the thin silicon layers under investigation deposited on c-Si textured wafer is not possible as this laser presents a too high d_p and would probe the underlying c-Si wafer.

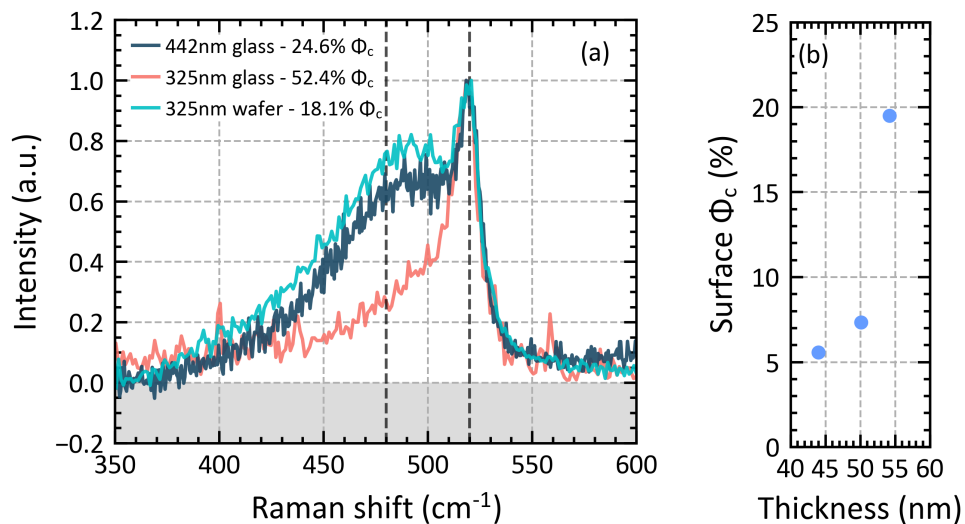


Figure 3.14 – (a) Normalised Raman spectra of three nc-Si:H(n) layers deposited on glass and c-Si textured wafer substrate measured with the UV 325 nm or the blue 442 nm laser. (b) Surface Raman crystallinity factor as a function of the thickness of a given nc-Si:H(n) layer.

Penetration depth d_p (nm)		
Material	laser 325 nm	laser 442 nm
a-Si:H	9.3	23
nc-Si:H	8.5	38
c-Si	8.0	426

Table 3.2 – Penetration depth (d_p) related to two different laser wavelengths of 325 and 442 nm given for the three typical materials under investigation in this work which are amorphous (a-Si:H), nanocrystalline (nc-Si:H) and crystalline (c-Si) silicon. Data extracted from [Carpenter 2017].

Raman spectroscopy can also be used to measure the thickness of thin material layers. One major advantage of this method is the fact that it allows one to measure the thickness directly on textured c-Si wafers in addition to flat ones, contrary to spectroscopy ellipsometry and profilometry which cannot be used to measure the thickness of thin material layers deposited on rough surfaces. The RS thickness measurement method is based on the Beer-Lambert law, which states that the light intensity in light-absorbing media is expressed by:

$$I = I_0 \cdot e^{-\alpha \cdot d} \quad (3.16)$$

where d is the thickness of the absorbing film, α is the absorption coefficient and I_0 is the initial intensity of the incident light. The initial intensity is the reference Raman intensity (expressed in count) used to define the layer thickness, i.e., the highest intensity of the measurements. In general, this parameter I_0 is measured directly on a bare c-Si wafer or on a c-Si wafer coated with thin a-Si:H(i) layer, which in both cases lies below the layer under investigation. Then, the c-Si Raman intensity measured on the thin overlayer under study (I) is reduced by a factor of $e^{-\alpha d}$ due to absorption of the excitation laser in this overlayer. Since the Raman signal is also absorbed in the layer on the way back to the detector, the total attenuation factor is equal to $e^{-2\alpha d}$. Thus, from equation 3.16 the thickness of the absorbing layer can be directly calculated as follows [Ledinský 2016]:

$$d = \frac{1}{2\alpha} \cdot \ln\left(\frac{I_0}{I}\right) \quad (3.17)$$

During this work, the blue 442 nm laser was used to perform such measurements as it has enough absorption in the amorphous and mixed-phase layers under study while still penetrating the c-Si wafer. In addition, the value of α is assumed to be constant between the incoming and the back-scattered light. The α parameter can be measured by spectroscopic ellipsometry for layers deposited on glass or c-Si substrates. Its default value for this work was fixed at

$1.852 \times 10^5 \text{ cm}^{-1}$.

To perform a RS thickness measurement with our setup, the blue 442 nm laser was used combined with the x10 objective lens. In addition, in this configuration, the required acquisition time for accurate profiling usually stands between 20 and 30 s for a unique accumulation. The crystalline peaks of each measurement are fitted with a Lorentzian function followed by an integration in the range 510 to 535 cm^{-1} to evaluate the peak intensity with reduced noise as presented in [Ledinský 2016]. Figure 3.15 shows two Raman spectra obtained with the 442 nm laser. The first one is the reference intensity spectrum of a c-Si wafer coated with a thin a-Si:H(i) layer, i.e. I_0 (turquoise curve), and the second one is the spectrum of an nc-Si:H(n) layer deposited on top of the c-Si/a-Si:H(i) stack (dark blue curve). Both spectra reveal a prominent sharp c-Si Raman peak at 520 cm^{-1} , but their respective intensity differs significantly, allowing one to compute the thickness of the nc-Si:H(n) layer, which is 16 nm in that case.

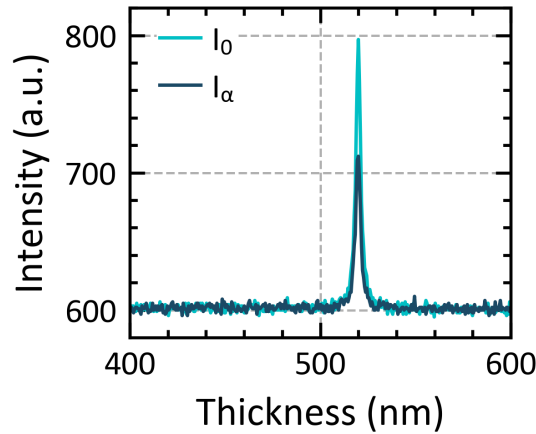


Figure 3.15 – Raman spectra measured on c-Si/a-Si:H(i) stack for reference intensity I_0 (turquoise curve) and on c-Si/a-Si:H(i)/nc-Si:H(n) (dark blue curve) designed as attenuated intensity I_α . The nc-Si:H(n) presents a thickness of 16 nm.

A particular application of this method is to measure the thickness profile of patterned layers which are present in devices such as, for example, IBC cells. To perform thickness profiling, a scan along one dimension is performed in a given range and the Raman intensity is measured for each point x defined by a given step, during the scan. The setup uses an xy-stage to perform such line scans. The range and the step are given and the focus is performed at the initial point of the scan. To increase the precision of measurement, it is possible to adapt the acquisition time and the number of accumulations for each acquisition as well as the number of passes of the scan. In the case of profiling, the average value of I_0 is calculated over a given range outside the patterned layer. Similar profiling can be performed to measure the surface crystallinity profile of a given patterned layer. However, it must be combined with a measurement of the thickness profile in order to define the x -position of the layer under investigation. Such

profiles are presented in Figure 3.16a and b.

Note that to perform and manage all these data treatments, computations, and analysis, several Python scripts were developed and optimised.

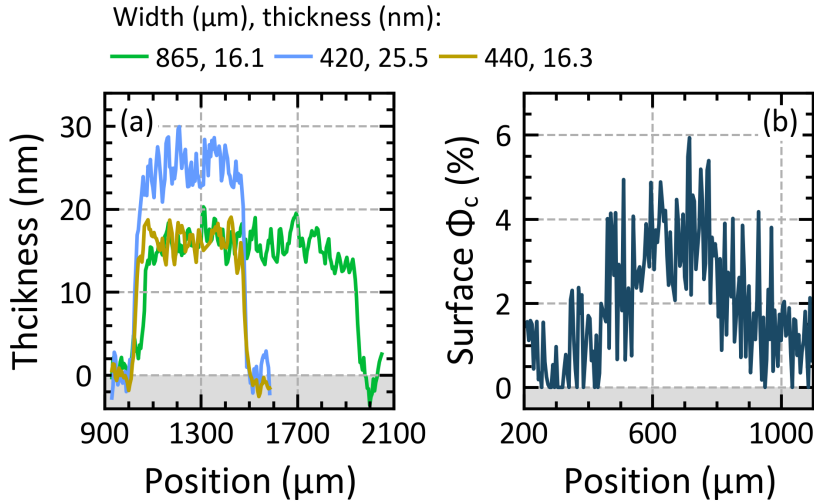


Figure 3.16 – (a) Thickness profiles of IBC $nc\text{-Si:H}(n)$ fingers for two different shadow mask openings and different deposition parameters. (b) Surface Raman crystallinity factor profile of an IBC $nc\text{-Si:H}(n)$ finger.

Transfer length method

The transfer length method (TLM) is one of the most commonly used techniques to measure the specific contact resistivity (ρ_c) of an individual material layer or of a stack of several material layers [Berger 1972a, Berger 1972b, Halevy 2011, Schroder 1984]. The specific contact resistivity is expressed in Ωcm^2 and is also sometimes referred to as *contact resistivity*, the one employed in this work, or as specific contact resistance [Schroder 2006]. In particular, the TLM makes it possible to characterise ρ_c from the extraction of the contact resistance (R_c) and to extract the sheet resistance (R_{sh}) of the TLM conductive layer, i.e., the layer in which the TLM current flows, and the transfer length (L_T). In this technique, an array of identical pads composed by the individual layer or the stack of layers under study and completed by a contacting metallic layer is deposited on a substrate (see Figure 3.17a). This substrate must be a conductive material such as, for example, a TCO layer deposited on a glass substrate or a textured or polished c-Si wafer. The pads are all assumed to be identical with a width w and length L and they are unequally spaced by distances d_i , with i being the number of one interpad distance. In addition, the pads are aligned in a mesa isolation with the same width w as the pads, as illustrated in Figure 3.17b. The mesa isolation is important to confine the current flow and to avoid additional error caused by edge effects, i.e., to prevent the current to flow away from the edges of the TLM pads before being recollected [Schroder 2006].

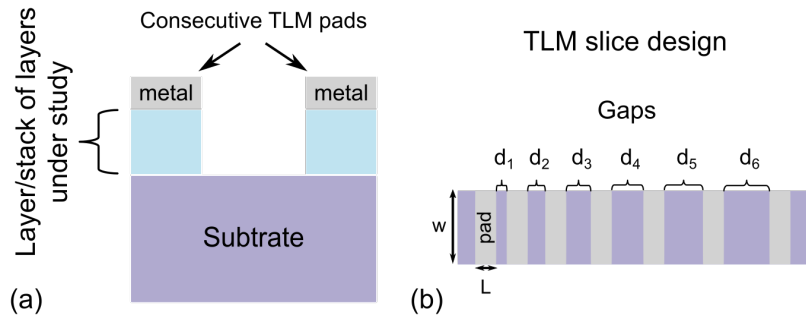


Figure 3.17 – (a) Cross-section of typical TLM samples and (b) top view showing the TLM pads layout as well as the different gaps separated by variable distances d_i .

To perform the TLM computation, the total resistance (R) between each pad is calculated by measuring the corresponding current-voltage (I - V) curves and by applying the Ohm's law. Then, the resistance is plotted as a function of each interpad distance d_i . The TLM and its computation require several hypotheses and conditions to be fulfilled. The first one is that the I - V curves must be linear in order to apply the Ohm's law, i.e., R is assumed to be constant for any current and voltage condition. The second one is that the metallic layers on top of the pads are assumed to be perfectly conductive, so that the lateral transport inside this layer does not contribute to the total resistance. Finally, the last hypothesis is that the conductive layer must be unique and homogeneous to ensure a constant R_{sh} regardless of the current for a given interpad distance; moreover, its thickness is assumed to be zero. The conductive layer is hence fully characterized by its R_{sh} . This last assumption implies only the possibility of a one-dimensional current flow between two pads [Schroder 2006]. Such a structure composed by two pads featuring an interpad distance d is represented in Figure 3.18 along with the corresponding resistances.

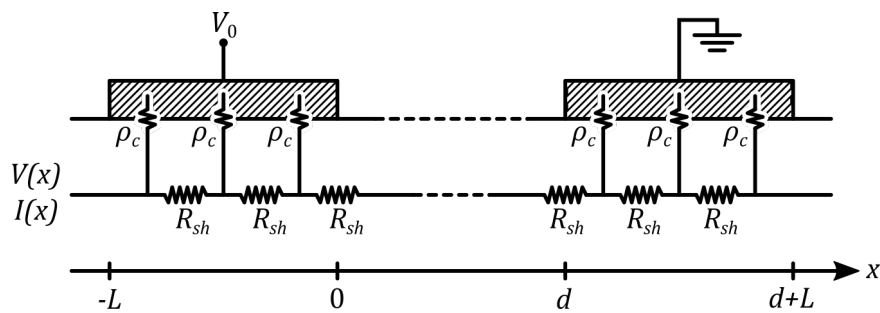


Figure 3.18 – Schematic description of a TLM structure with two pads. The structure is described as a mesh of contact resistivity and sheet resistance elements. Reproduced from [Halevy 2011].

Chapter 3. Experimental processes and characterization systems

From this structure, first the TLM computation starts by applying the Kirchhoff's law and the Ohm's law below the left TLM pad to obtain the differential spatial evolutions of the current and the voltage along the x direction (one-dimensional case) as follows:

$$dI = (V_0 - V(x)) \cdot \frac{w \cdot dx}{\rho_c} \quad (3.18)$$

$$dV = -\frac{R_{sh} \cdot I(x)}{w} \cdot dx \quad (3.19)$$

with V_0 the voltage at the left pad terminal as presented in Figure 3.18.

Then, by differentiating equation 3.19 and replacing $\frac{dI}{dx}$ using equation 3.18 it is possible to obtain the differential equation ruling the spatial evolution of the voltage along the x direction given by:

$$\frac{d^2V(x)}{dx^2} - \frac{R_{sh}}{\rho_c} \cdot V(x) = -\frac{R_{sh}}{\rho_c} \cdot V_0 \quad (3.20)$$

The general form of the solution for this second order differential equation 3.20 is given by:

$$V(x) = A \cdot e^{\alpha x} + B \cdot e^{-\alpha x} + C \quad (3.21)$$

And its derivative is given by:

$$\frac{dV(x)}{dx} = A \cdot \alpha e^{\alpha x} - B \cdot \alpha e^{-\alpha x} \quad (3.22)$$

with $C = V_0$ and $\alpha = \sqrt{R_{sh}/\rho_c} = 1/L_T$, where L_T is introduced as the *transfer length*. The transfer length corresponds to the distance below one TLM pad for which the voltage drops to 1/e of its initial value.

Secondly, it is possible to define the differential relation for the voltage in the area between two TLM pads which is:

$$dV(x) = \frac{-R_{sh} \cdot I_0}{w} \cdot dx \quad (3.23)$$

Integrating this equation 3.23 leads to:

$$V(x) = \frac{-R_{sh} \cdot I_0}{w} \cdot x + cst \quad (3.24)$$

with $I_0 = I(x = 0)$.

Then considering the symmetry of the system which implies $V(d) = V_0 - V(0)$, the voltage in the area between both TLM pad becomes:

$$V(x) = -\frac{R_{sh} \cdot I_0}{w} \cdot x + \frac{1}{2} \cdot \left(\frac{R_{sh} \cdot I_0}{w} \cdot d + V_0 \right) \quad (3.25)$$

Note that the symmetry of the system imposes an identical contact resistance for the two contacts.

Now considering equation 3.22 at $x = 0$ and $x = -L$, the boundary conditions of the system which imply $I(x = -L) = I(d + L) = 0$ as well as the continuity of equations 3.22 and 3.23 at $x = 0$, it is possible to explicit the two coefficients A and B which are given by:

$$A = -\frac{1}{\alpha} \cdot \frac{R_{sh} \cdot I_0}{w} \cdot \frac{1}{1 - e^{-2\alpha L}} \quad (3.26)$$

$$B = -\frac{1}{\alpha} \cdot \frac{R_{sh} \cdot I_0}{w} \cdot \frac{1}{e^{2\alpha L} - 1} \quad (3.27)$$

Finally, considering the continuity of equations 3.21 and 3.25 at $x = 0$, the total contact resistance (R_T) measured between two TLM pads with an interpad distance d can be expressed as:

$$R_T = \frac{V_0}{I_0} = \frac{R_{sh}}{w} \cdot d + 2 \cdot \left(\frac{\rho_c}{w \cdot L_T} \right) \cdot \coth\left(\frac{L}{L_T}\right) \quad (3.28)$$

Thus, to perform TLM computation, R_T is measured for various interpad distances and plotted against each other resulting in a linear relation, as illustrated in Figure 3.19b. Three parameters are extracted from this linear plot. First, the slope allows one to extract the value of R_{sh} of the conductive layer knowing the contact width w , which is independently measured, with the relation: slope = R_{sh}/w . Secondly, the x-intercept (d_0 , with $d_0 < 0$) at $R_T = 0$ gives the transfer length by solving the implicit equation: $L_T = -d_0/(2 \cdot \coth(L/L_T))$. Thirdly, knowing L_T , the

y-intercept (R_{T0}) at $d = 0$ gives the contact resistance with $R_c = R_{T0}/2 = \frac{\rho_c}{w \cdot L_T} \cdot \coth(L/L_T)$.⁴ Finally, the contact resistivity is calculated using the relation:

$$\rho_c = \frac{R_c \cdot w \cdot L_T}{\coth(L/L_T)} \quad (3.29)$$

In particular, for the case of $L_T \ll L$, the coth term is approximated to 1 and R_T is expressed as:

$$R_T = \frac{R_{sh}}{w} \cdot d + 2 \cdot \left(\frac{\rho_c}{w \cdot L_T} \right) \quad (3.30)$$

Leading to R_c directly equal to $\rho_c/(w \cdot L_T)$ and L_T equal to $-d_0/2$. This highlights the importance and meaning of the transfer length as, in this case, the entire current can be represented as passing through a specific area ($w \cdot L_T$).

Inversely, in the case of $L_T \gg L$, R_T is expressed as:

$$R_T = \frac{R_{sh}}{w} \cdot d + 2 \cdot \left(\frac{\rho_c}{w \cdot L} \right) \quad (3.31)$$

Leading to $R_c = \rho_c/(w \cdot L)$ with all the current homogeneously distributed below both TLM pads along the distance L and passing then through the area ($w \cdot L$). In addition, in this case, L_T becomes equal to $\sqrt{\left(\frac{-Ld_0}{2}\right)}$ and is no longer included in the equation of ρ_c .

Thus, the transfer length method gives an exhaustive materials and devices characterization by providing the R_{sh} of the conductive layer as well as the three parameters related to the layer or stack of layers under investigation which are L_T , R_c as well as ρ_c .

In this work, to perform an actual TLM measurement, I - V curves were measured between each consecutive pad in four-probe sensing configuration on a given current-voltage range (see Figure 3.19a). Then, the total resistance was calculated from the slope of the linear fit of the I - V curves (this thus assumes the contact to follow the Ohm's law, as presented in Figure 3.19a), and plotted as a function of the interpad distance (see Figure 3.19b). The resistance as a function of the interpad distance was then fitted by a linear function, and the sheet resistance was calculated from the slope of this linear function, the transfer length from the x-intercept,

⁴At this stage it is important to keep in mind that the value of R_c encompasses the resistance of the TLM current passing in both flow directions, i.e., from the metallic pad to the conductive substrate and from the conductive substrate to the metallic pad. It is then the sum of both contributions, which may differ from the flow experienced in actual solar cell, as in that case the current flows from the c-Si to the metallic electrodes only. However, the contributions of these two current flow directions are similar in the case of Ohmic contacts.

and the contact resistance from the y-intercept as detailed above. Finally, corrections to the value of ρ_c considering the conductive layer thickness of the TLM samples were performed for each measurement as presented in [Eidelloth 2014]. Figure 3.19a and b present a typical example of TLM measurement with the I - V curves and the resulting R_T as a function of the interpad distance d . The parameters of this particular stack of layer extracted using the TLM computation are a R_{sh} of $116 \Omega/\text{sq}$, a R_c of 4.35Ω , a L_T of 0.22 mm , and a final ρ_c of $0.06 \Omega \text{ cm}^2$.

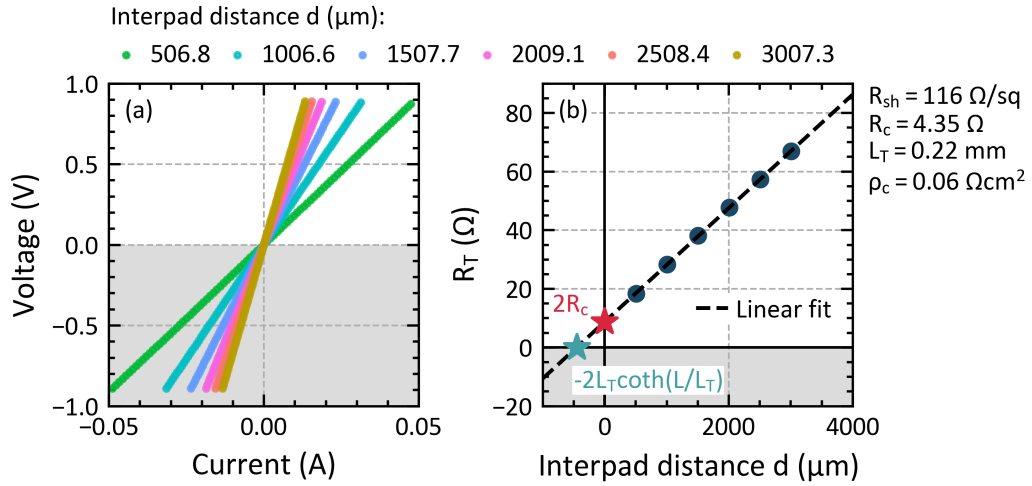


Figure 3.19 – (a) I - V curves for the different interpad distances of a typical TLM sample. The interpad distances range from 506.8 to $3007.3 \mu\text{m}$. (b) The corresponding R_T as a function of the interpad distance d .

In this work, the contact resistivity was characterized with TLM measurements and used to quantify the electrical losses induced by the resistive effect of SHJ solar cell shells. As detailed in section 2.1.2, a shell encompasses different interfaces between its different components, as well as the bulk regions of each component resulting in a global shell contact resistance. During this work, TLM samples were prepared with various SHJ layers in single or multilayer combinations (referred to here as the *shell part under study*) and deposited on one side of textured c-Si wafers (see Figure 3.20). To create the TLM pads two methods were used. The first one consists to deposit a full 400-nm -thick silver (Ag) blanket layer by PVD on top of the shell part under study and then to inkjet-print the desired TLM pattern. Then, the silver and the TCO layers were etched away with chemical solutions and the inkjet-printed resist was removed. The second method to create the TLM pads consists to directly screen-print the silver layer with the appropriate TLM design on top of the shell part under study and then to etch away the TCO layer between each pad using an adapted chemical solution. Thus in this case, the silver print layer acts as the protective mask. Finally, the TLM samples were annealed at a given temperature and time corresponding to the ones used in actual solar cells. It is important to notice that in the case of SHJ shells components, only the TCO and the silver layers must be etched away, in case they are employed, since the thin nanocrystalline and

amorphous silicon layers which are studied in this work feature sheet resistances way larger than the one of the c-Si wafer, i.e., they are not participating to the lateral transport of the TLM current. The c-Si wafer is hence the unique and homogeneous conductive layer. The R_{sh} resulting from the TLM measurement is then the one of the c-Si wafer itself and gives direct information on its electrical properties, such as its doping concentration. After these patterning and etching steps, the TLM samples were cut with a selected width w to create the mesa isolation. To do this, the TLM samples were first pre-cleaved at the rear side using a laser and then cut manually. Then, the interpad distances were precisely measured thanks to a microscope, as they may slightly differ from their nominal value. A sketch of a cross-section of a typical TLM sample in the case of a-Si:H(i)/a-Si:H(n)/nc-Si:H(n)/AZO SHJ shell part is given in Figure 3.20.

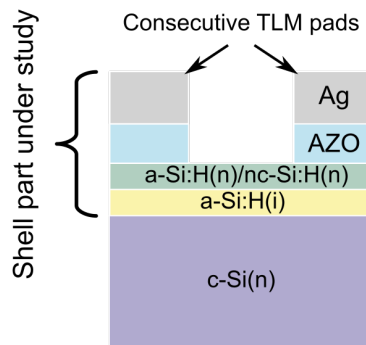


Figure 3.20 – Cross-section of typical TLM sample with SHJ layers. The shell part under study is composed by a stack of a-Si:H(i)/a-Si:H(n)/nc-Si:H(n)/AZO layers deposited on a c-Si(n) wafer.

In the specific case of an absorber TLM conductive layer such as c-Si wafers, TLM measurements can be performed under illumination to target various injection levels. To do this, both sides of the absorber must first of all be well passivated in order to maximize the injected carrier concentration reached inside the bulk of the TLM samples for a given illumination. In the case of SHJ shells, the TLM conductive layer is the crystalline silicon wafer and the TLM side is already efficiently passivated by the layers under investigation. In contrast, the back side must be passivated by the deposition of additional layers providing passivation in addition to optimal light collection, while preventing any TLM current to go through these additional rear layers, hence restricting it to the c-Si bulk. In this work, a-Si:H(i)/a-Si:H(p)/TCO stack, in case of n-type c-Si wafer, or a-Si:H(i)/a-Si:H(n)/TCO, in the case of p-type c-Si wafer, as well as a-Si:H(i)/SiNx stack, for any wafer doping type, were used for that purpose. Then, I - V curves measurements were performed on completed TLM samples in dark conditions and under different illuminations using a Wacom class AAA light simulator and different filters to reach various injected electron and hole densities inside the c-Si wafer. The TLM samples were illuminated from the rear side using a flip table to ensure a homogenous injection below and between each TLM pad. From these I - V curves, the TLM computation was performed and the standard output parameters, namely, R_{sh} , L_T , R_c and ρ_c were extracted as detailed above.

3.2.2 Cell characterization

The different methods and systems used to characterize the shell at different process steps as well as the final solar cell performance (*bottom-up*) are presented in this section.

Photoconductance decay measurement

The photoconductance decay (PCD) measurement is used to quantify the effective minority-carrier lifetime (τ_{eff}) of photogenerated carriers inside semiconductor materials. As introduced in section 2.2.2, τ_{eff} accounts for both the surface and the bulk recombinations of the semiconductor. The PCD measurement is a contactless method based on the inductive measurement of the change in photoconductivity, i.e., the conductivity (σ) impacted by electron-hole pairs creation within the semiconductor material, after illuminating it with a flash of light of a given duration. Then, from the time evolution, i.e., the decay of the semiconductor photoconductivity induced by the recombination of carriers, it is possible to calculate the effective minority-carrier lifetime as a function of the injection level ($\Delta n = \Delta p$) reached inside the bulk. This method can be employed at different process steps of solar cell development, i.e., in a *bottom-up* approach, from PECVD to PVD deposition as well as after annealing. However, PCD measurements cannot be performed with metallization such as a silver grid or blanket layer, as the metallization will affect the value of σ measured by induction.

First, the injection level (Δn) is extracted from the measure of the conductivity (σ) with [Sinton 1996]:

$$\sigma(\Delta n) = q \cdot \mu_n \cdot n + q \cdot \mu_p \cdot p = q \cdot \mu_n \cdot (n_0 + \Delta n) + q \cdot \mu_p \cdot \Delta n \quad (3.32)$$

$$\Delta n = \frac{\sigma - q\mu_n n_0}{q(\mu_n - \mu_p)} \quad (3.33)$$

with, in the case of an n-type c-Si wafer, the injected carrier concentration $\Delta n = \Delta p \gg p_0$, n_0 and p_0 the dark equilibrium electron and hole concentrations, n and p the total electron and hole concentrations, q the elementary charge, as well as μ_n and μ_p the electron and the hole mobility, respectively.

Then, from Δn it is possible to deduce τ_{eff} from the continuity equation given by:

$$\frac{d\Delta n}{dt} = G(t) - U(t) - \frac{1}{q} \nabla J \quad (3.34)$$

with U the recombination rate equal to $\frac{\Delta n}{\tau_{eff}} = \frac{J_{rec}}{qw}$ and G the photogeneration rate (defined by the flash) given by $G = \frac{J_{gen}}{q \cdot w}$, with J_{rec} the recombination current density and J_{gen} the generation

Chapter 3. Experimental processes and characterization systems

current density given in (mA cm^{-2}) as well as w the wafer thickness. More details are given in [Kerr 2002]. In addition, as PCD measurement are performed at open-circuit condition, the term $\frac{1}{q}\nabla J$ is equal to zero and equation 3.34 can be rewritten as the generalized expression of τ_{eff} as follows [Nagel 1999, Sinton 1996, Sinton 2013]:

$$\tau_{eff}(\Delta n) = \frac{\Delta n(t)}{G(t) - \frac{d\Delta n(t)}{dt}} \quad (3.35)$$

From this generalized equation, short lifetimes can be measured using the quasi-steady-state (QSS) mode for which the data are taken over a long, slowly varying light pulse so that the wafer Δn is essentially in steady state over time. In that case, $\frac{d\Delta n}{dt} = 0$ and τ_{eff} becomes:

$$\tau_{eff}(\Delta n) = \frac{\Delta n(t)}{G(t)} \quad (3.36)$$

Conversely, in the case of long lifetimes, a short light pulse is employed to measure the photoconductance decay in transient mode, i.e., with $G = 0$, and τ_{eff} is given by:

$$\tau_{eff}(\Delta n) = \frac{-\Delta n(t)}{\frac{d\Delta n(t)}{dt}} \quad (3.37)$$

Figure 3.21a plots τ_{eff} as a function of Δn in transient mode for a given SHJ passivated c-Si wafer. Moreover, from the evolution of Δn over time it is possible to compute the implied voltage (iV) as a function of Δn with equation 2.8 introduced in chapter 2.2.1 [Sinton 1996]:

$$iV(\Delta n) = \frac{k_B T}{q} \ln\left(\frac{n \cdot p}{n_i^2}\right) = \frac{k_B T}{q} \ln\left(\frac{(\Delta n + n_0)\Delta n}{n_i^2}\right) \quad (3.38)$$

with n_i the intrinsic carrier density, k_B the Boltzmann constant, and T the temperature of the semiconductor (in the case of an n-type semiconductor bulk with $\Delta n = \Delta p \gg p_0$, i.e., $p = \Delta n$). $iV(\Delta n)$ represents the quasi-Fermi level splitting present inside the semiconductor bulk as a function of the injection level without the impact of carrier extraction, i.e., without the impact of resistive effect and selectivity. In addition, considering each point of the PCD measurement in QSS allows one to extract an implied current iJ and to reconstruct a full implied J - V curve.

The iJ can be deduced from the implied sun parameter ($iSun$) which is expressed as a function of the one sun condition for which a J_{SC} is attributed. To do this, first a value of J_{SC} at one sun

($J_{SC}(1 \text{ sun})$) is fixed, ideally the one of the finished device corresponding to the shell or shell part under investigation. Then, considering open-circuit condition and QSS, the continuity equation 3.34 becomes:

$$\frac{J_{\text{gen}}(\Delta n)}{qw} = \frac{J_{\text{rec}}(\Delta n)}{qw} = \frac{\Delta n}{\tau_{\text{eff}}(\Delta n)} \quad (3.39)$$

Assuming $J_{\text{gen}}(1 \text{ sun}) \cong J_{SC}(1 \text{ sun})$, it follows:

$$i \text{sun}(\Delta n) = \frac{J_{\text{gen}}(\Delta n)}{J_{SC}(1 \text{ sun})} = \frac{\Delta n qw}{\tau_{\text{eff}}(\Delta n)} \cdot \frac{1}{J_{SC}(1 \text{ sun})} \quad (3.40)$$

Finally, from the $i \text{sun}$ parameter it is possible to extract iJ for each Δn :

$$iJ(\Delta n) = J_{SC}(1 \text{ sun}) - J_{\text{rec}}(\Delta n) = J_{SC}(1 \text{ sun}) \cdot (1 - i \text{suns}) \quad (3.41)$$

Thus, from $iV(\Delta n)$ and $iJ(\Delta n)$ it is possible to build a complete implied J - V curve (iJ - iV), corresponding to an upper limit of the J - V curve. Indeed, the iJ - iV curve corresponds to the J - V curve free from resistive effects and selectivity, i.e., only considering the different recombination mechanisms which are defined by the bulk quality and the shell passivation ability. From a given iJ - iV curve, the implied solar cell parameters such as the implied V_{OC} (iV_{OC}) and the implied FF (iFF) can be extracted. These parameters represent then the upper limit of the solar cell final performance. The iV_{OC} corresponds to the iV at one sun and is associated to the lifetime at high injection levels ($\Delta n \cong 1 \times 10^{16} \text{ cm}^{-3}$). In addition, it represents the upper limit for the V_{OC} . An example of iV as a function of suns for a given SHJ passivated c-Si wafer is plotted in Figure 3.21b with the value of iV at one sun highlighted. The iFF is associated to the lifetime at low injection levels at one sun condition ($\Delta n \cong 1 \times 10^{15} \text{ cm}^{-3}$) corresponding to the maximum power point conditions and represents the FF expected with perfect transport and selectivity, only taking into account the different recombination mechanisms. Thus, iFF represents an upper limit for the FF of the final device.

Finally, in a *bottom-up* approach, PCD measurements allow for tracking the passivation quality and its impact on the voltage and FF of the solar cell at each process step and to compare them with the final device performance.

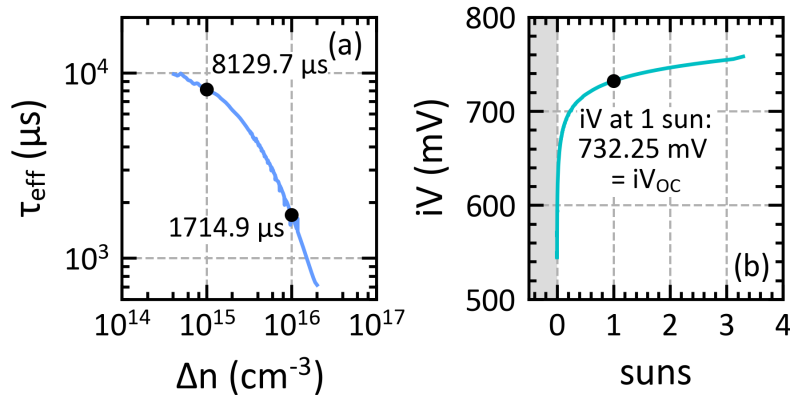


Figure 3.21 – (a) Lifetime curve as a function of the injection level and (b) iV as a function of suns, for a given SHJ passivated c-Si wafer.

Photoluminescence imaging

Photoluminescence imaging is a fast experimental technique providing insights into the spatial quality of semiconductor materials such as c-Si wafers. This technique provides a qualitative mapping of the carrier lifetime by illuminating the material with a laser at a given wavelength, corresponding to an energy higher than the energy bandgap of the material, to generate electron-hole pairs and then by collecting the photons emitted by radiative recombination (see section 2.2.2). These photons have an energy corresponding to the semiconductor bandgap and are detected by a camera which images the full area of the sample under investigation. The number of detected photons is related to the local excess carrier density Δn . The setup used during this work features a laser diode with a wavelength of 808 nm and in the case of c-Si wafers, an IR camera is used to measure the emitted photons which feature energy close to the band gap corresponding to about 1.12 eV, i.e., to about 1107 nm. In addition, the laser light reflected back on the sample surface is blocked with a filter located between the sample and the camera. In this way the homogeneity of the global recombination mechanisms (i.e., the passivation quality) of the wafer is measured, making it possible to precisely localize areas of high passivation quality, appearing brighter as most of the carriers recombine radiatively in these areas, in contrast to areas dominated by defect recombination (SRH, see section 2.2.2) [Trupke 2006]. Thus, it is possible to probe the homogeneity of the surface passivation quality and of the semiconductor bulk recombination quality as well as defects and cracks present inside the semiconductor. In addition, by using different light intensities it is possible to reach different injection levels inside the semiconductor and to probe the corresponding passivation quality. In this work, a low injection level close to the maximum power point and a high injection level close to open-circuit condition were used to study the passivation homogeneity of our solar cells. In addition, as PL is a contactless method, it makes it possible to monitor the passivation quality after each process step, from the first PECVD deposition to the final fully metallized solar cells. Figure 3.22 shows typical PL images obtained for two

bifacial solar cells on 6-inch c-Si wafer presenting a poor and a good homogeneity of radiative recombination. On the left picture, cracks are present leading to local areas with poor radiative recombination (blue color) whereas on the right picture, few defects are present, leading to a highly homogeneous radiative recombination over the whole 6-inch c-Si wafer (red color). Figure 3.23 shows PL images of an IBC solar cell at low and high injection level. It is observed that the impacts of the defects on the radiative recombination are more important at low injection than at high injection.

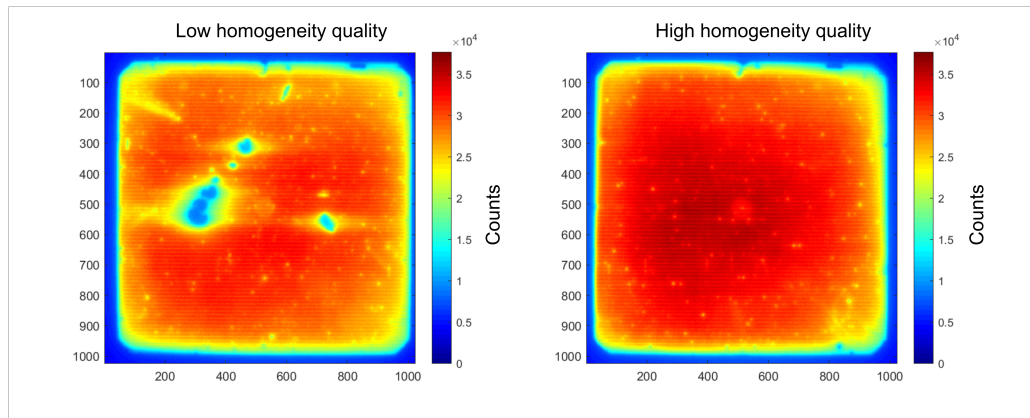


Figure 3.22 – PL images of two bifacial solar cells on 6-inch c-Si wafer with a poor (left) and a good (right) homogeneity of radiative recombination. On the left image, defects are present on the c-Si wafer, locally reducing the radiative recombination signal.

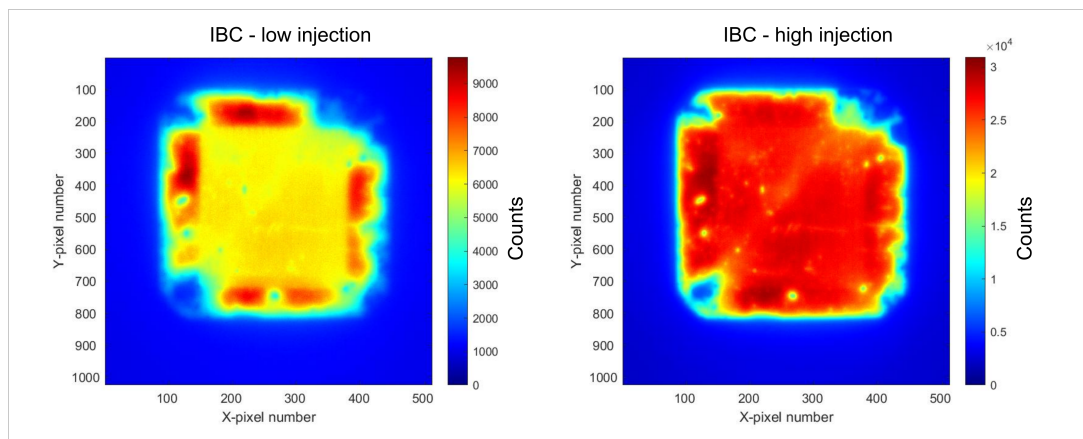


Figure 3.23 – PL images of an IBC solar cell under low (left) and high (right) injection level. On the left image at low injection level, the defects impact more the radiative recombination than at high injection level.

External quantum efficiency measurement

The efficiency with which a solar cell converts photons into collected charge carriers at a given wavelength (λ) can be characterized with three parameters. The first one is the external quantum efficiency (EQE) which is defined as the ratio of the number of collected charge carriers to the number of impinging photons at the solar cell surface and which is given in (%). The second one is the internal quantum efficiency (IQE), which is defined as the ratio of the number of collected charge carriers over the number of photons that enter inside the solar cell given in (%). The EQE and IQE are linked by the total reflectance of the solar cell (R), which corresponds to the reflected light of the solar cell, i.e., the part of the light that does not enter the solar cell and which is lost by reflection, as follows:

$$IQE(\lambda) = \frac{EQE(\lambda)}{1 - R(\lambda)} \quad (3.42)$$

And the third parameter is the spectral response (SR), which is defined as the ratio of the collected charge carrier current to the power of photons incident on the solar cell. The SR is given in (AW^{-1}) and is connected to the EQE as follows:

$$SR(\lambda) = \frac{q}{hc} \cdot EQE(\lambda) \cdot \lambda \quad (3.43)$$

with q the elementary charge, h the Planck constant and c the velocity of light in vacuum. These three parameters, EQE, IQE and SR, give insights into the loss mechanisms affecting the J_{SC} of solar cells. The J_{SC} can be computed from the EQE measurement by multiplying the $SR(\lambda)$ curve by the AM1.5g spectrum ($\phi_{AM1.5g}(\lambda)$ ($Wm^{-2}nm^{-1}$)) and by integrating this resulting product between the spectral region of interest $[\lambda_1, \lambda_2]$:

$$J_{SC} = \int_{\lambda_1}^{\lambda_2} SR(\lambda) \cdot \phi_{AM1.5g}(\lambda) d\lambda \quad (3.44)$$

For c-Si based solar cells, the spectral region extends usually from 350 to 1200 nm. Note that these definitions are accurate assuming a linear dependence between the current and the illumination. If this is not the case, the EQE has to be measured at different background intensity and then the measured EQEs have to be integrated from 0 to 1 sun to find the correct value.

Combining both R and EQE spectra enable to identify the short-circuit current losses occurring in a solar cell as well as their mechanisms. Indeed, they provide a complete measurement of

the behaviour of light incident on a solar cell in short-circuit condition. Such spectra for a typical monofacial $2\text{ cm} \times 2\text{ cm}$ SHJ solar cell are shown in Figure 3.24. The upper blue dashed area accounts for the shadowing, assumed to be 4% here, induced by the metallic front grid and corresponds to a parasitic J_{SC} loss of about 1.8 mA cm^{-2} . The red dashed area represents the proportion of reflected light which induces a total reflection loss of about 1.7 mA cm^{-2} . The whole area below the EQE curve represents the proportion of light absorbed in the wafer and converted into current which represents a solar cell J_{SC} value of 38.22 mA cm^{-2} here. Finally, the green dotted area between the EQE and the 1-R curves represents the proportion of all the parasitic light absorptions occurring in the solar cell leading to a J_{SC} loss of about 3.3 mA cm^{-2} here. These absorptions are split into the UV and IR parts corresponding to a J_{SC} loss of 2.2 mA cm^{-2} and 1.0 mA cm^{-2} , respectively, and are induced, in this particular case of SHJ cell, by the additional a-Si:H, TCO and metal layers, i.e., by the SHJ shell components [Holman 2013b].

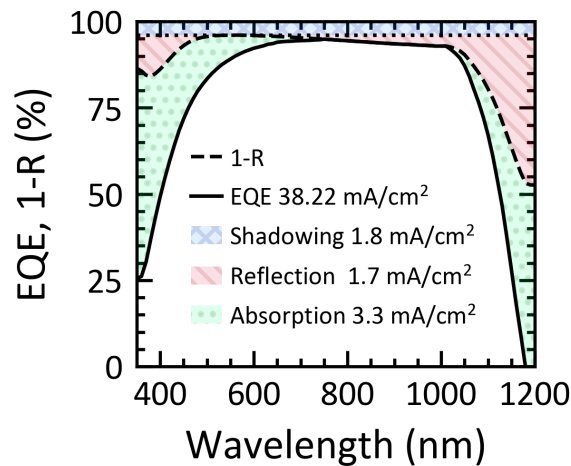


Figure 3.24 – EQE and 1-R spectra of a monofacial $2\text{ cm} \times 2\text{ cm}$ SHJ solar cell in function of the wavelength. The blue dashed area corresponds to J_{SC} loss induced by the metallic front grid shadowing which is assumed to be about 4% here. The red dashed area corresponds to J_{SC} loss induced by reflection and the green dotted area to J_{SC} loss induced by parasitic absorption.

In order to identify and quantify these losses, the spectrum is divided into different wavelength regions. Here, in the case of a SHJ monofacial solar cell presented in Figure 3.24, it is observed that between 700 and 1000 nm, the EQE and the 1-R curves nearly touch each other because almost all absorbed light is converted into current. Below 1000 nm, the light is little reflected thanks to the well-optimised front antireflecting coating and to the pyramid-textured surface. Below 700 nm, the EQE and the 1-R curves separate because of the parasitic absorption of high energy photons occurring in the front thin silicon and TCO layers. This area (left green dotted area part) represents then the UV losses which are induced by these two layers. Above 1000 nm, R increases as the wafer becomes more transparent to penetrating light with low energy photons. These light can enter the cell and bounce back and forth between the front

and back side of the cell before being absorbed or reemitted at the front side. Thus, the secondary escape reflection increases and is added to the primary front surface reflection. In this region, parasitic light absorption also increases because of free-carriers absorption (FCA) occurring in both the front and rear TCO layers and of rear plasmonic absorption induced by the rear metallic layer. This region represents then the IR losses induced by these two effects [Holman 2013c]. Hence, the losses in the high-energy photons range, i.e., at low wavelength, are mainly related to the front side of the cell whereas losses in the low-energy photons range, i.e., at long wavelength, include both the front and the back sides of the cell.

The system to perform EQE and R measurements in this work is a pv-tools system using a halogen light source which is monochromated at a specific wavelength in the 350 to 1200 nm range. The EQE measurement is performed by illuminating a completed solar cell or a small area of the cell with the monochromatic light beam source and by measuring the current generated by the solar cell in short-circuit condition while the wavelength of the incoming light beam is varied. The solar cell is connected to a source meter to measure the current generated when illuminated at each wavelength. The incoming photon flow is determined by measuring the response of a photodiode and the EQE of a reference cell under the same light source. To measure R, an integrating sphere is placed on the top of the illuminated complete cell or small area, which enables to measure the reflected light at each wavelength.

Illuminated current-voltage measurement

To determine the final performances of any type of finished solar cell, such as its maximum output power and efficiency, the most basic and valuable technique is to measure its current density-voltage (J - V) characteristic under standard test condition (STCs). STCs are defined by a cell temperature set at 25 °C and at an irradiance of 100 mW cm⁻² with a light spectrum matching the AM1.5g solar spectrum. This spectrum is related to an air mass of 1.5 corresponding to solar spectrum reaching the earth when the sun is at about 41 ° above the horizon. To characterize the J - V characteristic, the solar cell under study is illuminated at STCs and a sourcemeter (Keithley 2651A) is used to sweep the voltage in a given range from the reverse bias up to above the cell V_{OC} , while measuring the resulting electrical current corresponding to each voltage. In this work, a Wacom WXS-220S-L2 AM1.5g class AAA solar simulator including xenon and halogen lamps, to respectively cover the blue and the red part of the solar spectrum, was used as illumination source. As a first step before the measurements, a calibrated reference cell of the desired architecture (e.g., monofacial, bifacial, or IBC) is measured and the intensity of the xenon lamp is adjusted to match the reference J_{SC} of the calibrated cell. Then, following the calibration step, the cell under study is measured. To ensure a precise temperature control, the cell is placed on a chuck adapted to its architecture with either an integrated temperature controller using Peltier elements or a temperature probe to monitor it. The chuck features front and/or back contacts which are optimised to avoid any contribution from the probes resistance. In addition, during the measurement, a shadow mask with the appropriate shape is used to avoid illuminating non-active cell areas. Figure 3.25 shows a

typical illuminated J-V curve together with the related extracted cell parameters which are:

- The short-circuit current density (J_{SC}), expressed in mAcm^{-2} , which is the current density measured at zero voltage, i.e., when the cell is shorted and thus for which the entire current of the cell is extracted. This value depends mainly on the amount of light reaching the bulk and participating to the generation of the electron-hole pairs. Different effects such as parasitic absorption and light reflection can lead to J_{SC} losses.
- The open-circuit voltage (V_{OC}) which is the voltage obtained when no current is extracted, i.e., at $J_{SC}=0$. This parameter depends on all recombination processes described in section 2.2.2. Indeed, any of these recombination processes lowers the excess carrier density (Δn) reached inside the absorber bulk and hence the maximum achievable voltage at open-circuit (but also at any injection).
- The power at the maximum power point (P_{MPP}) which is the maximal power which can be delivered by the cell and which is given by the result of the product of the current density at MPP (J_{MPP}) and the voltage at MPP (V_{MPP}), i.e., $P_{MPP} = J_{MPP} \cdot V_{MPP}$. Thus, to deliver the maximum power available, MPP is the targeted operating point of solar cells.
- The fill factor (FF) which represents the squareness of the J - V curve, i.e., the ratio between the ideal square-shaped curve defined by the ideal power resulting from the product of J_{SC} and V_{OC} and the actual maximum power at MPP. The FF value is defined by the result of the combination of recombination and electrical losses affecting the solar cell, i.e., any loss reducing the squareness of the J - V curve.

$$FF = \frac{P_{MPP}}{J_{SC} \cdot V_{OC}} = \frac{J_{MPP} \cdot V_{MPP}}{J_{SC} \cdot V_{OC}} \quad (3.45)$$

- And finally, the energy conversion efficiency (simply referred as efficiency) of the solar cell (η) which is defined as the ratio of the maximal power output P_{MPP} of the solar cell to the power input of the solar spectrum (P_{in}), equal to 100 mWcm^{-2} :

$$\eta = \frac{P_{MPP}}{P_{in}} = \frac{J_{MPP} \cdot V_{MPP}}{P_{in}} = \frac{FF \cdot J_{SC} \cdot V_{OC}}{P_{in}} \quad (3.46)$$

As depicted in Figure 3.25, the J - V curve of solar cells presents a diode behaviour, or more precisely, a current-generating diode behaviour. During this work, to fit such J - V curves, the double-diode model representing an equivalent electrical circuit for a solar cell was generally used [Suckow 2014]. This circuit is presented in Figure 3.26 and the equation linking the current density to the voltage is expressed as:

$$J(V) = J_L - J_{01} \left[\exp \left(\frac{q(V + JR_s)}{n_1 k_B T} - 1 \right) \right] - J_{02} \left[\exp \left(\frac{q(V + JR_s)}{n_2 k_B T} - 1 \right) \right] - \frac{V + JR_s}{R_{shunt}} \quad (3.47)$$

Chapter 3. Experimental processes and characterization systems

with V the voltage, J_L the photogenerated current (generally equal to J_{SC}), R_s the series resistance (presented in more details in section 3.2.2), R_{shunt} the shunt resistance, q equal to the elementary charge, k_B the Boltzmann constant, T the absolute temperature of the solar cell in Kelvin, n_1 and n_2 the ideality factors of both diodes and J_{01} and J_{02} the recombination currents associated to the two diodes which account for two different recombination contributions.

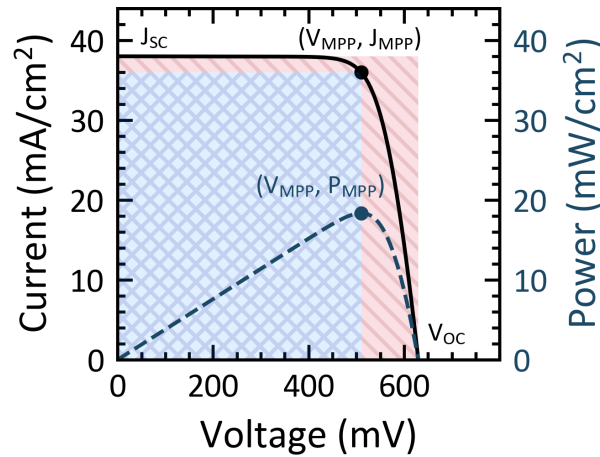


Figure 3.25 – Typical J-V curve of a SHJ solar cell along with its power as a function of the voltage curve. The different cell parameters which are J_{SC} , V_{OC} , V_{MPP} , J_{MPP} and P_{MPP} are depicted.

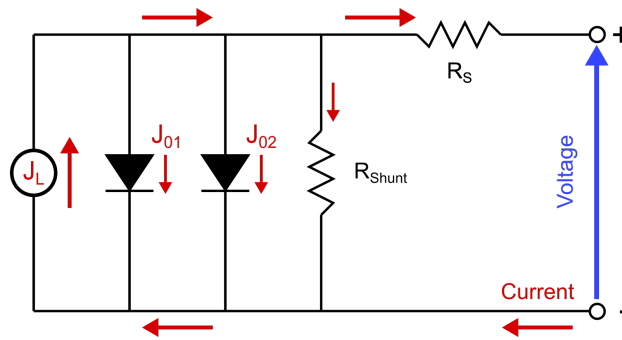


Figure 3.26 – Equivalent circuit of a solar cell using the two-diodes model.

J-V measurements can also be performed under variable temperature. This provides an additional characterization method to study the opto-electrical properties of solar cells. Indeed, most of the physical properties of solar cells depend on temperature. In general, the J_{SC} of solar cells increases with increasing temperature mainly due to a decrease of the bandgap of the absorber. Conversely, the V_{OC} is found to decrease with the temperature increase. The trend of the FF is more complicated and depends strongly on the cell technology. While homojunction solar cells demonstrate an increase of FF with temperature decrease, SHJ solar

cells demonstrate a more complex trend combining first a rise of the FF as the temperature decreases and a decrease of FF at low temperature. This is mainly due to transport issues caused by the nature of the hetero-interfaces which build different energy barriers. As the lower the temperature, the lower the thermal energy of charge carriers, the carriers accumulate at the different energy barriers. This induces an increase of the series resistance, resulting eventually to important S-shaped J - V curves. The system used in this work to perform J - V measurements in temperature allows one to obtain temperatures down to -160°C and up to 80°C . The temperature of the complete solar cell is monitored using a vacuum chuck fixed on four Peltier modules. The temperature is measured using a PT100 probe located inside the chuck. Before each J - V measurement, the temperature is first reached and then stabilised. More details on the temperature-dependent J - V measurement can be found in [Cattin 2020a].

Electrical transport losses free current-voltage curve measurement

Based on the aforementioned illuminated current-voltage measurement performed under variable illumination, it is possible to build a pseudo J - V curve (pJ - pV) of a complete solar cell to obtain information about its fundamental characteristics free from electrical transport losses, and, in particular in the case of ohmic transport, free from series resistance (R_S) effects [Sinton 2000]. The pJ - pV curve is obtained by measuring several pairs of J_{SC} and V_{OC} values at different light intensities (expressed as multiples or fractions of the 1 sun light intensity x , referred to in the following as $x\text{sun}$) of a given solar cell. From these values, it is possible to compute the corresponding pJ and pV values [Wolf 1963]. The method to build the pJ - pV curve is based on the continuity equation 3.37 in steady state conditions (presented in section 3.2.2) applied to a complete solar cell. This can be expressed as:

$$\frac{\Delta n}{\tau(\Delta n)} = G - E = \frac{J_{gen}}{q \cdot w} - \frac{J}{q \cdot w} \quad (3.48)$$

with E standing for the extraction related to J the extracted current density at a given voltage V .

Based on this relation, it is possible to find a steady state condition without current extraction which is equivalent to the state of a given solar cell under one sun generation current with an extracted current density J at given voltage V (under an arbitrary load). This is achieved by illuminating the cell at low intensity to target a lower generation current than obtained at one sun, referred here to as $J_{gen}(x\text{sun})$, and measuring the voltage of the cell under open circuit (OC) condition. In other words, it is possible to find a lower $x\text{sun}$ illumination applied to a solar cell under OC condition which makes it possible to match its steady state obtained at one sun with given voltage V and extracted current density J . Assuming $J_{gen} = J_{SC}$ this leads to:

$$J_{SC}(xsun) = J_{SC}(1sun) - J \quad (3.49)$$

$$J = J_{SC}(1sun) - J_{SC}(xsun) \quad (3.50)$$

From these considerations, the continuity equation 3.48 under one sun generation and at a given voltage V can be expressed as:

$$\frac{\Delta n}{\tau(\Delta n)} = \frac{J_{SC}(1sun)}{q \cdot w} - \frac{J}{q \cdot w} \quad (3.51)$$

And at open circuit condition under $J_{SC}(xsun)$ generation, equation 3.48 can be expressed as:

$$\frac{\Delta n}{\tau(\Delta n)} = \frac{J_{SC}(xsun)}{q \cdot w} \quad (3.52)$$

and combining this last equation 3.52 with equation 3.49, this becomes:

$$\frac{\Delta n}{\tau(\Delta n)} = \frac{J_{SC}(1sun)}{q \cdot w} - \frac{J}{q \cdot w} \quad (3.53)$$

which is equal to equation 3.51, demonstrating that for a fixed $xsun$ illumination both cases are equivalent and the recombination currents ($J_{rec} = \frac{\Delta n}{\tau(\Delta n)}$) are equal.

To illustrate further both cases, Figure 3.27 presents the leaky bucket analogy which illustrates here the solar cell steady state in the case (a) of $J_{SC}(1sun)$ generation with the extracted current density J for a given voltage V and (b) of $J_{SC}(xsun)$ generation under open circuit condition (V_{OC}). The recombination current (J_{rec}) is similar in both cases. From these considerations, it follows that for a given $J_{SC}(xsun)$ generation, the measured V_{OC} matches the solar cell voltage V at one sun, but without the effect of electrical transport losses. The measured V_{OC} at $xsun$ corresponds then to the pseudo-voltage pV and equation 3.49 gives the pseudo-current pJ . Thus, by measuring J_{SC} and V_{OC} for various $xsun$ illumination intensities, it is possible to built the complete pJ - pV curve by plotting the pseudo-current expressed by $J_{SC}(1sun) - J_{SC}(xsun)$ as a function of the V_{OC} obtained at $xsun$.

Finally, the two diodes model, expressed by equation 3.47 in section 3.2.2, free of R_S becomes:

$$J(V) = J_L - J_{01} \left[\exp\left(\frac{qV}{n_1 k_B T} - 1\right) \right] - J_{02} \left[\exp\left(\frac{qV}{n_2 k_B T} - 1\right) \right] - \frac{V}{R_{shunt}} \quad (3.54)$$

which relates the current directly to the voltage. This equation can be used to fit given pJ - pV curve and to extract different cell parameters such as the pseudo- FF (pFF) including the pseudo V_{MPP} and J_{MPP} (pV_{MPP} and pJ_{MPP} , respectively) as well as the series resistance R_S at any voltage, i.e., at any injection level inside the cell (see section 3.2.2). Figure 3.28 shows a typical illuminated J - V curve together with its related pJ - pV curve and some extracted cell parameters. Note that the pJ - pV curve is not free of shunt resistance (R_{shunt}).

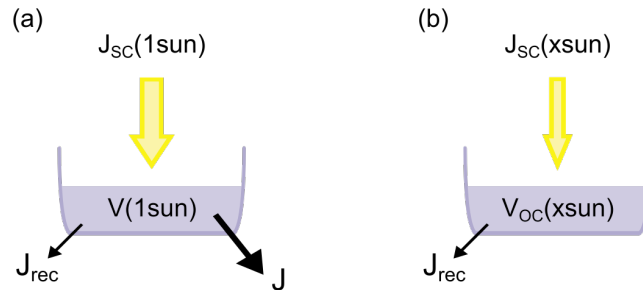


Figure 3.27 – Leaky bucket representation of solar cell steady state for (a) under 1 sun generation and with current density extraction (J) and (b) under x sun generation and at open circuit condition (OC). The recombination currents (J_{rec}) are similar in both cases.

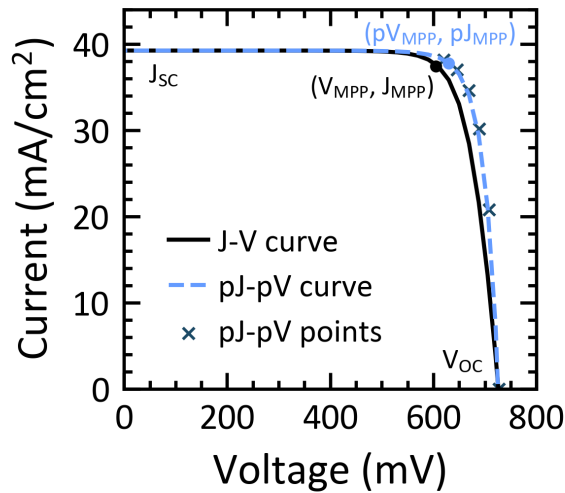


Figure 3.28 – Typical J - V curve of a SHJ solar cell with its related pJ - pV curve. The different cell parameters which are J_{sc} , V_{oc} , V_{MPP} , J_{MPP} , P_{MPP} as well as pJ_{MPP} and pV_{MPP} are depicted.

Series resistance

As introduced in section 2.2.4, the series resistance (R_S) of solar cells accounts for the global electrical voltage drop induced by resistive effects occurring in the device during the transport of the carriers (for a given current density) from the silicon bulk to the external load, passing through the whole shell. The different contributions to the R_S depend on the absorber bulk and on the shell, as well as on the cell architecture. To decouple the different contributions, it is possible to separate them as follows: bulk series resistance, passivation and/or selectivity series resistance as well as electrode series resistance. More specifically, for SHJ solar cells, the contributions to the series resistance can be separated as:

- Silicon wafer bulk resistance;
- Passivating and selective layers resistance (bulk and interfaces);
- TCO resistance (interfaces and bulk transversal or lateral transport, or a combination of both depending on the cell architecture);
- Metal blanket and/or grid resistance (depending on the cell architecture).

The bulk series resistance is defined as the resistance induced by the non-modified bulk properties in addition to the resistance occurring within the modified bulk part close to the surface and, depending on the solar cell architecture, the current can flow in these two regions in one or two dimensions. The resistance induced by the passivating and selective layers depends generally only on transversal current flow, involving several resistive physical phenomena which were detailed in section 2.2.5, induced by the bulks and interfaces. The electrode series resistance encompasses the resistance induced by the TCO and the metal layers. For the TCO layers, the coupling with the underlying passivating and selective layers will define a resistance at the interface. In addition, a one or two-dimensional current flow can occur inside the TCO itself depending on the cell architecture, resulting in transversal and/or lateral resistance contributions. Both resistances are generally different because of the non-isotropic TCO properties and on the current path length. Finally, in the case of blanket metal layers and metal grids, the interface with the underlying TCO will induce a resistive contribution in addition to the current flow inside the metal bulk which may be one or two-dimensional depending on the external contacts shape and location. Importantly, the value of R_S might depend on the voltage at which the current of the solar cell is extracted.

Different methods exist to extract the R_S value from J - V curves [Pysch 2007]. During this work, three methods were mainly considered. The first method extract the R_S value from the double-diode model given by equation 3.47 applied to fit a complete J - V curve. This series resistance is called in this work $R_{S,fit}$ and does not depend on the voltage. The second method is based on the comparison of the pJ - pV curve, which is free from series resistance effects,

with the complete J - V curve. In this way, it is possible to calculate the series resistance using the following equation for any given voltage V [Wolf 1963]:

$$R_S(V) = \frac{\Delta V}{J} = \frac{pV - V}{J} \quad (3.55)$$

where ΔV is the voltage difference between the voltage of the R_S -free pJ - pV curve (pV), and the voltage of the J - V curve (V), for a fixed current density J . J corresponds to the current density of the J - V curve at voltage V , i.e., to a given point $((V, J))$ on the J - V curve. With this method, the R_S value can be extracted for any voltage V of the J - V curve, especially at the maximum power point (MPP) where the FF is defined. The R_S at MPP, given by $R_S(V) = \frac{pV - V_{MPP}}{J_{MPP}}$, is the value used to study the impact of the series resistance on the final solar cell performance. This method is the most accurate one to extract correct values of R_S . The last method is based on the pJ - pV curve extraction method but does not require the drawing of the entire pJ - pV curve. It is a fast method which focuses directly on the measurement of R_S close to MPP. To do this, following a line of reasoning similar to section 3.2.2, equation 3.55 can be expressed as [Bowden 2001]:

$$R_S(V) = \frac{pV - V}{J} = \frac{V_{OC}(xsun) - V}{J_{SC}(1sun) - J_{SC}(xsun)} \quad (3.56)$$

which is given for one fixed illumination intensity $xsun$ giving a point on the pJ - pV curve related to a (V, J) point on the J - V curve sharing the same current density J . Thus, the ideal level of illumination $xsun$ must be targeted for each solar cell such that $J_{MPP} = J_{SC}(1sun) - J_{SC}(xsun)$. Thus, by calculating the appropriate $xsun$ for a given solar cell using $x = (J_{SC}(1sun) - J_{MPP}(1sun)) / J_{SC}(1sun)$, which is generally about 7 to 10 % of illumination, it is possible with only one additional value of J_{SC} and V_{OC} at $xsun$ illumination to compute the value of R_S at MPP. This last method is the one which was mainly used during this work. To perform such measurement, a filter providing an illumination of about 7 % is used. Note that the value of R_S obtained with this method fluctuates around the actual MPP value. The R_S values obtained with these three methods are depicted in Figure 3.29 for the case of an a-Si:H(i) layer thickness variation.

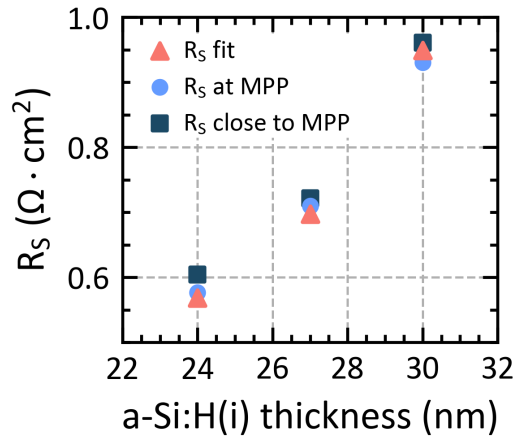


Figure 3.29 – R_S values as a function of a-Si:H(i) layer thickness obtained with the three methods presented in this section. R_S fit stands for the value of R_S obtained with the fit of the J-V curve using the two-diode model, R_S at MPP stands for the value of R_S obtained from the difference between the pJ-pV and J-V curves and the R_S close to MPP stands for the value of R_S obtained by targeting an illumination intensity x_{sun} to reach the closest as possible $J_{MPP} = J_{SC}(1sun) - J_{SC}(x_{sun})$ [Bowden 2001].

Fill factor losses analysis

Recombination and resistive losses influence the solar cell FF in two different ways. The first source of FF losses are the recombination mechanisms which impact the internal voltage as it is directly linked to the splitting of the quasi-Fermi levels in the device. The second source of FF losses are the parasitic resistive effects which can be separated in two global contributions which are the series resistance (R_S) and the shunt resistance (R_{shunt}). As introduced in section 3.2.2, the R_S is the sum of the different resistive effects the carriers undergo when flowing from the absorber to the external electrodes causing a global electrical voltage drop defined to the global bulk and shell properties, lumped into the R_S value. The R_{shunt} is often caused by manufacturing defects and low value of this resistance provides an alternative current path for the carriers, leading to power losses (see Figure 3.26). Overall, the higher the shunt resistance, the higher the FF , and conversely, the lower the series resistance, the higher the FF .

For process optimization and electrical losses analysis of solar cells, it is important to quantify the influence of resistive and recombination losses mechanisms on the FF [Leilaieoun 2016]. The upper physical limit for the FF of crystalline silicon solar cells is defined by the recombination losses inside the absorber and at its surfaces. Then, the series resistance, shunt resistance, and additional recombination currents further lower the fill factor. The different FF losses contributions can be quantified by the use of several calculations and characterization methods performed at different process steps. Such a FF breakdown is detailed in Figure 3.30 which shows the different fill factors often used in the literature to decouple the different contributions to the total FF losses and which can be monitored during the process fabrication

of a solar cell. In the specific case of crystalline silicon solar cells, the FF breakdown starts first with a maximum theoretical value of 89 % calculated assuming a 100 μm -thick wafer limited only by radiative and Auger recombination processes, and an ideal shell (i.e. inducing zero electrical and parasitic optical losses) [Tiedje 1984]. Then, the first experimentally measurable parameter is the implied FF (iFF), introduced in section 3.2.2, which accounts for all recombination losses inside the solar cell (bulk and interface recombinations). iFF is thus linked to the internal voltage, called implied V (iV), of the cell which is usually measured using a photoconductance decay system. In particular, for SHJ solar cells, this measurement can be performed, e.g., after deposition of the intrinsic and doped thin hydrogenated silicon layers, and after the addition of the TCO overlayers. Moreover, note that this measurement takes also into account the internal shunt paths related to the R_{shunt} . Then, the second measurable value is the pseudo fill factor (pFF) introduced in section 3.2.2 which represents the FF of a complete solar cell at its external voltage but without the effect of the series resistance. This measurement gives information on the decrease of the quasi-Fermi levels from the absorber to its terminal electrode, i.e., the voltage drop between the internal and the external voltage. The last (and the lowest) FF value is the one measured on the complete solar cell from its J - V curve. This value takes into account the global voltage drop at the MPP. Overall, this FF breakdown method allows one to quantify the different FF losses contributions and origins occurring in solar cells. In addition, from the final device performances, it is also possible to compute a numerical upper limit for the FF named FF_0 , which is calculated with the formula presented in [Green 1981] and which assumes that R_{shunt} and R_S have negligible effect on cell performances, i.e., $R_{\text{shunt}} \rightarrow \infty$ and $R_S = 0$. FF_0 depends on the measured V_{OC} value and on the ideality factor (n) extracted considering the one-diode model to fit the J - V curve. In this work, to compute FF_0 values, the method presented in [Bowden 2001] is used. In that case, for a given solar cell, the FF_0 value calculated is close to the one of the pFF extracted from the pJ - pV curve built with the method presented in section 3.2.2. Finally, Figure 3.31 presents the typical J - V , pJ - pV and iJ - iV curves of a SHJ solar cell with the position of the MPP points depicted for the three curves.

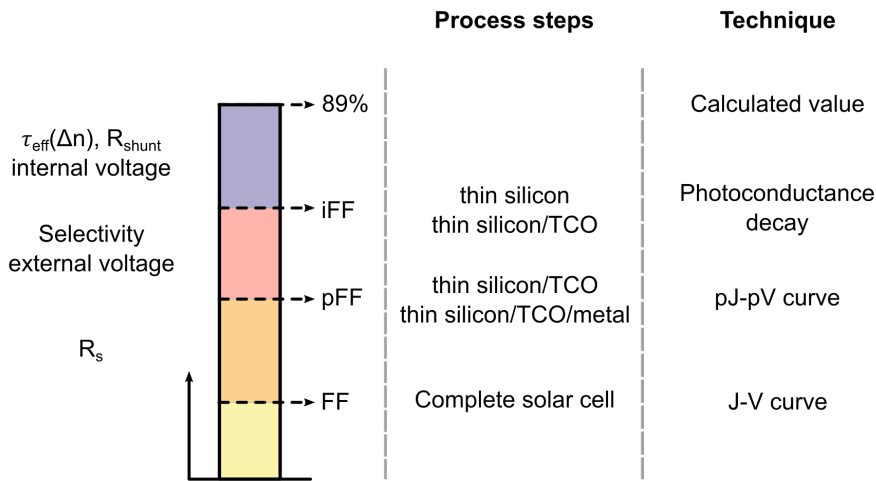


Figure 3.30 – Summary of the FF losses breakdown. Reproduced from [Demaurex 2014a].

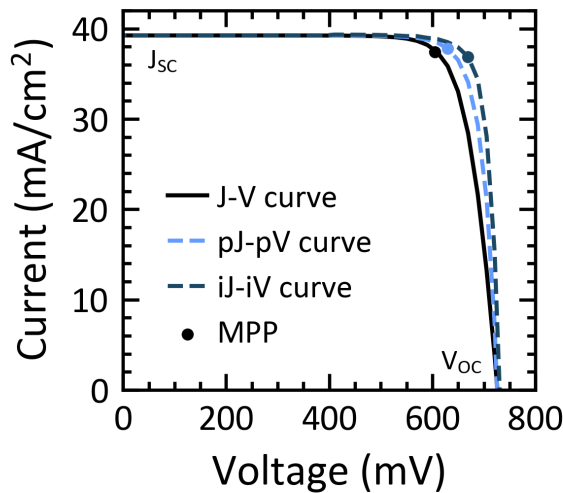


Figure 3.31 – Typical J-V, pJ-pV, iJ-iV curves of a SHJ solar cell. The position of the MPP points is depicted on the three curves.

3.3 Conclusion

In this chapter, we presented in a first part the main processes and equipment used during this thesis for the fabrication of the three SHJ solar cell architectures under study, which are the monofacial, the bifacial, and the IBC. A detailed presentation of the different process steps and tools including wafer texturing and cleaning, PECVD, PVD, screen-printing metalization, selective material etching as well as thermal evaporation was given. In the second part, we presented different tools and methods which were developed and optimized to (i) characterize the different shell sublayers individually or in various stacks, used for the *top-down* approach,

and (ii) to characterize the evolution of the shell properties along the different process steps as well as the final solar cell performance, used for the *bottom-up* approach. In particular, a significant focus was put on the transfer length method, the Raman spectra measurement, the dark conductivity measurement, the photoconductance decay computations, as well as on the pJ - pV curves extraction method which were presented in a thorough way.

In the following chapters 4, 5 and 6, these tools and methods are applied to manufacture actual SHJ solar cells and to perform in-depth layer and cell characterizations. The different physical parameters obtained with the different characterization techniques will be investigated to provide insights aiming to unveil the link between the final shell properties and the resulting performances of solar cells.

4 Advanced methods for the electrical characterization of solar cell shells using transfer length method Measurements under variable illumination

Summary

This chapter presents a novel advanced characterization method based on an upgraded theoretical framework of transfer length method (TLM) measurements. TLM measurements under variable illumination were performed to further study specific shells including different electron and hole-selective parts employed in the silicon heterojunction (SHJ) technology. We demonstrated that TLM under variable illumination is a relevant characterization method to investigate and assess the carrier transport quality of SHJ shells integrating thin silicon layers featuring various properties. To this end, three specific studies were conducted.

First, SHJ shells integrating several n-type thin silicon layers with various activation energies (E_a) were studied. Here, we demonstrated that illumination has a strong impact on the contact resistivity (ρ_c) value. Noticeably, it was found that ρ_c increases with the illumination, i.e., with the rise of the injected carrier density. In addition, the injected carrier density increase was observed to induce an important diminution of the c-Si sheet resistance (R_{sh}). From these results, the importance of considering the MPP injection level to measure the ρ_c when aiming to accurately study the impact on the transport losses and thus on the actual value of FF of solar cells was highlighted. In addition, this method showed that different n-type shell parts featuring various E_a are impacted differently by illumination, i.e., that they present different illumination responses reflected by the slopes of the $\rho_c = f(R_{sh})$ curves. These results were supported by TCAD simulations with a particular focus on the E_a of the n-type thin silicon layers which is used to vary the accumulations at the c-Si(n)/a-Si:H(i) interface. In addition, two suspected limitations of this method, namely, the non-ohmic behaviour of TLM I - V curves appearing under illumination and edge recombination, were cleared up. Secondly, we compared the impacts of variable illumination and of the variation

Chapter 4. Advanced methods for the electrical characterization of solar cell shells using transfer length method Measurements under variable illumination

of the c-Si bulk doping density on the value of ρ_c . Interestingly, the two impacts were found to be significantly different: ρ_c decreased with R_{sh} wafer doping, whereas it increased when the illumination-impacted R_{sh} decreased. Finally, the ρ_c values were observed to be more impacted by the illumination for high R_{sh} wafer doping, i.e., for lowly-doped wafers. Finally, we investigated and discussed the applicability of TLM measurements under illumination to measure p-type shell parts on n-type c-Si wafers. Comparing the ρ_c values at high illumination of similar p-type shell parts deposited either on c-Si(n) or on c-Si(p) wafers, it was observed that the values are of the same order of magnitude. However, the illumination-impacted R_{sh} were found to be lower than expected and the TLM I - V curves at low illumination were observed to be superimposed, revealing a significant contribution of ρ_c hiding the R_{sh} effect. Consequently, these two major observations put in evidence that the relevance of TLM under variable illumination to measure the value of ρ_c for the case of p-type shell parts deposited on c-Si(n) wafers is still questionable. Additional studies are required to establish the validity of this method and to complete the global description and understanding of the physical phenomena behind these behaviours.

Overall, this work provides important insights into the fundamental understanding and the practical characterization of SHJ solar cells, as well as useful methods to guide the efficiency improvements of such devices towards their practical efficiency limits.

4.1 Introduction

As introduced in section 2.2.5, one way to quantify the resistive losses induced by the electrical transport of carriers and their extraction through a shell is to measure its contact resistivity value (ρ_c). This parameter characterizes the carrier transport quality through all the interfaces and materials composing the shells. Any change to the energy barriers or to the bulk properties of the materials constituting the shell and of the absorber bulk will directly affect the ρ_c value [Procel 2019]. The parameter ρ_c reflects then the resistive losses of the carrier transport induced by the global band bending resulting from the coupling of the different material properties and is therefore a relevant parameter to investigate different interfaces and couplings *within* and *induced* by the shells. As presented in section 3.2.1, the transfer length method (TLM) is one of the most commonly used techniques to measure the ρ_c of an individual material layer or of a stack of several material layers, such as the ones constituting solar cell shells. Currently however, two restrictions of this method are present when studying electrical losses of solar cells. First, the ρ_c characterization is only performed in dark conditions, and secondly, in the case of c-Si-based solar cells, it is not possible to measure the ρ_c value of a shell part presenting the opposite type (n or p-type) to the c-Si bulk of the actual solar cell. Commonly, to measure the ρ_c values of p-type shell parts, p-type c-Si wafers are used and conversely, to measure the ρ_c values of n-type shell parts, n-type c-Si wafers are used [Lachenal 2016, Luderer 2020].

Consequently, two major questions are addressed in this chapter. First, considering that

the final electrical transport quality, and thus ρ_c , are defined by the coupling of the c-Si bulk properties and the shell sub-components properties, is the ρ_c value measured in dark conditions similar to the one that would be measured for c-Si bulk experiencing an injection level similar to actual solar cells, i.e., in MPP conditions? Secondly, in the case of n-type c-Si bulk-based solar cells, it is questionable if the value of ρ_c of p-type shell parts measured on p-type c-Si wafers accounts correctly for the actual transport losses once these p-type shell parts are deposited onto n-type wafers. Indeed, in the particular case of SHJ solar cells, the global transport quality is partly connected to the band bending at the c-Si/a-Si:H(i), a-Si:H(i)/doped thin silicon layer, and doped thin silicon layer/TCO interfaces. More specifically, at the vicinity of the c-Si/a-Si:H(i) interface, a change of the c-Si bulk properties, such as a change of its charge-carrier density or charge-carrier type (i.e. a Fermi or quasi-Fermi level change inside the c-Si bulk), will affect the local band bending inside the c-Si bulk and thus affect the accumulation of carriers at the vicinity of the c-Si/a-Si:H(i) interface, potentially impacting the ρ_c value. On other words, for a given shell part, the value of ρ_c is expected to depend strongly on the charge-carrier density and charge-carrier type inside the c-Si bulk. On the other hand, the energy band bending also rules the selectivity of a given shell. Indeed, in the case of SHJ, selectivity is ruled by the ratio between the conductivities of the majority and minority charge carriers inside the absorber at the vicinity of the c-Si/a-Si:H(i) interface [Wurfel 2015]. Yet, as electron and hole mobilities are of the same order of magnitude inside c-Si [Klaassen 1992a, Klaassen 1992b], a high selectivity requires a high asymmetry in carrier concentration close to this interface. In the case of SHJ, this asymmetry results in carrier accumulation inside the c-Si bulk close to the c-Si/a-Si:H(i) interface, such as the higher the accumulation, the higher the selectivity [Cuevas 2018, Brendel 2016]. Similarly, a change of the c-Si bulk properties, such as a change of its charge-carrier density or charge-carrier type, will affect the local accumulation of carriers at the vicinity of the c-Si/a-Si:H(i) interface, then potentially impacting the selectivity. Consequently, for given SHJ shells, the ρ_c and the selectivity are both expected to depend on the actual properties of c-Si bulk which in turn depend on the injection or the doping carrier type: this forms the rationale of our investigation.

Based on this reflection, we conducted three different studies. First, we investigated the impact of variable illumination (i.e., of different injected carrier densities inside the c-Si bulk) on the ρ_c value for selected n-type shell parts. In this first study, we settled and elucidated the different suspected limitations and physical phenomena which appear during such TLM measurements. Secondly, we compared the impact of the injected carrier density on the ρ_c value with that of the doping density of the c-Si bulk. Finally, based on the results obtained under variable illumination, we studied the possibility of measuring the ρ_c of shell parts deposited on the opposite wafer type, more precisely here p-type shell parts on c-Si(n) wafers. In these three studies, various n- and p-type shell parts featuring different properties were specifically developed to obtain different accumulation conditions at the c-Si/a-Si:H(i) interface. To enforce different accumulation conditions, the doping level of the thin silicon layers, which can be accounted for by their activation energy (E_a) value (see section 3.2.1), was proven to be a relevant parameter. Indeed, as demonstrated in [Procel 2018], a low (respectively high) E_a

was found to allow for a high (respectively low) selectivity, owing to a high (respectively low) accumulation close to the c-Si/a-Si:H(i) interface (for both electron and hole selectivities). Then, these different shell parts were combined with several c-Si wafers featuring different dopings and types.

4.2 Experimental details

4.2.1 TLM samples and case studies

The three studies under investigation are referred to as (a), (b), and (c) and are presented in Figure 4.1. To carry them out, TLM samples were fabricated on various textured c-Si(n) and c-Si(p) wafers featuring different thicknesses and resistivities. For the study (a), TLM samples were fabricated on 245 μm -thick textured c-Si(n) wafers with a resistivity of 2.8 Ωcm (see bottom part of Table 4.1). For the study (b), TLM samples were fabricated on 160 μm -thick textured c-Si(n) wafers with different resistivities of 0.3, 0.4, 1.6, 1.9, 2.8, 5.6 and 11.8 Ωcm ¹. Finally, for the third study (c), TLM samples were fabricated on textured c-Si(n) and c-Si(p) wafers presenting resistivities of about 3.0 and 11.5 Ωcm and thicknesses of 245 and 160 μm , respectively. At the TLM samples rear side a thin blanket a-Si:H(i) layer was deposited. Then, either a stack composed of a p-type a-Si:H film (a-Si:H(p)) completed with an indium tin oxide (ITO) layer or a single silicon nitride (SiNx) layer was afterwards deposited on top of the a-Si:H(i) layer (see Figure 4.1). The thickness of the rear ITO layer measured on planar bare glass substrate was 110 nm and the one of the SiNx was about 120 nm which leads in both cases to an optimal thickness for antireflecting coating on textured wafer. Thus, the combination of either a-Si:H(i)/a-Si:H(p)/ITO or a-Si:H(i)/SiNx stack at the rear side of the TLM samples allows one to reach a good passivation quality together with an optimized ARC, and thus to maximize the injected carrier concentration reached inside the c-Si bulk of the TLM samples for a given illumination. In addition, the presence of either the a-Si:H(p) layer or the a-Si:H(i)/SiNx stack as presented in Figure 4.1 prevents any TLM current to go through the rear layers, hence restricting it to the c-Si bulk.

On the front side of the TLM samples, the shell parts under investigation, featuring thin doped silicon layers with different doping and types, were deposited. For the first study (a), a thin blanket intrinsic a-Si:H (a-Si:H(i)) layer was deposited. Then, different n-type thin silicon multilayers combining a thin bottom amorphous buffer layer and different top nanocrystalline layers (referred to as a-Si:H(n)/nc-Si:H(n)) were deposited on top of the a-Si:H(i) layer, to reach different activation energy E_a (see top part of Table 4.1). The thin bottom buffer a-Si:H(n) layer was kept the same for all multilayers. For the second study (b), different n-type thin silicon layers were deposited on top of an a-Si:H(i) layer, to reach different thicknesses and activation energies (E_a) (see top part of Table 4.2). Finally, for the third study (c), a thin blanket a-Si:H(i) layer was deposited and then completed with three different a-Si:H(p) layers which were processed with three different TMB flows, namely low (50 sccm), medium (75 sccm) and

¹These wafers were provided by Jordi Veirman from CEA-INEA whose contribution is gratefully acknowledged.

high (100 sccm) to obtain three different a-Si:H(p) layer dopings (see top part of Table 4.3). Then, for all three studies, aluminium-doped zinc oxide (AZO) was deposited on the different thin doped silicon layers. This AZO layer features a thickness of 180 nm on glass substrate and a carrier concentration of $1.5 \times 10^{20} \text{ cm}^{-3}$ for the study (a) and of $4.42 \times 10^{19} \text{ cm}^{-3}$ for the two studies (b) and (c). Finally, a 400-nm-thick silver (Ag) blanket layer was sputtered over the whole AZO layer. After this step, the TLM samples were annealed at 210 °C for 30 minutes. Then, TLM patterns featuring a length (L) of 2 mm as well as gaps of 0.5, 1.0, 1.5, 2.0, 2.5, and 3.0 mm for the studies (a) and (b) and gaps of 0.25, 0.50, 0.75, 1.00, 1.25, 1.50 and 2.00 mm for the study (c) were inkjet-printed. The Ag and AZO layers were then etched between the pads, and the ink was removed. After these etching steps, the TLM samples were cut with a selected width (w) of 6 mm to create the mesa isolation. *I-V* measurements were performed on each completed TLM sample in dark conditions and under different illumination intensities, namely, 7%, 13%, 50%, and 100% of equivalent AM1.5G one sun intensity, to reach different injected carrier densities (injected electron and hole densities are equal $\Delta n = \Delta p$) inside the c-Si bulk. Finally, for each illumination, the injected carrier density values were calculated from the sheet resistance (R_{sh}) of the c-Si wafer, taking into account the dependence of the electron mobility on the injection [Klaassen 1992a, Klaassen 1992b]. More details about this calculation are provided in appendix A.2.

The different shells manufactured as presented above and used for these three studies are listed and summarized in Tables 4.1, 4.2 and 4.3. Note that the sheet resistance values of each wafer are given and named $R_{sh \text{ wafer doping}}$ (obtained by dividing the corresponding dark wafer resistivity (ρ_{wafer}) by the thickness).

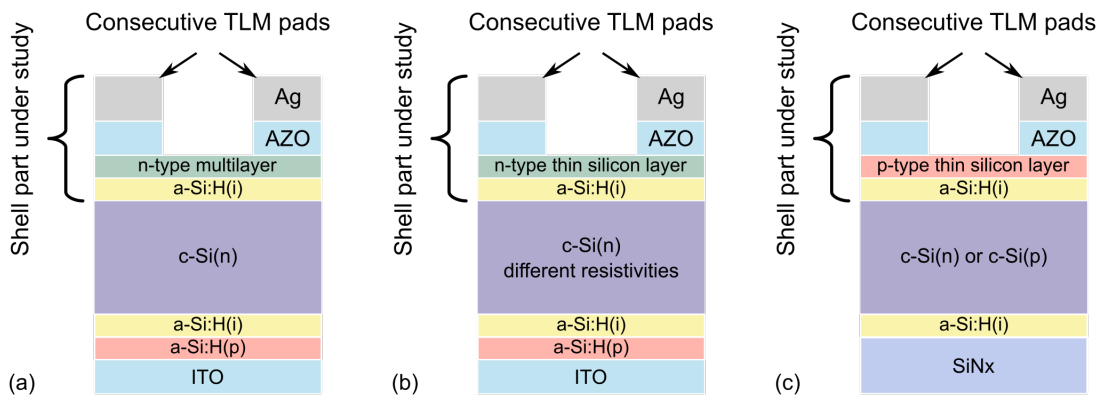


Figure 4.1 – Cross-section of the different experimental samples for the three studies with (a) different *n*-type multilayers and one *c*-Si(*n*) wafer (b) different *n*-type thin silicon layers and different *c*-Si(*n*) wafer dopings and (c) different *p*-type thin silicon layers deposited either on *c*-Si(*n*) or on *c*-Si(*p*) wafers.

Chapter 4. Advanced methods for the electrical characterization of solar cell shells using transfer length method Measurements under variable illumination

	n-type multilayer		
Shell	E_a (meV)	Thickness (nm)	Rear side passivation quality
#1n	265	39	High
#2n	173	34	High
#3n	48	37	High
#4n	17	89	High
#5n	173	34	Low

wafer type	ρ_{wafer} (Ωcm)	R_{sh} wafer doping (Ω/sq)	Thickness (μm)
c-Si(n)	2.83	116	245

Table 4.1 – Study (a) - Top: List of the different shells under study with the activation energy and thickness values of the a-Si:H(n)/nc-Si:H(n) multilayers as well as the quality of the rear side passivation. The rear passivation quality is tuned with the a-Si:H(i)/a-Si:H(p) stack. Bottom: c-Si wafer type, dark wafer resistivity (ρ_{wafer}) with the corresponding R_{sh} wafer doping and thickness.

	n-type thin silicon layer		
Shell	E_a (meV)	Thickness (nm)	Rear side passivation quality
#6n	-	15	High
#7n	-	30	High
#8n	536	15	High
#9n	251	30	High
#10n	69	50	High

wafer type	ρ_{wafer} (Ωcm)	R_{sh} wafer doping (Ω/sq)	Thickness (μm)
c-Si(n)	0.3	19	160
c-Si(n)	0.4	25	160
c-Si(n)	1.6	97	160
c-Si(n)	1.9	120	160
c-Si(n)	2.8	165	160
c-Si(n)	5.6	350	160
c-Si(n)	11.8	700	160

Table 4.2 – Study (b) - Top: List of the different shells under study with the activation energy and thickness values of the n-type thin silicon layers as well as the quality of the rear side passivation. The rear passivation quality is tuned with the a-Si:H(i)/a-Si:H(p) stack. Bottom: c-Si wafer type, dark wafer resistivity (ρ_{wafer}) with the corresponding R_{sh} wafer doping and thickness.

p-type thin silicon layer			
Shell	TMB flow	Thickness (nm)	Rear side passivation quality
#1p	low	19	High
#2p	medium	19	High
#3p	high	19	High

wafer type	ρ_{wafer} (Ωcm)	$R_{\text{sh wafer doping}}$ (Ω/sq)	Thickness (μm)
c-Si(n)	3.44	202	170
c-Si(p)	11.5	718	160

Table 4.3 – Study (c) - Top: List of the different shells under study with the TMB flows and thickness values of the p-type thin silicon layers as well as the quality of the rear side passivation. The rear passivation quality is tuned with the a-Si:H(i)/SiNx stack. Bottom: c-Si wafer type, dark wafer resistivity (ρ_{wafer}) with the corresponding $R_{\text{sh wafer doping}}$ and thickness.

4.2.2 Finite Element Simulations for TLM

To model the TLM structure and to simulate the value of ρ_c as a function of the c-Si bulk-injected carrier density, opto-electrical simulations were performed using TCAD Sentaurus [Sentaurus 2015]. This software numerically solves the drift-diffusion equations and simulates the interface physics (including tunnelling, thermionic emission, recombination, etc.). This allows one to consistently assess the transport mechanisms through the hetero-interfaces of the SHJ shells under study. The simulated TLM structure consists in two identical contact pads on top of a c-Si(n) bulk spaced by variable gaps as used on actual samples (0.5, 1.0, 1.5, 2.0, 2.5 and 3.0 mm). Each contact width is 1.0 mm and the n-type shell part is formed by 6 nm of a-Si:H(i), 30 nm of n-type thin silicon layer and 180 nm of TCO. The c-Si(n) wafer features a bulk resistivity of $3 \Omega\text{cm}$ corresponding to a doping of $1.55 \times 10^{15} \text{cm}^{-3}$. The E_a values of the n-type thin silicon layer were adjusted by a uniform doping concentration in a defective background of doped layers to achieve 17, 48, 173 and 265 meV (hence close to the experimental values presented in the top part of Table 4.2). The TCO was modelled as a degenerate semiconductor [Procel 2018, Klein 2010], thus work-function mismatches and induced band bendings are accurately considered. The TCO carrier concentration (N_{TCO}) was set to $1.44 \times 10^{20} \text{cm}^{-3}$. Further details on the TLM modelling can be found in [Procel 2018, Procel 2019, Procel 2020]. To change the injected carrier density inside the c-Si bulk for a given shell, different injection levels, and thus different electron quasi-Fermi levels (E_{Fn}), are emulated inside the c-Si bulk absorber using different carrier generation rates equivalent to the targeted light intensities. A reference optical generation profile was adjusted based on ray-tracing optical simulations to reach 39mA cm^{-2} , which is the typical current density in solar cells using SHJ shells. This generation profile was fixed to be the 100 % of illumination and accordingly, TLM structures were evaluated in dark, 7, 13, 50 and 100 % illumination by scaling the generation rate. The recombination rate inside the c-Si bulk (τ_{bulk}) was adjusted to reach a Δn of about $4.85 \times 10^{15} \text{cm}^{-3}$ at full illumination (i.e., 100 %). The corresponding energy-band

diagrams for these different illuminations were simulated and analyzed. Using these diagrams, the SCR width (w_{SCR}) inside the c-Si(n) bulk was calculated considering its extent from the first decreasing point of the energy conduction band (E_c) to the c-Si(n)/a-Si:H(i) interface location. The conduction band energy height (E_h) was also calculated considering the energy difference between the flat part of the E_c and the minimum energy at the c-Si(n)/a-Si:H(i) interface. Finally, the electron and hole accumulations were calculated performing the ratio of the electron (resp. hole) density at c-Si(n)/a-Si:H(i) interface to the electron (resp. hole) density inside the bulk. These parameters were calculated for the different illuminations and E_a under study. Then, each TLM structure was simulated to obtain its current-voltage response from -1 to 1 V and the TLM methodology was applied to extract R_{sh} and ρ_c^2 .

4.3 TLM measurement under variable illumination - impact on ρ_c and suspected limitations

4.3.1 Introduction

The first study focuses on the ρ_c behaviour as a function of variable illumination for different n-type thin silicon multilayers deposited on c-Si(n) type wafers as presented and listed in Table 4.1. The shells #1n to #4n feature similar high passivation quality at the rear side but different n-type multilayers at the front side, with thickness varying from 34 to 89 nm and E_a varying from 17 to 265 meV. The shell #5n features the same n-type multilayer than shell #1n but a low rear side passivation quality. The different E_a values are expected to enforce different accumulation conditions at the vicinity of the c-Si/a-Si:H(i) interface, with the aim of targeting different dark initial conditions and thus different dark ρ_c values. Thus, I - V measurements are performed on each completed TLM sample in dark conditions and under different illuminations to reach injected electron density (Δn) up to about $5.96 \times 10^{15} \text{ cm}^{-3}$ at the 100 % of illumination. To complete our experimental results, Technology Computer-Aided Design (TCAD) simulations, presented in section 4.2.2, are used to model the TLM structure and to identify the physical phenomena and the key parameters affecting the ρ_c and the selectivity of several SHJ n-type shell parts. In addition, the different physical phenomena which induce a non-ohmic behaviour of the TLM I - V curves appearing during TLM measurements under variable illumination are elucidated.

4.3.2 Illumination and non-ohmic behaviour

While performing TLM measurements under variable illumination, the first major phenomenon we observed was the presence of a non-ohmic I - V curve behaviour appearing as the illumination increase. This phenomenon was first suspected to be an issue as it does not fulfill the fundamental hypothesis of ohmic behaviour required for TLM computation. However,

²All TCAD simulations were performed by Paul Procel from TUDelft University whose contribution is gratefully acknowledged.

4.3. TLM measurement under variable illumination - impact on ρ_c and suspected limitations

based on TCAD simulations and experimental measurements, we demonstrate below that this hypothesis is actually not broken as the non-ohmic behaviour of I - V curves is revealed to be induced by the c-Si bulk properties and not by the shell part under investigation.

Simulation of non-ohmic behaviour

Figure 4.2a shows the simulated I - V curves obtained between two TLM pads as a function of the illumination for a shell with τ_{bulk} of 0.4 ms. It is observed that a non-ohmic behaviour appears above a certain illumination threshold, here 13 %. This non-ohmic behaviour becomes stronger as the illumination increases and is independent of the different E_a under study. Additionally, Figure 4.2b plots the simulated I - V curves between two TLM pads under 13 % illumination for different τ_{bulk} . In this case, it is observed that the non-ohmic behaviour becomes increasingly noticeable upon increasing τ_{bulk} , again regardless of the E_a value. In both cases presented in Figure 4.2a and Figure 4.2b, increasing the illumination or the τ_{bulk} results in an increase of the generated carrier concentration inside the c-Si bulk. Thus, the trigger for the non-ohmic behaviour is revealed to be the number of injected carriers inside the c-Si(n) bulk, rather than the illumination level or the recombination mechanisms alone. The experimental evidences as well as the physical origin of the non-ohmic behaviour and a method to accurately extract the value of ρ_c in these conditions are presented below³.

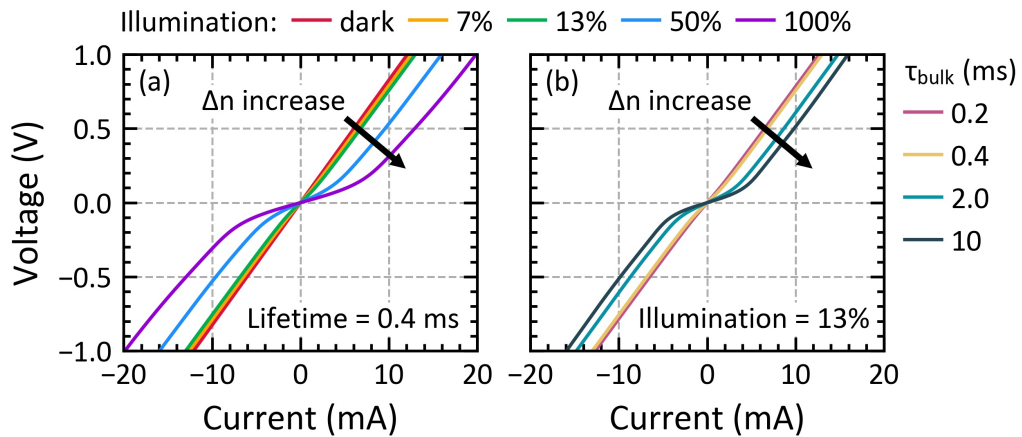


Figure 4.2 – Simulated I - V curves between two TLM pads (a) for different illuminations with a τ_{bulk} fixed at 0.4 ms and (b) for different bulk lifetimes with an illumination fixed at 13 %.

³These simulations were performed by Paul Procel from TUDelft University whose contribution is gratefully acknowledged.

Experimental evidences of non-ohmic behaviour

Figure 4.3a plots the I - V curves experimentally measured for the shell #2n, featuring an n-type multilayer with $E_a = 173$ meV and high rear side passivation quality, under different illuminations and between two consecutive TLM pads spaced by 2.5 mm. The major observation here is the excellent agreement between the simulations presented in Figure 4.2 and the experimental results: The non-ohmic behaviour gets stronger with higher illumination and thus with higher Δn . The Δn corresponding to the different illumination conditions are given in Table 4.4. Markedly, the non-ohmic behaviour appears above a certain injected carrier density threshold, which is here $2.2 \times 10^{15} \text{ cm}^{-3}$ for an illumination of 50%. In addition, as observed in simulations, the non-ohmic behaviour is present for all shells with high passivation quality under study here (shells #1n to #4n), as listed in Table 4.1. It appears at a similar illumination intensity threshold with similar Δn values (data not shown), confirming that these shells feature similar passivation quality. Furthermore, the onset of the non-ohmic behaviour is experimentally shown to depend on the passivation quality of the shell under study. This is illustrated in Figure 4.3b, which plots the TLM I - V curves under illumination of shell #5n, featuring the same n-type multilayer as shell #2n (with E_a of 173 meV) but presenting a low rear side passivation. Although the TLM I - V curves of shell #2n become non-ohmic as the illumination increases, the curves of shell #5n stay ohmic for all illuminations. This is due to the different passivation qualities and hence to the different injected carrier densities actually reached inside the c-Si(n) bulk for a given illumination. The injected electron density induced by the illumination for both shells is listed in Table 4.4. Thus, it is experimentally validated that the injected electron density inside the c-Si(n) drives the non-ohmic behaviour of TLM samples. This non-ohmic behavior is therefore proven not to stem from an effect of the shell properties but from the c-Si bulk properties.

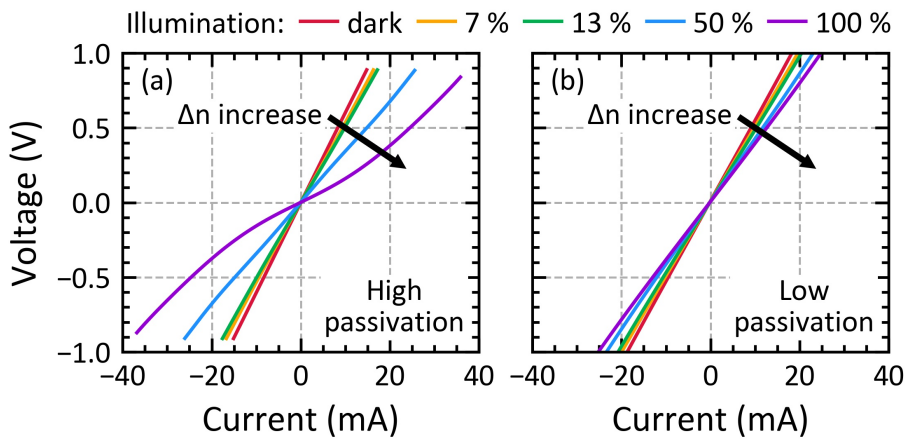


Figure 4.3 – I - V curves as a function of the illumination (for a TLM gap of 2.5 mm) of shells (a) #2n and (b) #5n, featuring the same n-type multilayer with $E_a = 173$ meV, but with a high and a low rear side passivation quality, respectively.

4.3. TLM measurement under variable illumination - impact on ρ_c and suspected limitations

Illumination	Δn (cm ⁻³)	
	Shell #2n	Shell #5n
Dark	0	0
7%	3.14×10^{14}	1.30×10^{14}
13%	4.85×10^{14}	2.22×10^{14}
50%	2.23×10^{15}	5.31×10^{14}
100%	6.55×10^{15}	7.84×10^{14}

Table 4.4 – Injected electron density (Δn) as a function of the illumination for the shells #2n and #5n, featuring an n-type multilayer with $E_a = 173$ meV, but with a high and a low rear side passivation quality, respectively.

Simple explanation for the non-ohmicity

Here, the appearance of the non-ohmic regime is demonstrated to be due to a drift of the free carriers induced by the voltage applied between two consecutive TLM pads, leading to a non-homogeneous carrier density and thus a variation of the wafer R_{sh} below the TLM pads and the gap in-between. Indeed, it is demonstrated by simulation, for the case of a c-Si(n) wafer, and presented in Figure 4.4a and Figure 4.4b (top sketches) that for zero TLM bias ($\Delta U = 0V$) the generated carriers are homogeneously distributed inside the bulk (Figure 4.4a), but as soon as a non-zero TLM bias is applied, here simulated for one volt ($\Delta U = 1V$), a drift of the generated carriers arises, leading to an inhomogeneous carrier density inside the bulk and below both TLM pads (Figure 4.4b). A simplified case study to illustrate the impact of this effect is presented in Figure 4.4c and Figure 4.4d (bottom sketches) for the case of a c-Si(n) wafer. Under illumination and at $\Delta U = 0V$ (no TLM voltage bias), the generated electrons (and holes) are homogeneously distributed inside the c-Si(n) bulk along the distance L , and their density equals $n_0 + \Delta n$, with n_0 the bulk doping density, everywhere within the sample bulk⁴. Under a TLM applied bias $\Delta U = \alpha V$ (with $\alpha > 0$), the electrons drift because of the applied external field. We now assume these electrons to be distributed following a simple non-homogeneous distribution: in the sample region $0 < x < L/2$, the electron density is now n_0 , whereas in the region $L/2 < x < L$, the electron density is $n_0 + 2\Delta n$. Note that the total number of electrons (and hence holes) is chosen to be constant inside the whole volume of the sample in both the 0V and the αV cases. This is equivalent to assuming the same total recombination rate in both cases. Computing now the equivalent resistance of the sample bulk seen by the electrons in the 0V and the αV cases (R_{0V} and $R_{\alpha V}$, respectively), it turns out that $R_{0V} < R_{\alpha V}$ (see the appendix A.1 for the full calculation details). In other words, the wafer resistance depends on the applied bias ΔU , i.e. $R = R(\Delta U)$. Hence, the higher the TLM applied bias, the higher the total resistance seen by the TLM current between two TLM pads (as $R_{\alpha V}$ gets consistently larger values compared to R_{0V}). This explains the non-ohmic shape of the I - V curve obtained between two TLM pads measured under illumination. At low voltages,

⁴These simulation were performed by Paul Procel from TUDelft University whose contribution is gratefully acknowledged.

Chapter 4. Advanced methods for the electrical characterization of solar cell shells using transfer length method Measurements under variable illumination

however, a linear I - V regime is still present because the drift of charges is small. But as soon as the voltage increases, the non-ohmic I - V behaviour appears, then stabilises at high voltages to a second linear I - V regime. This stabilisation is due to the presence of a maximal drift of carriers, such that the carriers are all completely depleted through the whole silicon bulk. In addition, this second linear regime features a higher slope (i.e., a higher resistance) than the first linear one, evidencing the increase of the c-Si global resistance with the voltage increase (see Figure 4.3a). Importantly, in any case where the TLM bias induces a non-negligible drift of carriers, two different injection conditions are present below the two TLM pads, which then makes it impossible to perform the TLM computation. Thus, to stay in a near-uniform injection throughout the wafer, we chose to perform the TLM computation taking the slope in the first linear regime of the I - V curves (symmetrically around the origin). Illustrative examples of such linear ranges are given in Figure 4.5 in the case of shell #2n.

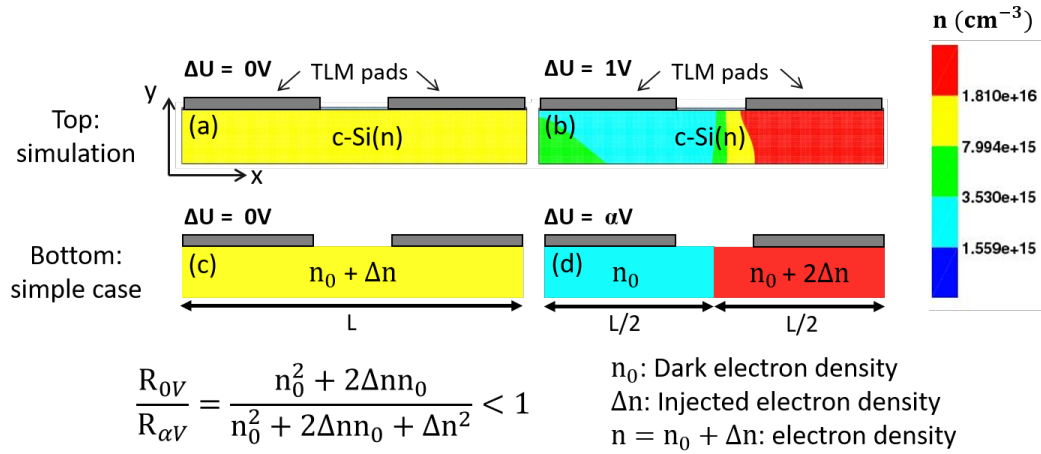


Figure 4.4 – Top: electron density for 1 sun illuminated TLM sample, under (a) 0 and (b) 1 V TLM voltage; Bottom: simplified case study at (c) 0V with the total number of electrons homogeneously distributed inside the c-Si bulk along the distance L , and (d) at αV , a particular non-homogeneous distribution.

4.3. TLM measurement under variable illumination - impact on ρ_c and suspected limitations

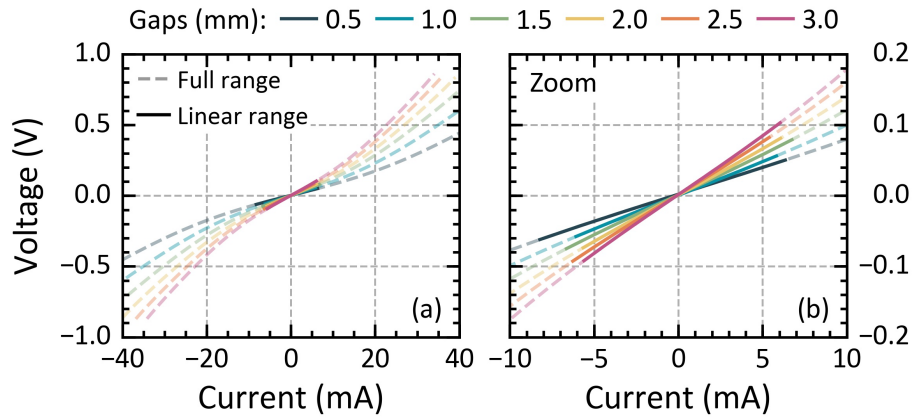


Figure 4.5 – I-V curves of shell #2n showing the linear ranges where TLM computation is performed with 100% illumination and for the different gaps. (a) Full I-V range and (b) zoom on the linear range.

Experimental evidences of the drift of carriers

This drift of charge carriers was observed experimentally on actual TLM samples using PL measurement at different applied bias. Figure 4.6 shows PL images obtained between two TLM pads at different TLM bias from 0 to 5 V. On the bottom right corner of Figure 4.6 a schematic description illustrating the position of both TLM pads on each image as well as the sign of the voltage is given. It is clearly observed that the higher the TLM bias, the higher the carriers drift toward the positively-polarised TLM pad. Here, a significant drift of carriers is present for 3 and 5 V whereas the drift stays small between 0.01 to 0.05 V.

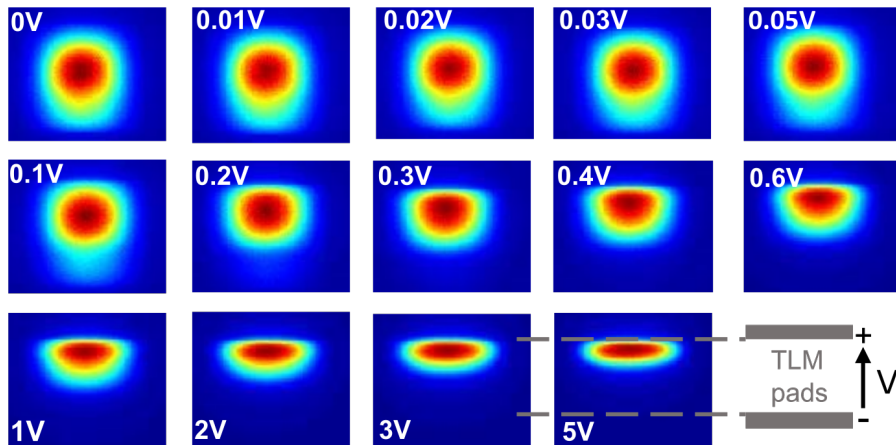


Figure 4.6 – PL images between two TLM pads at different applied bias from 0V to 5V. As the PL scale is different for each voltage, it is not displayed on this Figure. However, the brighter the signal, i.e., the more reddish, the higher the carrier concentration and thus the radiative recombination (see section 3.2.2).

4.3.3 Illumination and its impact on ρ_c : simulation and experiment

Finite Element Simulations for TLM measurements

Figures 4.7-4.10 show the impact of changing the E_a of the n-type thin silicon layer (17, 48, 173 and 265 meV) and of varying the illumination on the conduction band energy in the space domain (Figure 4.7), on the two band parameters w_{SCR} and E_h (Figure 4.8), the electron and hole accumulations (Figure 4.9), and on the ratio of electrons to holes at the c-Si(n)/a-Si:H(i) interface (Figure 4.10). First, it is observed that as expected, in the dark, the electron accumulation is more pronounced for low E_a than for high E_a . Upon increasing E_a from 17 meV to 265 meV, w_{SCR} decreases from 820 to 725 nm and E_h decreases from 0.22 to 0.13 eV (see Figure 4.8), resulting in an electron accumulation decreasing from 2.91×10^3 to 8.86×10^1 (see Figure 4.9a). In contrast, the hole accumulation is found to be higher for high E_a than for low E_a , increasing from 3.25×10^{-4} to 1.13×10^{-2} (see Figure 4.9b). Finally, looking at the ratio of electrons to holes at the c-Si(n)/a-Si:H(i) interface, it is observed that it is higher for lower E_a (see Figure 4.10). Overall, this highlights that a higher electron accumulation and thus a higher electron selectivity in the dark is obtained for lower E_a , as discussed in section 4.1. Then, looking at the different illuminations, we observe that for each E_a considered here, the conduction band and the quasi-Fermi level are getting closer, resulting in an electron density increase (see Figure 4.7) and affecting the band parameters: indeed, E_h and w_{SCR} decrease upon increasing illumination (see Figure 4.8). This will directly affect the electron accumulation, which is indeed found to decrease as the illumination increases (Figure 4.9a). In addition, by increasing the illumination, the hole density increases as well, impacting the hole accumulation, which is found to increase upon illumination for all different E_a under investigation (see Figure 4.9b). In particular, the ratio of electrons to holes at the c-Si(n)/a-Si:H(i) interface decreases as the illumination increases, demonstrating that the electron selectivity is therefore impacted by illumination such that the higher the illumination, the lower the electron selectivity (Figure 4.10). Overall, Figures 4.7-4.9 show that the decrease in the value of these parameters is independent of E_a but is only dependent on the illumination. In addition, when the illumination varies, the electron (resp. the hole) accumulation for low E_a stays always higher (resp. lower) than for high E_a .

4.3. TLM measurement under variable illumination - impact on ρ_c and suspected limitations

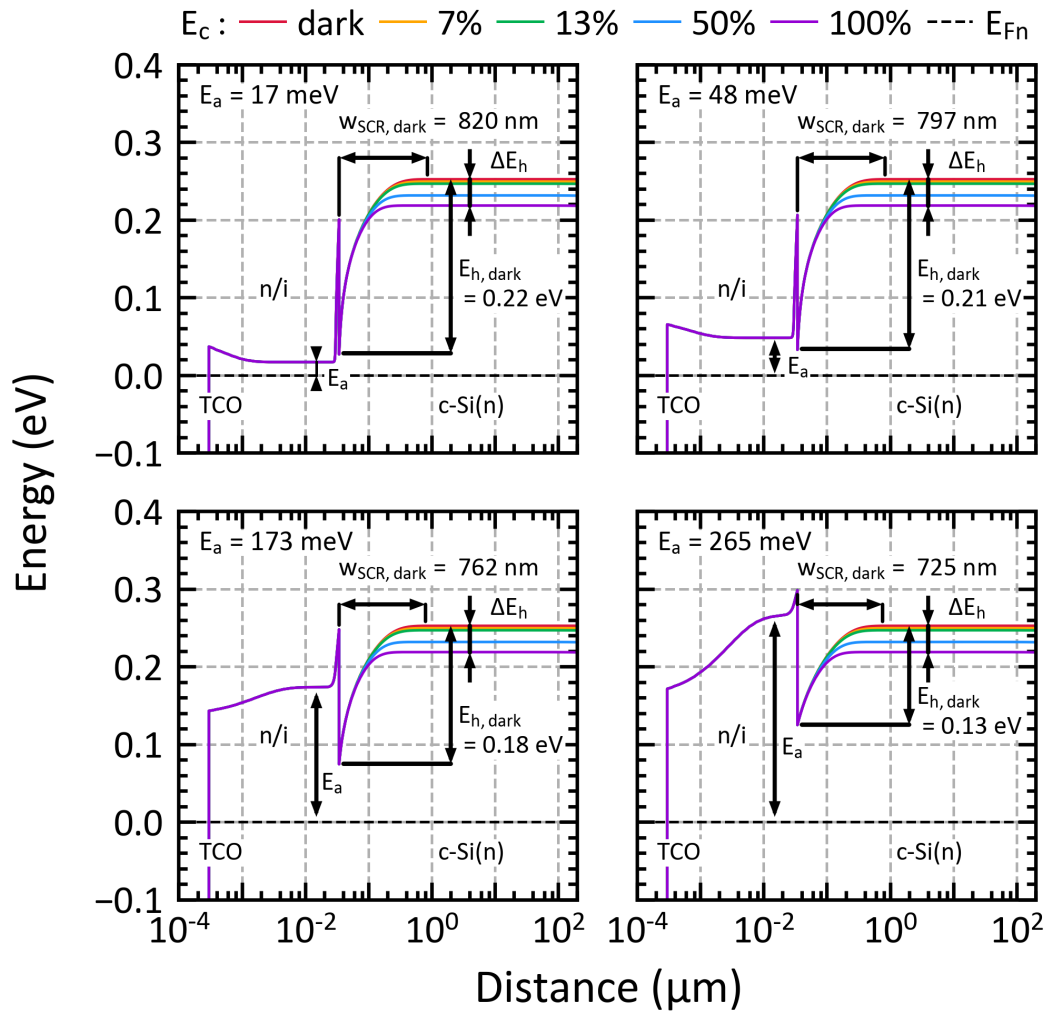


Figure 4.7 – Energy-band diagrams illustrating the different E_c as a function of the illumination for the different n-type thin silicon layers featuring E_a of 17, 48, 173 and 265 meV. The w_{SCR} and the E_h in dark conditions, as well as the difference of E_h between dark and 100% illumination (ΔE_h) are depicted.

Chapter 4. Advanced methods for the electrical characterization of solar cell shells using transfer length method Measurements under variable illumination

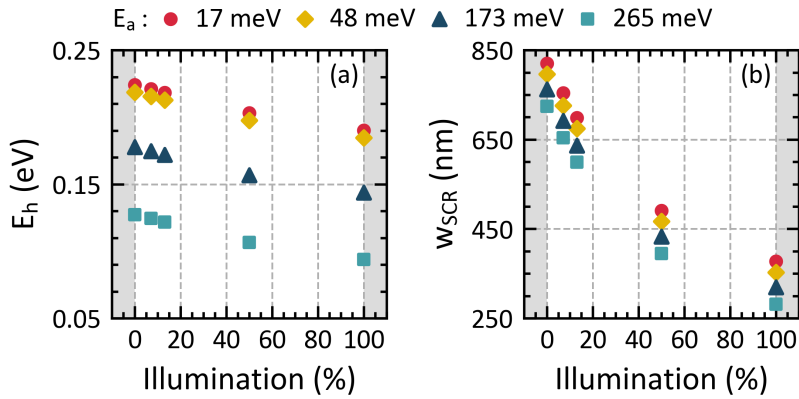


Figure 4.8 – E_h (a) and w_{SCR} (b) as a function of the illumination for the different E_a .

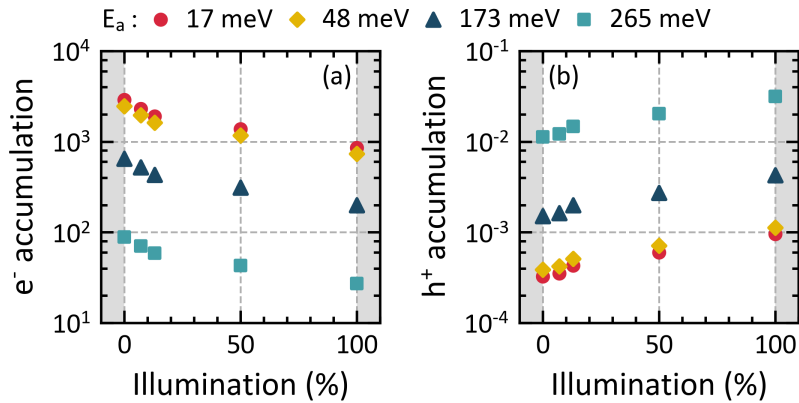


Figure 4.9 – (a) Electron and (b) hole accumulations as a function of the illumination for the different E_a .

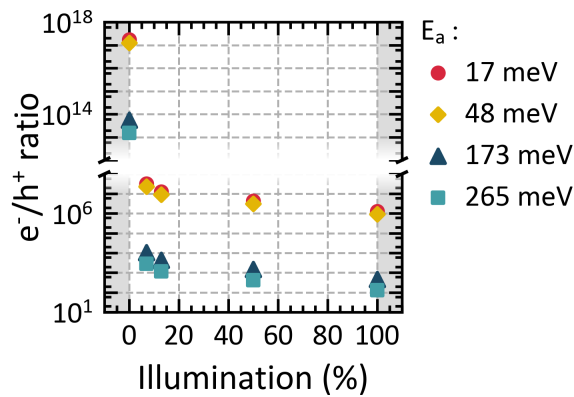


Figure 4.10 – Ratio of electron to hole at $c\text{-Si}(n)/a\text{-Si:H}(i)$ interface as a function of the illumination for the different E_a .

4.3. TLM measurement under variable illumination - impact on ρ_c and suspected limitations

Figures 4.11a-d show the R_{sh} and ρ_c values extracted from TLM simulations for the different E_a and the various illuminations. Figure 4.11a shows that, as expected, the R_{sh} decreases with increasing illumination; this behaviour directly owes to an increase of the electron density (n) under higher illumination, which is found to be similar for the four different E_a as the passivation quality is similar for the different shells under study. In contrast, Figure 4.11b shows that ρ_c drastically increases with the illumination for all the investigated E_a . It is observed that the higher the E_a , the higher the increase of ρ_c with illumination. Figure 4.11c shows ρ_c as a function of R_{sh} . Starting from the R_{sh} value in the dark (hence the bottom right points in the graph), it is observed that for all E_a , ρ_c increases linearly as the R_{sh} decreases, but with different slopes. These slopes correspond to the response of the n-type shell parts to the illumination; in other words, the higher the slope, the higher the impact of the illumination, and thus of the injected carrier density on the contact resistivity. The slopes extracted from the $\rho_c = f(R_{sh})$ linear curves are plotted in Figure 4.11d. Here, we observe that the higher the E_a , the higher the slope of the $\rho_c = f(R_{sh})$ curve and thus the higher the impact of the illumination on the shell under study. This may suggest that a higher electron accumulation, and thus a higher electron selectivity in the dark, will result in a lower slope and thus in a lower impact of the illumination on the shell properties. However, it is actually found that the absolute values of ρ_c are not directly related to the carrier accumulation variation upon illumination. Indeed, first of all, the variation of the electron and the hole accumulations in the dark with the increase of E_a is significant: from 2.91×10^3 to 8.86×10^1 for electrons and from 3.25×10^{-4} to 1.13×10^{-2} for holes, whereas the ρ_c variation remains relatively small, namely from 1.06×10^{-2} to $1.63 \times 10^{-2} \Omega \text{cm}^2$. Conversely, the electron and the hole accumulation variations with the illumination increase are significantly smaller: from 2.91×10^3 to 8.59×10^2 for electrons and from 3.25×10^{-4} to 9.61×10^{-4} for holes. However, in that case, the ρ_c variation is much larger, from 1.06×10^{-2} to $1.77 \times 10^{-1} \Omega \text{cm}^2$ (for the case of $E_a = 17 \text{ meV}$). In other words, as prime example, the ρ_c value at 100 % of illumination of shell #4n featuring an E_a of 17 meV is higher than the ρ_c value in the dark of shell #1n featuring an E_a of 265 meV, despite a higher electron and lower hole accumulation⁵.

An additional outcome of these results is that, considering a Δn of about $2.0 \times 10^{15} \text{ cm}^{-3}$ at MPP [Lachenal 2019] and thus a R_{sh} of about $50 \Omega/\text{sq}$, the difference between the ρ_c value calculated in dark conditions (corresponding to $R_{sh} \sim 110 \Omega/\text{sq}$) and at MPP is between 0.11 to $0.14 \Omega \text{cm}^2$ for the four different E_a , as presented in Figure 4.11c. Hence, considering that a $1 \Omega \text{cm}^2 R_s$ induces a FF loss of $\sim 5 \%$ abs [Pysch 2007], the difference between the induced FF loss calculated at MPP illumination and the one in the dark is between 0.55% abs to 0.70% abs. It is therefore important to measure the ρ_c at MPP condition to study accurately the actual impact of a shell on the transport losses and thus on the corresponding effect on FF of solar cells.

⁵These TCAD simulation were performed by Paul Procel from TUDelft University whose contribution is gratefully acknowledged.

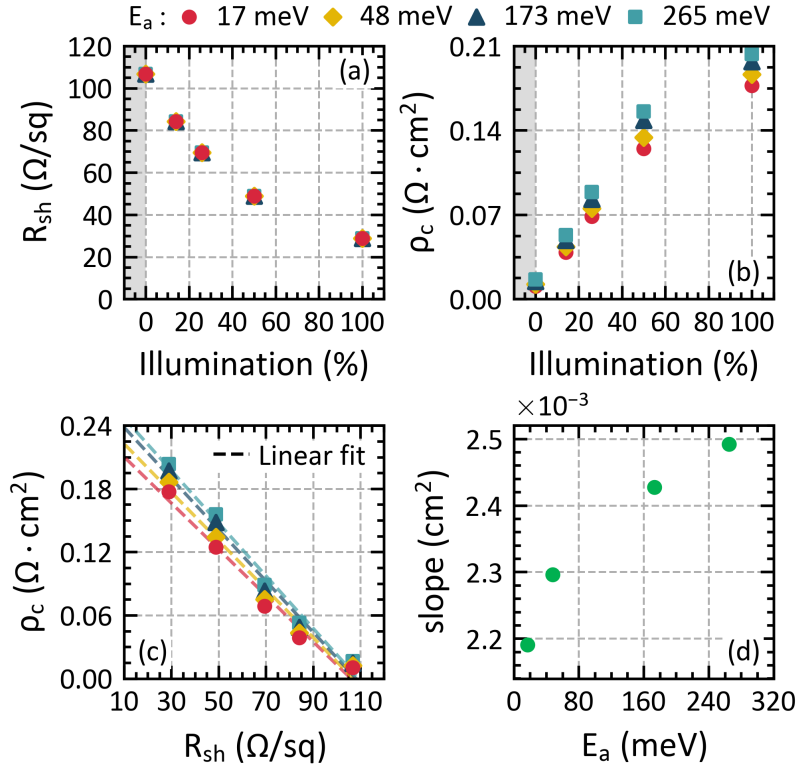


Figure 4.11 – Simulated (a) R_{sh} and (b) ρ_c as a function of the illumination and (c) simulated ρ_c as a function of the R_{sh} with the corresponding linear fits, for the different n-type thin silicon layer with activation energy from 17 to 265 meV and (d) the corresponding slopes from the simulated linear dependences of $\rho_c = f(R_{sh})$ as a function of the activation energy.

Experimental evidences

Figures 4.12a-c plot the TLM parameters obtained from our experimental measurements and for the shells #1n to #4n featuring different E_a (17, 48, 173 and 265 meV, respectively). Figure 4.12a shows that, consistently with our simulations, the R_{sh} decreases with increasing illumination for the different E_a . In addition, it is observed that for the different illuminations the R_{sh} present similar values for each E_a , hence revealing similar passivation quality for the different shells under study. The injection conditions corresponding to the different illuminations are listed in Table 4.5. Figure 4.12b shows first that the values of ρ_c in the dark stand between 0.02 to 0.10 Ωcm^2 , which is in line with the typical values reported in literature for n-type shell parts characterized on c-Si(n) wafers [Procel 2020, Luderer 2020]. Secondly, it is observed that the ρ_c drastically increases with the illumination for all the investigated E_a . In particular, it is observed that as the illumination increases, the distribution of ρ_c for the different E_a stays the same but the difference in the values of ρ_c between the different E_a becomes more pronounced. Figure 4.12c plots the ρ_c as a function of the R_{sh} experimentally obtained for the four different shells along with the linear $\rho_c = f(R_{sh})$ fitting curves. Remark-

4.3. TLM measurement under variable illumination - impact on ρ_c and suspected limitations

ably, our experimental results are consistent with those obtained from numerical simulations (see section 4.3.3). Indeed, the ρ_c value is found to increase linearly with the R_{sh} decrease and the $\rho_c = f(R_{sh})$ fitting curves present different slopes for the different shells. The values of the slopes are presented in Figure 4.12d. Looking at the three E_a values of 17, 48 and 173 meV, it is observed that the higher the E_a , the higher the $\rho_c = f(R_{sh})$ curve slope as predicted by simulation. Generalizing the rationale explained in sections 4.1 and 4.3.3, we can therefore assume that the shell featuring E_a of 17 meV is the least sensitive to illumination thanks to a high dark electron accumulation and that the shell featuring E_a of 173 meV presents the highest illumination sensitivity because of a lower dark electron accumulation.

From these considerations, it is also important to discuss the drop of the slope for E_a of 265 meV. This drop suggests that despite a higher E_a , its illumination impact is lower than the shell featuring the E_a of 173 meV. This highlights the fact that, as already well known, E_a is not the only parameter ruling the accumulation and the illumination response in SHJ solar cells. Other key parameters, especially defect density, are involved and must be considered [Varache 2012, Schulze 2010].

In addition, it is observed that the shells with E_a of 265 and 48 meV feature similar ρ_c in the dark (0.05 and $0.04 \Omega \text{cm}^2$, resp.) but different slopes of 2.4×10^{-3} and $1.8 \times 10^{-3} \text{cm}^2$, respectively. This result highlights the relevance of our approach: in addition to compare shells based on their resistive losses, it is possible to compare their response to the illumination. A second major observation is that for all E_a under study, the ρ_c value obtained under MPP conditions (here for $\Delta n = 2.07 \times 10^{15}$ and R_{sh} of $54 \Omega/\text{sq}$) is between 0.07 to $0.17 \Omega \text{cm}^2$ higher than under dark conditions. Hence, the difference between the induced FF loss calculated at an illumination corresponding to around MPP and the one in the dark is between 0.35 to 0.85% abs [Psych 2007]. Thus, to design efficient n-type shell parts, a small dark contact resistivity and/or the smallest $\rho_c = f(R_{sh})$ curve slope must be targeted, so that the shell is as little as possible sensitive to illumination. This again pinpoints the pertinence of our method to assess the quality of the carrier transport under the conditions experienced in the field by solar cells, where injected carriers play an important role.

Chapter 4. Advanced methods for the electrical characterization of solar cell shells using transfer length method Measurements under variable illumination

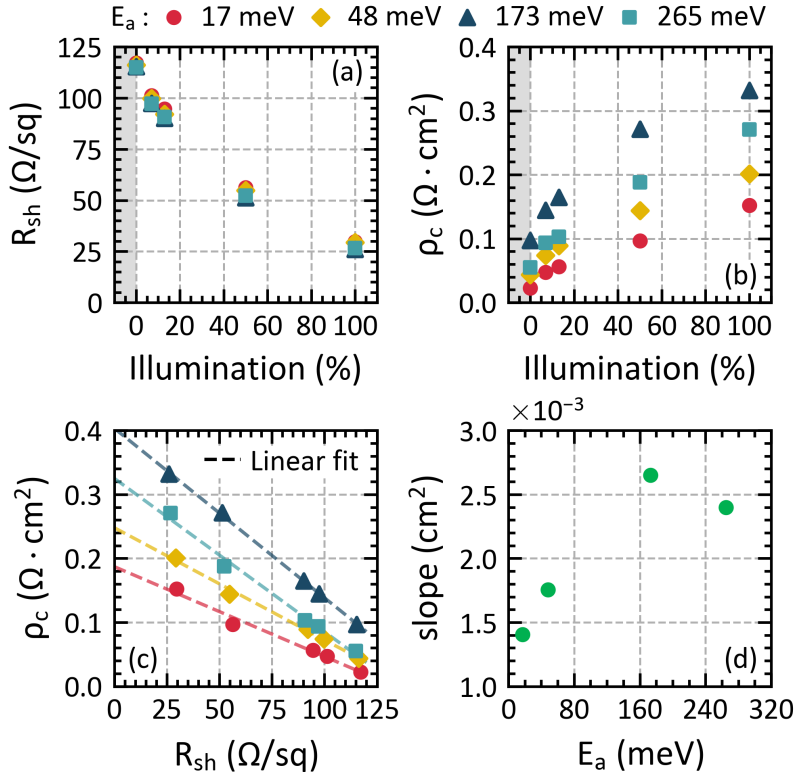


Figure 4.12 – (a) R_{sh} and (b) ρ_c as a function of the illumination and (c) ρ_c as a function of the R_{sh} with the corresponding linear fits, for the different n -type thin silicon layer with activation energy from 17 to 265 meV and (d) the corresponding slopes from the simulated linear dependences of $\rho_c = f(R_{sh})$ as a function of the activation energy.

Illumination	R_{sh} (Ω/sq)	n (cm^{-3})	Δn (cm^{-3})
Dark	116	1.64×10^{15}	0
7%	99	1.94×10^{15}	2.96×10^{14}
13%	92	2.09×10^{15}	4.55×10^{14}
50%	54	3.71×10^{15}	2.07×10^{15}
100%	28	7.60×10^{15}	5.96×10^{15}

Table 4.5 – Average experimental values of R_{sh} , n and Δn of the different shells under study.

4.3.4 Edge recombination and its impact on contact resistivity measurement

As described in section 3.2.1, the TLM samples under investigation have cut edges to create current isolation. Their edges are consequently unpassivated and important recombination losses occur there. Under illumination, this induces a non-homogeneous excess carrier concentration from the middle of the TLM pad width (w) to its edges, and thus leads to a

4.3. TLM measurement under variable illumination - impact on ρ_c and suspected limitations

corresponding c-Si(n) wafer resistivity variation. The latter is expected to be lower at the centre of the pads than at the edges. Consequently, the R_{sh} of the c-Si(n) TLM conductive layer is non-homogeneous and varies along the w direction. This again breaks one of the fundamental hypotheses of TLM which assumes homogeneous R_{sh} to ensure an evenly distributed current flow between two pads. A priori, there is no simple way to rigorously extract the contact resistivity in such cases. However, it is possible to evaluate its impact on the ρ_c value extracted with the standard TLM approach. To do this, the one-dimensional drift-diffusion solver PC1D [Clugston 1997] was used to simulate an inhomogeneous excess carrier concentration profile inside a 1D structure, making it possible to consider one direction corresponding to the direction parallel to w in real samples. The material of the 1D structure is defined as a c-Si(n) bulk with a doping of $1.7 \times 10^{15} \text{ cm}^{-3}$, which is close to the value measured on experimental samples. Its length was set to 6 mm corresponding to the width of actual TLM samples. The interface recombination velocities for electron (S_n) and holes (S_p) at both edges were assumed to be equal to $S_n = S_p = 1 \times 10^7 \text{ cm s}^{-1}$, which corresponds to the highest thermal velocity of carrier transport and is large enough to consider that all excess carriers have recombined at the edges. The simulated 1D structure used is depicted in Figure 4.13 and compared to an actual TLM sample. To simulate the different illuminations under study, several generation profiles were defined. Each of them is established to be homogeneous for each position inside the simulated structure in order to reproduce the experimental generation of TLM samples. As TLM samples are illuminated from the back side, the generation is homogeneous along the w direction. The 1 sun generation profile was set to an average constant generation of $9.68 \times 10^{18} \text{ cm}^{-3} \text{ s}^{-1}$. This generation corresponds to the typical value presents inside SHJ solar cells using similar thin silicon layers, TCO and bulk thickness as the actual TLM samples. Finally, the carrier lifetimes defined experimentally by bulk and shell passivation quality are simulated in PC1D using the single Shockley-Read-Hall lifetime parameters (τ_{SRH}). Thus, by solving the drift-diffusion equation for this 1D test structure with PC1D, it is possible to simulate the electron density profile ($n(x)$) along the 1D direction. This profile is expected to be representative of what can be observed in an experimental TLM structure, along the pad width direction, assuming negligible transport in the other directions. Thus, considering a TLM c-Si(n) bulk of thickness t , it is possible to calculate the corresponding electron sheet resistance profile ($R_{sh}(x)$) for any x_i position below the TLM pad using the equations 4.1 and 4.2 which link the electron conductivity (σ_n) to the sheet resistance, with q equal to the elementary charge and considering an electron mobility (μ_n) of $1330 \text{ cm}^2 \text{ V}^{-1} \text{ s}^{-1}$ (assuming that the photogenerated carriers have little impact on mobility in the range under study) [Klaassen 1992a, Klaassen 1992b].

$$\sigma_n(x_i) = q \cdot \mu_n \cdot n(x_i) \quad (4.1)$$

$$R_{sh}(x_i) = \frac{1}{\sigma_n(x_i)} \cdot \frac{1}{t} \quad (4.2)$$

Chapter 4. Advanced methods for the electrical characterization of solar cell shells using transfer length method Measurements under variable illumination

Here x_i stands for the i -th position of the simulation domain mesh. From the $R_{sh}(x)$ profiles it is then possible to calculate an average value of equivalent R_{sh} ($R_{sh\text{ eq.}}$) with equation 4.3, which is approximated by considering the conduction of parallel resistances between two TLM pads. This approach thus neglects the lateral transport effects in the wafer along the TLM width direction, as was done in [Guo 2017] for evaluating the impact of silver line resistance on TLM structures, where it was shown to have very little impact.

$$R_{sh\text{ eq.}} = \frac{1}{\sum \left(\frac{\Delta x_i}{R_{sh}(x_i)} \right)} \cdot \sum x_i \quad (4.3)$$

Under injection, $R_{sh}(x)$ is experimentally driven by the bulk and the surface recombination of the actual TLM samples. In the simulation, all recombinations are lumped into one τ_{SRH} term, which is then adjusted such that for each illumination the value of $R_{sh\text{ eq.}}$ (obtained from the PC1D simulations) matches the average value of R_{sh} (obtained from experimental measurements). Then, the contact resistivity profile ($\rho_c(x)$), induced by the $R_{sh}(x)$ profile present below the TLM pad width, can be calculated considering the dependence between ρ_c and the illuminated R_{sh} as presented in sections 4.3.3 and 4.3.3. Thus, from $\rho_c(x)$, the transfer length profile ($L_T(x)$) and contact resistance profile ($R_c(x)$) present below a pad are obtained using the TLM equations (equations 4.4 and 4.5), with $L = 2\text{ mm}$ the TLM pad length.

$$L_T(x_i) = \sqrt{\frac{\rho_c(x_i)}{R_{sh}(x_i)}} \quad (4.4)$$

$$R_c(x_i) = \frac{\rho_c(x_i)}{\Delta x_i \cdot L_T(x_i)} \cdot \coth\left(\frac{L}{L_T(x_i)}\right) \quad (4.5)$$

Then, knowing R_c and R_{sh} for all position x_i on the x -mesh, and considering all the resistance in parallel (i.e. neglecting here again lateral transport along the TLM width direction), the total TLM resistance (R_{TLMk}) for each interpad distance k is computed using equations 4.6 and 4.7.

$$\frac{1}{R_{TLMk}(x_i)} = \frac{1}{2 \cdot R_c(x_i) + R_{sh}(x_i) \cdot \frac{gap_k}{\Delta x_i}} \quad (4.6)$$

$$R_{TLMk} = \sum \left(\frac{1}{R_{TLMk}(x_i)} \right)^{-1} \quad (4.7)$$

Finally, the values of $R_{sh\text{ eq.}}$, R_c , L_T , and in turn ρ_c , can be evaluated from the distribution of R_{TLMk} as a function of the interpad distance k . These parameters (obtained here considering an inhomogeneous profile for $R_{sh}(x)$) are then compared to the experimental results using

4.3. TLM measurement under variable illumination - impact on ρ_c and suspected limitations

the standard TLM computation, which assumes R_{sh} to be homogeneous, i.e., which neglects the inhomogeneities due to edge recombination.

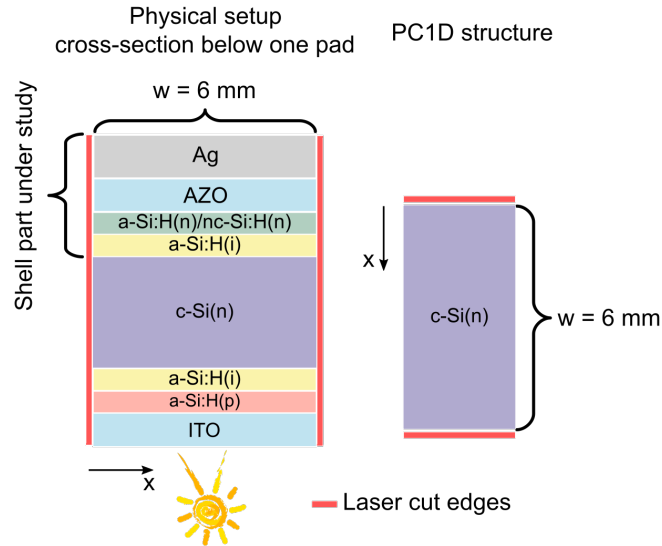


Figure 4.13 – Schematic description of the PC1D structure for simulating the recombination effects at the TLM samples edges.

Figure 4.14 plots the simulated $R_{sh}(x)$ profiles present below the TLM pad for the different illuminations. These profiles are defined such that the $R_{sh\ eq.}$ obtained with equation 4.3 matches the corresponding experimental value of R_{sh} obtained for the case of $E_a = 265$ meV (shell #1n) presented in Table 4.5. It is observed that $R_{sh}(x)$ is significantly affected by edge recombination: a strong increase at the TLM pad edges is clearly visible. This is due to a strong decrease of the excess carrier concentration from the middle of the pad to its edges induced by the edge recombination. Then, the contact resistivity profile ($\rho_c(x)$) was calculated considering the experimental dependence between ρ_c and the illuminated R_{sh} presented in section 4.3.3. For each $R_{sh}(x)$ profile, the $\rho_c(x)$ profile is calculated for the case of $E_a = 256$ meV using the experimental dependence presented in Figure 4.12c and is plotted in Figure 4.14b. Based on the experimental evidences of section 4.3.3, it is observed that the higher the R_{sh} , the lower the ρ_c . Thus, a significantly lower value of ρ_c is observed at the edges compared to the middle of the pad. Then, using equations 4.4 to 4.7, TLM computations are performed, with $R_{TLM\ k}$ depending on the interpad distance of gap k. The output values of ρ_c are presented in Table 4.6 and compared to the experimental ones. It is observed that both experimental and computed values are close: their difference spans from -5.8% to 3.3% . This difference is representative of the global errors calculated for all the n-type multilayers under study which were found to be between $\pm 5.8\%$. This demonstrates that the final values of ρ_c obtained considering the spatial distribution of $R_{sh}(x)$ are in very good agreement with the ones extracted experimentally with the standard TLM computation, which considers a homogeneous R_{sh} . In addition, note that PC1D simulations neglect the conduction of free

Chapter 4. Advanced methods for the electrical characterization of solar cell shells using transfer length method Measurements under variable illumination

carriers inside the thin silicon/TCO stacks which were recently demonstrated to provide efficient lateral transport when combined with the c-Si(n) bulk [Cattin 2020b]. Should this lateral transport be relevant for the samples investigated in this paper, it would lead to a homogenisation of the R_{sh} profile which is then expected to mitigate the edge effects. The impact of the inhomogeneity of R_{sh} on the final extracted value of ρ_c using the standard TLM computation is then limited. Thus, our method to extract ρ_c under variable illuminations yields a negligible error and is therefore accurate enough to study the ρ_c behaviour as a function of the excess carrier concentration.

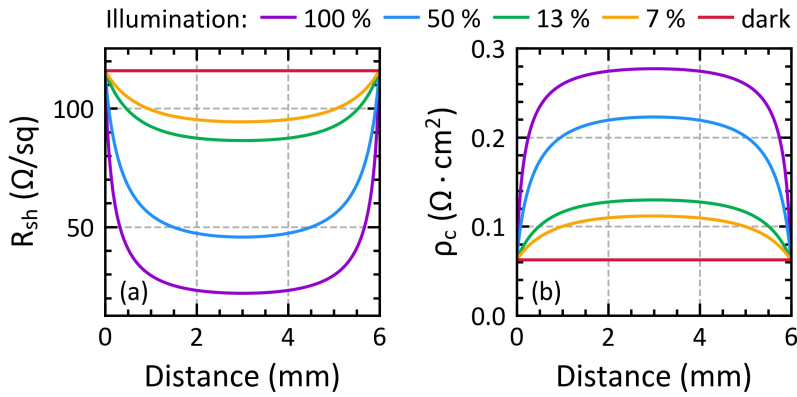


Figure 4.14 – (a) Equivalent electron sheet resistance profile and (b) contact resistivity profile below the TLM pad width considering the different illuminations, for the case of $E_a = 265$ meV (shell #1n).

Illumination (%)	ρ_c (Ωcm ²)			Error (%)
	Experimental	Computed	Difference	
7	1.07×10^{-1}	1.01×10^{-1}	-6.22×10^{-3}	-5.8
13	1.16×10^{-1}	1.16×10^{-1}	4.06×10^{-4}	0.4
50	1.96×10^{-1}	2.03×10^{-1}	6.43×10^{-3}	3.3
100	2.75×10^{-1}	2.67×10^{-1}	-8.17×10^{-3}	-3.0

Table 4.6 – Experimental and computed value of ρ_c for the case of $E_a = 265$ meV (shell #1n) and for the different illumination intensities.

4.3.5 Conclusion

In this study, we presented a new methodology to characterize the electrical transport quality of SHJ solar cells. TLM measurement under variable illumination was demonstrated to be a relevant characterization method to investigate and assess the carrier transport quality of different SHJ shells integrating several n-type thin silicon layers with various properties. This method revealed a strong dependence of ρ_c as a function of the illumination. Noticeably, it was demonstrated that the ρ_c increases with the illumination augmentation, i.e., with the rise

4.4. Doping carrier density and its impact on ρ_c - Comparison with injected carrier density

of the injected carrier density. In addition, the injected carrier density increase was observed to induce an important diminution of the c-Si R_{sh} . From these results, the importance of considering the MPP injection level to measure the ρ_c when aiming to accurately study its impact on the transport losses, and thus on the real value of FF of solar cells, was addressed. In addition, this method showed that different n-type shell parts featuring various E_a are impacted differently by illumination, i.e., that they present different illumination responses evidenced by the slope of the $\rho_c = f(R_{sh})$ curve. These results were supported by TCAD simulation with a particular focus on the E_a of the n-type thin silicon layers to change the accumulation at the c-Si(n)/a-Si:H(i) interface. In addition, two suspected limitations of this method, namely, the non-ohmic behaviour of TLM I - V curves induced by the TLM applied voltage under illumination and edge recombination, were elucidated.

4.4 Doping carrier density and its impact on ρ_c - Comparison with injected carrier density

4.4.1 Introduction

Section 4.3 demonstrated the strong dependence of the contact resistivity on the c-Si bulk R_{sh} variation induced by different injected carrier densities. Based on these results, this section studies the contact resistivity behaviour as a function of the R_{sh} as well, but this time induced by the doping variation of the c-Si(n) wafers themselves. The aim is to compare the two ρ_c behaviours to push forward the understanding of the ρ_c dependence to the c-Si bulk properties for given shells. To this end, different n-type thin silicon layers were processed to feature several thicknesses of 15, 30 and 50 nm and various E_a of 536, 251 and 69 meV as presented in Table 4.2 and integrated in the electron-selective part of SHJ shells as presented in Figure 4.1b. The different c-Si(n) wafers present seven different dopings resulting in seven values of sheet resistance, named $R_{sh\text{ wafer doping}}$, which are 700, 350, 165, 120, 97, 25 and 19 Ω /sq (in the dark) as presented in Table 4.2. Then, TLM measurements were performed in dark conditions and under several illuminations (dark, 7, 13, 50 and 100%, as presented in section 4.3).

4.4.2 Results and discussion

Figure 4.15 plots the contact resistivity, obtained from the TLM measurements performed in dark conditions, as a function of the $R_{sh\text{ wafer doping}}$ for the two shells #6n and #7n featuring either an a-Si:H(n) layer of 15 or 30 nm, respectively. The first major observation here is that the ρ_c is found to decrease with decreasing $R_{sh\text{ wafer doping}}$. This is the inverse trend to the one observed with the different injection levels presented in section 4.3.3 which showed an increase of the ρ_c values with decreasing illumination-impacted R_{sh} . These results reveal that the impact of the doping carrier density and the injected carrier density on ρ_c are significantly different. Note that the observed decrease of ρ_c with the increase of the c-Si(n) doping is close to what is observed for metal-semiconductor contacts. Indeed, it is well known from literature

Chapter 4. Advanced methods for the electrical characterization of solar cell shells using transfer length method Measurements under variable illumination

that a lower contact resistivity is reached with higher semiconductor doping densities for several direct metal-semiconductor contacts [Schroder 2006]. In addition, when comparing similar R_{sh} ranges between the two methods, corresponding here to the range between 19 to 120 Ω/sq , it is observed that the variation of the ρ_c as a function of the R_{sh} wafer doping is between 7.73×10^{-3} to $9.30 \times 10^{-3} \Omega \text{cm}^2$ when the carrier density is varied via the wafer doping, whereas the variation of the ρ_c as a function of the R_{sh} was found to be between 1.30×10^{-1} to $2.35 \times 10^{-1} \Omega \text{cm}^2$ when the carrier density was varied using different illuminations (see section 4.3.3). The ρ_c variation as a function of the R_{sh} wafer doping is then two orders of magnitude smaller than the variation of ρ_c with the R_{sh} impacted by variable illumination.

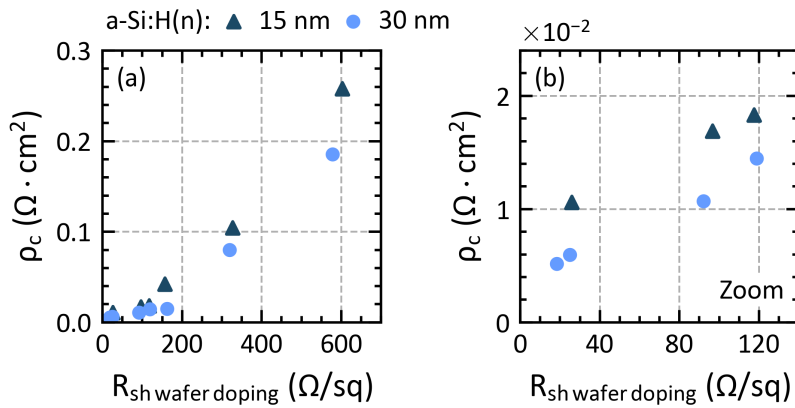


Figure 4.15 – Contact resistivity obtained with TLM measurement performed in dark conditions as a function of the R_{sh} wafer doping for the two shells #6n and #7n featuring either an a-Si:H(n) layer of 15 or 30 nm, respectively. (a) Full behaviour and (b) zoom in the range between 19 and 120 Ω/sq corresponding to the same range investigated with the illumination-impacted R_{sh} presented in section 4.3.3.

In a further experiment, the shells #8n, #9n, and #10n were deposited on the c-Si(n) wafers featuring the various R_{sh} wafer doping, as listed in Table 4.2. Then, TLM measurements under variable illumination were performed to study the impact of the illumination on the value of ρ_c for the different R_{sh} wafer doping and the different E_a of the three shells under study.

First, Figures 4.16a-c show the ρ_c as a function of the illumination-impacted R_{sh} for the different R_{sh} wafer doping, plotted separately for each shell under study featuring different n-type thin silicon layers with E_a of 69 meV (a), 251 meV (b) and 536 meV (c). The first major observation is that the ρ_c behaviour as a function of the illumination-impacted R_{sh} is similar to the one observed in section 4.3.3: ρ_c is found to increase with the R_{sh} decrease. In addition, the impact of the illumination on ρ_c is more significant for wafers presenting high R_{sh} wafer doping, i.e. the lower the wafer doping, the higher the impact of the illumination, and this regardless of the n-type thin silicon layer E_a . The ρ_c increase with the illumination-impacted R_{sh} decrease stands between 4.54×10^{-1} to $8.73 \times 10^{-1} \Omega \text{cm}^2$ for a R_{sh} wafer doping of 700 Ω/sq compared to 2.33×10^{-3} to $5.96 \times 10^{-3} \Omega \text{cm}^2$ for a R_{sh} wafer doping of 19 Ω/sq , which is hence two orders of

4.4. Doping carrier density and its impact on ρ_c - Comparison with injected carrier density

magnitude lower. Moreover, it is observed that at 100 % illumination the measured R_{sh} of the c-Si(n) bulks featuring a R_{sh} wafer doping of 700, 350, 165, 120 and 97 Ω/sq present all very similar values (see Table 4.7). This is due to the fact that at 100 % illumination, these wafers are in high injection level and thus present similar resulting electron density (n) values (as seen in Figure 4.18a-c). Note that overall, the injected carrier densities (Δn) for a given illumination are close for each R_{sh} wafer doping but present an increasing spreading with increasing illumination (see Figure 4.18a). This could be due to different wafer qualities obtained for the different R_{sh} wafer doping which may then present different SRH recombination rates as introduced in section 2.2.2.

Secondly, Figures 4.17a-g plots ρ_c as a function of the illumination-impacted R_{sh} , here plotted separately for the different R_{sh} wafer doping under study. First, in the dark, no consistent ρ_c trend is observed between the different E_a for all the wafer dopings under study. Indeed, comparing the wafer dopings between them, the ρ_c values in the dark are not arranged identically for the different E_a and feature significantly different orders of magnitude for the different R_{sh} wafer doping. However, it is observed that for the two lowest R_{sh} wafer doping values of 25 and 19 Ω/sq , the difference in value of ρ_c between the three different E_a is more pronounced in the dark as well as for the different illumination-impacted R_{sh} , compared to the other R_{sh} wafer doping.

In addition, a drop of ρ_c is observed in the range of 50% to 100 % illumination for the three lowest wafer dopings under study, namely those presenting a dark R_{sh} wafer doping of 165, 350 and 700 Ω/sq . This phenomenon may be correlated with the injection level reached inside the c-Si(n) bulk compared to the initial doping level (n_0). Indeed, looking at the ratio of $\Delta n/n_0$ presented in Figure 4.18c, it is observed that under these illuminations, the wafers featuring a dark R_{sh} wafer doping of 350 and 700 Ω/sq are at very high injection, with $\Delta n/n_0$ ratio values over 570 up to about 3400, compared to the lower R_{sh} wafer doping of 19, 25, 97 and 120 Ω/sq which present a maximum ratio of about 270 (reached for the R_{sh} wafer doping of 120 Ω/sq). Moreover, looking again at the $\Delta n/n_0$ ratio value, it is observed that the lower the wafer doping, the higher the increase of the ratio with the illumination increase and the higher the impact on ρ_c . Indeed, to reach a ratio value of about 125 for the R_{sh} wafer doping of 700 Ω/sq , a 7% illumination is required and the corresponding ρ_c increases by $+0.63 \Omega cm^2$ from dark conditions. Comparatively, to reach a similar ratio of about 125 for the R_{sh} wafer doping of 97 Ω/sq , a 50% illumination is required and the corresponding ρ_c increases only by $+0.07 \Omega cm^2$. This highlights again that the impact of the illumination on ρ_c is much more significant for wafers presenting high R_{sh} , wafer doping and it seems not to be directly related to the value of the $\Delta n/n_0$ ratio. Overall, it is observed that the higher the wafer doping, i.e. the lower the dark R_{sh} wafer doping, the lower the ρ_c values obtained in the dark and at high injection levels.

Chapter 4. Advanced methods for the electrical characterization of solar cell shells using transfer length method Measurements under variable illumination

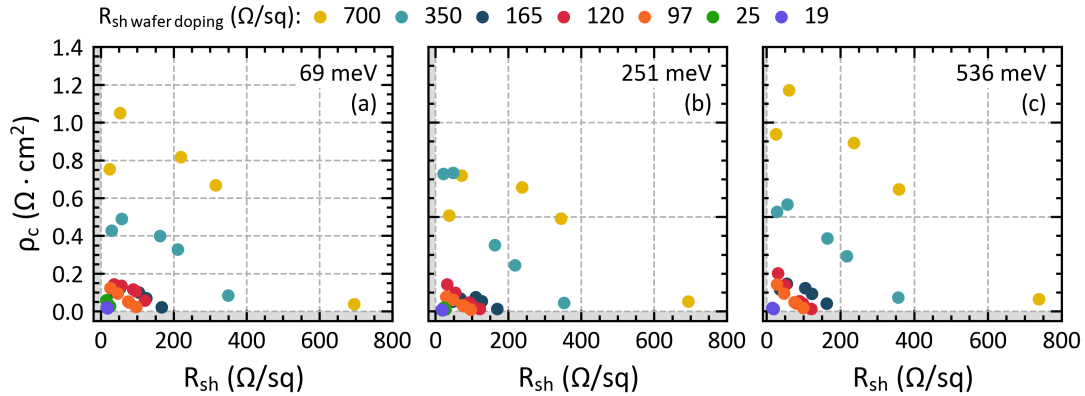


Figure 4.16 – Contact resistivity as a function of the R_{sh} impacted by illumination for the different R_{sh} wafer doping of 700, 350, 165, 120, 97, 25 and 19 Ω/sq . as well as for the three shells #8n, #9n and #10n featuring different n-type thin silicon layers with E_a of (a) 69 meV, (b) 251 meV and (c) 536 meV. For a fixed R_{sh} wafer doping, each R_{sh} value is related to one of the five illuminations which are dark, 7%, 13%, 50% and 100%, from right to left.

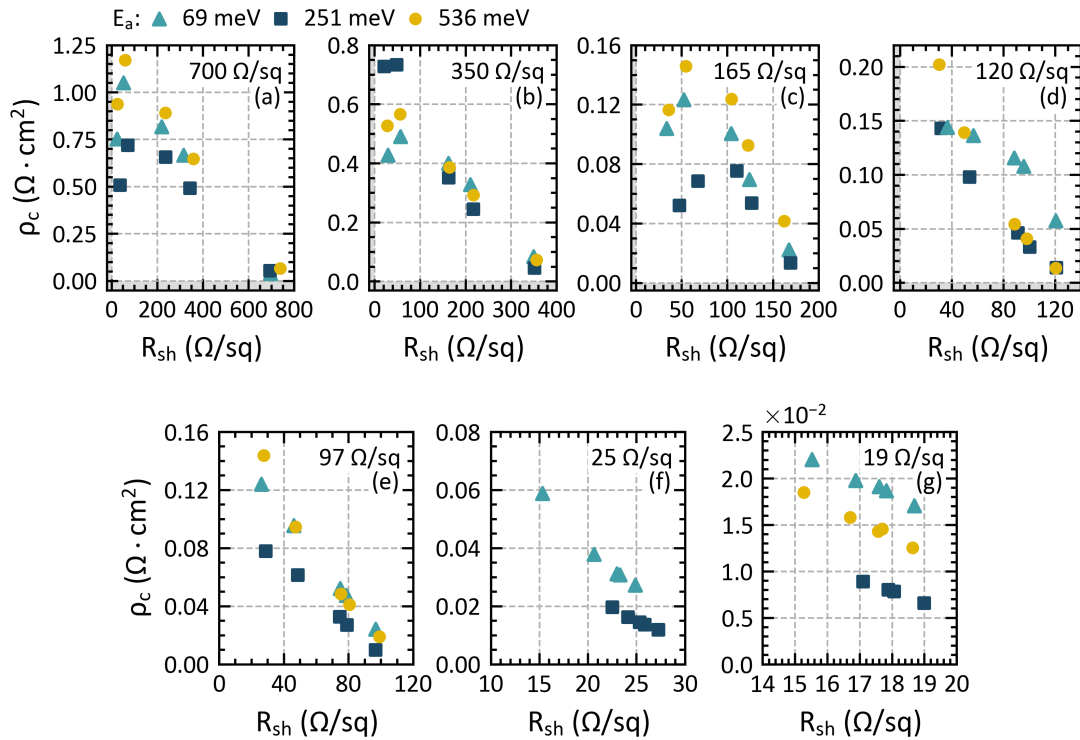


Figure 4.17 – Contact resistivity as a function of the R_{sh} impacted by illumination for the different E_a of 69, 251 and 536 meV as well as for the different R_{sh} wafer doping of (a)-(g) 700, 350, 165, 120, 97, 25 and 19 Ω/sq . For a fixed E_a , each R_{sh} value is related to one of the five illuminations which are dark, 7%, 13%, 50% and 100%, from right to left.

4.4. Doping carrier density and its impact on ρ_c - Comparison with injected carrier density

R_{sh} wafer doping (Ω /sq) / E_a (meV)	R_{sh} at 100% illumination (Ω /sq)						
	700	350	165	120	97	25	19
536	25	28	36	30	28	-	15
251	37	22	-	32	29	23	17
69	24	29	34	37	26	15	16

Table 4.7 – Values of R_{sh} obtained at 100 % illumination for the different R_{sh} wafer doping and E_a .

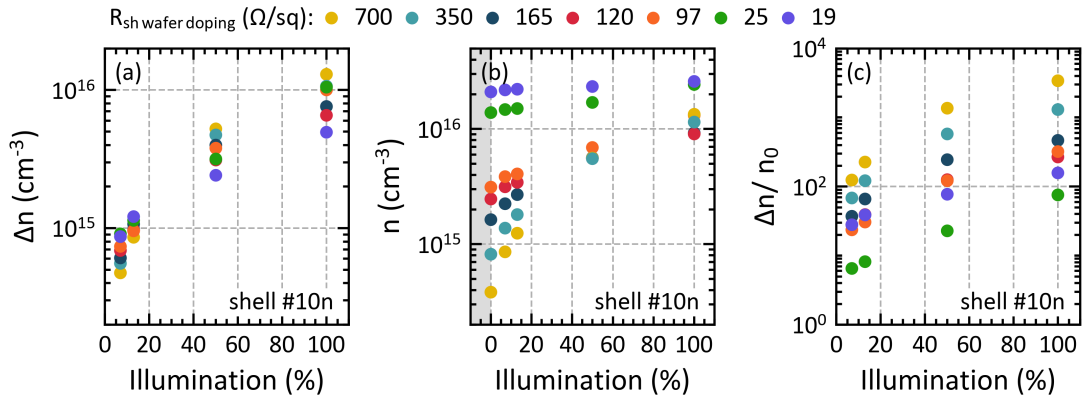


Figure 4.18 – (a) Injected carrier density (Δn), (b) electron density (n) as well as (c) the ratio of $\Delta n/n_0$ reached inside the different c-Si(n) bulks as a function of the illuminations for the different R_{sh} wafer doping of 700, 350, 165, 120, 97, 25 and 19 Ω /sq, in the case of shell #10n featuring an a-Si:H(n) layer with E_a of 69 meV.

Interestingly, when looking at the illumination response of the different shells under investigation here, it is observed in Figures 4.19a-g that the values of the slope of their $\rho_c = f(R_{sh})$ linear relation feature always the same trend, regardless of the R_{sh} wafer doping values and despite the different orders of magnitude of ρ_c variation upon illumination-impacted R_{sh} decrease observed in Figures 4.16 and 4.17, which were shown to be dictated by the c-Si(n) wafer doping. More precisely, the slope of shell #9 (featuring an E_a of 251 meV) presents always the lowest value, followed by those of shells #8 (69 meV) and #10 (536 meV). Note that for the case of the R_{sh} wafer doping of 165, 350 and 700 Ω /sq, the slope is extracted excluding the data after the drop of ρ_c . These results show that the comparison of the impact of the illumination for each E_a is similar for all the different wafer dopings, i.e. the trend in illumination response between each E_a is similar regardless of the wafer doping.

Chapter 4. Advanced methods for the electrical characterization of solar cell shells using transfer length method Measurements under variable illumination

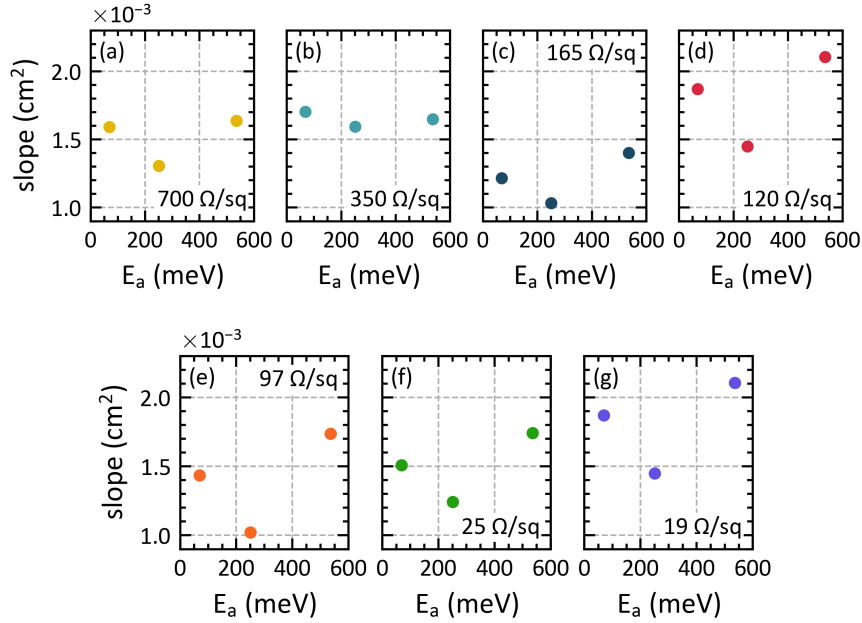


Figure 4.19 – Slopes of the $\rho_c = f(R_{sh})$ for the different injection levels as a function of the different a-Si:H(n) layers E_a of 69, 251 and 536 meV as well as for the different c-Si(n) R_{sh} wafer doping of 700, 350, 165, 120, 97, 25 and 19 Ω/sq (a)-(g).

Figure 4.20 plots the ρ_c values as a function of R_{sh} , in the case of shell #9n featuring an a-Si:H(n) layer with E_a of 251 meV, obtained either by c-Si(n) wafer doping (red points) or by different illuminations (i.e. injected carrier density) applied to given c-Si(n) wafer dopings. In this way, it is possible to compare the ρ_c values obtained for a similar final value of R_{sh} resulting either from the doping density (n_0) only or from the doping density completed with the injected carrier density ($n = n_0 + \Delta n$). It is observed that the values of ρ_c obtained by completing the initial n_0 with illumination (i.e. with addition of Δn) are always higher than the one obtained in dark conditions for similar R_{sh} . This demonstrates further that the impact of the doping density on ρ_c is significantly different than that of the injected carrier density. The results are similar for the case of shells #8n and #10n featuring a-Si:H(n) with E_a of 536 meV and 69 meV respectively (data not shown).

A first step to gain further insights into the understanding of the different impacts of doping and injected carrier density on the ρ_c value was to simulate the band diagram of a given electron-selective shell part and to apply different illuminations while ensuring the same total electron densities, and then to study the different output parameters. Figure 4.21 presents the conduction band energy as a function of the position in the case of a a-Si:H(n)/a-Si:H(i) stack (named n/i here) deposited on a c-Si(n) bulk with different doping densities and completed with the adapted injected carrier densities to reach the same final electron density of $2 \times 10^{15} \text{ cm}^{-3}$. Looking at the energy band bending, a slight difference in the band bendings is observed at $n = 2 \times 10^{15} \text{ cm}^{-3}$ between the cases with and without completion with

4.4. Doping carrier density and its impact on ρ_c - Comparison with injected carrier density

injected carrier density. Whether this band bending difference alone is responsible for the different impacts of doping and injected carrier density on the ρ_c value or not requires further investigation.

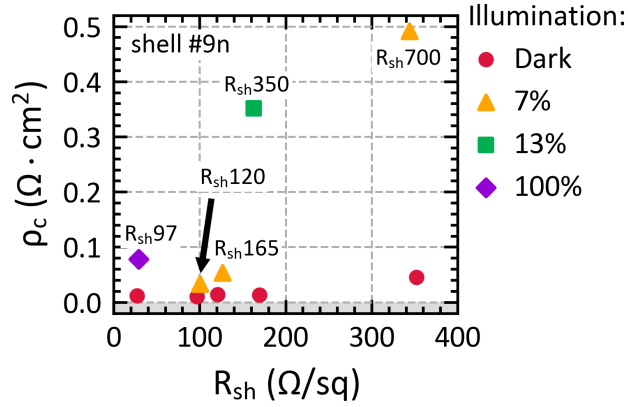


Figure 4.20 – ρ_c as a function of R_{sh} in the case of shell #9n with $a\text{-Si:H}(n)$ layer featuring an E_a of 251 meV, obtained either by $c\text{-Si}(n)$ wafer doping variation (red points) or by illumination (i.e. injected carrier density) variation applied to given $c\text{-Si}(n)$ wafer doping. The different $c\text{-Si}(n)$ wafer R_{sh} presented and targeted are 350, 165, 120, 97 and 25 Ω/sq . Here on the graph for the sake of clarity, the notation R_{sh} close to each illuminated point refers to R_{sh} wafer doping. To reach a R_{sh} of 350 Ω/sq , the R_{sh} wafer doping of 700 Ω/sq was illuminated at 7%, to reach a R_{sh} of 165 Ω/sq , the R_{sh} wafer doping of 350 Ω/sq was illuminated at 13%, to reach a R_{sh} of 120 Ω/sq , the R_{sh} wafer doping of 165 Ω/sq was illuminated at 7%, to reach a R_{sh} of 97 Ω/sq , the R_{sh} wafer doping of 120 Ω/sq was illuminated at 7% and finally to reach a R_{sh} of 25 Ω/sq , the R_{sh} wafer doping of 97 Ω/sq was illuminated at 100%.

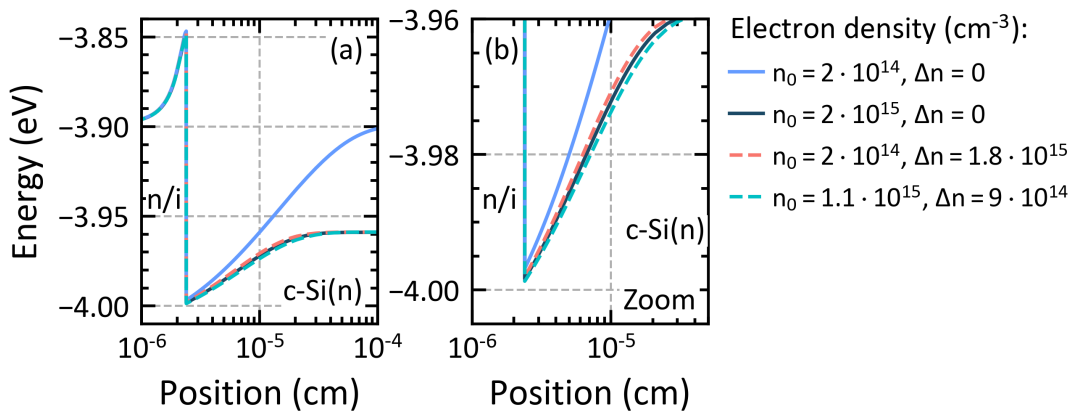


Figure 4.21 – Conduction band energy as a function of the position in the case of an $a\text{-Si:H}(i)/a\text{-Si:H}(n)$ stack (named n/i here) deposited on a $c\text{-Si}(n)$ bulk featuring a n_0 of 2×10^{14} , 1.1×10^{15} and $2 \times 10^{15} \text{ cm}^{-3}$ and completed with Δn of 1.8×10^{15} (orange), 9×10^{14} (turquoise) or 0 cm^{-3} (dark blue) respectively, to target a final electron density of $2 \times 10^{15} \text{ cm}^{-3}$.

4.4.3 Conclusion

In this section, we compared the impact on ρ_c induced either by different doping densities of c-Si(n) wafers or by different injected carrier densities induced by variable illumination. Interestingly, the two impacts were found to be significantly different: a decrease of ρ_c with the R_{sh} wafer doping decrease was observed, whereas an increase of ρ_c with the illumination-impacted R_{sh} decrease was observed. Moreover, the latter effect is two orders of magnitude larger than the former. In addition, the ρ_c values were observed to be more impacted by the illumination for high R_{sh} wafer doping, i.e. lowly-doped wafers. Moreover, different illumination responses were also observed for the different shells under study featuring a-Si:H(n) layers with various properties. In particular, the slope trend present between the different shells is found to be independent of the R_{sh} wafer doping. Overall, it was observed that the lower the R_{sh} wafer doping, the lower the dark ρ_c value and the lower the impact of the illumination on the ρ_c value for a given shell. Noticeably, it would be interesting to investigate the drop of ρ_c appearing for the high R_{sh} wafer doping in more details starting with the study of the behaviour of ρ_c for R_{sh} wafer doping = 120 Ω /sq at higher illumination, in order to elucidate whether the ratio $\Delta n/n_0$ is directly related to the appearance of the drop. In addition, this drop was already simulated with AFORSHET and TCAD simulations and some answers are expected to be found in the output parameters of these simulations. These in-depth studies may also provide additional keys to understand the dependence in the behaviour of ρ_c on the injected carrier density and the doping carrier density as well as the difference between both behaviours.

4.5 Hole-selective shell parts on c-Si(p) and c-Si(n) wafers

4.5.1 Introduction

Based on the results presented in section 4.3, the applicability of TLM measurements under variable illumination to the case of hole-selective shell parts deposited either on c-Si(p) or c-Si(n) wafers was investigated. First, the ρ_c behaviour under variable illumination of hole-selective shell parts deposited on c-Si(p) wafers was studied. As introduced in section 4.1, the study of the resistive transport losses induced by hole-selective shell parts in SHJ solar cells is commonly carried out using c-Si(p) wafers as the conductive layer to perform contact resistivity measurements, as it is not possible to perform such measurements directly on c-Si(n) wafers. Indeed, in this case case, the junction created between the p-type part and the n-type c-Si wafer makes it impossible to perform contact resistivity measurements in dark conditions, neither using TLM nor symmetric vertical structures [Lachenal 2016, Luderer 2020]. This is why the hole-selective shell parts under study are commonly characterized when deposited on the same type of wafer, i.e. c-Si(p) here⁶ [Lachenal 2016, Luderer 2020]. Secondly, as the coupling of p-type shell parts deposited on c-Si(p) wafers is expected to differ significantly from when deposited on c-Si(n) wafers, TLM measurement under variable illumination was applied to samples featuring a p-type shell part deposited on a c-Si(n) wafer. The applicability

⁶Note that electron-selective shell parts are also always characterized on c-Si(n) wafers for the same reason.

4.5. Hole-selective shell parts on c-Si(p) and c-Si(n) wafers

of TLM to measure p-type shell parts on n-type wafers under illumination is expected to be possible thanks to the photogeneration inside the c-Si(n) bulk which provides free holes, which in turn render the n-type wafer hole-conductive, and thus, possibly allowing one to conduct TLM measurements and computations.

For this study, three different a-Si:H(p) layers were integrated in shell parts deposited either on c-Si(n) or on c-Si(p) wafers as presented in Figure 4.1c. Three TMB flows were used during the deposition process, namely, low, medium, and high, to obtain three final a-Si:H(p) layer properties resulting in three distinct shell characteristics (see Table 4.3). Then, TLM measurements were performed in the dark and under variable illumination (dark, 7, 13, 50 and 100% as presented in sections 4.3 and 4.4) for the different conditions under study. Finally, the different ρ_c values obtained either on c-Si(p) or c-Si(n) wafers in the dark and under variable illumination are studied and compared.

4.5.2 Results and discussion

Hole-selective shell parts on c-Si(p) wafers

Figure 4.22a plots the resulting ρ_c behaviour as a function of the illumination-impacted R_{sh} for the three shells #1p, #2p, and #3p featuring three different a-Si:H(p) layers, namely low, medium, and high. As for the case of electron-selective shell parts on c-Si(n) wafers presented in sections 4.3 and 4.4, the ρ_c is found to increase with the R_{sh} decrease and this dependence presents different slopes for the different a-Si:H(p) layers (see Figure 4.22b). In particular, it is observed that the dark ρ_c value of shell #2p (featuring the a-Si:H(p) layer with a medium TMB flow) is the highest with a value of $0.28 \Omega \text{ cm}^2$, whereas shells #1p and #3p, featuring an a-Si:H(p) layer with low and high TMB flow, present close values of 0.21 and $0.19 \Omega \text{ cm}^2$, respectively. These values are one order of magnitude higher than the dark ρ_c values obtained for the different electron-selective shell parts presented in section 4.3 integrating the different n-type thin silicon layers. As a reminder, the dark ρ_c values were found to be between 0.02 to $0.1 \Omega \text{ cm}^2$ for a c-Si(n) bulk with a doping density of $1.65 \times 10^{15} \text{ cm}^{-3}$. Note that these ρ_c values obtained for both cases are in close agreement with the literature [Procel 2020, Luderer 2020]. In addition, it is observed that under illumination ρ_c increases up to about $+0.3$ to $+0.44 \Omega \text{ cm}^2$, similarly to what was observed in sections 4.3 and 4.4. Thus, the ρ_c behaviour of p-type shell part on c-Si(p) wafer is similar than the one of n-type shell part on c-Si(n) wafer.

Considering now the slope of the linear dependence of $\rho_c = f(R_{sh})$, the three shells present three different illumination responses. Again, this pinpoints that depending on the shell subcomponents properties, here different a-Si:H(p) layer properties, the resulting coupling will shape distinctly the final shell illumination response. In particular, despite the close dark ρ_c values of the a-Si:H(p) layers with the low and the high TMB flow, their slopes are significantly different with values of 8.87×10^{-4} and $6.18 \times 10^{-4} \text{ cm}^2$, respectively. This demonstrates again that under variable illumination, different shells may present distinct illumination responses and thus significantly different transport losses once integrated in real solar cells. Finally,

Chapter 4. Advanced methods for the electrical characterization of solar cell shells using transfer length method Measurements under variable illumination

Figure 4.22a reveals also a drop of ρ_c for the two highest illuminations of 50% and 100%, i.e. for the two lowest R_{sh} . This phenomenon is similar to the one observed in section 4.4 for lowly-doped c-Si(n) wafers and may then be correlated to the c-Si(p) wafer properties featuring here a high R_{sh} wafer doping of about $725 \Omega/\text{sq}$.

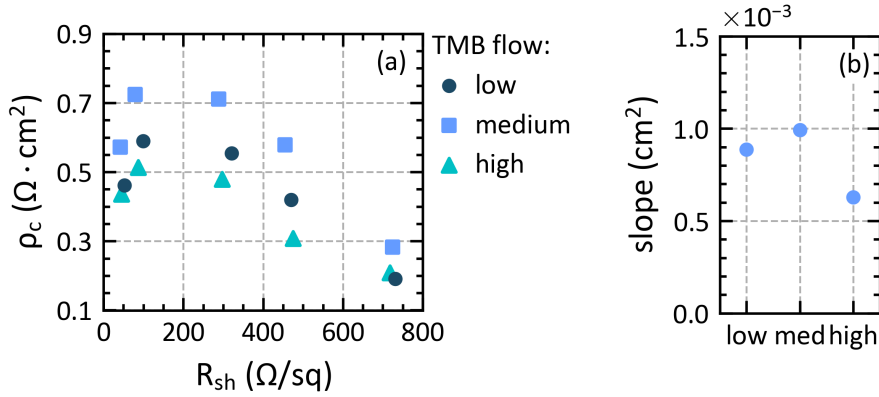


Figure 4.22 – (a) ρ_c as a function of the illumination-impacted R_{sh} for the three shells #1p, #2p, and #3p featuring different a-Si:H(p) layers with the three different TMB flows, namely low, medium and high, respectively, and deposited on c-Si(p) wafer. For a fixed shell, each R_{sh} value is related to one of the five illuminations which are dark, 7%, 13%, 50% and 100%, from right to left. (b) Slopes of the linear relation $\rho_c = f(R_{sh})$ for the three shells #1p, #2p, and #3p under study.

Hole-selective shell parts on c-Si(n) wafers

Figure 4.23a plots the energy-band diagrams for an a-Si:H(p)/a-Si:H(i) layer stack (denoted p/i here) deposited either on a c-Si(p) (blue) or on a c-Si(n) (red) wafer in dark conditions. It is clearly observed and highlighted that the resulting coupling of the p/i stack with the two distinct c-Si bulks leads to different energy-band alignments and thus, expectedly, to different ρ_c values as presented in the previous sections. Moreover, in the case of the c-Si(n) wafer, an inversion layer, i.e., a p-type area inside the c-Si(n) bulk [Filipič 2013, Maslova 2013], here of 252 nm width, is present and highlighted in light red-dashed area in Figure 4.23a. Thus, the junction created between the p-type shell subcomponents and the n-type c-Si bulk is clearly visible. Figure 4.23b plots the energy-band diagrams for the same p/i stack deposited on a c-Si(n) bulk under four different injection levels, from dark with zero injection up to $4.4 \times 10^{15} \text{ cm}^{-3}$. It is observed that the injected carriers open the blocking junction, i.e., the photogeneration provides free holes, making the n-type c-Si wafer hole-conductive in addition to electron-conductive, and the inversion layer therefore disappears. These injection conditions are thus expected to enable an external applied current, such as the one applied in TLM measurements, to flow in both directions, from the p/i layers to the c-Si(n) bulk and conversely, while additionally flowing through the c-Si(n) bulk thanks to the free generated holes.

4.5. Hole-selective shell parts on c-Si(p) and c-Si(n) wafers

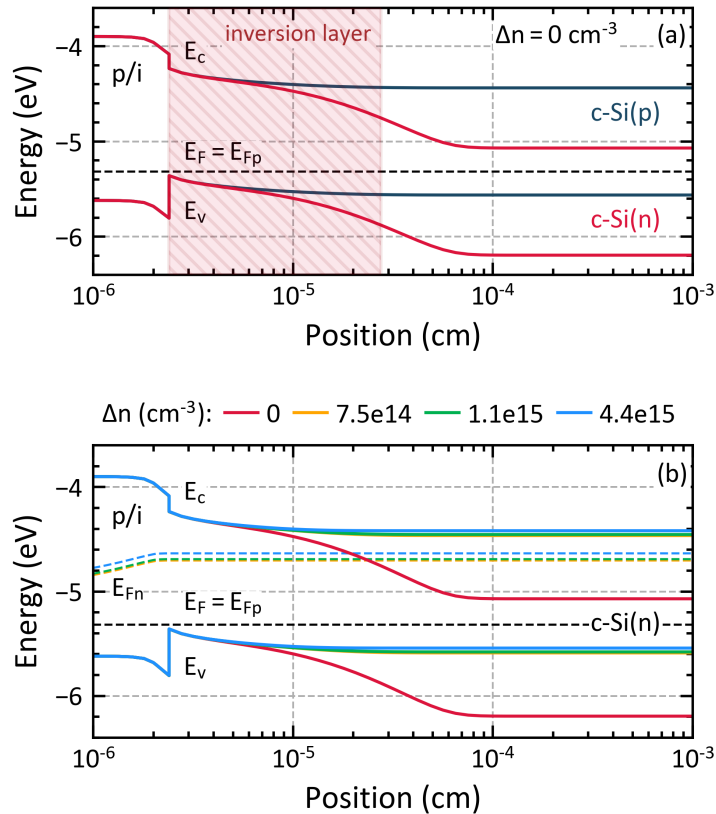


Figure 4.23 – Energy-band diagrams in the space domain for an *a*-Si:H(*p*)/*a*-Si:H(*i*) layer stack (denoted *p/i* here) deposited on (a) a *c*-Si(*p*) as well as on a *c*-Si(*n*) wafers in dark conditions ($\Delta n = 0 \text{ cm}^{-3}$). (b) *p/i* layer stack deposited on a *c*-Si(*n*) wafers in dark conditions and under three different injection levels of $\Delta n = 7.5 \times 10^{14}$, 1.1×10^{15} and $4.4 \times 10^{15} \text{ cm}^{-3}$. The conduction and the valence band energies (E_c and E_v , respectively), as well as the Fermi level (E_F) and both electron and hole quasi-Fermi levels (E_{Fn} and E_{Fp} , respectively) are represented spatially. In addition, the inversion layer present inside the *c*-Si(*n*) bulk in dark conditions is highlighted in light red dashed area.

To complete these simulations, Figure 4.24 shows the experimental *I-V* curves obtained between two TLM pads with an interpad distance of 2 mm and for the shell #3p with the high TMB flow *a*-Si:H(*p*) layer. Interestingly, it is observed that the higher the illumination, i.e. the higher the injection level, the higher the resulting current for a same applied voltage, evidencing a decrease of the total resistance with the illumination increase. The variations among the illumination of the total resistance extracted from these *I-V* curves are presented in Table 4.8. The total resistance decrease with the illumination increase actually stands from 1.01×10^5 down to $3.01 \times 10^1 \Omega$. This demonstrates that owing to the injected carriers, the blocking junction is suppressed (as observed by simulation, see Figure 4.23b), and in addition the *c*-Si(*n*) wafer conductivity increases at the same time, thus in overall leading to a decrease of the global resistance encountered by the external current flow.

Chapter 4. Advanced methods for the electrical characterization of solar cell shells using transfer length method Measurements under variable illumination

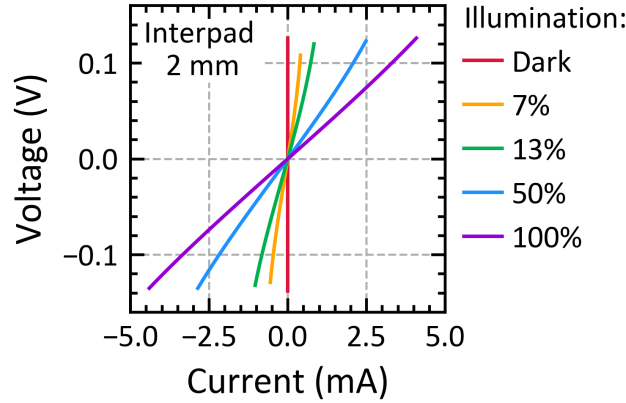


Figure 4.24 – I-V curves for the different illuminations in the case of a TLM gap of 2 mm and for the high TMB flow a-Si:H(p) layer (shell #3p) deposited on c-Si(n) wafer.

Illumination	dark	7%	13%	50%	100%
Resistance (Ω)	1.01×10^5	2.29×10^2	1.28×10^2	4.69×10^1	3.01×10^1

Table 4.8 – Resistance extracted from each I-V curves presented in Figure 4.24 for the different illuminations under studies.

From these results, the possibility to perform TLM measurements of p-type shell parts coupled with their inverse c-Si(n) bulk type was carried out. To this end, TLM measurements under variable illumination were performed on the shells featuring the different a-Si:H(p) layers under study. Figure 4.25 shows the ρ_c behaviour as a function of the illumination-impacted R_{sh} for the shells #2p and #3p featuring two different a-Si:H(p) layers, namely with a medium or high TMB flow, and deposited on c-Si(n) wafers. Interestingly, here ρ_c is found to decrease with the R_{sh} decrease which is the opposite trend to the one observed with n- or p-type shell parts deposited on c-Si(n) and c-Si(p) wafers, respectively. The ρ_c decreases down to 0.37 and 0.47 $\Omega \text{ cm}^2$ for the high and medium TMB flow a-Si:H(p) layers, respectively.

Interestingly, looking at the slope of the plot of the total resistance obtained between two TLM pads as a function of the interpad distance in dark conditions, it is observed that this slope presents very high values (data not shown). From this slope, the R_{sh} values are extracted with high accuracy even if the full TLM computation is limited (see section 3.2.1). Here, the measured R_{sh} presents values between 2.82×10^5 to $3.57 \times 10^5 \Omega/\text{sq}$, as presented in Table 4.9. Now, considering the R_{sh} of the a-Si:H(p) layers which is about $4.39 \times 10^{10} \Omega/\text{sq}$, these measured R_{sh} values are found to be the ones of the inversion layer present inside the c-Si(n) bulk in dark conditions (as presented in Figure 4.23a). Indeed, as the a-Si:H(p) layer features a R_{sh} five orders of magnitude higher than the measured TLM R_{sh} , the current is expected to flow in the inversion layer only. This demonstrates that TLM measurements of p-type shell parts deposited on their inverse type c-Si(n) bulks allow one to characterize the properties of

4.5. Hole-selective shell parts on c-Si(p) and c-Si(n) wafers

the c-Si inversion layer (as must also be the case also for n-type shell parts on c-Si(p) bulk). This result may complete other studies for the investigation of the inversion layer properties, as those presented by [Filipič 2013, Maslova 2013, Kamioka 2021].

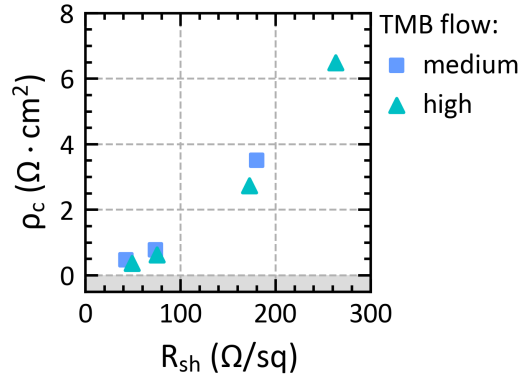


Figure 4.25 – ρ_c as a function of the illumination-impacted R_{sh} for the shells #2p and #3p featuring two different a-Si:H(p) layers, namely with a medium and a high TMB flow, respectively, deposited on c-Si(n) wafer. For a fixed shell, each R_{sh} value is related to one of the four illuminations which are 7%, 13%, 50% and 100%, from right to left.

a-Si:H(p) layer	medium	high
R_{sh} dark (Ω/sq)	3.57×10^5	2.82×10^5

Table 4.9 – Dark R_{sh} obtained by applying TLM measurement in the dark for the shells #2p and #3p featuring two different a-Si:H(p) layers, namely with a medium and a high TMB flow, respectively, deposited on c-Si(n) wafer.

Figures 4.26a and b show the ρ_c values as a function of the illumination-impacted R_{sh} for the shells #2p and #3p deposited either on c-Si(p) or on c-Si(n) bulks. The shells #2p and #3p feature the two different a-Si:H(p) layers with a medium and a high TMB flow, abbreviated here med and high, respectively. These Figures allow one to compare, for similar shells, the different ρ_c behaviours as a function of the illumination-impacted R_{sh} decrease obtained for the two c-Si bulk types (p and n-type). It results from this comparison that the ρ_c values and trends are different between the c-Si(n) and c-Si(p) cases. This reveals that the properties coupling of p-type shell parts with the c-Si bulk has a non-negligible impact on the resulting value of ρ_c , highlighting the importance of measuring given shell parts with their appropriate c-Si bulk, i.e., the one used in actual solar cells, in order to investigate the resistive transport losses.

Figure 4.27 presents the ρ_c values of the two different shells #2p and #3p, featuring the two different a-Si:H(p) layers with a medium and a high TMB flow, respectively, deposited either on c-Si(n) or c-Si(p) wafers, for the different illuminations of 13%, 50% and 100%. First, it is

Chapter 4. Advanced methods for the electrical characterization of solar cell shells using transfer length method Measurements under variable illumination

observed that at sufficiently high illumination, i.e., for low R_{sh} values obtained at 50% and 100% illumination here, the ρ_c values obtained for a given shell on c-Si(n) and c-Si(p) wafers are close to each other. Secondly, it is observed that the trend of ρ_c changes between 50% and 100% illumination, as the values obtained on c-Si(n) and on c-Si(p) cross each others with the R_{sh} decrease. Moreover, the ρ_c values obtained for both the c-Si(n) and c-Si(p) cases at an illumination of 50%, giving an injection level close to the MPP in the study presented in section 4.3, are higher than the ρ_c values obtained in the case of c-Si(p) in dark conditions (see Table 4.10).

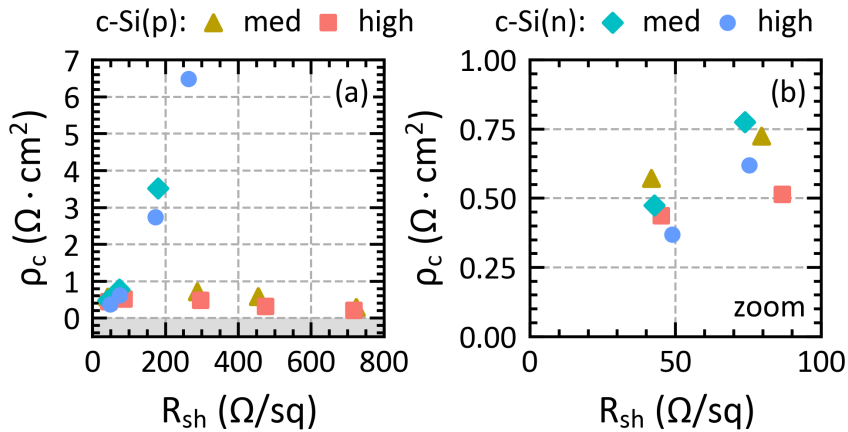


Figure 4.26 – ρ_c as a function of the illumination-impacted R_{sh} for the shells #2p and #3p featuring two different TMB flows, namely medium (med) and high, respectively, and deposited either on c-Si(n) or c-Si(p) bulk.

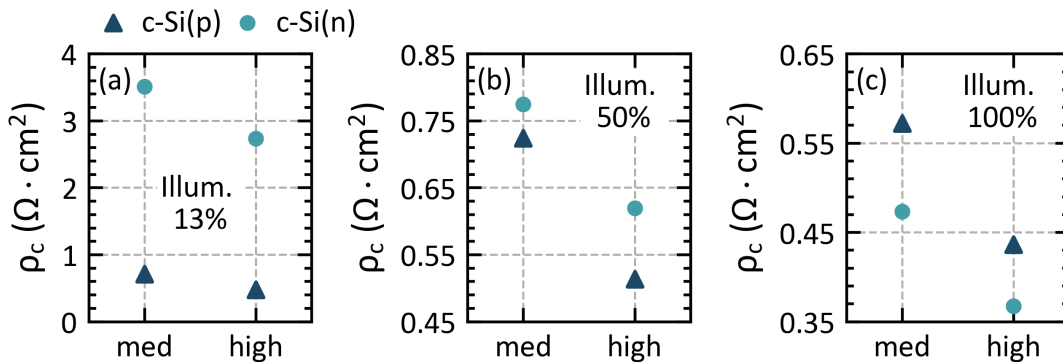


Figure 4.27 – ρ_c as a function of the two different shells #2p and #3p featuring two different a-Si:H(p) layers with the two TMB flows of medium (med) and high, respectively, deposited either on c-Si(n) or c-Si(p) wafer and for the different illuminations of 13%, 50% and 100%.

4.5. Hole-selective shell parts on c-Si(p) and c-Si(n) wafers

	ρ_c (Ωcm^2)	
	medium	high
a-Si:H(p)		
dark c-Si(p)	0.28	0.21
50% c-Si(p)	0.72	0.51
50% c-Si(n)	0.77	0.62

Table 4.10 – ρ_c values for the shells #2p and #3p featuring two different a-Si:H(p) layers with the two TMB flows, namely medium and high, respectively, and deposited either on c-Si(p) or c-Si(n) wafer in dark conditions and at 50% illumination.

As a first conclusion, the fact that the ρ_c values obtained on c-Si(n) bulks under illumination are of the same order of magnitude than the ones obtained on c-Si(p) for the two high illuminations of 50% and 100% strengthens the confidence in the applicability of this new characterisation method to measure accurately the ρ_c value of p-type shell parts on their opposite wafer type. However, when looking more closely at the illumination-impacted R_{sh} values for the case of c-Si(n) wafers, it is observed that they are significantly lower than expected when assuming only holes flowing inside the c-Si(n) wafer. Table 4.11 presents the obtained R_{sh} values for the shell #3p along with the calculated injection level considering either the R_{sh} as the one of holes (Δp) or the one of electrons (Δn). It is observed that if the obtained R_{sh} is effectively the one of the holes as assumed above, the injection levels are found to be significantly higher for each illumination compared to the ones obtained in the first case study presented in section 4.3.3 for similar n-type c-Si wafers. These values are recalled in Table 4.12 which presents the injected carrier densities obtained in this previous experiment and which were expected for the present case study (see column "expected Δn "). Table 4.12 gives also the corresponding hole and electron R_{sh} ($R_{sh p}$ and $R_{sh e}$, respectively). The resulting $R_{sh p}$ values are significantly higher than the ones obtained here experimentally for similar illuminations. Rather, the obtained R_{sh} values presented in Table 4.12 are found to closely match the values of $R_{sh e}$ presented in Table 4.11 for 13%, 50% and 100% illumination. In addition, the injected carrier density calculated considering the obtained R_{sh} as the one of electrons are close to the one obtained in the first case study of section 4.3.3 for the 13%, 50% and 100% illumination. Note that here, for the case of 7% illumination, the calculation of Δn is not possible as the obtained R_{sh} value is found to be too high to consider electrons flowing through the c-Si(n) wafer, as it exceeds the doping density in the dark giving a $R_{sh e}$ of $202 \Omega/\text{sq}$. These results suggest that the extracted TLM R_{sh} for illuminations higher than 7% may be the one of electrons and not the one of the holes as assumed, with a transition state which is present around 7% illumination.

To complete these observations, Figure 4.28 plots the I-V curves of the different TLM gaps of shell #2p deposited on a c-Si(n) wafer, for the different illumination of 7% (a), 13% (b), 50% (c) and 100% (d). Interestingly, at 7% illumination all the I-V curves are superimposed, but the more the illumination increases, the more the curves separate and present the expected TLM trend as a function of the gap. In addition, the case of 13% of illumination seems to present

Chapter 4. Advanced methods for the electrical characterization of solar cell shells using transfer length method Measurements under variable illumination

a transition state with some of the I - V curves being superimposed whereas some others are separated. Noticeably, the superposition of the IV curves at 7% and 13% of illumination can be explained by a contribution of the ρ_c to the total resistance which dominates significantly the R_{sh} one. An hypothesis to explain this phenomenon could be that, at low illumination, the holes injected at the first TLM electrode, which are thus present in the valence band (E_v) at the vicinity of the a-Si:H(i)/c-Si interface, recombine with free generated electrons in the conduction band (E_c), then travel through the c-Si(n) wafer as electrons, and then recombine again with a hole in the E_v at the vicinity of the second a-Si:H(i)/c-Si interface to reach the second TLM electrode. At low injection, this phenomenon could result in a very high value of ρ_c compared to the value of R_{sh} induced by the flow of electrons inside the c-Si(n) bulk. Then, as the injected carrier density increases, this recombination mechanism may be enhanced, therefore promoting an important reduction of the ρ_c contribution, revealing again the expected contribution of the R_{sh} on the TLM I - V curves and explaining the obtained R_{sh} values which match with the one of the electrons rather than holes. Another hypothesis explaining this recombination mechanism as well as its dependence on the illumination could be that the probability of radiative recombination increases as the injected carrier density increases, which may promote the recombination between between TLM injected holes and free generated electrons. These hypothesis should however be further investigated with additional experiments and simulations. In addition, this phenomenon may be related to the drop of ρ_c appearing at high illumination for the case study presented in section 4.4.2. It would be interesting to study these two behaviours together and investigate if they may be correlated with similar physical phenomena. However, it is worth mentioning that other parameters may be responsible for these intriguing results, such as issues in the TLM samples processing leading to misleading results. Additional possibilities could be that the passivation quality of the TLM samples of this study are higher than obtained previously or that possible effects of imperfection in the calibration may be present, resulting in higher injection levels.

To further consolidate these results, additional studies need to be conducted. First, the reproducibility of the results should be validated; secondly, a higher statistical sampling is required in order to identify correctly and precisely the physical phenomena resulting in the presence of these low R_{sh} values and peculiar I - V behaviours. Then, the validity of this new method to measure the ρ_c value of shell parts with the opposite type to the c-Si wafer could be thoroughly assessed.

Illumination (%)	R_{sh} (Ω/sq)	Δp (cm^{-3})	Δn (cm^{-3})
7	263	3.16×10^{15}	-
13	173	4.88×10^{15}	2.69×10^{14}
50	75	1.16×10^{16}	2.51×10^{15}
100	49	1.84×10^{16}	4.81×10^{15}

Table 4.11 – R_{sh} values for the shells #3p featuring the a-Si:H(p) layers with the high TMB flow for the different illuminations as well as the injection levels Δp and Δn assuming the R_{sh} being the one of holes ($R_{sh, p}$) or the one of electrons ($R_{sh, e}$), respectively.

4.5. Hole-selective shell parts on c-Si(p) and c-Si(n) wafers

Illumination (%)	Expected Δn (cm^{-3})	$R_{sh\ p}$ (Ω/sq)	$R_{sh\ e}$ (Ω/sq)
7	2.85×10^{14}	2761	166
13	4.32×10^{14}	1827	153
50	1.91×10^{15}	422	86
100	5.20×10^{15}	160	45

Table 4.12 – Injected carrier densities obtained for the different illuminations in the previous case study presented in section 4.3.3 (expected Δn) along with the related hole and electron R_{sh} ($R_{sh\ p}$ and $R_{sh\ e}$, respectively).

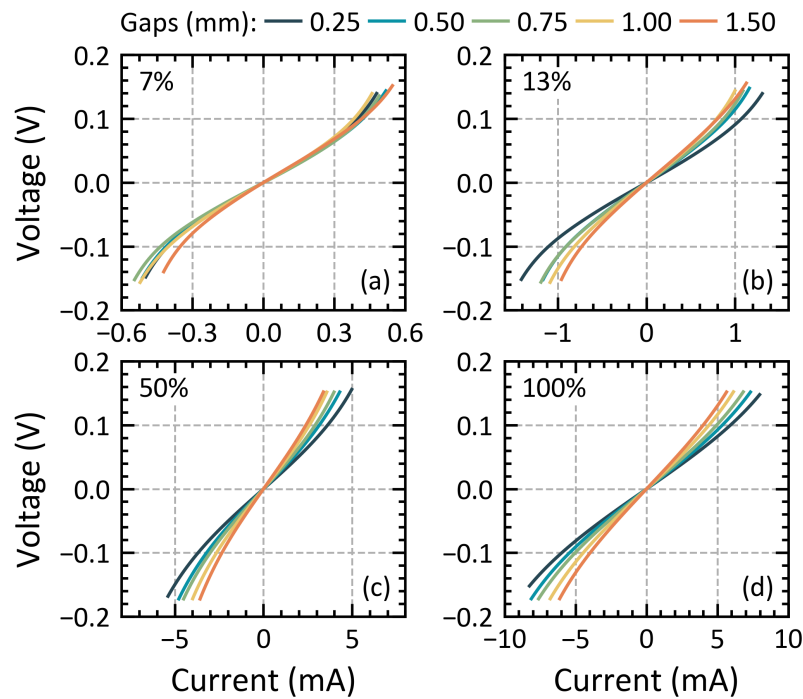


Figure 4.28 – I-V curves of the different TLM gaps of shell #2p featuring the a-Si:H(p) layers with the medium TMB flow deposited on c-Si(n) wafer, for the case of (a) 7%, (b) 13%, (c) 50% and (d) 100% illumination.

4.5.3 Conclusion

In this section, we demonstrated that the behaviour of ρ_c as a function of the illumination is similar between the cases of p-type shell parts on c-Si(p) wafer and of n-type shell parts on c-Si(n) wafer. In both cases, the ρ_c value is found to increase with the rise of the illumination, i.e., with the decrease of the illumination-impacted R_{sh} , and the orders of magnitude of the variation of ρ_c are similar. In addition, the different shells under study present different slopes revealing different illumination responses depending on the a-Si:H(p) layer properties as was the case for the study of n-type shell parts on c-Si(n). Furthermore, the study and discussion

Chapter 4. Advanced methods for the electrical characterization of solar cell shells using transfer length method Measurements under variable illumination

of the applicability of TLM measurements to measure p-type shell parts on n-type c-Si wafers were addressed. First, in that case, contrary to what has been observed for the case of shell parts with same type as the bulk, the ρ_c values are found to decrease with the illumination-impacted R_{sh} decrease. Then, comparing the ρ_c values at high illumination of 50% and 100% of similar shells deposited either on c-Si(n) or on c-Si(p) bulks, it is observed that their values are of the same order of magnitude. These results are first found to give confidence in the extraction of ρ_c values by this new characterization method. However, the small value of R_{sh} obtained and the $I-V$ curves behaviour at low illumination suggest that unexpected physical phenomena are present, resulting in high unpredicted contributions of ρ_c , and a R_{sh} corresponding to the one of the electrons rather than to the one of the holes as expected. In particular, the $I-V$ curve superpositions at low illumination suggest that an important barrier is present for TLM injected holes which consequently may promote recombination processes to create a current path flow between both TLM pads. This interesting observation remains to be further investigated. Consequently, the relevance of TLM under variable illumination to measure the value of ρ_c for the case of p-type shell parts deposited on c-Si(n) wafers is still questionable. Thus, additional studies are required to establish the validity of this method and to build a global picture allowing for a complete description and understanding of the physical phenomena behind these behaviours.

4.6 Practical implications for the design and operation of solar cells

As highlighted in chapter 2, solar cells using passivating contact are nowadays reaching high conversion efficiencies and approaching their intrinsic efficiency limit. In this quest for maximal efficiency, the higher the device performance, the more difficult it is to identify the way to further improvements. The method presented in this work may insightfully complete already existing ones, such as SunsVoc at very high injection [Bivour 2014a] or the works presented in [Fell 2017, Brendel 2016], to further understand and study the electrical transport in solar cells with the aim of guiding their actual efficiency improvement. In addition, this method might prove particularly relevant considering the increase of the injection level at MPP which goes along with the continuous increase of solar cell efficiencies. Nowadays, record-breaking SHJ devices present MPP injection levels around $2.9 \times 10^{15} \text{ cm}^{-3}$ [Yoshikawa 2017] and the theoretical limit of single junction devices presented in [Richter 2013] predicts an MPP injection level up to around $7.9 \times 10^{15} \text{ cm}^{-3}$. Therefore, the higher the MPP injection, the higher will be the difference between the contact resistivity measured in dark conditions and its actual value at MPP for a given shell. Moreover, to accurately measure the global ρ_c value of a shell and its impact once integrated in solar cells, its different parts must be characterized once coupled with the appropriate c-Si wafer, i.e., the one used in actual solar cells and featuring the appropriate type and doping, to investigate the actual resistive transport losses, in addition to be characterized at MPP injection level.

The importance of characterizing ρ_c at MPP injection level is illustrated in Figure 4.29 which plots the FF loss difference between different injection conditions and in the dark, considering

4.6. Practical implications for the design and operation of solar cells

the linear dependence of the ρ_c on the R_{sh} of shell #3n featuring an E_a of 48 meV (see section 4.3.3, Figure 4.12c). The injection levels considered are those listed in Table 4.5. The cases of planar and localized IBC contacts are studied assuming an IBC n-type contact fraction of 40 % [Procel 2018]. The FF loss difference would actually be about 0.9 %_{abs} considering the theoretical limit of single junction devices as presented in [Richter 2013], and it would go up to about 1.5 %_{abs} for the case of Kaneka’s record IBC device [Yoshikawa 2017]. This demonstrates that the higher the MPP injection, the less relevant the contact resistivity measured in dark conditions would be for an accurate FF losses breakdown. Note that in both cases, the contribution of the c-Si(n) bulk to the final FF loss decreases with the illumination augmentation as its resistivity is reduced. Indeed, a reduction in the FF loss difference between MPP injection and in the dark up to -0.18 %_{abs} is expected for planar contacts and up to -1.0 %_{abs} for IBC contact, which will partly counterbalance the augmentation of the FF loss induced by the increase of ρ_c . Last but not least, it is important to recall that we focused so far on the influence of E_a only. Yet, it is well known that E_a is not the only parameter ruling the accumulation and the illumination response in SHJ solar cells. Other key parameters, especially defect density, are involved and must be considered [Varache 2012, Schulze 2010]. Overall, our method provides valuable information about the global illumination response of a given shell regardless of the individual parameters of each of its sub-components and can then be further generalized to the investigation of other parameters than E_a . Furthermore, we believe our approach to have a broader validity and to be equally applicable to investigate shells based on other technologies than SHJ, such as the POLO and the TOPCon ones.

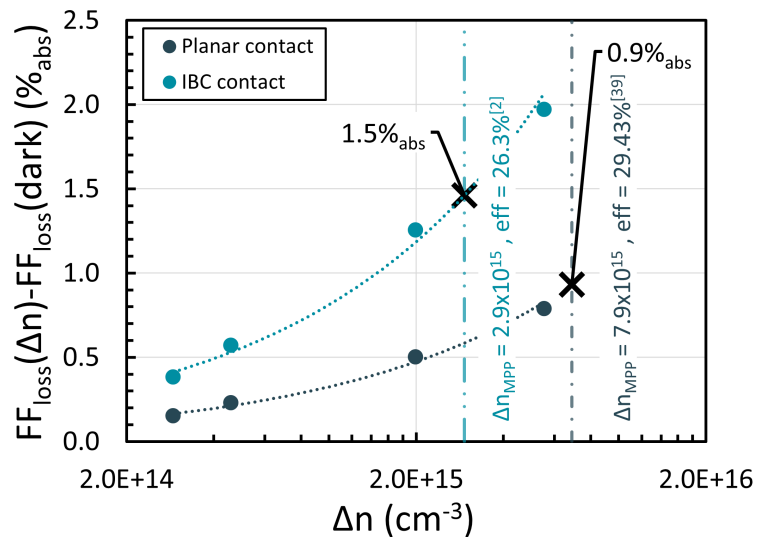


Figure 4.29 – FF loss difference between different injection levels and in the dark, considering the linear dependence of the contact resistivity on the injection of the shell #3n for a planar (grey) and an IBC (blue) architecture. The two dotted lines are guides to the eyes to follow both FF loss behaviours.

4.7 Conclusion

In this chapter, we presented a new methodology to characterize the electrical transport quality of SHJ solar cells. TLM measurement under variable illumination was demonstrated to be a relevant characterization method to investigate and assess the carrier transport quality of different SHJ shells integrating various n-type and p-type thin silicon layers. First, this method revealed a strong dependence of ρ_c as a function of the c-Si wafer R_{sh} impacted by variable illumination, i.e. impacted by various injected carrier densities. In addition, the behaviour of ρ_c as a function of the illumination-impacted R_{sh} was demonstrated to be similar for the case of p-type shell parts on c-Si(p) wafers and for the case of n-type shell parts on c-Si(n) wafers. In both cases the ρ_c value was found to increase with the illumination increase, i.e., with the decrease of the illumination-impacted R_{sh} , and the orders of magnitude of the ρ_c variation between both conditions are similar. Secondly, various c-Si(n) wafer dopings were investigated for several n-type shell parts and the impact on ρ_c induced by the different c-Si(n) doping densities was compared to the one induced by different injected carrier densities. Interestingly, the two impacts were found to be significantly different: a decrease of ρ_c with R_{sh} wafer doping decrease was observed, whereas an increase of ρ_c with illumination-impacted R_{sh} decrease was observed. Moreover, the latter effect is two orders of magnitude larger than the former. Overall, the ρ_c values were observed to be more impacted by the illumination for high R_{sh} wafer doping, i.e. for the case of lowly-doped wafers. Moreover, a drop of ρ_c was observed at high illumination for the three highest R_{sh} wafer doping under study. This drop seems to be correlated to the ratio of injected carrier density over the doping density, i.e. $\Delta n/n$, but the physical phenomena behind this behaviour remain to be addressed and investigated. Noticeably, for all these case studies, the different shells under investigation present different slopes, extracted from the linear relation of ρ_c as a function of the illumination-impacted R_{sh} , revealing different illumination responses. These slopes were found to be directly defined by the thin silicon layer properties. Finally, the study and discussion of the applicability of TLM measurements to measure p-type shell parts on n-type c-Si wafers were conducted. In that study, in contrast to what has been observed for the case of shell parts with similar type to the c-Si bulk, the ρ_c values were found to decrease with the illumination-impacted R_{sh} decrease. Comparing then the ρ_c values at high illumination of similar shells deposited either on c-Si(n) or on c-Si(p) wafers, it was observed that the values are of the same order of magnitude. However, the illumination-impacted R_{sh} were found to be lower than expected assuming holes traveling inside the illuminated c-Si bulk as TLM current. In addition, the TLM $I-V$ curves at low illumination of 7% and 13% were observed to be superimposed, revealing a significant contribution of ρ_c hiding the R_{sh} effect as a function of the interpad distance. Consequently, these two major observations put in evidence that the relevance of TLM under variable illumination to measure the value of ρ_c of p-type shell parts deposited on c-Si(n) wafers is still questionable. Additional studies are required to establish the validity of this method and to complete the global description and understanding of the physical phenomena behind these behaviours.

To strengthen these results, additional investigations must be conducted. First, the relevance of measuring ρ_c at MPP injection must be further investigated and compared to the one obtained with the standard TLM performed in dark conditions. Indeed, even if the values of ρ_c actually differ between dark and MPP injection conditions, TLM measurement in the dark is already a trustworthy and widely used method to guide solar cell developments and improvements, as it gives relevant insights into the electrical losses when comparing different shells integrated in actual solar cells. This is why the additional accuracy, insights and physical information provided by ρ_c extracted at MPP still need to be addressed and validated. Thus, to study the relevance of this new method, a way could be to compute a precise R_S breakdown to compare the results obtained with the ρ_c value obtained either at MPP injection or in dark conditions. To compare both R_S breakdown, TLM samples directly related to given solar cells must be processed alongside. Secondly, the physical phenomena responsible for the increase of the ρ_c with the illumination increase, as well as the difference between doping and injected carrier density impact on ρ_c are still matters of investigation. TCAD and preliminary AFORS2T simulations were able to reproduce both behaviours, giving the possibility to be a source of information and answers to understand these phenomena. Finally, different architectures to characterize ρ_c , such as the ones presented in [Gogolin 2014, Cox 1967], may be used to investigate further the possibility of characterizing ρ_c values of shell parts presenting the opposite type than the c-Si wafer, hence insightfully complete the results obtained in this work with TLM under variable illumination.

Based on this study, chapters 5 and 6 will present several layer and solar cell developments integrating the TLM measurement under variable illumination to study the electrical transport losses of various SHJ solar cells. In particular, TLM under illumination will be integrated with the *top-down* approach and completed with the *bottom-up* approach with the aim of building a complete R_S breakdown associated with actual solar cell performance. In this way, the R_S breakdowns calculated with the ρ_c values obtained either at MPP injection or in dark conditions will be compared.

5 Top-down and bottom-up approaches to overcome electrical limitations

Summary

This chapter presents an in-depth study of the electrical losses affecting the collection of photogenerated carriers in SHJ solar cells, looking to accurately characterize them and to provide means to mitigate them. More specifically, the material properties controlling the coupling effects between the doped thin hydrogenated silicon and the TCO layers on one hand, and between the intrinsic and doped thin hydrogenated silicon layers on another hand, were studied. To this aim, the *top-down* and the *bottom-up* approaches were applied to develop different material layers and to study the final device performance once these layers are integrated in actual solar cells. First, the *top-down* method was applied to engineer different thin hydrogenated silicon and TCO layers and multilayers featuring various properties and to characterize them. Then, the *bottom-up* approach was used to study the properties of the shells incorporating these developed layers at different process steps. Combining both methods was demonstrated to make it possible to decouple the different material layer contributions to the properties coupling which defines the final shell characteristics, as well as the resulting solar cell performance. In addition, the development of multilayers was demonstrated to allow for the exploration and fine-tuning of the shell characteristics by focusing directly on the different properties couplings present between the material layers at different levels inside the shell. In particular, the multilayer development was shown to allow for an important R_s reduction but revealed a challenging trade-off between R_s reduction and passivation quality improvement. Multilayers were also demonstrated to be a relevant solution to mitigate and optimize the different trade-offs present inside the shell by adapting the final properties coupling of the material layers. In the best optimization scheme, the use of such multilayers was demonstrated to provide significant R_s reductions combined with high passivation quality.

5.1 Introduction

As introduced in chapter 1, one of the major objectives of this work is to accurately investigate and characterize the electrical losses affecting the collection of photogenerated carriers in SHJ solar cells and to provide means to mitigate them. To this aim, several characterization methods were selected, improved, and developed, and a methodology combining the shell concept as well as both *top-down* and *bottom-up* approaches was established (see chapters 2 and 3). Indeed, as detailed in section 2.1.2, the overall shell characteristics resulting from the properties coupling of the different shell sub-components are difficult to anticipate and to assess as different physical phenomena are involved. Thus, to study the final resulting shell characteristics and to decouple the different contributions arising from the various material layers and their resulting coupling, the *top-down* and *bottom-up* approaches were introduced in section 2.3. In the present chapter, these approaches are applied to develop and study different material layers, to investigate their properties couplings arising at different levels inside the shells, and to relate them to the final device performance once integrated in actual solar cells. We will demonstrate how combining these two methods makes it possible to study the resulting electrical transport quality by first investigating selected physical key parameters of given material layers with the *top-down* approach and, secondly, by studying how they impact the final solar cell performance by analysing the shell properties obtained with the *bottom-up* approach. In particular, this allows one (i) to precisely consider the different interfaces and bulk material properties which define the physical properties coupling at different levels inside the shell, and (ii) to optimize the resulting shell performances according to the specific constraints of the different solar cell architectures the shell must fit in. The properties coupling arising between the c-Si bulk and the intrinsic and doped thin hydrogenated silicon layer was already studied in chapter 4. In this chapter, the properties coupling arising at two additional important levels within SHJ shells are investigated, namely, between the doped thin hydrogenated silicon and the TCO layers, and between the intrinsic and doped thin silicon layers.

5.2 Rationale and experimental details

Figure 5.1 illustrates the different material properties couplings which are considered in this study. These are: the coupling arising between the doped thin hydrogenated silicon layer and the TCO on the electron- and on the hole-selective shell parts (see, respectively, A and B in Figure 5.1), and the coupling present between the intrinsic and the p-type thin hydrogenated silicon layer (see C in Figure 5.1). To investigate these different cases, the *top-down* and the *bottom-up* approaches were used alongside each other to link the different material physical parameters to the resulting shell properties and final solar cell performance. More precisely, using the *top-down* approach, various thin hydrogenated silicon layers and TCOs were developed and characterized. The thickness, activation energy (E_a) as well as Raman spectra along with the corresponding bulk and surface crystallinity factors (Φ_c) were measured for several thin silicon layers. Similarly, the thickness, carrier density and sheet resistance (R_{sh})

of the TCO layers under study were measured. Then, these developed layers were integrated in dedicated shell parts and their resulting contact resistivity (ρ_c) was characterized under dark and at MPP conditions. Subsequently, using the *bottom-up* approach, the passivation quality and the final cell parameters were characterized and studied. The passivation quality was tracked at different shell process steps which are illustrated by light green rectangles on Figure 5.1. The first process step is considered after the deposition of double side a-Si:H(i) layers completed with the n-type thin hydrogenated silicon layer deposited on one side, and with the p-type thin hydrogenated silicon layer deposited on the other side (named step#1 or in/ip). The second and third steps are considered after the deposition of the TCO on the top of the p-type thin silicon layer (named step#2) and after the deposition of the TCO on the top of the n-type thin silicon layer (named step#3). Finally, the last fourth step is considered after the final annealing, which is the one applied after the print process and whose exact parameters (curing temperature and time) depend on the solar cell architecture (named step#4). Finally, the final cell parameters were measured on complete c-Si(n) based solar cells integrating the different developed shells and featuring Ag screen-printed grids. The studied solar cell architectures are the 2 cm \times 2 cm monofacial and the 6-inch bifacial. The different *I-V* parameters were studied with a particular focus on the R_s , FF , FF_0 and V_{OC} values to study in detail the resulting electrical losses. The three case studies A, B, and C are presented in Table 5.1 along with the parameters studied using the *top-down* and the *bottom-up* approaches which are presented in Table 5.2.

In case A, the coupling between n-type thin hydrogenated silicon and TCO layers is considered. To this aim, various layers were engineered. First, case A.1 focuses on the development of several n-type thin silicon layers in amorphous and nanocrystalline phases and combined in single and multilayers configurations. Then, the *top-down* approach was applied to characterize their thicknesses, activation energies (E_a) as well as crystallinity factors (Φ_c). Furthermore, their resulting properties coupling with two different TCOs, namely, aluminium-doped zinc oxide (AZO) and indium tin oxide (ITO) were studied. These two TCOs are expected to induce two different properties coupling for a given n-type thin hydrogenated silicon layer owing to different band alignments. In this regard, n-type multilayers were purposely developed to investigate and decouple the impact of the properties coupling with given TCOs, depending on the surface and on the bulk properties of the thin silicon layers. These layers were then integrated in the rear electron-collecting shell part of 2 cm \times 2 cm screen-printed monofacial SHJ solar cells. Secondly, case A.2 investigates the role of the TCO properties to define the final passivation quality provided by the shell. To this aim, the passivation quality was tracked at the four process steps introduced previously, for a given n-type multilayer selected from case A.1 and coupled with an AZO and an ITO layer. In addition, the passivation quality as a function of ITO layers deposited using various oxygen contents is studied. Finally, case A.3 presents the development of AZO layers combined in single and multilayers configurations. Their properties coupling with the n-type amorphous thin hydrogenated silicon layer and their R_{sh} were investigated and optimized to decrease the transversal and the lateral transport resistive losses, respectively, once integrated in the front electron-collecting shell part of 6-inch

Chapter 5. Top-down and bottom-up approaches to overcome electrical limitations

bifacial solar cells. To this aim, several AZO single and multilayers were developed with various carrier densities, sheet resistance and thicknesses which were measured using the *top-down* approach.

In case B, the coupling between the p-type thin hydrogenated silicon layer and different ITOs is considered. ITO layers featuring various carrier densities, R_{sh} and thicknesses, measured using the *top-down* approach, were investigated. The ITO properties were adapted to efficiently optimize the coupling with the p-type amorphous layer to decrease the resistive losses and increase the passivation quality, once integrated in the rear hole-collecting shell part of 6-inch solar cells.

The last case C addresses the properties coupling arising between the intrinsic (a-Si:H(i)) and the p-type amorphous silicon layers. In this regard, various multilayers combining a-Si:H(i) and boron microdoped a-Si:H(i) (named μD) layers were developed. First, the thickness of the a-Si:H(i) layer was varied. Secondly, boron microdoping was introduced inside a part of the a-Si:H(i) layer. Then, a-Si:H(i)/boron microdoped a-Si:H(i) multilayers (named $i/\mu D$) were developed and investigated using various TMB quantities inside the process gas flows of the μD layer, as well as various a-Si:H(i) and μD thicknesses. Finally, the different a-Si:H(i) layers and $i/\mu D$ multilayers were integrated in the rear hole-collecting shell part of 6-inch bifacial solar cells.

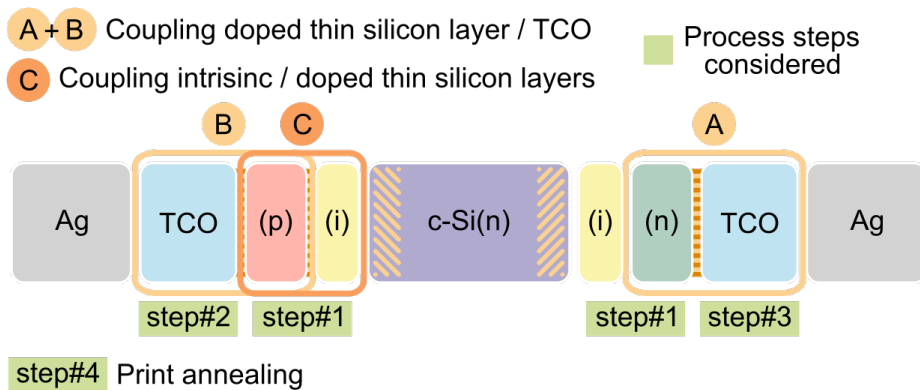


Figure 5.1 – Illustration of the SHJ solar cell shell presented in section 2.1.2 highlighting the different material couplings considered in this study. These are named A and B for the coupling arising between the doped thin silicon layer and the TCO (on the electron- and on the hole-selective shell parts, respectively) and C for the coupling present between the intrinsic and the p-type thin silicon layer. The different shell process steps from step#1 to step#4 are also depicted.

5.2. Rationale and experimental details

Case	Doped thin silicon layer	TCO	Architecture	Section
A.1	n-type amorphous and nanocrystalline single and multilayers	ITO & AZO	2 cm × 2 cm monofacial	5.3.2
A.2	n-type amorphous and nanocrystalline single and multilayers	ITO	2 cm × 2 cm monofacial	5.3.3
A.3	n-type amorphous layer	AZO single and multilayer	6-inch bifacial	5.3.4
B	p-type amorphous layer	ITO	6-inch bifacial	5.3.5
C	intrinsic and p-type microdoped amorphous multilayer	ITO	6-inch bifacial	5.4

Table 5.1 – List of the different case studies presented in this chapter along with details on the doped thin hydrogenated silicon and TCO layers as well as the solar cell architecture integrating the different shells under study. The last column gives the section presenting the case study.

Case	Top-down		Bottom-up
	Doped thin silicon layer	TCO	
A.1	Thickness	Thickness	Passivation tracking
	Φ_c surface & bulk	Carrier density	
	E_a		Final cell parameters
	ρ_c dark and MPP		
A.2	-	Carrier density	Passivation tracking
A.3	-	Thickness	Final cell parameters
		Carrier density	
		R_{sh}	
	ρ_c dark and MPP		
B	-	Thickness	Final cell parameters
		Carrier density	
	R_{sh}		
ρ_c dark			
C	Thickness	-	Final cell parameters
	TMB process gas quantity		

Table 5.2 – List of the different parameters related to the doped thin hydrogenated silicon and TCO layers obtained with the top-down and bottom-up approaches for the different case studies.

5.3 Cases A & B: Doped thin hydrogenated silicon and TCO layers coupling investigation

5.3.1 Introduction

In this section, the material properties coupling present between doped thin silicon and TCO layers is investigated with four different case studies, namely A.1, A.2, A.3, and B (see Table 5.1). These studies investigate various material layers with a particular focus on their bulk and surface properties. First, n-type thin silicon amorphous and nanocrystalline layers and multilayers were developed and combined with ITO and AZO layers (cases A.1 and A.2). Then, for a given n-type amorphous thin silicon layer, AZO single and multilayers were developed (case A.3). Finally, the ITO layer properties coupling with the p-type amorphous layer was investigated (case B). The resulting properties couplings were studied first with the *top-down* approach focusing on selected physical parameters. This aims to investigate and improve the transport losses by decoupling the bulk and surface characteristics of the material layers which are required to target optimal properties couplings at different levels inside the shell. Then, the impacts of these couplings on the final solar cell performance were studied with the *bottom-up* approach at different shell processing steps, and once the shells were fully integrated in complete devices featuring different architectures.

5.3.2 Case A.1: n-type thin silicon multilayers development

The first case study A.1 focuses on the development of n-type thin silicon layers coupled with AZO and ITO layers, as well as on their integration inside actual solar cells. To do this, various layer developments were first performed. Single and multilayers of n-type thin silicon were developed by combining amorphous (*am*) and nanocrystallines (*nc*) layers as presented in Table 5.3. The *nc* layer presents an amorphous buffer layer such that the interface with the a-Si:H(i) layer underneath is kept the same in all configurations. Here, only the interface between the n-type single or multilayer and the TCO is changed. The *am* and *nc* single layers have a thickness between 25 and 28 nm and the *am/nc* and *nc/am* multilayers have a thickness between 51 and 52 nm (including the thickness of the a-Si:H(i) layer underneath).

Then, the second parameter of our n-type thin silicon layers investigated with the *top-down* approach was the crystallinity factor. Figures 5.2a and b present the surface and bulk Raman spectra and Figure 5.2c presents the corresponding crystallinity factor values. It is first observed that the *am/nc* multilayer presents the highest surface crystallinity factor with 24.3% and the highest bulk crystallinity factor of 12.7%. The *nc* single layer presents a surface Φ_c of 8.7% with a small bulk Φ_c of 3.3%. Finally, the two layers ending with the *am* part are amorphous at the surface and inside the bulk, as they present a bulk and surface Φ_c of 0%.

5.3. Cases A & B: Doped thin hydrogenated silicon and TCO layers coupling investigation

Layers	Acronym	Total Thickness (nm)
a-Si:H(i)/a-Si:H(n)	<i>am</i>	28
a-Si:H(i)/nc-Si:H(n)	<i>nc</i>	25
a-Si:H(i)/a-Si:H(n)/nc-Si:H(n)	<i>am/nc</i>	51
a-Si:H(i)/nc-Si:H(n)/a-Si:H(n)	<i>nc/am</i>	52

Table 5.3 – List of the four single and multilayers under study presenting the full stack of layers, their acronym as well as their total thickness.

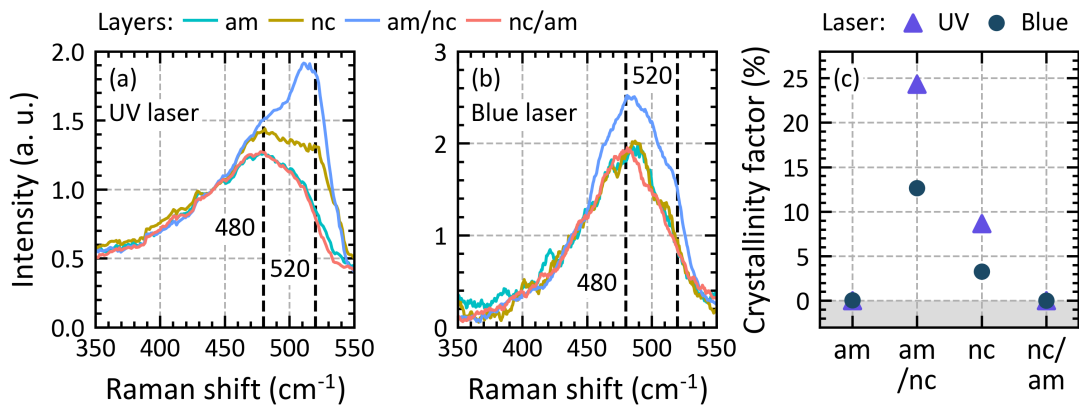


Figure 5.2 – Raman spectra of the different *n*-type single and multilayers under study obtained either with (a) the UV laser or (b) the blue laser to probe their surface and bulk properties, respectively. (c) Corresponding crystallinity factor values for the different *n*-type single and multilayers.

In a second step, these layers were integrated in the rear electron-collecting shell part of 2 cm × 2 cm screen-printed monofacial solar cells. In addition, they were coupled with either an AZO or an ITO layer. Here, the AZO layer presents a thickness of 170 nm and a carrier concentration of $1.84 \times 10^{20} \text{ cm}^{-3}$ whereas the ITO layer presents a thickness of 150 nm and a carrier concentration of $3.18 \times 10^{19} \text{ cm}^{-3}$. Figure 5.3 presents the R_s , J_{SC} , FF , V_{OC} , efficiency and pFF of the 2 cm × 2 cm solar cells, integrating the different *n*-type single and multilayers as well as either the ITO or the AZO layer.

First, looking at the parameters of solar cells integrating the ITO layer, it is observed that single and multilayers ending with the *am* part present a lower FF and a higher R_s than the ones ending with the *nc* part. This evidences the prominent role of the surface characteristics of the *n*-type thin silicon layer in the resulting properties coupling with the ITO. Moreover, it is observed that the *am/nc* multilayer presents the highest FF and the smallest R_s , among all cells integrating ITO. This highlights the importance of the *n*-type thin silicon bulk properties to define the electrical properties of the shell when coupled with a given TCO. Secondly, looking at the parameters of the solar cells with AZO, it is observed that the R_s of the *nc* single layer is

Chapter 5. Top-down and bottom-up approaches to overcome electrical limitations

slightly lower than the *am* single layer, and that the R_s of both multilayers present the lowest values and are similar. This suggests that in contrast to ITO, the resulting coupling with AZO is mainly sensitive to the n-type silicon bulk properties and only slightly dependent on the n-type silicon surface properties. Note that here, the two smallest R_s values obtained for both multilayers coupled with AZO correspond to the two highest FF values, evidencing that the electrical losses of the shells under study are reduced thanks to a low R_s combined with high passivation quality. Indeed, noticeably here, the V_{OC} values are all similar except for the two multilayers coupled with AZO, which present a gain of about +3.5 mV. This behaviour is directly linked to the pFF of these devices, which also present the two highest values for the case of the two multilayers coupled with AZO. This demonstrates that, in addition to significantly reducing the R_s , the resulting properties coupling of both n-type multilayers with AZO allows for an increase of the passivation quality.

Noticeably, it is also observed that higher J_{SC} values are obtained for solar cells integrating the AZO layer, compared to cells integrating the ITO layer. These high J_{SC} values are reached thanks to an optimized AZO rear reflector as presented in [Senaud 2019]. Thus, the combination of optimal electrical and optical properties results in the two highest efficiency values of about 22.85% which are obtained for the shells integrating the two n-type multilayers coupled with AZO. Note that here, for all conditions, the efficiency values are mainly driven by the FF behaviour.

5.3. Cases A & B: Doped thin hydrogenated silicon and TCO layers coupling investigation

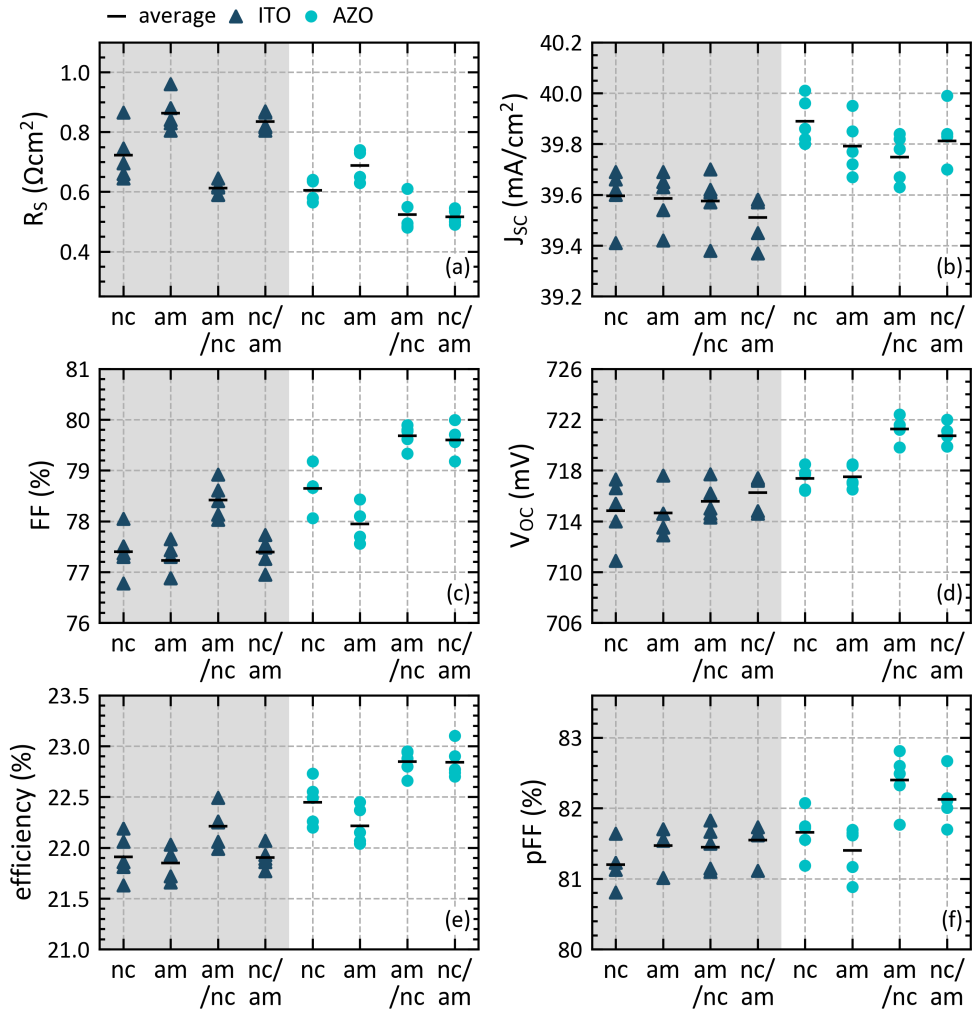


Figure 5.3 – I-V parameters of the 2 cm × 2 cm screen-printed monofacial solar cells under study integrating the different n-type single and multilayers as well as either an ITO (dark blue triangles and grey-shaded area) or an AZO (light blue dots and white area) layer.

These results demonstrated the relevance of using n-type thin silicon multilayers coupled with different TCOs to investigate the different contributions of the shell sub-components in the resulting electrical transport quality. In addition, relevant physical parameters dictating the material properties coupling were pinpointed, such as the bulk and surface crystallinity factors and the thickness of the thin silicon layers. Overall, our results are consistent with the literature. Indeed, it has previously been demonstrated that the thin silicon layer's crystallinity improves the coupling with a TCO by minimizing the contact resistance [Nogay 2016] and that the thin silicon layer's thickness is also of importance to improve the electrical transport when coupled to a TCO [Procel 2018]. In particular, the contribution of [Procel 2018] states that thicker doped thin silicon layers build wider energy barriers, but also reduce the influence of the TCO workfunction on the band bending at the c-Si/a-Si:H(i) interface. This highlights that

Chapter 5. Top-down and bottom-up approaches to overcome electrical limitations

the thickness of the doped thin silicon layer has a significant impact on the electrical transport quality. Furthermore, it is also known from the literature that a low activation energy (E_a) is required for n-type thin silicon layer to improve the transport quality of electron-collecting shell parts [Procel 2018].

Thus, based on our results presented above and on this literature review, we further optimized our electron-collecting shell parts by focusing on these three relevant physical parameters, namely, the activation energy, crystallinity factor and thickness of the n-type thin silicon multilayer. With this focus, three novel n-type *am/nc* multilayers were developed and are presented in Table 5.4. These multilayers present a similar *am* buffer layer, to keep a constant interface with the a-Si:H(i) layer, and two different thicknesses of 50 and 100 nm. The obtained Raman spectra are presented in Figures 5.4a and b and a wide range of crystallinity factor values was obtained, between 10% to 62% for their surface and between 4% to 53% for their bulk (see Figure 5.4c). Their activation energy values were also successfully varied and present values from 265 to 17 meV and are directly correlated to the crystallinity. Indeed, it is observed in Figure 5.4c that the higher the crystallinity factor, the lower the activation energy.

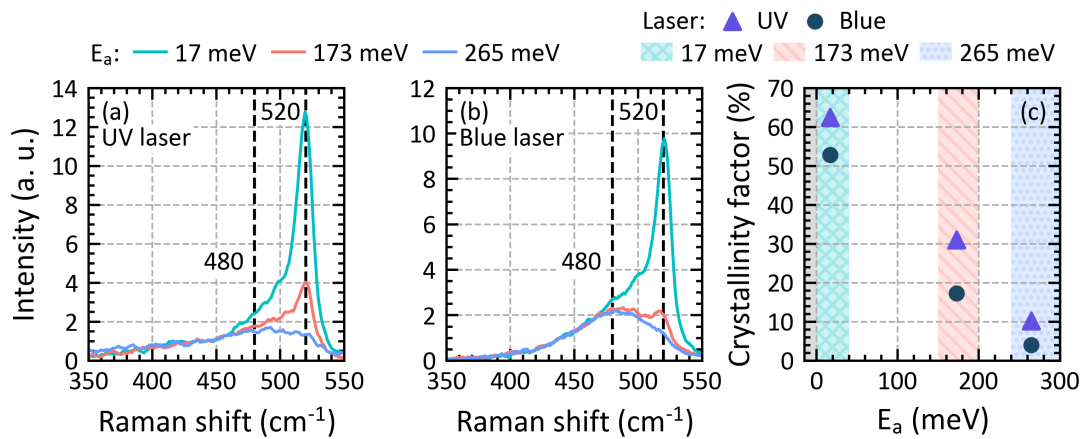


Figure 5.4 – Raman spectra obtained with (a) the UV laser, for the surface, and (b) the blue laser, for the bulk, of the three *am/nc* multilayers under study referred by their activation energies of 17, 173 and 265 meV. (c) Surface and bulk crystallinity factors as a function of the activation energy.

5.3. Cases A & B: Doped thin hydrogenated silicon and TCO layers coupling investigation

<i>am/nc</i> multilayer	E_a (meV)	Bulk Φ_c (%)	Surface Φ_c (%)	Thickness (nm)
High E_a	265	4	10	50
Medium E_a	173	17	31	50
Low E_a	17	53	62	100

Table 5.4 – Activation energy (E_a), bulk and surface crystallinity factors (Φ_c) as well as thickness of the three *am/nc* multilayers under study. These multilayers are hereafter referred by their E_a values, namely high, medium and low.

Then, using the *bottom-up* approach, the passivation quality and the voltage drop were studied at step#1 and step#4 of solar cell processing. In this context, different shells integrating the three n-type *am/nc* multilayers coupled with an AZO layer (similar to the one previously investigated) in the rear electron-collecting shell part, as well as a similar front hole-collecting shell part, were processed. In addition, these shells were integrated in 2 cm × 2 cm screen-printed monofacial solar cells. Figure 5.5a-c presents the iV_{OC} values measured at step#1 and step#4 as well as the V_{OC} and V_{MPP} of the final devices. It is observed that in step#1 (in/ip deposition), the iV_{OC} are quite similar with values close to 732 mV. Noticeably, the iV_{OC} values measured at step#4 are higher than those measured at step#1, with significant implied-voltage gains, standing between +3.6 mV and +6.2 mV. These gains are the sign of a rise of the quasi-Fermi level splitting inside the c-Si bulk which probably owes to an increased field effect passivation caused by the coupling between the TCO and the doped thin silicon layers, leading to band alignment rearrangements [Tomasi 2016, Demaurex 2014a]. In addition, this implied-voltage gain is observed to depend on the *am/nc* multilayers, and hence on their properties coupling with the AZO. The highest gain is obtained for the *am/nc* multilayer with a medium E_a of 173 meV. More precisely, it seems that this enhancement is induced by a decrease of E_a , but can be counterbalanced by a too high thickness of the multilayer (compare the shell with (50 nm, 173 meV) to the one with (100 nm, 17 meV) in Figures 5.4a-b). These results highlight the importance of considering the complete shell when investigating its passivation quality, as the passivation quality measured at step#1 may differ from the one measured at final step#4.

Moreover, considering that the difference between the quasi-Fermi level splitting inside the bulk and at the metal electrodes corresponds to the global voltage drop across the whole shell, and thus to the electrical losses occurring there [Roe 2019], the final solar cell V_{OC} values were compared to the iV_{OC} measured at the final step#4. A significant voltage drop between 7.5 to 14 mV is observed for the three n-type multilayers, resulting in a final V_{OC} higher for the medium E_a multilayer. In addition, it is observed that the low E_a multilayer presents the lowest V_{OC} with the highest voltage drop of -13.9 mV (see Figure 5.5b). Looking also at MPP conditions, it is observed that the V_{MPP} follows globally the same trend than V_{OC} , with the low E_a multilayer presenting a significantly lower value of V_{MPP} compared to the two other multilayers (see Figure 5.5c).

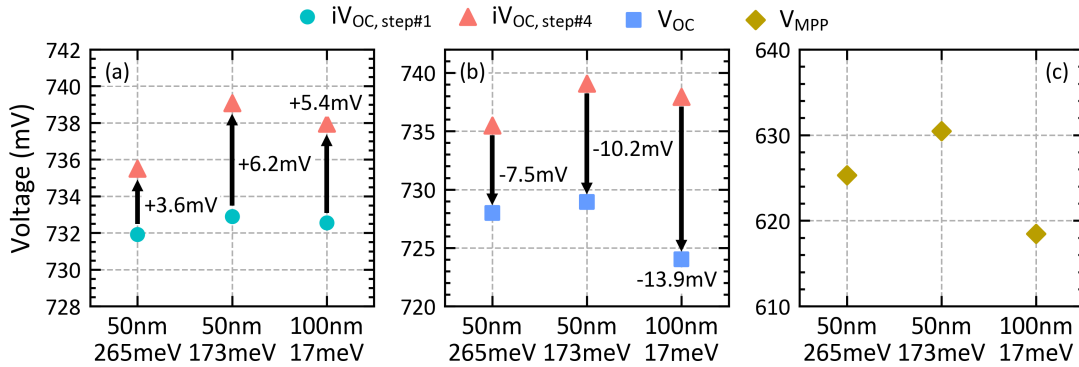


Figure 5.5 – Implied open circuit voltage (iV_{OC}) after step#1 (a) and step#4, (a) and (b), as well as related final $2\text{ cm} \times 2\text{ cm}$ screen printed monofacial solar cell V_{OC} (b) and V_{MPP} (c) for the shells integrating the three different am/nc multilayers featuring a high, medium and low E_a of 265, 173 and 17 meV, respectively. The V_{OC} and V_{MPP} values are the average values computed over three to five cells co-processed on a same c-Si(n) wafer.

Finally, combining the *top-down* and the *bottom-up* approaches, we investigated further the resistive losses of the three different shells once integrated in solar cells. Table 5.5 presents the contact resistivity (ρ_c) obtained in dark and at MPP conditions, as well as R_S , V_{MPP} , FF_0 , FF and efficiency (eff.) of the final devices integrating the three different n-type am/nc multilayers. First, it is observed that the smallest ρ_c and R_S values are obtained with the low E_a multilayer. This is consistent with the high crystallinity factor inside the bulk of this multilayer and at its surface, known to improve the electrical transport [Procel 2018, Nogay 2016]. However, despite its low resistive losses, this multilayer, once integrated in a solar cell, presents the lowest FF because of a low FF_0 value, consistent with the low passivation quality already observed through the evolution of the voltage along the different process steps (see Figure 5.5a-c). This combination of low R_S and low passivation quality has a direct impact on the final device efficiency which presents here the lowest value of 23%. Secondly, it is observed that the medium E_a am/nc multilayer presents the highest efficiency value of 23.6% thanks to a high passivation quality which compensates the highest ρ_c values, obtained in dark and at MPP conditions, resulting in the highest R_S values. Overall, a significant trade-off between passivation quality and resistive effect is present for the three am/nc multilayers under study.

Interestingly, it is observed that the ρ_c of the multilayers featuring the high and the medium E_a are similar under dark conditions, whereas they present a difference of $0.03\ \Omega\text{ cm}^2$ at MPP injection (here corresponding to about $2.0 \times 10^{15}\ \text{cm}^{-3}$, see section 4.3.3, chapter 4). Overall, it is observed that taking the ρ_c difference at MPP instead of the one in dark conditions is closely matching the actual R_S difference between the three multilayers. Indeed, a MPP ρ_c difference of $0.03\ \Omega\text{ cm}^2$ is observed between the high and the medium E_a multilayers, a value close to their actual R_S difference of $0.04\ \Omega\text{ cm}^2$ compared to the dark ρ_c difference of only $0.01\ \Omega\text{ cm}^2$. Similarly, a MPP ρ_c difference of $0.09\ \Omega\text{ cm}^2$ is observed between the medium and the low E_a multilayers, here again closer to their R_S difference of $0.10\ \Omega\text{ cm}^2$ than the dark ρ_c difference

5.3. Cases A & B: Doped thin hydrogenated silicon and TCO layers coupling investigation

of $0.04 \Omega \text{cm}^2$. In addition, considering that the MPP ρ_c gives the correct contribution to the final R_S , about $0.30 \Omega \text{cm}^2$ remains for the contribution of the front hole-collecting shell part in addition to the the small contribution of carrier transversal transport inside the c-Si(n) bulk. This is consistent with what was demonstrated in [Haschke 2020]. Note that the front hole-collecting shell contribution takes into account the lateral transport inside the TCO and c-Si(n) bulk in addition to the front ρ_c contribution. To support these observations, an in-depth computation of the R_S losses breakdown will be given in chapter 6.

Finally, this case study and its results illustrate that the *top-down* and the *bottom-up* approaches are complementary to provide relevant insights and directions to improve the solar cell performance.

<i>am/nc</i> multilayer	ρ_c dark ($\Omega \cdot \text{cm}^2$)	ρ_c MPP ($\Omega \cdot \text{cm}^2$)	R_S ($\Omega \cdot \text{cm}^2$)	V_{MPP} (mV)	FF_0 (%)	FF (%)	eff. (%)
High E_a	0.07	0.20	0.51	625.3	84.1	81.3	23.4
Medium E_a	0.08	0.23	0.55	630.5	84.6	81.9	23.6
Low E_a	0.04	0.14	0.45	618.5	82.6	80.7	23.0

Table 5.5 – Contact resistivity (ρ_c) in dark and at MPP conditions along with the R_S , V_{MPP} , FF_0 , FF and efficiency (eff.) values obtained from final devices integrating the three am/nc multilayers with high, medium and low E_a . The R_S , V_{MPP} , FF_0 , FF and efficiency (eff.) values are the average values computed over three to fives cells co-processed on a same c-Si(n) wafer.

5.3.3 Case A.2: TCO and passivation quality

This section focuses in more detail on the impact of the TCO on the final passivation quality of SHJ solar cell as presented in section 5.3.2. First, the carrier lifetime evolution is tracked for each single process step from step#1 to step#4 of $2 \text{ cm} \times 2 \text{ cm}$ SHJ monofacial solar cells using the *bottom-up* approach. Here, the shells under study integrate the *am/nc* multilayers featuring the high E_a of 265 meV coupled with either a back AZO or ITO layer. Figures 5.8a and b show the lifetime curves as a function of the injected carrier density obtained for the four steps and for the two back TCOs under study. It is observed that the final lifetime curves at step#4 present higher values than right after the step#1 for both conditions (a) and (b). This reveals again the important role of the TCO properties to define the final passivation quality of the shell resulting from the coupling properties of each of its sub-components and not solely induced by the first in/ip layer stacks [Demaurex 2014b, Tomasi 2016]. In addition, it is observed that right after the front ITO deposition the lifetime curves are significantly degraded. This is due to the sputtering damage induced by TCO deposition [Demaurex 2012]. At the third step, the lifetime curves present already slightly increased values for both TCOs. This can be explained by a partial recovery of the sputter damage induced by the front ITO due to the thermal annealing occurring during the back TCO deposition [Demaurex 2012]. This partial recovery is observed to be more important for AZO, which may be due to a slightly higher

temperature during deposition than for ITO and thanks to RF sputtering which induces less damage than DC sputtering. Then, at the final step#4, for which the samples were thermally annealed at an optimized temperature to recover almost completely from sputter damage, the lifetime curves show their final values resulting from the global shell characteristics. Overall, it is observed that the resulting properties coupling of the complete shell allows for higher final lifetime values at all injected carrier densities, with a higher increase at low injection, i.e., close to MPP conditions.

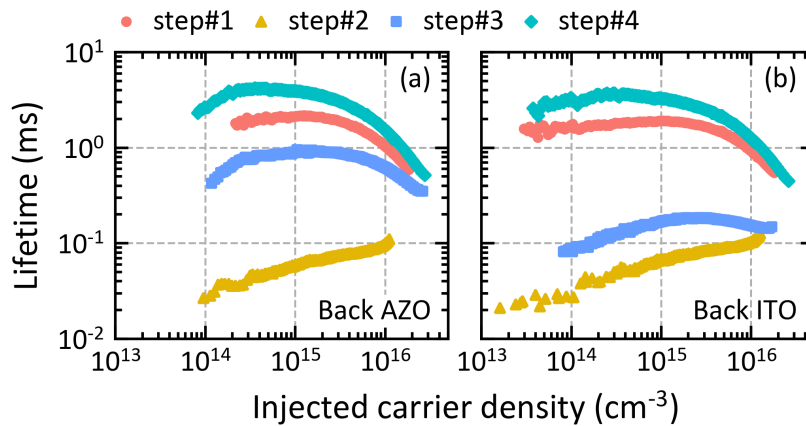


Figure 5.6 – Lifetime as a function of the injected carrier density for the four different steps, namely step#1 after in/ip deposition (orange dots), step#2 after front ITO deposition (yellow triangles), step#3 after back TCO deposition (blue squares) and step#4 after final print annealing (turquoise diamonds) as well as for two different back TCO, namely AZO (a) and ITO (b).

In addition, to investigate further the effects of annealing on the shell sub-components and the coupling of their properties, the annealing effect applied directly at the step#1 was studied. Figure 5.7 plots the lifetime as a function of the injected carrier density for two identical samples after the step#1 without and with additional final annealing, referred to as "not annealed" and "annealed", respectively. It is observed that the annealing at the step#1 is not responsible alone for the lifetime increase observed previously at final step#4. Indeed, the lifetime curves of both conditions are similar at high injection and only slightly different at low injection, presenting a reduced lifetime for the "annealed" conditions. This demonstrates further that the higher lifetime obtained at step#4 results from the global properties coupling of all shell sub-components and consequently, it is not entirely determined by the in/ip deposition at step#1 nor by the impact of an additional annealing on the in/ip layers.

To complete the study of the influence of the TCOs on the final passivation quality of SHJ shells, ITO layers featuring variable carrier density were integrated in the rear electron-collecting shell part of 2 cm × 2 cm SHJ monofacial solar cells. Figure 5.8 shows (a) the carrier density, (b) iV_{OC} at final step#4 and final V_{OC} , as well as (c) the selectivity obtained with the ratio V_{OC}/iV_{OC} (see section 2.2.3), as a function of the ITO oxygen (O₂) quantity in the deposition gas flow. First, it is

5.3. Cases A & B: Doped thin hydrogenated silicon and TCO layers coupling investigation

observed that, as expected, the higher the O₂ quantity, the lower the ITO carrier concentration. Secondly, the final V_{OC} values are observed to be similar for all O₂ quantity, whereas the iV_{OC} values are observed to be significantly impacted (see Figure 5.8b). In particular, it is observed that the final iV_{OC} decreases with the O₂ quantity increase. Combining both behaviours, this leads to a selectivity increase with the O₂ quantity increase. These results suggest that despite a lower final quasi-Fermi level splitting inside the c-Si(n) bulk, the voltage drop between iV_{OC} and V_{OC} decreases with the rise of the O₂ quantity thanks to a selectivity increase. In addition, this selectivity increase seems to compensate the passivation loss. These results highlight the importance of combining the different parameters obtained with the *bottom-up* approach to accurately study the shell sub-component properties coupling and their final impact once integrated in solar cells. Indeed, from these results it could be concluded that a high selectivity is not directly synonym of high passivation quality, and thus a solar cell with high selectivity may result in poor final performance if the passivation quality is low.

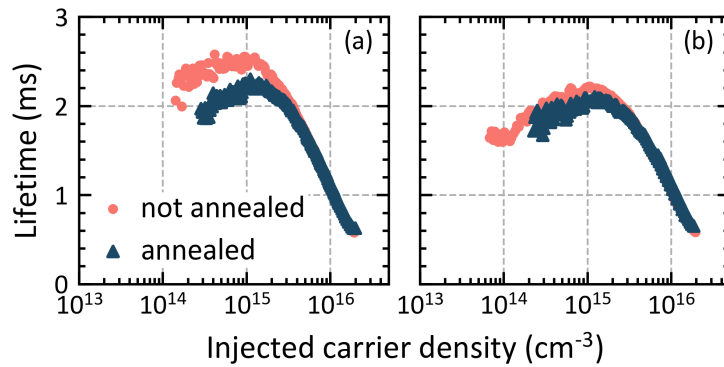


Figure 5.7 – Lifetime as a function of the injected carrier density for two identical samples (a) and (b) after the step#1 without (orange dots) and with (dark blue triangles) additional final annealing (same annealing than step#4), referred to as "not annealed" and "annealed".

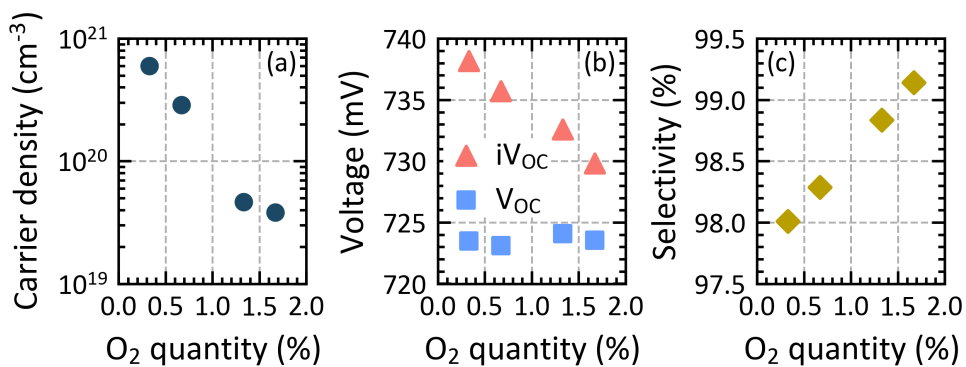


Figure 5.8 – (a) Carrier density, (b) iV_{OC} obtained at the last step#4 (orange triangles) as well as final device V_{OC} (blue squares) and (c) selectivity obtained with the ratio V_{OC}/iV_{OC} given in %, as a function of the O₂ quantity in the deposition gas flow.

5.3.4 Case A.3: Aluminium-doped zinc oxide development

Based on a similar procedure, the *bottom-up* and the *top-down* approaches were further applied to investigate the electrical losses of solar cells integrating aluminium-doped zinc oxide (AZO) with various properties. In this study, AZO layers were developed and integrated as front TCO in 6-inch bifacial SHJ solar cells and compared to the baseline reference front ITO layer. In our previous work, AZO has already demonstrated a clear potential to act as a high-quality indium-free back TCO in the rear electron-collecting shell part of $2\text{ cm} \times 2\text{ cm}$ SHJ screen-printed monofacial solar cells [Senaud 2019]. In the present work, AZO is further optimized as an indium-free alternative material, but integrated this time in the front electron-collecting shell part of bifacial solar cells. The development of AZO at the front side must take into account the requirements for optimal lateral transport to the finger grid in addition to optimal transversal transport. The former is defined by the R_{sh} of the AZO, whereas the latter by the contact resistivity of the front electron-collecting shell part. Both resistive contributions will directly affect the final R_S value of the device¹.

First, AZO layers were developed by varying the carrier density using different O_2 contents in the deposition gas flow, varying from 0.02 to 0.10%_{rel} as listed in Table 5.6. Their thickness was set at about 120 nm, which is similar to the reference front ITO, to target an effective front antireflecting coating (ARC). Then, using the *top-down* approach, the carrier density and the contact resistivity (ρ_c) were measured. The ρ_c values of the electron-collecting shell part integrating the complete stack of layers a-Si:H(i)/a-Si:H(n)/AZO or ITO were measured by TLM. Figure 5.9 depicts (a) the carrier density and (b) the ρ_c of the front reference ITO and the different AZO layers. It is observed in Figure 5.9a that the higher the O_2 content of the AZO layer, the lower the carrier density, and that the AZO B, C and D present a carrier density lower than the reference ITO. Now looking at the ρ_c values presented in Figure 5.9b, it is first observed that TLM measurements were not possible to perform for AZO A, as it presents non-ohmic I - V behaviours in dark conditions (see Figure 5.9). Overall, for all AZO layers under investigation, the ρ_c values are found to decrease with the O_2 quantity increase, going down to $0.067\ \Omega\text{ cm}^2$ for the AZO D. Furthermore, AZO C and D present significantly lower ρ_c than the reference ITO, which presents a ρ_c value of $0.37\ \Omega\text{ cm}^2$.

Additionally, the non-ohmic behaviour of the dark I - V curves of the AZO A was investigated under variable illumination. Figure 5.9 plots the I - V curves obtained between two TLM pads for different illuminations and for the cases of AZO A and AZO C. First, it is observed that the dark non-ohmic I - V curve of AZO A presents a typical shape induced by a Schottky barrier resulting from a non-optimal coupling of the TCO with the n-type thin silicon layers [Ritzau 2014, Schroder 1984, Jeong 1998]. Interestingly, it is observed that upon increasing illumination, the I - V curves become linear. Secondly, comparing the I - V curves of AZO A with those of AZO C, presenting an ohmic behaviour under dark conditions, it is observed that the non-ohmic behaviour induced by illumination (presented in detail in section 4.3.2) presents

¹The results presented in this section were obtained in collaboration with Gabriel Christmann whose contribution is gratefully acknowledged.

5.3. Cases A & B: Doped thin hydrogenated silicon and TCO layers coupling investigation

the inverse shape than the one induced by a Schottky barrier. Indeed, in the case of the Schottky barrier (dark I - V curve of AZO A), it is observed that the higher the voltage, the lower the resistance. This result shows that the voltage augmentation provides an increased energy to the carriers, making it easier for them to pass the Schottky barrier. In contrast, the non-ohmic behaviour upon variable illumination is induced by an increase of the resulting c-Si(n) bulk resistance with the rise of the voltage (presented in detail in section 4.3.2). From these results, it would be interesting to study further the validity of performing TLM measurements and computation under illumination for shell parts featuring dark TLM I - V curves with a non-ohmic behaviour like AZO A. Indeed, two aspects may be worth investigating. First, it is possible that the Schottky barrier varies or even disappears upon the increase of the injection, making it possible to perform TLM computation in the linear range around the origin, i.e., for small applied TLM bias (see section 4.3.2). Secondly, the linearity of the I - V curve obtained between 50% and 100% illumination may result from the sum of two opposite contributions: that of the Schottky barrier and that of the c-Si bulk, which cancel each other in the final I - V curve characteristics.

Table 5.7 presents the TCO R_{sh} for the reference ITO and the four AZO layers, as well as the corresponding induced R_S computed considering the lateral transport to the fingers to occur solely inside the front TCO and a pitch of 1.93 mm. The formula used for this computation can be found in the appendix section of [Haschke 2020]. It is observed that all the AZO R_{sh} are significantly higher than that of the ITO layer, passing from 188 up to 1143 Ω /sq. These high R_{sh} values obtained for AZO are mainly due to a very low electrical mobility of this material, which stands between 4 to 10 $\text{cm}^2\text{V}^{-1}\text{s}^{-1}$ where it is of about 31 $\text{cm}^2\text{V}^{-1}\text{s}^{-1}$ for the ITO layer.

AZO name	A	B	C	D
O ₂ quantity (%)	0.02	0.05	0.07	0.10

Table 5.6 – AZO O₂ quantity in the deposition gas flow given in relative % along with the different corresponding AZO names which are A, B, C and D.

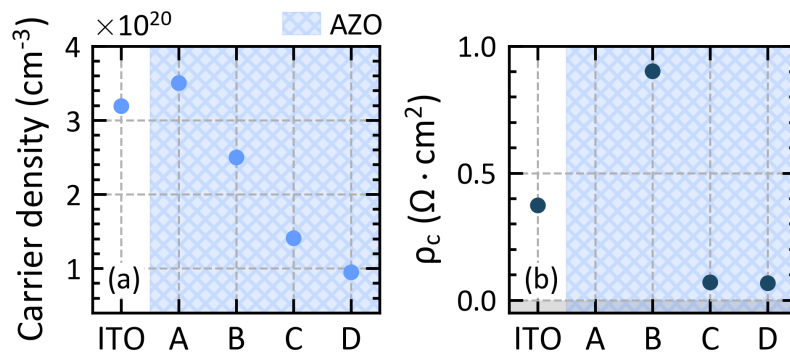


Figure 5.9 – (a) Carrier density and (b) ρ_c values measured for the reference ITO layer and the different AZO layers presenting the various O₂ quantity, namely A, B, C and D.

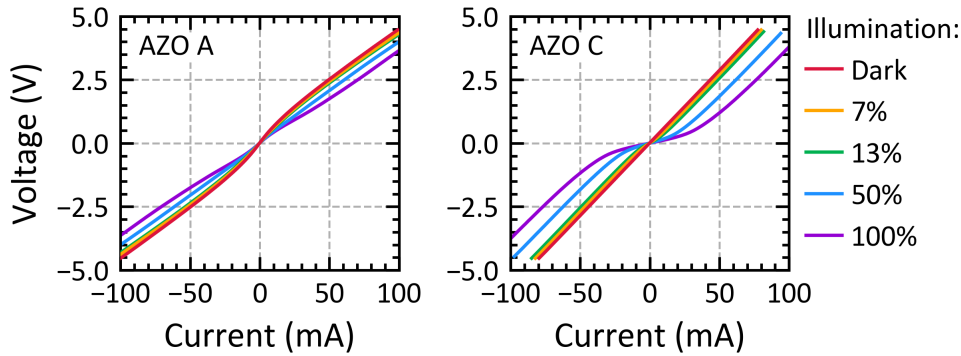


Figure 5.10 – I-V curves obtained between two TLM pads for the different illuminations which are dark, 7%, 13%, 50% and 100% for the AZO A and AZO C layers.

	ITO	AZO A	AZO B	AZO C	AZO D
R_{sh} (Ω/sq)	50	188	434	981	1143
R_S from R_{sh} (Ωcm^2)	0.16	0.58	1.35	3.05	3.55

Table 5.7 – R_{sh} along the corresponding induced R_S computed considering only lateral transport to the fingers inside the front TCO and a finger pitch of 1.93 mm, for the ITO and the four different AZO layers under study namely A, B, C and D.

In a second step, these AZO layers were integrated in the front electron-collecting shell part of 6-inch bifacial solar cells and their final performances were studied and compared to the ITO reference layer. The two selected AZO layers were the A and the B, as the R_S induced by the R_{sh} of AZO layers C and D present high values, and are therefore expected to induce high R_S contribution, calculated to be $> 3 \Omega cm^2$ (see Table 5.7). Figure 5.11 presents the I - V parameters for the three conditions under study. First, looking at the J_{SC} values, it is observed that the J_{SC} is lower for AZO A than for AZO B. This owes to the higher carrier density of AZO A compared to AZO B, which induces higher free-carrier absorption (FCA) in the infrared part of the solar spectrum [Senaud 2019]. In contrast however, despite a lower carrier density of AZO B compared to ITO, the former presents a slightly lower J_{SC} . This may be due to other TCO parameters, such as the optical mobility. Indeed, according to the Drude model, the FCA is directly proportional to the carrier density and inversely proportional to the optical mobility of the material [Chopra 1983]. In addition, both parameters depend on oxygen vacancies in TCO and are therefore varying with the change of O_2 quantity in the deposition gas flow. Secondly, it is observed that the final passivation quality is lower for AZO A, which presents the lowest O_2 quantity, as it features the lowest FF_0 and V_{OC} values. This behaviour was usually observed for AZO integrated in the front electron-collecting shell part of our bifacial solar cells, such that the higher the O_2 quantity, the higher the passivation quality, i.e., the higher the V_{OC} and FF_0 (data not shown). Overall, the ITO layer presents the highest passivation quality with the highest V_{OC} and FF_0 .

5.3. Cases A & B: Doped thin hydrogenated silicon and TCO layers coupling investigation

Interestingly, looking now at the R_S values, it is observed that despite the non-ohmic TLM I - V curve obtained for AZO A under dark conditions, this AZO presents a lower R_S value once integrated in solar cells than AZO B. From this peculiar result, we gain two different insights. First, it seems that the ρ_c value of the AZO A, once integrated in a solar cell with a given architecture, here bifacial, and under MPP injection conditions, eventually provides a smaller contribution to the R_S than expected when looking only at the properties of the TLM I - V curves obtained under dark conditions. Secondly, the R_S difference between AZO A and AZO B is about $0.95 \Omega \text{ cm}^2$. Assuming the lateral transport to the finger to flow only inside the front TCO, the R_S induced from their R_{sh} are $0.58 \Omega \text{ cm}^2$ and $1.35 \Omega \text{ cm}^2$, for AZO A and AZO B respectively (see Table 5.7). Thus, the difference in R_S between AZO A and B owing only to their R_{sh} is about $0.77 \Omega \text{ cm}^2$. Therefore, the effect of high ρ_c expected for AZO A seems to be compensated by a lower R_{sh} , i.e., compensated by a smaller resistive losses contribution of the lateral transport once integrated at the front side of bifacial solar cells. Note that this difference is anyway smaller than the actual R_S difference of $0.95 \Omega \text{ cm}^2$ observed here. One explanation might be that the ρ_c of AZO A is actually smaller than that of AZO B once integrated in a bifacial solar cell and measured at MPP conditions, despite AZO B features a dark ohmic TLM curve with a ρ_c of $0.90 \Omega \text{ cm}^2$. Importantly, these results demonstrated that a shell part presenting non-ohmic TLM I - V curves under dark conditions may eventually be a better candidate than expected once integrated in solar cells, both by providing high lateral transport quality to the fingers (hence fulfilling specific architecture constraints), as well as providing a low final ρ_c contribution.

Overall, the ITO presents the smallest R_S value of $0.75 \Omega \text{ cm}^2$ thanks to a combination of a dark ρ_c value of $0.37 \Omega \text{ cm}^2$ and a low R_{sh} of about $50 \Omega/\text{sq}$, the latter inducing a R_S contribution of only $0.16 \Omega \text{ cm}^2$ (see 5.7) which is significantly low compared to those of both AZO layers A and B. Finally, in the case of AZO, the FF is observed to be mainly driven by the R_S values, leading to the lowest FF for AZO B, despite higher V_{OC} and FF_0 than AZO A. Finally, both AZO layers feature very low final efficiencies compared to the reference ITO, due to a combination of degraded passivation quality and high R_S .

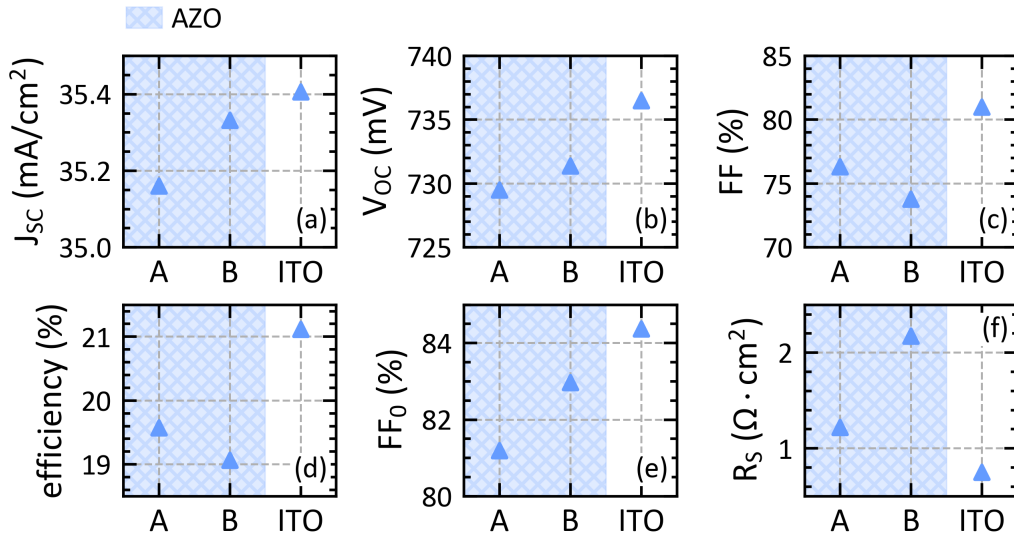


Figure 5.11 – J_{SC} , V_{OC} , FF, efficiency, FF_0 and R_s average values over three cells for the three conditions under study which are AZO A, AZO B and reference ITO.

Based on these results, AZO multilayers were engineered and investigated following procedures similar to the n-type thin silicon multilayers presented in section 5.3.2. In this context, AZO D was selected to act as the first TCO layer deposited on top of the a-Si:H(n) layer, as it presents the lowest ρ_c value of $0.067 \Omega \text{ cm}^2$, which is significantly lower than the ITO ρ_c of $0.374 \Omega \text{ cm}^2$ (see Figure 5.9), in addition to be known to provide higher passivation quality than AZO A and AZO B. Moreover, as AZO D presents a very high R_{sh} of $1143 \Omega/\text{sq}$ (see Table 5.7), a top AZO layer with a lower R_{sh} is required to provide an adapted conductive layer to the fingers. Thus, multilayers AZO D/A and AZO D/B were developed and integrated in the front electron-collecting shell part of 6-inch bifacial solar cells. Their final performances were studied and compared to those of the front ITO reference layer. The AZO D thickness was set at 20 nm and the AZO A and B at 100 nm to ensure a total thickness of 120 nm corresponding to an appropriate ARC. The AZO A and B are kept as thick as possible to target a low R_{sh} and the AZO D is kept thick enough to provide a low ρ_c when coupled with the a-Si:H(n) layer underneath.

Figure 5.12 presents the I - V parameters for the three conditions under study. Similarly to what was observed for the case of single layer AZO, the J_{SC} is lower for the multilayer AZO D/A than for the D/B one. This again is due to the higher FCA provided by the AZO multilayers with the top AZO A presenting the highest carrier density. In addition, the highest J_{SC} is still obtained for the ITO layer, showing that both AZO multilayers still induce high parasitic optical absorption despite the first 20 nm of AZO D which features the lowest carrier density. The final resulting coupling of AZO D/A and AZO D/B does not mitigate enough the FCA. Looking at the passivation quality, it is again observed that both AZO conditions present lower V_{OC} and FF_0 values than ITO, despite the use of the thin AZO D layer which was demonstrated to provide

5.3. Cases A & B: Doped thin hydrogenated silicon and TCO layers coupling investigation

higher passivation quality when deposited as single layer. However here, both multilayers present close values of V_{OC} and FF_0 , demonstrating that the properties coupling of AZO A and B with the thin AZO D layer provides a small gain in passivation. Indeed, as previously observed in Figures 5.11b and e, AZO A presented significantly lower FF_0 and V_{OC} values than AZO B. Finally, looking at the resistive losses, it is observed that the R_S obtained with the multilayer AZO D/A is in average $0.14 \Omega \cdot \text{cm}^2$ lower than that of ITO and the R_S of the multilayer AZO D/B is similar to the ITO. Again here, the R_S value of AZO D/B is found to be higher than that of AZO D/A because of the higher resistive losses induced by the lateral transport inside AZO B. This demonstrates that AZO multilayers allow one to decrease significantly the R_S value once integrated in a solar cell by (i) providing low ρ_c by optimizing the material properties coupling between the a-Si:H(n) and AZO layers, and (ii) minimizing the resistive losses induced by lateral transport thanks to a highly conductive top AZO layer. However, due to the remaining low passivation quality and low J_{SC} of both AZO multilayers, their final efficiencies are globally lower than that of ITO. Note that the FF value of AZO D/A is similar to that of ITO thanks to the low R_S which compensates the low FF_0 value.

Further experiments are required to optimize further the AZO multilayers with the aim to keep low R_S while allowing for passivation and J_{SC} gain. To do this, first the thicknesses of both AZO parts must be optimized to mitigate the trade-off between passivation loss and R_S gain. Care must be taken here as the TCO properties are found to depend on their thicknesses (see appendix A.3), making then important to precisely characterize each sub-layer to optimize properly the whole AZO multilayers. Secondly, the carrier density of the top AZO can also be increased while testing even smaller O_2 contents. In both cases, these investigations must be conducted by additionally targeting a decrease of the optical absorption of AZO multilayers.

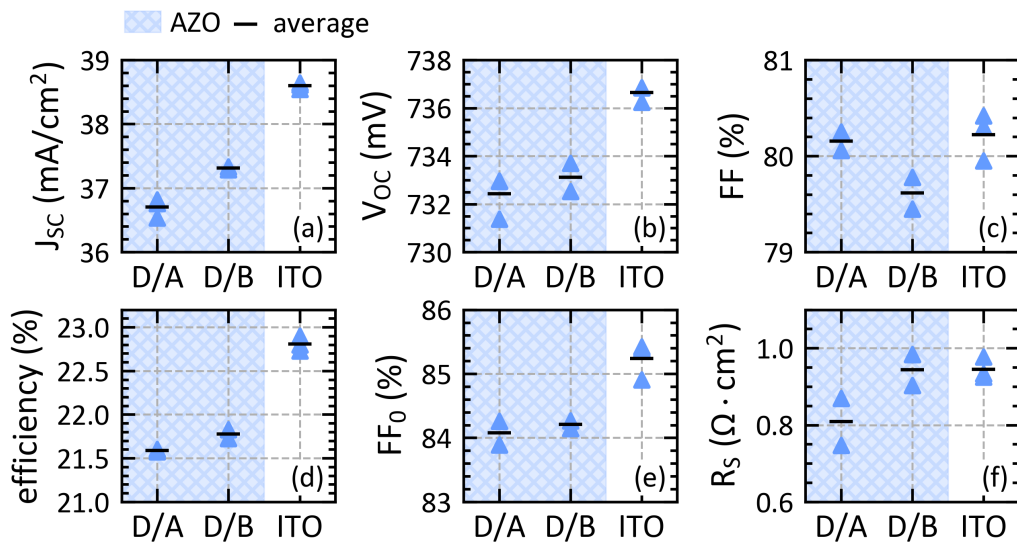


Figure 5.12 – J_{SC} , V_{OC} , FF, efficiency, FF_0 and R_S values for the two AZO multilayers D/A and D/B as well as for the reference ITO.

5.3.5 Case B: Indium tin oxide development

During our investigations, various ITO layers integrated in the rear hole-collecting shell part of 6-inch bifacial solar cells were investigated. The *top-down* approach was used to perform TLM under dark conditions as well as Hall measurements to study the influence of the properties coupling between ITO and p-type thin silicon layers on the final cell performance. Three ITO were investigated, that is, the reference back ITO, named ITO E, as well as two front ITOs, named ITO F and G. Note that ITO G is the reference front ITO presented in the previous section 5.3.4. Table 5.8 depicts the thicknesses, the carrier density and the sheet resistance of these three ITOs, as well as the dark ρ_c measured considering the complete rear hole-collecting shell part a-Si:H(i)/a-Si:H(p)/ITO. First, it is observed that ITO G presents a slightly lower ρ_c value of $0.33 \Omega \text{ cm}^2$ when coupled with the rear a-Si:H(i)/a-Si:H(p) stack (referred to as i/p), compared to a value of $0.37 \Omega \text{ cm}^2$ when coupled with the front a-Si:H(i)/a-Si:H(n) stack (presented in section 5.3.4, Figure 5.9). Secondly, the properties couplings of both ITOs F and G with the rear i/p stack present lower ρ_c values than that of the back reference ITO E. In addition, the ITO G presents the lowest R_{sh} . Thus, it is observed that both front ITOs F and G present the potential for R_S reduction compared to the reference back ITO E. Based on these *top-down* parameters, we then integrated both ITO F and G in the rear hole-collecting shell part of bifacial 6-inch solar cells and compare their performances to the reference ITO E.

ITO name	Thickness (nm)	Carrier density (cm^{-3})	R_{sh} (Ω/sq)	ρ_c dark ($\Omega \cdot \text{cm}^2$)
ITO E (ref)	75	2.71×10^{20}	75	0.40
ITO F	122	4.52×10^{20}	73	0.29
ITO G	120	3.06×10^{20}	37	0.33

Table 5.8 – Thickness, carrier density, R_{sh} as well as dark ρ_c obtained for the different ITOs under study, namely ITO E, the reference back ITO, ITO F and ITO G, the reference front ITO.

Figure 5.13 shows the I - V parameters of the 6-inch bifacial solar cells integrating the different ITO layers, namely, E, F, and G in the rear hole-collecting shell part. The I - V parameters presented here are measured using a dedicated edge exclusion mask resulting in an active area of 220.63 cm^2 compared to 244.34 cm^2 in the case of full area cells. This mask allows for the reduction of the losses and noise induced by edge damage. The first interesting observation here is the clear decrease in R_S provided by both ITO F and G compared to the reference back ITO E. Indeed, ITO F and G present average R_S values between 0.73 to $0.74 \Omega \text{ cm}^2$ compared to $0.82 \Omega \text{ cm}^2$ for the reference back ITO E. Note that here, despite slightly lower ρ_c obtained for ITO F, similar R_S values are obtained for ITO F and G once integrated in solar cells. This may be due to the difference in R_{sh} which was found to be higher for ITO F which may lead to slightly higher induced R_S by lateral transport inside the rear ITO. Remarkably here, the passivation quality is also found to be improved by both ITO F and ITO G. The FF_0 presents a gain of about $+1.2\%_{abs}$ for both ITOs. This FF_0 gain is shown to be induced by a passivation quality improvement at low injection. Indeed, the V_{MPP} values are found to be higher for both ITO F and ITO G and the V_{OC} values are found to be similar to that of ITO E. Finally, high

5.3. Cases A & B: Doped thin hydrogenated silicon and TCO layers coupling investigation

passivation quality improvements combined with significant R_S reductions result in a final FF gain of about $+1.45\%_{abs}$, going from an average FF of 81.08%, for the reference back ITO E, to a FF of 82.53% for both ITOs F and G. This results in a global average efficiency gain standing between 0.40 to $0.51\%_{abs}$. Note that both ITOs F and G present similar $I-V$ parameters except a slight difference in J_{SC} .

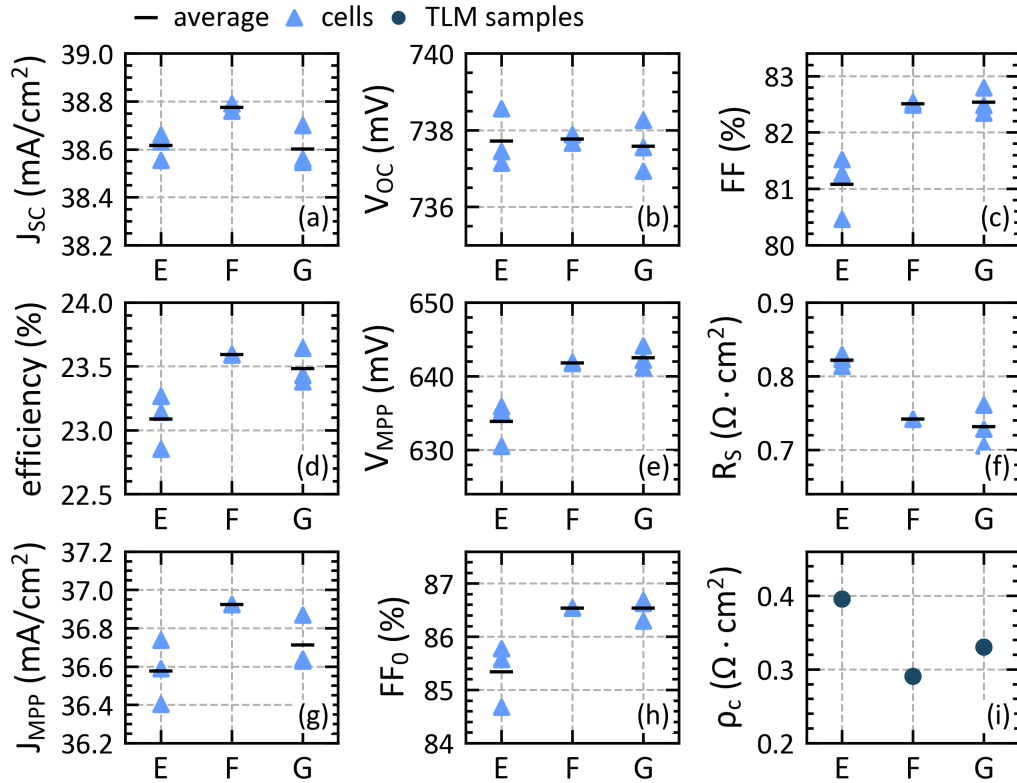


Figure 5.13 – $I-V$ parameters of the 6-inch bifacial solar cells under study integrating the different ITOs, namely E, F and G.

5.3.6 Conclusion

In this section, the use of multilayers was demonstrated to allow for significant R_S reduction thanks to optimized properties couplings between the doped thin silicon and the TCO layers. In addition, the use of the *top-down* and *bottom-up* approaches was demonstrated to allow us to (i) study precisely the different properties couplings arising at different levels inside the shell, (ii) to reveal the contributions of various layer characteristics to these couplings, and finally, (iii) to relate them to the final electrical transport quality of solar cells.

As a first step, n-type multilayer properties such as their thickness, activation energy, as well as bulk and surface crystallinity factors, were demonstrated to play an important role when coupled with AZO and ITO layers. In particular, a high surface crystallinity factor

Chapter 5. Top-down and bottom-up approaches to overcome electrical limitations

combined with a low activation energy was demonstrated to improve the electrical transport when coupled to both TCOs. In addition, improved electrical transport was found for thick n-type multilayers. Furthermore, the final properties coupling of AZO with n-type *am/nc* multilayers was shown to provide an increase of the passivation quality in addition to a R_{S} reduction. Finally, the investigation of the properties couplings between the n-type *am/nc* multilayers and the AZO layer by combining the *top-down* and *bottom-up* approaches gave us an in-depth understanding of the trade-off present between passivation and resistive losses. Interestingly, it was also demonstrated that the ρ_c values measured at MPP match more precisely the differences in R_{S} between the electron-collecting shell parts compared to the ρ_c values measured under dark conditions. However, to consolidate these results, further investigations are required, such as the ones which will be presented in chapter 6.

As a second step, the TCO properties were demonstrated to play an important role in defining the final passivation quality of the shell. Indeed, the final properties coupling of the thin silicon layer with the TCOs showed an increase of the lifetime, demonstrating that the global properties coupling must be considered for a correct assessment of the passivation ability of a given shell. As a third step, AZO multilayers were demonstrated to provide a reduction of R_{S} thanks to optimized coupling with the a-Si:H(n) layer, allowing for a ρ_c reduction while providing optimal lateral transport to the fingers thanks to reduced R_{sh} . However here, the trade-off between passivation and R_{S} was strongly present and further optimizations are required to mitigate it with the aim of improving the passivation quality. Finally, the ITO coupling with the a-Si:H(p) layer was optimized allowing for a significant decrease of R_{S} as well as an important passivation quality increase. In that case, the trade-off between R_{S} and passivation was successfully mitigated, leading to a significant *FF* and efficiency improvement.

Overall, this section demonstrates the importance of the whole shell sub-components properties coupling to shape the resulting shell characteristics and thus, to define the final solar cell performance.

5.4 Case C: Intrinsic and doped thin silicon layers coupling investigation

5.4.1 Introduction

In this section, the resulting properties coupling arising between the a-Si:H(i) and the a-Si:H(p) layers are investigated. The main roles of both layers are to provide, respectively, chemical and field effect passivation, in addition to selectivity. However, a-Si:H(i) layers are known to induce high resistive losses arising from the transverse carrier transport through it, as it is a very high resistive material layer, and from the energy barrier present at the heterointerface created with the c-Si bulk. The resulting coupling of the a-Si:H(p) layer with the a-Si:H(i) one tends to decrease the bulk resistivity of the intrinsic layer by depleting the energy band, resulting in a shift of the Fermi energy level closer to the valence band, which renders the a-Si:H(i) layer more conductive [Procel 2018]. However, the presence of the boron-doped a-Si:H layer on top of the a-Si:H(i) layer was demonstrated to generate Si dangling bond defects which degrade the electronic passivation resulting from the coupling of both layers [DeWolf 2007]. The boron concentration present inside the thin silicon layer must then be carefully adapted in order to provide high enough selectivity and low bulk resistivity while allowing for high passivation quality. In addition, it has been demonstrated that the defect density induced by the doping gas can be negligible if the presence of dopants is low [Olibet 2007b, Olibet 2007a, Olibet 2009]. This last point was demonstrated in the particular case of adding only a few parts per million (ppm) of doping gas to the deposition gas mixture used for the a-Si:H(i) layer growth. Such low-level doping has been called microdoping [Olibet 2009]. In this contribution, the addition of boron microdoping directly inside the a-Si:H(i) was proven to provide increased passivation quality thanks to additional field effect. In the present work, the applicability of boron microdoping inside the a-Si:H(i) was further investigated, aiming to decrease the resistive losses induced by the a-Si:H(i) layer while allowing for a high passivation quality. This section presents the first developments and proof of concept which are based on prior laboratory developments and know-how².

5.4.2 a-Si:H(i) layer thickness and microdoped multilayer

The first study was the investigation of the impact of the a-Si:H(i) layer thickness on the final device performance and the comparison of this impact with that of an a-Si:H(i)/boron microdoped a-Si:H(i) multilayer (named $i/\mu D$) of similar thickness. To do this, four different thin silicon layers were developed and integrated in the rear hole-collecting shell part of 6-inch bifacial solar cells. These layers are three a-Si:H(i) layers of thickness 8, 11, and 14 nm, as well as a $i/\mu D$ multilayer of 14 nm. The multilayer is composed of 7 nm of a-Si:H(i) layer completed with 7 nm of p-type microdoped a-Si:H(i) layer (referred as (μD)) deposited using a boron quantity of 84 part per million in the deposition gas flow. The a-Si:H(p) and ITO layers present

²The results presented in this section were obtained in collaboration with Antoine Descoeurdes whose contribution is gratefully acknowledged.

in the rear hole collecting shell part are kept constant for each condition.

	a-Si:H(i)			i/μD
Thickness (nm)	8	11	14	14

Table 5.9 – List of the three a-Si:H(i) layers as well as the a-Si:H(i)/boron microdoped a-Si:H(i) multilayer (named i/ μ D) under study along with their corresponding thicknesses.

Figure 5.14 shows the iFF and iV_{OC} measured at step#1, i.e., after front a-Si:H(i)/a-Si:H(n) and rear a-Si:H(i)/a-Si:H(p) or i/ μ D/a-Si:H(p) depositions, as well as the $I-V$ parameters of the solar cells integrating the three a-Si:H(i) layers and the i/ μ D multilayer. First, looking at the iFF and iV_{OC} values, it is observed that the passivation quality increases with the a-Si:H(i) thickness increase, both at high and low injection. This results in a higher FF_0 for the two thickest a-Si:H(i) layers. In addition, the R_S is found to significantly increase with the a-Si:H(i) layer thickness up to about $1.5 \Omega \text{cm}^2$, presenting an increase of $+0.09 \Omega \text{cm}^2$ per nm. This illustrates well the direct influence of the a-Si:H(i) layer on the final R_S value. Furthermore, an important trade-off between passivation quality and R_S is present, resulting in the highest FF values for the a-Si:H(i) layer of 11 nm, which presents the best ratio between the two contributions. Noticeably, the microdoped multilayer is actually found to decrease the R_S compared to a-Si:H(i) of similar thickness. Indeed, the i/ μ D multilayer provides a R_S decrease of $-0.18 \Omega \text{cm}^2$ compared to the a-Si:H(i) layer featuring a thickness of 14 nm. However, the expected performance gain resulting from this decrease of R_S is found to be jeopardised by a decrease of the passivation quality, which is clearly observed in the iFF , iV_{OC} and FF_0 values of the i/ μ D multilayer. Note that the highest V_{OC} obtained with the i/ μ D multilayer is not explained at the moment and may be due rather to process variations than physical properties. Furthermore, the V_{OC} values are found to be higher than the iV_{OC} ones measured at step#1, showing that the properties coupling of the thin silicon layers with both front and back ITOs promotes the passivation quality as presented in section 5.3.3. Finally, the efficiency value obtained for the a-Si:H(i) layer featuring a thickness of 11 nm is found to be similar to the one obtained for the microdoped multilayer. Interestingly, they are acting on two opposite sides of the passivation- R_S trade-off. Indeed, the a-Si:H(i) layer allows for a high passivation quality which is jeopardized by a high R_S value, whereas the i/ μ D multilayer allows for a low R_S value which is jeopardized by a low passivation quality. Thus, microdoping is found to allow for an important R_S reduction which is so far compensated by negative impacts on the passivation quality due to the boron dopants which are harmful to the passivation [DeWolf 2007].

5.4. Case C: Intrinsic and doped thin silicon layers coupling investigation

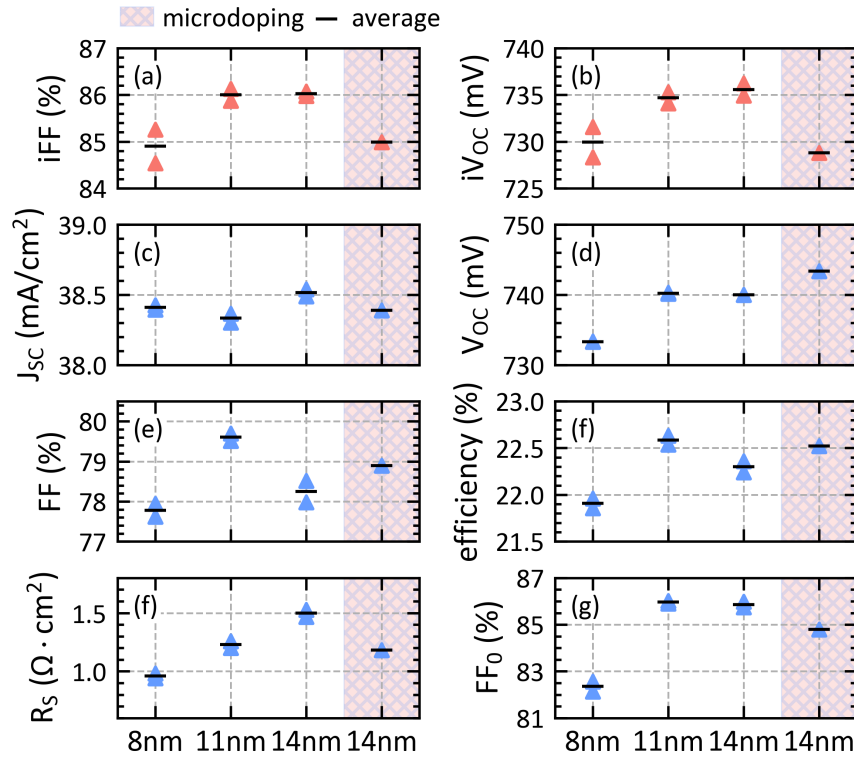


Figure 5.14 – iFF and iV_{OC} measured at step#1, i.e., after front $a\text{-Si:H}(i)/a\text{-Si:H}(n)$ and rear $a\text{-Si:H}(i)/a\text{-Si:H}(p)$ or $i/\mu D/a\text{-Si:H}(p)$ deposition along with the I-V parameters of the three different $a\text{-Si:H}(i)$ layer thickness of 8, 11 and 14 nm and the $i/\mu D$ multilayer of 14 nm.

5.4.3 Microdoped multilayer - boron quantity

Based on the previous results, $i/\mu D$ multilayers were further developed and investigated using a μD top layer featuring various TMB contents in the deposition gas flow and a total thickness of 11 nm. This thickness was demonstrated in the previous section to provide the best passivation- R_s trade-off of the $a\text{-Si:H}(i)$ layer. To build the different $i/\mu D$ multilayers, the $a\text{-Si:H}(i)$ layer thickness was set at 5 nm and the μD layer thickness at 6 nm, to target a final thickness of 11 nm. The different boron quantities used in the deposition gas flow are given in Table 5.10. The TMB flow is given in sccm and the corresponding boron quantity is given in ppm. The different $i/\mu D$ multilayers were then integrated in the rear hole-collecting shell part of 6-inch bifacial solar cells with fixed $a\text{-Si:H}(p)$ and ITO layers.

TMB flow (sccm)	Boron quantity (ppm)
3.5	84
7	168
14	334
21	496

Table 5.10 – List of the different TMB flows given in sccm along with the corresponding boron quantity given in part per million (ppm).

Figure 5.15 presents the iFF and iV_{OC} values measured at the step#1, i.e., after front a-Si:H(i)/a-Si:H(n) and rear $i/\mu D/a$ -Si:H(p) depositions, along with the different I - V parameters as a function of the TMB flow used for the deposition of the μD layer. First, it is observed that the R_S and FF_0 decrease with the TMB flow increase. Noticeably, an optimized trade-off is found for the 3.5 and the 7 sccm TMB flows which present similar FF and final efficiency, resulting from a compensation of either a high R_S and a high FF_0 , or a low FF_0 compensated by a low R_S , respectively. However, for the TMB flows higher than 7 sccm, the decrease of R_S does not compensate anymore the loss of passivation quality. Overall, the impact of boron on the passivation quality is clearly observed with the behaviour of iV_{OC} , V_{OC} , and FF_0 , which decrease with the boron content increase (i.e., with the TMB flow increase). These results evidence the strong positive and negative impacts of boron content on the R_S value and passivation quality, respectively. Note that the V_{OC} is found to be higher than the iV_{OC} measured at step#1, showing again that the properties coupling of the thin silicon layers with both front and back ITOs promote the passivation quality. Note that the V_{OC} is found to be higher than the iV_{OC} measured at step#1, showing again that the properties coupling of the thin silicon layers with both front and back ITOs promote the passivation quality. Overall, it is observed that the R_S - passivation quality trade-off was not successfully mitigated in the range of TMB flow under study, leading to a global decrease of efficiency. To optimize this trade-off, lower TMB flows must be investigated while keeping the a-Si:H(i) layer thickness at 5 nm. In addition, we may expect that the thinner the a-Si:H(i) layer, the lower must be the boron quantity inside the μD layer to not damage the passivation quality. This is studied in more detail in the two following sections 5.4.4 and 5.4.5.

5.4. Case C: Intrinsic and doped thin silicon layers coupling investigation

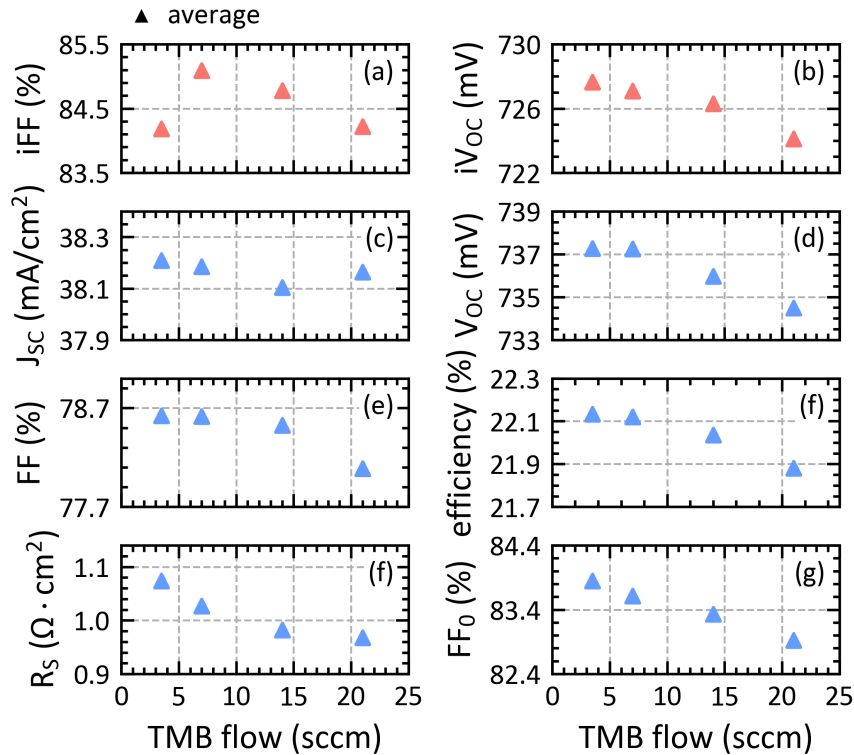


Figure 5.15 – iFF and iV_{OC} measured at step#1, i.e., after front $a\text{-Si:H}(i)/a\text{-Si:H}(n)$ and rear $i/\mu D/a\text{-Si:H}(p)$ depositions, along with the different I-V parameters as a function of the TMB flow, given in sccm, used for the deposition of the top μD layer.

5.4.4 Microdoped multilayer - thickness

To further investigate the impact of microdoping, this section focuses on the thicknesses of both $a\text{-Si:H}(i)$ and μD layers constituting the $i/\mu D$ multilayers. The impact of making the μD layer thicker and the $a\text{-Si:H}(i)$ layer thinner for a constant TMB flow is investigated with the aim to find the direction for optimal $i/\mu D$ multilayer development. The TMB flow was set at 3.5 sccm, corresponding to 84 ppm of boron in the deposition gas flow, the total $i/\mu D$ multilayer thickness was set at 10 nm, and the two $a\text{-Si:H}(i)$ and μD layers present various thickness combinations as presented in Table 5.11. Then, the different multilayers were integrated in the rear hole-collecting shell part of 6-inch bifacial solar cells with fixed $a\text{-Si:H}(p)$ and ITO layers.

Thickness (nm)		Thickness (nm)	
a-Si:H(i)	μD	a-Si:H(i)	μD
5	5	2	8
4	6	0	10

Table 5.11 – List of the different a-Si:H(i) and μD layers with their respective thicknesses used to build the different i/ μD multilayers.

Figure 5.16 plots the I - V parameters as a function of the μD layer thickness. First, it is observed that the FF_0 and V_{OC} values significantly decrease with the augmentation of the μD thickness, evidencing a significant reduction of the passivation quality, as observed previously. Conversely, the R_s is found to significantly decrease with the μD thickness increase, showing a minimal average value of $0.77 \Omega \text{ cm}^2$ against $0.86 \Omega \text{ cm}^2$ for the multilayer featuring the thickness combination of 5nm/5nm. However, the performance gain resulting from this R_s reduction does not compensate the passivation quality losses. Consequently, when increasing the μD thickness, the R_s and passivation quality trade-off is found to be only degraded and not improved. Consequently, the efficiency is found to decrease drastically with the μD thickness increase (starting from the case of i/ μD presenting the thickness combination of 5nm/5nm). Overall, the solar cell performances are shown to be extremely sensitive to the variation of the a-Si:H(i) layer thickness for a given μD layer. This demonstrated that the boron quantity must be adapted as a function of the a-Si:H(i) layer properties such as its thickness, to optimize the trade-off. From there, it is found that the thinner the a-Si:H(i) layer, the lower the boron content (i.e., the TMB flow) must be. Thus, for this fixed TMB flow of 3.5 sccm, an optimum is expected to exist for a thinner μD thickness, thus a thicker a-Si:H(i) thickness.

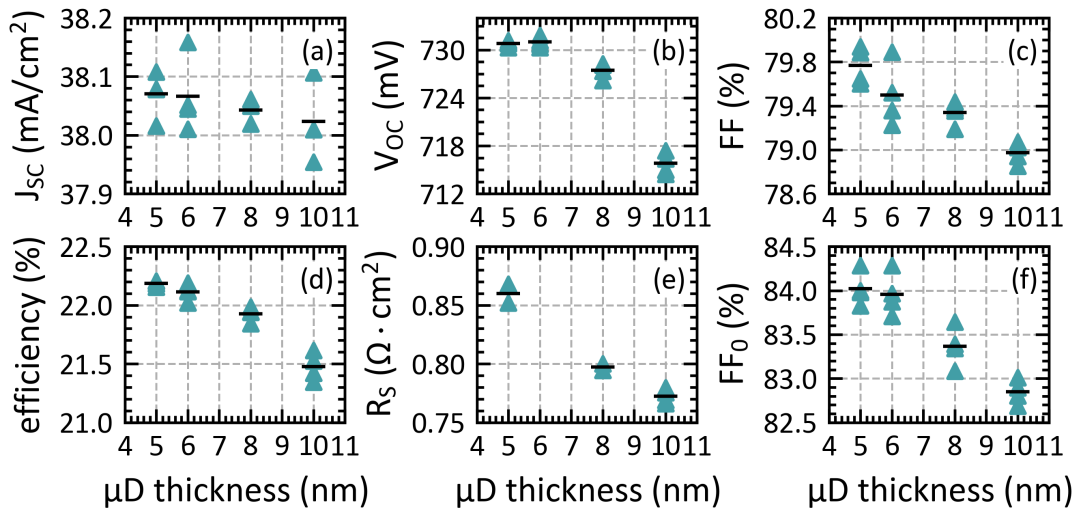


Figure 5.16 – I - V parameters as a function of the μD layer thickness. The total i/ μD thickness is kept constant at 10 nm.

5.4.5 Microdoped multilayer - boron quantity and thickness

Based on the previous results, the impact of the a-Si:H(i) layer thickness on the $i/\mu D$ multilayer properties was investigated. To do this, various boron quantities in the μD layer were used with two different thickness combinations of a-Si:H(i) and μD layers, targeting a total multilayer thickness of 27 nm. The aim here was to compare the effect of boron microdoping coupled with a thin and a thick bottom a-Si:H(i) layer and to investigate how the passivation quality is impacted by the μD overlayer. The different multilayer conditions under study are presented in Table 5.12. Three TMB flows of 2, 3.5, and 7 sccm were used, as well as two combinations of $i/\mu D$ thicknesses which are 14nm/13nm and 7nm/20nm. Then, as it has been done for the three previous studies, the different multilayers were integrated in the rear hole-collecting shell part of 6-inch bifacial solar cells with fixed a-Si:H(p) and ITO layers.

Thickness (nm)		Boron	
a-Si:H(i)	μD	TMB flow (sccm)	Boron quantity (ppm)
14	13	3.5	84
14	13	7	168
7	20	2	48
7	20	3.5	84

Table 5.12 – List of the different a-Si:H(i) and μD thicknesses as well as the TMB flows with the corresponding boron quantity given in part per million (ppm), used for the deposition of the different μD layers integrated in the multilayers $i/\mu D$. The $i/\mu D$ multilayers feature a total thickness of 27 nm.

Figure 5.17 plots the I - V parameters as a function of the TMB flow for the two groups of multilayer thicknesses which are 14nm/13nm (reddish left part of the graph) and 7nm/20nm (blueish right part of the graph). First, looking at the multilayers with the thick a-Si:H(i) layer of 14 nm, it is observed that the R_s decreases by about $-0.1 \Omega \text{ cm}^2$ when passing from 3.5 sccm to 7 sccm of TMB flow. Noticeably here, this R_s decrease goes along with a FF_0 increase of about $+0.23\%_{abs}$. Contrary to what has been observed for the previous experiments with thin a-Si:H(i) layers, the microdoping is found to provide additional passivation, which may be due to an improved field effect passivation [Olibet 2009]. In addition, the 3.5 sccm TMB flow of the 14nm/13nm condition allows for a higher FF_0 than those obtained for both multilayers with the thin a-Si:H(i) layers of 7 nm, but the obtained R_s is found to be the highest, showing the significant contribution of the 14 nm a-Si:H(i) layer to the resistive losses.

In the case of the 7nm/20nm multilayer, a clear R_s decrease is also observed with the TMB flow increase. The R_s decreases by $-0.1 \Omega \text{ cm}^2$ when passing from 2 sccm to 3.5 sccm of TMB flow. This is similar to the R_s decrease obtained when passing from 3.5 sccm to 7 sccm of TMB flow in the case of 14nm/13nm multilayers. This demonstrates again the high response of R_s to the TMB flow, i.e., to the boron quantity, for thin a-Si:H(i) layers. In parallel, however, the passivation quality is found to be directly jeopardized, leading to lower FF_0 and V_{OC} for 3.5

scm of TMB flow. This demonstrates that in addition to providing lower passivation quality compared to the thick a-Si:H(i) layer, the $i/\mu D$ multilayer with the thin a-Si:H(i) layer of 7 nm is very sensitive to the boron quantity. Furthermore, this $i/\mu D$ multilayer loses quickly its passivation quality with the increase of the TMB flow, which impacts directly its final efficiency as the R_s reduction is not enough to compensate the passivation quality loss. Finally, it is observed that the 2 sccm TMB flow is not high enough to decrease the resulting R_s as low as in the case of the 14nm/13nm multilayer with 7 sccm of TMB flow. It is also observed that passing from 3.5 sccm of TMB flow with the 14nm/13nm multilayer to 3.5 sccm of TMB flow with the 7nm/20nm multilayer, the R_s is significantly reduced but along with a significant reduction of the FF_0 value, which again leads to a jeopardized R_s - passivation trade-off.

Overall, the 14nm/13nm multilayers demonstrated a passivation which is resilient to boron microdoping, resulting in high FF_0 values. In particular, the 14nm/13nm multilayer with 7 sccm of TMB flow presents a low R_s value close to that of the 7nm/20nm multilayer with 3.5 sccm of TMB flow in addition to the highest FF_0 , together leading to the highest solar cell efficiency. This demonstrates the importance of the bottom a-Si:H(i) layer to provide a high passivation quality which must in addition be resilient to the boron quantity inside the top μD layer. However, an optimal R_s - passivation trade-off is still demonstrated to be challenging to reach. To face this issue, a relevant solution would be, for a given bottom a-Si:H(i) layer, to create a gradient of boron quantity inside the μD layer, such that the boron content increases with the μD thickness, and to fine-tune the R_s - passivation trade-off in that way.

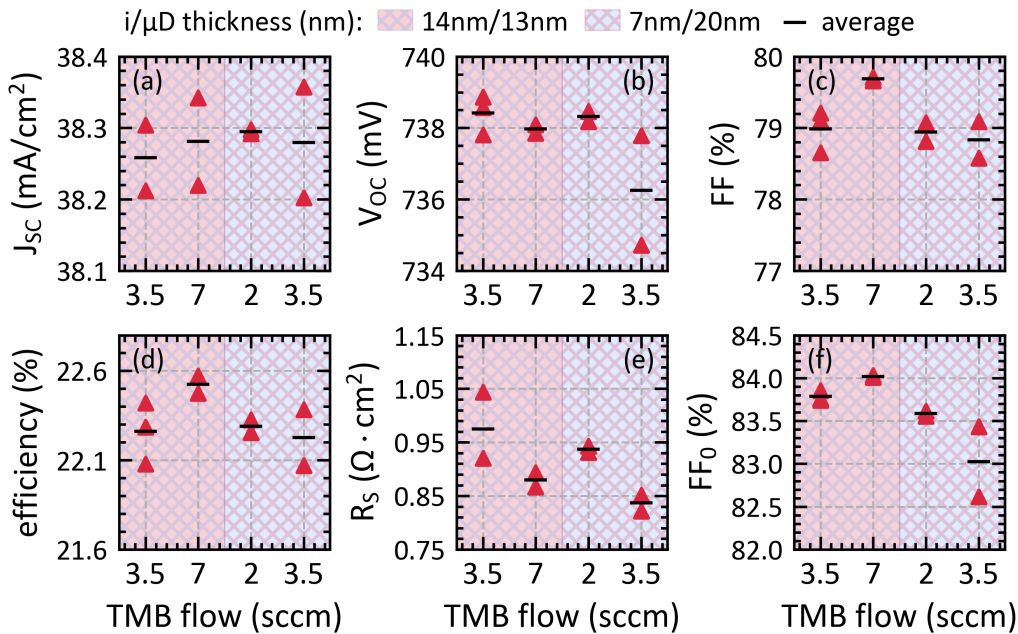


Figure 5.17 – I-V parameters as a function of the TMB flow given in sccm for the two groups of multilayer thicknesses which are 14nm/13nm (reddish left part of the graph) and 7nm/20nm (blueish right part of the graph).

5.4.6 Conclusion

This study demonstrated the potential of boron microdoping to decrease the final R_S of solar cells. Indeed, the $i/\mu D$ multilayers demonstrated a significant R_S decrease compared to single a-Si:H(i) layers of similar thickness. However, the passivation quality was also found to be reduced. This phenomenon was further evidenced with the increase of the boron quantity inside the deposition gas flow. Indeed, it was observed that the higher the boron quantity, the lower the R_S , as well as the lower the passivation quality, as seen in the decrease of both the V_{OC} and FF_0 values. Similarly, when decreasing the thickness of the bottom a-Si:H(i) layer, the R_S is found to decrease along with the passivation quality. The boron quantity as well as the bottom a-Si:H(i) layer thickness were thus found to both play a role on the R_S and the passivation quality. Finally, it was demonstrated that the ability of μD layers to decrease the R_S while allowing for high passivation quality was possible for thick a-Si:H(i) layers. Indeed, the 14nm/13nm $i/\mu D$ multilayer presents a significant R_S decrease with 7 sccm of TMB flow along with a FF_0 increase, whereas the R_S decrease occurs together with a passivation quality decrease for the 7nm/20nm $i/\mu D$ multilayer with TMB flows of 2 sccm and 3.5 sccm. From these results, it turns out that optimizing the trade-off between passivation quality and R_S of $i/\mu D$ multilayers is challenging, and that the μD layer must be adapted as a function of the a-Si:H(i) layer properties. Overall, it was demonstrated that the boron content has a direct effect on the R_S , regardless of the a-Si:H(i) layer thickness, and that the thinner the a-Si:H(i) layer for a given μD layer thickness, the lower the boron content must be inside the μD layer to not damage the passivation quality. Thus, a promising solution will be to adapt the boron quantity as a function of the distance to the a-Si:H(i) layer, such as to create a gradient of boron inside the μD layer. The gradient must start with very small boron quantity at the contact with the a-Si:H(i) layer and increase slowly with the μD thickness. Such a gradient may allow for the required R_S reduction without jeopardizing the passivation quality.

5.5 Conclusion

In this chapter, the applicability of the *top-down* and the *bottom-up* approaches to the investigation and mitigation of the electrical losses in SHJ solar cells has been demonstrated. First, applying the *top-down* method allowed for the engineering of layers featuring various material properties and their characterization. Then, the *bottom-up* approach made it possible to study at different process steps the properties of shells incorporating these layers. Combining both methods was demonstrated to allow us to study the resulting transport quality by first investigating selected physical parameters of various material layers with the *top-down* approach and, secondly, to study how they impact the final solar cell performance by analysing the shell properties obtained with the *bottom-up* approach. In addition, this was demonstrated to make it possible to optimize the resulting shell performance according to the different architectures the shell must fit in. In particular, the development of multilayers was proven to allow for electrical transport losses mitigation by decoupling the different material contributions and by tuning the material properties coupling arising at different levels inside

Chapter 5. Top-down and bottom-up approaches to overcome electrical limitations

the shell. More specifically, it was demonstrated that n-type multilayers allow one to decouple surface and bulk characteristics, allowing for optimal electrical coupling with the top TCO layers. In addition, the importance of the different trade-offs arising when optimizing the shells, such as the one between passivation quality and R_s losses were pinpointed. During these investigations, the properties of the TCO layers were demonstrated to play a significant role in the resulting shell's passivation quality. Furthermore, AZO multilayers demonstrated the necessity of optimizing separately the coupling with the a-Si:H(n) layer to target a low ρ_c , and the AZO R_{sh} required for optimal lateral transport to the fingers. In a similar approach, the optimization of the ITO coupling with the a-Si:H(p) layer demonstrated the possibility to successfully optimize the trade-off between R_s and passivation quality, resulting in a significant FF and efficiency improvement. Finally, multilayers incorporating a-Si:H(i) and microdoped a-Si:H(i) layers were demonstrated to allow for optimization of layer properties couplings resulting in significant R_s reductions. However here, the trade-off between passivation and R_s was demonstrated to be challenging to address.

Overall, the development of multilayers was demonstrated to allow the exploration and fine-tuning of the shell characteristics by focusing directly on the properties couplings arising between the material layers at different levels inside the shell. In particular, the multilayer development was shown to be a relevant solution to allow for R_s reduction and to optimize the significant trade-off between R_s reduction and passivation quality improvement, by adapting the final properties coupling of the material layers. More specifically, the bulk and the surface properties of the different material layers were demonstrated to be suitable levers to optimize the resulting properties coupling. Furthermore, we showed how the *top-down* and the *bottom-up* approaches combined together allow one to pinpoint the shell sub-component properties which are required for electrical losses mitigation. This was proven to be a powerful method to improve solar cells since it provides relevant characterizations which are needed to acquire knowledge and guidance to further analyse and optimize their performance. In particular, the concept of shell together with both the *top-down* and the *bottom-up* approaches has proved to be a great help for our developments, allowing us to speed up and guide more precisely the optimization of our baseline solar cells. This started and will continue to provide us with the knowledge and expertise necessary to pursue our developments with high precision. In parallel, to reach high device performance, the optical requirement of the shell must also be considered and optimized and can also be addressed with the use of the *top-down* and the *bottom-up* approaches.

In the following chapter 6, the most promising shells featuring various layers and multilayers developed and presented in this chapter will be integrated in actual best-in-class in-house baseline solar cells. In addition, the optical properties of the shells required to reach high solar cell efficiency will also be addressed.

6 Integration in solar cells

Summary

This chapter presents the outcomes of the application of the methodology combining the shell concept and both *top-down* and *bottom-up* approaches to study and mitigate the electrical transport losses as well as the integration of various material layers developed and presented in chapter 5, in the best baseline solar cells. First, a rigorous R_S losses breakdown analysis was performed to investigate the different contributions resulting from ρ_c values measured by TLM at MPP and in dark conditions. It was demonstrated that the ρ_c values measured at MPP of both electron and hole-collecting shell parts seem to better correspond to the actual R_S of solar cells than the ρ_c values measured in dark conditions. Secondly, record solar cells integrating the different layers and multilayers developed in chapter 5 were presented. Combining the shell concept with both the *top-down* and the *bottom-up* approaches was demonstrated to allow us to efficiently improve our solar cell baseline. Thanks to this methodology, optimal shells were developed and their integration in actual devices made it possible to reach FF up to 83.2%, in the case of full area 6-inch solar cells, and to engineer IBC cells with a size of 5 cm \times 5 cm demonstrating efficiencies up to 25.45%. Finally, further optimizations of the optical properties of shells were conducted. Consequently, a high J_{SC} of 40.81 mA cm⁻² was obtained for 2 cm \times 2 cm screen-printed SHJ monofacial solar cells and, combining optimal electrical and optical properties, an impressive efficiency of 24.24% was demonstrated in the case of AZO layers present in the rear electron-collecting shell part.

6.1 Introduction

This chapter presents the relevant outcomes resulting from the application of the methodology combining the shell concept and both *top-down* and *bottom-up* approaches to study and mitigate the electrical transport losses as well as the integration of promising shells, featuring various material layers developed in chapter 5, in the best baseline solar cells. First, the integration of the contact resistivity values obtained in dark and at MPP conditions in

rigorous R_S breakdowns is presented. The aim is to investigate if the ρ_c value obtained at MPP conditions is more relevant than the one obtained in dark conditions. The additional accuracy and insights the value of ρ_c measured at MPP conditions may provide compared to ρ_c values obtained in dark conditions are studied. Then, based on the layer developments presented in chapter 5, the most promising shells were integrated in the best baseline solar cells, for the different architectures under study. These are the full 6-inch bifacial, the $2\text{ cm} \times 2\text{ cm}$ monofacial, and the IBC, which were introduced in section 3.1.1. The shells were further developed to be integrated into the different process flows and to optimally fit with the different architecture constraints. The final device performances resulting from the different studies and the best SHJ solar cells obtained are presented. Finally, the importance of considering the optical quality while optimizing the electrical properties is addressed. Indeed, as presented in section 2.1.2, in addition to electrical properties, the shell must also comply with optical requirements so as not to hinder the light absorption in the c-Si bulk. In particular, an important trade-off is generally present between optical and electrical properties and it is challenging to optimize one of the two without jeopardizing the other. Such an optical optimization was performed in the case of aluminium-doped zinc oxide (AZO), which was further optimized to act as an optimal indium-free TCO in the rear reflector of $2\text{ cm} \times 2\text{ cm}$ SHJ monofacial solar cells.

6.2 R_S breakdown integrating MPP and dark ρ_c values

This section presents an analysis of R_S breakdown performed to further study the additional accuracy, inputs and insights the value of ρ_c measured at MPP conditions may provide compared to the one obtained in dark conditions. To do this, $2\text{ cm} \times 2\text{ cm}$ monofacial solar cells integrating two different electron-collecting shell parts at the rear side and a similar front hole-collecting shell part, namely shells #11n and #12n, were processed. Then, their R_S were characterized with the method presented in section 3.2.2. The ρ_c of the electron collecting shell parts (named ρ_{cn}) were characterized in dark and at MPP conditions. Then, a R_S breakdown was performed based on the method and computations presented in [Haschke 2020]. To perform this R_S breakdown, the different required data are presented in Table 6.2. A front R_{sh} TCO of $50\ \Omega/\text{sq}$, a finger pitch of 1.85 mm and a R_S induced by finger of $0.1\ \Omega\text{cm}^2$ were considered. In addition, the MPP injection is extracted for each cell and presents values between 2.34×10^{15} to $2.43 \times 10^{15}\text{ cm}^{-3}$, which are close to the value of $2.5 \times 10^{15}\text{ cm}^{-3}$ presented in section 4.3. Finally, the ρ_c value of the front hole-collecting shell part (named ρ_{cp}) was measured in dark and at MPP conditions on p-type wafer (with a R_{sh} of $700\ \Omega/\text{sq}$, see section 4.5.2, p-type part of shell #2p). The dark ρ_{cp} presents a value of $0.28\ \Omega\text{cm}^2$ which is close to the one obtained in [Haschke 2020] for the p-type amorphous silicon layer. Finally, R_S breakdowns were calculated for both shells #11 and #12, integrating the dark ρ_{cp} value as well as the ρ_{cn} values obtained either in the dark or at MPP conditions, and are presented in Table 6.1¹.

¹The R_S breakdown computations presented in this section were performed in collaboration with Luca Antognini whose contributions are gratefully acknowledged.

6.2. R_S breakdown integrating MPP and dark ρ_c values

First, it is observed that the computed R_S values using the dark ρ_{cn} and ρ_{cp} values are, for both shells, about $0.18 \Omega \text{cm}^2$ lower than the ones obtained in the actual solar cells. In addition, the computed R_S obtained when using the MPP ρ_{cn} values are also found to be lower by about 0.09 to $0.13 \Omega \text{cm}^2$. Assuming that the ρ_{cn} values at MPP are accurate, this suggests that the actual ρ_{cp} may present values between 0.37 to $0.41 \Omega \text{cm}^2$ instead of $0.28 \Omega \text{cm}^2$, which is still in line with values reported from literature [Haschke 2020, Luderer 2020, Lachenal 2019]. Overall, this suggests that the actual ρ_c values measured at MPP may correspond better to the actual R_S losses of solar cells. Secondly, the ρ_{cp} value measured at MPP conditions (see section 4.5.2) is found to be $0.72 \Omega \text{cm}^2$, which is about two times too high compared to the expected value of ρ_{cp} under MPP conditions. The ρ_{cp} value measured at MPP may be overestimated because of two different aspects: first, because of the high R_{sh} of the c-Si(p) wafer used here, which was demonstrated to lead to a higher ρ_c value at MPP compared to c-Si wafer with lower R_{sh} (see section 4.4.2) and secondly, because of the polarity of the c-Si(p) wafer used for ρ_{cp} measurement, which is the opposite of the polarity of actual solar cells featuring an n-type c-Si bulk. These two aspects are expected to result in inaccurate values of ρ_{cp} . To go further in this analysis, additional studies could be first, to measure ρ_{cp} values using c-Si(p) wafers with lower resistivity, secondly, to investigate further the possibility to extract ρ_{cp} values at MPP conditions of hole-collecting shell parts deposited on c-Si(n) wafer (based on the results presented in section 4.5.2), and finally, to insert these ρ_{cp} values in supplementary R_S breakdown to study the resulting outcomes. Overall, to have a better understanding, additional co-processed solar cells and TLM samples must be developed and similar R_S breakdowns must be calculated to have more statistics and broader insights into the outcomes of such R_S analysis.

Shell	$\rho_{cn} (\Omega \text{cm}^2)$		$R_S (\Omega \text{cm}^2)$		
	Dark	MPP	Cell	Computed dark	Computed MPP
#11n	0.014	0.107	0.74	0.57	0.65
#12n	0.014	0.081	0.75	0.57	0.62

Table 6.1 – ρ_c of the electron-collecting shell part of shells #11n and #12n obtained in dark and at MPP conditions along with the R_S obtained directly from the solar cells and the two computed R_S values using the R_S breakdown with either the dark or the MPP ρ_{cn} values.

Data for the R_S breakdown	
Finger pitch (cm)	0.185
R_S finger (Ωcm^2)	0.10
R_{sh} front TCO (Ω/sq)	50
ρ_{cp} dark (Ωcm^2)	0.28
MPP injection shell #11n (cm^{-3})	2.43×10^{15}
MPP injection shell #12n (cm^{-3})	2.34×10^{15}

Table 6.2 – List of the different data used for the R_S breakdown.

6.3 High quality SHJ shells for high performance solar cells

This section presents the high performance solar cells demonstrating the best FF , J_{SC} and efficiencies, which were processed during this work. These solar cells integrate high-quality SHJ shells featuring various layers and multilayers developed in chapter 5. The relevant outcomes resulting from the application of the methodology combining the shell concept alongside both the *top-down* and the *bottom-up* approaches for the development and improvement of our SHJ solar cell baseline, considering in addition the different architectures, are demonstrated.

6.3.1 Indium tin oxide optimization for 6-inch solar cells

Based on the results presented in section 5.3.5, the ITO G was integrated in the best baseline 6-inch bifacial solar cells. Then, the final solar cell performances were measured in three different conditions. First, in a bifacial full area configuration with a total area of 244.34 cm^2 , named "bifi", secondly in a bifacial configuration using a dedicated edge exclusion mask resulting in an active area of 220.63 cm^2 to reduce the losses and noise induced by edge damages, named "bifi EE", and finally after monofacialization and using the edge exclusion mask, named "mono EE" (see section 3.1.2). Figure 6.1 presents the FF and efficiency values obtained for the three conditions described above and for two different solar cell batches, named batch 1 and batch 2. It is observed that a high FF value of 83.2% with an efficiency of 24.38% and a high FF of 83.05% along with a high efficiency of 24.43% are reached. In addition, it is observed that the edge exclusion allows for higher FF and efficiency values thanks to the suppression of harmful edge effects. Moreover, the monofacialization combined with edge exclusion allows for significant FF and efficiency improvements thanks to optical and electrical quality enhancements (as presented in section 3.1.2) in addition to the suppression of the edge effects.

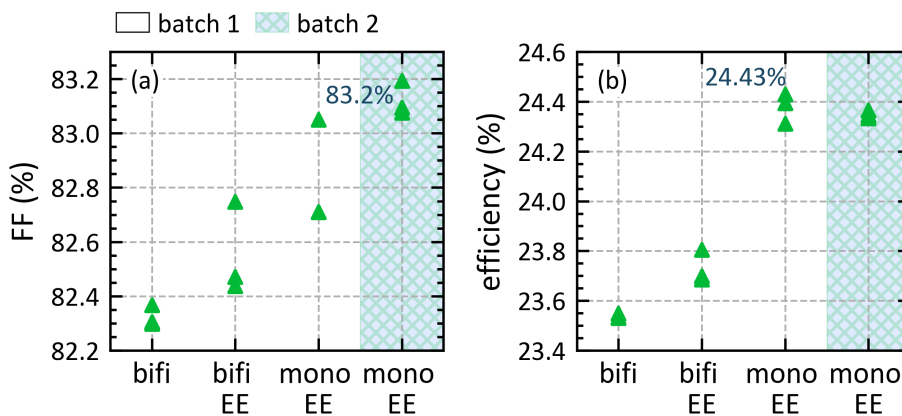


Figure 6.1 – FF and efficiency values obtained for the different configurations which are: bifacial (bifi), bifacial with edge exclusion (bifi EE) and monofacial with edge exclusion (mono EE) for two different solar cells batches, named batch 1 and batch 2.

6.3. High quality SHJ shells for high performance solar cells

From this study the best certified 6-inch monofacialized solar cell with a full area of 244.33 cm² presents an efficiency of 24.03% along with a high FF of 83.06%, a V_{OC} of 742 mV and J_{SC} of 38.99 mA cm⁻².²

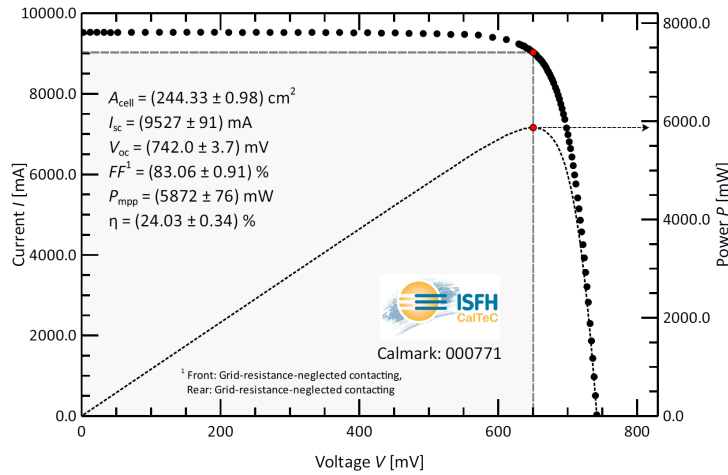


Figure 6.2 – Certified I-V curves and solar cell parameters for a high performances 6-inch monofacialized solar cell with a full area of 244.33 cm².

6.3.2 n-type thin silicon multilayer optimization for 2cm x 2cm monofacial solar cells

Based on the n-type thin silicon multilayer development presented in section 5.3.2, the medium E_a n-type am/nc multilayer was integrated inside the rear electron-collecting shell part of optimized 2 cm × 2 cm screen-printed monofacial solar cells and coupled with either an AZO or an ITO layer which present similar properties to those presented in section 5.3.2. From this integration, Figure 6.3 presents the $J-V$ curves and parameters of the best solar cells featuring either the AZO or the ITO rear layer. These devices demonstrated impressive FF values of 82.33% and 82.27% with high efficiency of 24.12% and 24.32%, respectively. This demonstrates that the am/nc multilayers are effective candidates to push further the performances of two-side contacted SHJ solar cells. Figure 6.4 presents the $I-V$ curve and solar cell parameters of the best certified 2 cm × 2 cm screen-printed monofacial solar cells integrating the medium E_a n-type am/nc multilayer and an ITO layer in the rear electron-collecting shell part. This device features a certified FF of 82.28% along with a high certified efficiency of 24.21%.

²The results presented in this section were obtained in collaboration with Antoine Descoedres and Jonas Geissbühler whose contributions are gratefully acknowledged.

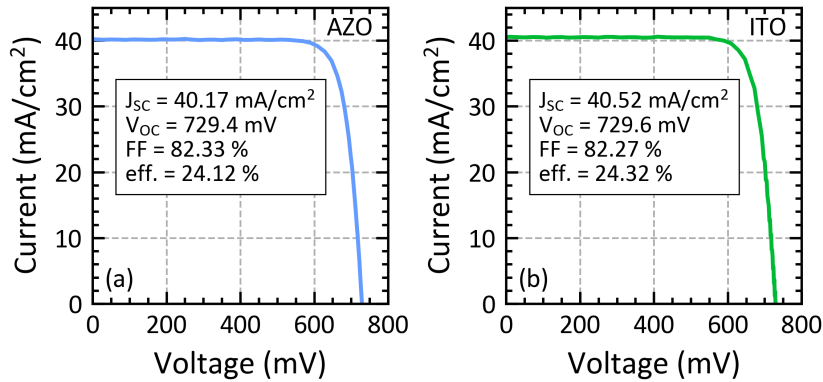


Figure 6.3 – J-V curves and parameters of the best 2 cm × 2 cm screen-printed monofacial solar cells featuring an AZO and an ITO rear layer.

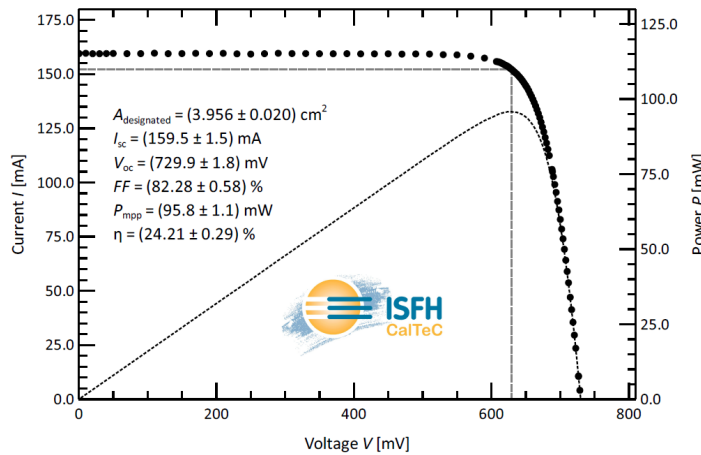


Fig. 2: Plot of the measured current-voltage characteristics under standard test conditions.

Figure 6.4 – Certified I-V curve and solar cell parameters for a high performance 2 cm × 2 cm monofacial solar cell integrating the medium E_a n-type am/nc multilayer and an ITO layer in the rear electron-collecting shell part.

6.3.3 Top-down and bottom-up approaches for IBC optimization

Then, based on the similar methodology using the shell concept combined with both the *top-down* and the *bottom-up* approaches, n-type *am/nc* multilayers fulfilling in addition tunnel junction requirements were developed and integrated into screen-printed tunnel IBC solar cells and completed with AZO layer. The best tunnel IBC solar cell demonstrated an impressive *FF* of 82.5% along with a very high efficiency of 25.45% (see Figure 6.5). From our IBC device investigations and development, the best certified IBC cell presents a high efficiency of 25.00%

6.3. High quality SHJ shells for high performance solar cells

(see Figure 6.6)³. This demonstrates further that the methodology using the shell concept and both the *top-down* and the *bottom-up* approaches together allows for effective device improvement by providing significant insights to guide our developments and is applicable for various solar cell architectures.

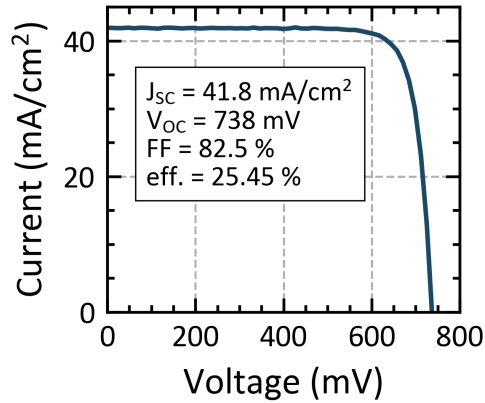


Figure 6.5 – J-V curve and solar cell parameters for a high performance IBC solar cell featuring an area of 25 cm².

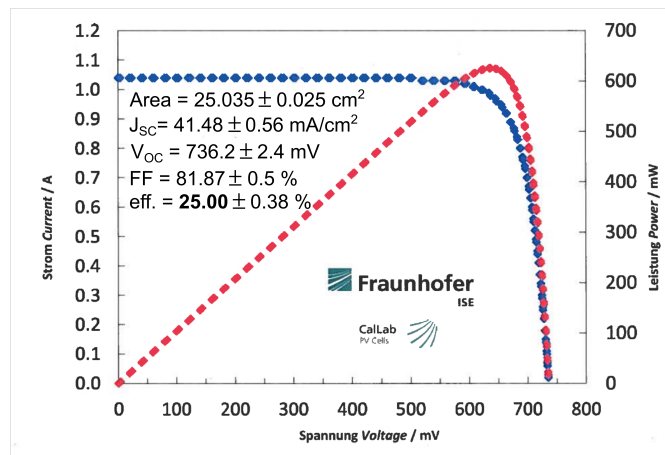


Figure 6.6 – Certified I-V curve and solar cell parameters for a high performance IBC solar cell featuring an area of 25.035 cm².

³The results presented in this section were obtained in collaboration with Bertrand Paviet-Salomon whose contribution is gratefully acknowledged.

6.4 SHJ shells - optical properties optimization

*This last section presents investigations on the optical properties of the rear reflector in $2\text{ cm} \times 2\text{ cm}$ monofacial solar cell integrating aluminium-doped zinc oxide in the rear electron-collecting shell part. These investigations are based on a paper published in *IEEE Journal of Photovoltaics* and reproduced with permission from [Senaud 2019]. Copyright 2019, IEEE.*

6.4.1 Introduction

This last section addresses the importance of combining high optical and electrical qualities together to reach high device efficiencies. Indeed, as presented in section 2.1.2, in addition to electrical properties, the shell must also comply with optical requirements so as not to hinder the light absorption in the absorber. Thus, importantly, while optimizing the electrical properties of a shell, care must be taken to not jeopardize its light collection. Indeed, the efficiency may significantly be limited by optical losses due to the parasitic absorption of light at the front and rear parts of SHJ shells [Holman 2013c, Holman 2013b]. In particular, in the rear shell part of monofacial SHJ solar cells, the TCO and metal reflector, if not properly optimized, are the origin of significant losses in the infrared (IR) part of the spectrum. These losses come from plasmonic absorption at the TCO/metal interface and from free-carrier absorption (FCA) inside the TCO [Holman 2013c, Holman 2013a]. Reducing these IR parasitic absorption losses constitutes an important challenge in the quest to improve the device short-circuit current density (J_{SC}) and therefore, the SHJ device efficiency. Plasmonic absorption is mainly induced by the parallel-polarized light of evanescent waves impinging on the metal surface, which excites surface plasmons [Holman 2013a]. In addition, this absorption has been demonstrated to depend on the metal type and on its surface roughness [Kim 2011]. FCA in contrast is induced by the free carriers contained inside the TCO, which mainly absorb light in the IR part of the solar spectrum. According to the Drude model, the FCA is directly proportional to the carrier density and inversely proportional to the optical mobility of the material [Chopra 1983]. As presented in section 3.1.2, both parameters depend on oxygen vacancies in TCO which can be modified by varying the oxygen partial pressure during TCO deposition. An increase in free carrier density induces a shift of the IR absorption edge to shorter wavelengths, thus narrowing the transmission window. This shift is determined by the plasma oscillation of the free carriers, which screen, for IR energy, the incident electromagnetic wave via intra-band transitions within the conduction band. This involves a sharp reduction of the optical transmission near the plasma resonance frequency. Thus any attempt to decrease the resistivity of the TCO by increasing the carrier density will increase the IR light absorption, which may result in a strong trade-off between electrical and optical quality. As the main part of the solar spectrum reaching the rear side of the SHJ solar cell actually consists of IR light, the back reflectors may suffer from both of the absorption mechanisms mentioned above. To reduce the plasmonic rear absorption, a moderately absorbing 150 to 200-nm-thick TCO layer is usually deposited on the back side of SHJ solar cells [DeWolf 2012, Battaglia 2016]. This thick layer reduces the amount of evanescent waves reaching the metal by increasing the

6.4. SHJ shells - optical properties optimization

internal reflectance at the rear surface, which yields an increase of the IR spectral response of the cell [Holman 2013c]. Such a structure with a thick back TCO efficiently reduces the plasmonic absorption in the metal. However, as the TCO layer becomes thicker, the FCA losses will become increasingly important (for given material properties). Therefore, care must be taken not to negate the optical gains provided by the reduction of the plasmonic absorption losses with an increase in FCA when thickening the TCO layer. In addition, as the rear TCO layer has to efficiently ensure high-quality electrical properties coupling when combined with the rear thin silicon and metal layers, several constraints on the electrical properties of the former are present. Therefore, the degrees of freedom available to tune it are reduced. There is then an important trade-off between the optical and electrical properties of SHJ shells evidencing that all shell components need to be considered together to improve both the final electrical and optical qualities, to result in high solar cell performance.

In this context, this last section aims at improving the back IR reflector of monofacial SHJ solar cells by mitigating its optical losses without compromising the electrical transport properties of the device, using aluminium-doped zinc oxide (AZO). In this last work, AZO is further optimized as an indium-free alternative material to the standard back ITO. Similarly to what was done in [Holman 2013c] for ITO, the thickness of the rear AZO layer and the oxygen (O₂) content in the deposition gas flow are varied to find the optimal combination leading to the highest J_{SC} . Table 6.3 shows the different AZO layers under study along with their referred numbers, the O₂ content in the deposition gas flow, carrier concentration (N) and thickness.

AZO layer	O ₂ (%)	N (cm ⁻³)	Thickness (nm)
#1	0.07	1.94×10^{20}	160
#2	0.10	9.37×10^{19}	160
#3	0.15	4.08×10^{19}	160
#4	0.15	9.45×10^{19}	65
#5	0.15	6.16×10^{19}	105
#6	0.15	3.90×10^{19}	245
#7	0.15	2.39×10^{19}	380

Table 6.3 – Parameters of the different AZO layers with their referred numbers, O₂ quantity, carrier concentration (N) and thickness.

6.4.2 Results and discussion

The J_{SC} of solar cells with different oxygen contents in the AZO deposition gas flow and a fixed thickness of 160 nm are depicted in Figure 6.7a. First, it is observed that J_{SC} strongly increases with the oxygen content. Namely, increasing the O₂ content in the deposition gas flow from 0.07 to 0.15 % increases the J_{SC} by 0.56 mA cm⁻². Consistently, the corresponding EQE curves (see Figure 6.8) are higher in the 1000 nm to 1200 nm spectral range for higher oxygen contents. Similarly to what was observed in [Holman 2013c] for the case of ITO, the

reflectivity value at 1200 nm (see also Figure 6.8) increases for higher oxygen contents (lower carrier concentrations). Overall, it is thus observed that the increase in oxygen content reduces the parasitic absorption in the AZO layer, as evidenced by the decrease in the 1-R-EQE curves (Figure 6.8). Hence, decreasing the AZO carrier concentration consistently reduces the FCA losses, resulting in an improved IR back reflector (higher escape light) allowing for higher J_{SC} .

The J_{SC} of cells with different AZO thicknesses and a constant O_2 content of 0.15 % are depicted in Figure 6.7b. A J_{SC} gain of 0.23 mA cm^{-2} is obtained when replacing the 65-nm-thick AZO layer by a 380-nm-thick one. Compared to the oxygen series, this means that an additional 0.11 mA cm^{-2} gain with respect to the 160 nm and 0.15 % AZO layer could be obtained. Consistently, the EQE, 1-R (total absorption) and 1-R-EQE (parasitic absorption) curves in Figure 6.8 show the lowest IR parasitic absorption losses in the 1000 to 1200 nm range for the device with a 380-nm-thick rear AZO layer. As a first conclusion we can hence state that this additional J_{SC} gain comes from a reduction of the plasmonic absorption as the thickness increases, since fewer evanescent waves reach the blanket silver layer.

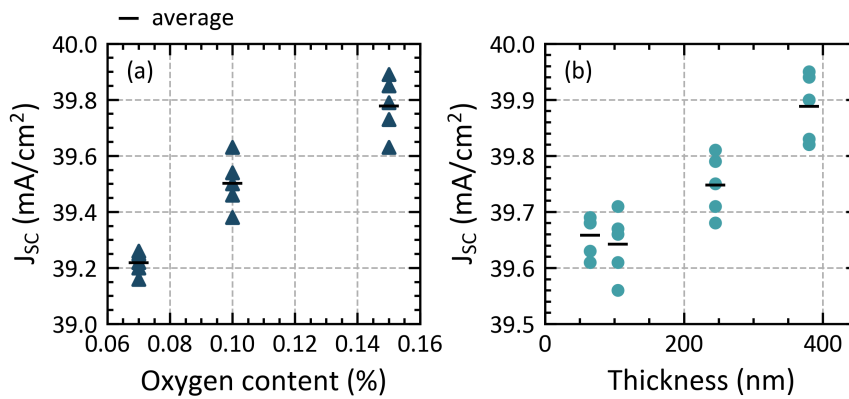


Figure 6.7 – J_{SC} of co-deposited $2 \text{ cm} \times 2 \text{ cm}$ solar cells with (a) varying O_2 content in the AZO deposition gas flow and fixed thickness of 160 nm and with (b) varying AZO thickness with a fixed O_2 content of 15%. The black dash represents the mean value over 5 cells, each represented by the data points.

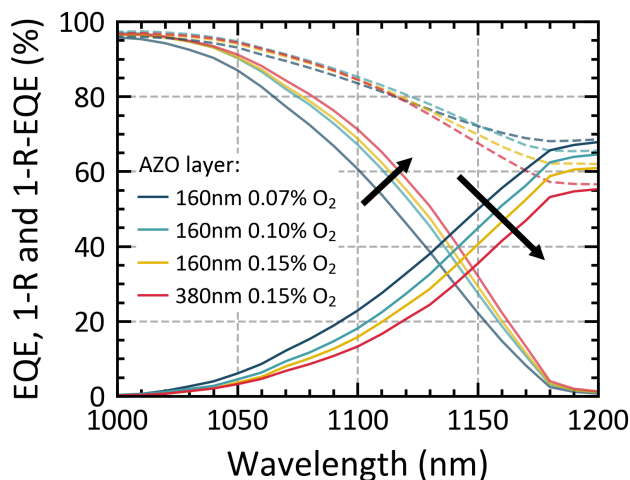


Figure 6.8 – EQE (solid light), 1-R (dashed light) and 1-R-EQE (solid) of co-deposited 2 cm × 2 cm solar cells with varying O₂ content in the AZO deposition gas flow for a fixed thickness of 160 nm along with the highest thickness of 380 nm with 0.15 % of O₂ content. The black arrows provide a visual guide to highlight the increase of EQE and decrease of the total parasitic absorption with respect to the considered layers.

However, the measurements given in Table 6.3 reveal that, for a given oxygen content, the carrier concentrations of the investigated AZO layers decrease when their thickness increases (see layers #4 to #7 in Table 6.3). This may be due to a higher defect density near the substrate interface induced by the nucleation layer of the TCO. Such defects, like oxygen vacancies, can act as donor levels hence increasing the carrier concentration. Such a dependence of the carrier concentration to the thickness has already been observed in [Holman 2013c] for the case of ITO layers, and further material analysis are proposed in [Look 2013]. Therefore, the carrier concentration within the AZO layer and its thickness cannot be considered as two independent parameters. To be free of this bias, it is more accurate to investigate the J_{SC} as a function of D , the total number of carriers per unit area, hereafter simply calculated as the carrier concentration multiplied by the layer thickness: $D = N \cdot t$. This quantity is directly related to FCA as the larger the carrier concentration or the thickness (i.e. the larger D), the larger the FCA. Note that the optical mobility is expected to be affected by the carrier concentration through impurity scattering. Higher carrier concentrations will lead to lower optical mobilities. However the changes will be of a much smaller magnitude compared to the carrier concentration variation in the investigated range of this work. About 20 % change of optical mobility is expected for an order of magnitude change in carrier concentration [Steinhauser 2007]. Both effects will affect the FCA in the same direction; however, the dominant effect will be the carrier concentration. The data of Figures 6.7a and b, as well as several additional data for the oxygen content series, are plotted in Figure 6.9 as a function of D . With such a representation, it is possible to calculate and decouple the J_{SC} gain owing to the FCA reduction and the one owing to the plasmonic absorption reduction. The blue data points in

Figure 6.9 represent the J_{SC} variation for a fixed AZO thickness of about 160 nm but a change of carrier concentration from 2.6×10^{19} to $2.0 \times 10^{20} \text{ cm}^{-3}$. Here, the J_{SC} steadily increases when D decreases. This is clearly related to the FCA reduction associated to the carrier concentration decrease. In contrast, the red data points represent the thickness series from 65 to 380 nm (see layers #4 to #7 in Table 6.3). For these layers, a J_{SC} gain of 0.25 mA cm^{-2} is observed for similar values of D , i.e., for the same amount of FCA losses. Hence, this gain is the result of the plasmonic absorption reduction. Overall, the reduction in the plasmonic absorption losses obtained with thicker AZO layers is larger than the additional FCA losses implied by a thicker AZO layer, eventually leading to a J_{SC} increase. Finally, note that, as commonly observed for TCOs, the refractive index of AZO in the IR spectral range is correlated to its carrier concentration: the lower the carrier concentration, the higher the refractive index. Hence, the Fresnel coefficients at the c-Si/TCO and TCO/metal interfaces will change with the TCO carrier concentration. The consequences of FCA and plasmonic absorption losses have been thoroughly investigated in [Holman 2013c] in the case of ITO, and it was shown that for most of the incident angles, absorption losses decrease when the TCO carrier concentration decreases. Therefore, potential IR reflection gains from lower TCO refractive index never offset FCA losses and the IR EQE always benefits from a reduction of the TCO carrier concentration, as we observe for AZO here.

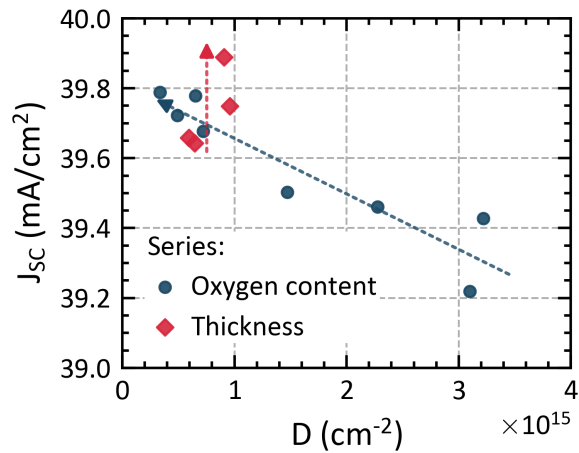


Figure 6.9 – J_{SC} as a function of D , the total number of carriers per unit area, for different AZO layers. Each data point is the J_{SC} value averaged over 5 devices. The oxygen content variation is represented by the blue data points and the thickness variation by the red data points. Two arrows highlight the J_{SC} gain which owes to the FCA decrease (blue dashed arrow) and to the plasmonic absorption decrease (red dashed arrow).

6.4. SHJ shells - optical properties optimization

During our investigations, the 160-nm-thick AZO layer with 0.10 % O₂ content was integrated in the rear reflector of 2 cm × 2 cm monofacial solar cells with front hole-collecting shell part and about 3.25% optical shadowing. In addition, this device features an improved front double antireflecting coating combining ITO and MgF₂ layers. This led to a champion device featuring a significantly high J_{SC} of 40.81 mA cm⁻² without compromising the V_{OC} and the FF , which present good values of 726 mV and 80.87 %, respectively (see Figure 6.10). Overall, this leads to a high efficiency of 23.96 %⁴.

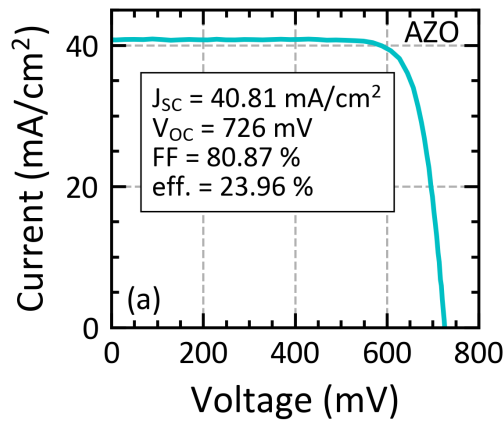


Figure 6.10 – J-V curves of 2 cm × 2 cm monofacial solar cells with front double antireflecting coating presenting significantly high J_{SC} values with the integration of the 160-nm-thick AZO layer with 0.10 % O₂ content.

From these results, even higher solar cells performances are within reach, as the thickness and the oxygen content of the rear AZO layer can be further optimized, as demonstrated in Figures 6.7a and b. In a more global approach, each TCO (ITO and AZO, as developed in this work, being two prominent examples) can in principle be optimized to meet the required trade-off between FCA and plasmonic absorption losses mitigation to achieve high J_{SC} . However, because of the additional existing trade-off between the electrical and the optical properties of the shells, the electrical performances of these TCO must be well controlled alongside their optical ones to convert the J_{SC} gain into higher solar cell efficiency. Eventually, the best TCO will then be the one which, once integrated in a complete shell, allows for the most efficient light collection (highest J_{SC}) while allowing for the highest electrical performances (i.e. high passivation quality and low R_s). Figure 6.11 shows the best performance of solar cell integrating an AZO layer in the rear electron-collecting shell part of 2 cm × 2 cm monofacial device. It is observed that a high J_{SC} of 40.35 mA cm⁻² is reached along with high electrical performances as evidenced by the high V_{OC} of 729.8 mV and high FF of 82.33 %. This optimized electrical-optical trade-off allows for a very high efficiency of 24.24 %. This optimization was made possible by combining the thin silicon layer developments of chapter 5 with a high

⁴The results presented in this section were obtained in collaboration with Gabriel Christmann whose contribution is gratefully acknowledged.

quality AZO rear reflector. AZO thus demonstrates a clear potential to act as a high-quality indium-free back TCO in the rear electron-collecting shell parts of SHJ monofacial solar cells to reach a high efficiency of 24.24%.

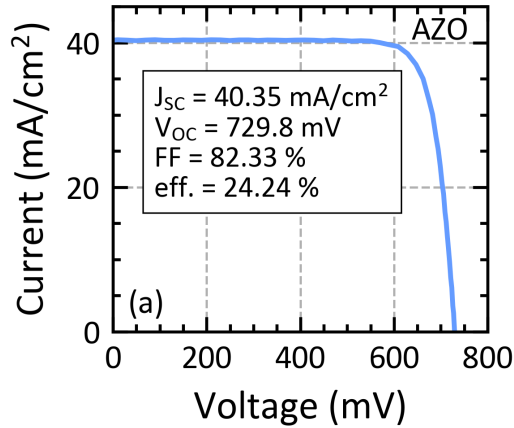


Figure 6.11 – J-V curves of the best 2 cm × 2 cm monofacial solar cells integrating an AZO layer in the rear electron-collecting shell part.

As part of industrial projects and in-house developments, the stability of AZO was investigated through life cycle and damp heat processes. Remarkably, AZO demonstrated performance stability through both processes, thus revealing its reliability once integrated in a complete PV module. Overall, to ensure a successful industrial deployment of AZO, it is now still necessary to check thoroughly the quality of the AZO target, the utilisation rate, the integration in the global process flow, the total cost, among others. These topics are actually under investigation by various institutes and companies and are already revealing promising results.

6.5 Conclusion

This chapter presented the integration of the advanced characterization methods presented in chapter 4 and of the different layers developed in chapter 5 in actual baseline solar cells.

First, the integration of advanced TLM measurements under variable illumination in rigorous R_S breakdowns was presented. It has been demonstrated that using the ρ_c values obtained in dark conditions of both electron and hole-collecting shell parts does not allow for an accurate R_S breakdown. Indeed, the R_S value obtained with the integration of these dark values in the R_S breakdown is $0.18 \Omega \text{ cm}^2$ smaller than the R_S extracted from the final device. Moreover, adding the ρ_c values of the electron-collecting shell part obtained at MPP still yields R_S values that are too low, but closer to the actual R_S value. In addition, considering that the ρ_{cn} values at MPP are accurate, this suggests that ρ_{cp} may present values between 0.37 to $0.41 \Omega \text{ cm}^2$, which is coherent with what is expected from literature. Overall, these results suggest that

the ρ_c values obtained at MPP are more accurate than those obtained in the dark to assess the electrical losses of solar cells. However, additional dedicated experiments are required to consolidate these results. Secondly, a demonstration was made of the applicability of the methodology combining the shell concept and both the *top-down* and the *bottom-up* approaches to the study and mitigation of the electrical losses in the best baseline solar cells. This methodology was routinely used allowing us to collect significant insights to guide our baseline development and to improve the device's performance. Thanks to this methodology, the final shell characteristics obtained and their integration in actual devices made it possible to reach FF up to 83.2% along with an efficiency of 24.38% for full area 6-inch solar cell. It also allowed us to reach a FF of 82.27% along with an efficiency of 24.32% in $2\text{ cm} \times 2\text{ cm}$ screen-printed SHJ monofacial solar cells, as well as a FF of 82.50% with an efficiency of 25.45% for IBC devices with a size of $5\text{ cm} \times 5\text{ cm}$. Finally, the importance of considering the optical quality of shells in addition to their electrical quality was assessed. Aluminium-doped zinc oxide was optically optimized to act as an optimal indium-free TCO in the rear reflector of $2\text{ cm} \times 2\text{ cm}$ SHJ monofacial solar cells. It was demonstrated that the rear AZO layer can be optimized to behave as an optical layer which minimizes free-carrier and plasmonic absorptions in addition to providing high electrical properties inside the rear electron-collecting shell part. The J_{SC} improvement resulting from the important FCA and plasmonic absorption decrease combined with the optimal electrical properties of the rear electron-collecting shell part eventually led to an efficiency of 24.24%.

7 Conclusion and prospects

This chapter presents a general conclusion of the work carried out during this thesis. First, we give an overview of the different aspects and outcomes presented in this work as well as their relevant impacts and limitations. Secondly, we give a status on solar cell efficiency at our institute and we discuss the prospects of this work with a focus on the broader applicability of our methodology.

7.1 Conclusion

This work as a whole presents various concepts and methods developed to accurately describe, quantify, and mitigate the optical and electrical transport losses occurring in state-of-the-art SHJ solar cells, with a particular focus on the properties of the carrier-selective passivating contacts (CSPCs) of these cells. In particular, this work contributes to bridging the gap between theory and experiment by bringing a new methodology, advanced characterization methods, and layer developments which provide relevant information about the electrical quality of SHJ solar cells. In addition, it gives new means to identify suitable materials and processes to optimize the solar cell performance. Finally, this work contributes to spreading the SHJ and CSPCs knowledge required to reach high solar cell efficiencies.

The outcomes of this work can be separated into four main aspects.

New theoretical concepts and advanced methodology for CSPCs investigation

First, fundamental theoretical concepts about solar cells and their contacts were reviewed, and a new methodology combined with two novel approaches were presented in chapter 2. This unveiled new important aspects for the understanding of CSPCs and their development, thus offering novel levers for solar cell optimization. In this context, the *shell* concept was presented to illustrate the importance of considering the final properties coupling of all solar cell components. In particular, we presented and demonstrated that the coupling of the physical properties of the different shell sub-components and those of the absorber bulk defines the overall optical and electrical properties of the solar cell and thus determines its

final performance. A major focus was put on the electrical properties of the shell and the energy band diagrams were demonstrated to be a relevant approach to illustrate the material properties coupling impacting the electrical quality of solar cells, as presented in chapters 2 and 4. Indeed, band diagrams allow one to illustrate the different energy barriers and material resistivities, in addition to taking into account the injection level evidenced by the quasi-Fermi levels. Overall, the *shell* concept was demonstrated to be a relevant frame to deeply understand the physics behind CSPCs (chapters 2, 4, 5 and 6). Then, we presented in chapter 2 two characterization approaches named the *top-down* and the *bottom-up* approaches. We demonstrated that combining both approaches make it possible to study, decouple and establish how good and adapted a material will be for defining the final shell properties, as presented in chapters 5 and 6. Further combining the *shell* concept and both characterization approaches allowed us (i) to fill part of the lack of general understanding on CSPCs, (ii) to bring a new methodology to predict whether a material with given properties will act as an efficient part of CSPCs and can be part of the shell or not, and (iii) how these properties are linked to the final solar cell performance. Indeed, it was demonstrated in chapters 5 and 6 that the layer and cell characterizations provide key elements of understanding to guide the solar cell development and to establish what are the strengths and weaknesses of our solar cells, i.e., to assess their actual electrical and optical qualities. Furthermore, as many physical properties are intertwined in the final solar cell performance, the *top-down* and the *bottom-up* approaches were demonstrated to make it possible to characterize and decouple the coupling effects at different levels inside the shell. Combining both methods allowed us to pinpoint the different sources of electrical losses, such as passivation quality and resistive effects, as well as to decouple and distinguish the electrical and optical losses as presented in chapter 6. Overall, chapters 5 and 6 demonstrated that combining layer and device characterizations, i.e., the *top-down* and the *bottom-up* approaches, makes it possible to quickly and effectively select the shells with the most promising performance and to implement them inside real devices. This provides a robust and thorough understanding that can be integrated into solar cell baseline development. This methodology was applied during this work to the specific case of SHJ but can be applied to any solar cell technology such as other carrier selective and passivating contacts (e.g., TopCON-like CSPCs), perovskite or tandem to name a few. In addition, a detailed investigation on the optical performance of solar cells could also be conducted with the same methodology, using the *top-down* approach to investigate the physical parameters of given materials related to optical properties and the *bottom-up* approach to investigate the optical response of the shell once integrated in actual solar cells.

Improved and advanced characterization methods

Secondly, experimental characterization methods were demonstrated to allow for in-depth understanding of material layers and device properties. On the one hand, various characterization systems along with strong data treatments were studied, improved, and developed, as presented in chapter 3. This provides effective measurable parameters to analyse accurately the physical characteristics of the different material layers constituting SHJ solar cells in addition to the solar cells themselves. On the other hand, the TLM measurement under illu-

mination, presented in chapter 4, demonstrated the importance of considering the injection level for effective electrical losses investigation and to link more precisely the contribution of the contact resistivity (ρ_c) to the series resistance of the solar cell extracted at MPP conditions. In addition, this study demonstrated the necessity to consider the adapted wafer properties such as its doping carrier density and doping type to accurately measure the value of the contact resistivity. Indeed, as the resulting properties coupling depends on each shell sub-component and on the c-Si bulk characteristics, changing a solar cell component will result in different final coupling properties and thus in different contact resistivity values. Consequently, the applicability of TLM measurements under variable illumination to measure p-type shell parts on n-type c-Si wafers was investigated. However, we put in evidence that the relevance of this method is still questionable. Additional studies are required to establish the validity of this method and to complete the global description and understanding of the physical phenomena involved when performing such characterizations. Other TLM sample optimisations and/or test structures have to be considered and compared. Finally, chapters 5 and 6 presented preliminary results demonstrating that the ρ_c values of n-type shell parts measured at MPP injection level seem to be more relevant than ρ_c measured under dark conditions when integrated in complete R_S breakdown of monofacial $2\text{ cm} \times 2\text{ cm}$ solar cells. In this regard, additional complete and extensive R_S breakdowns as presented in chapter 6 must be undertaken to strengthen the additional accuracy and information the measurement of ρ_c at MPP conditions actually provides. Overall, this new advanced characterization method advances the understanding of electrical losses in SHJ solar cells and our results build the basis for further investigation towards accurate ρ_c measurements which are a prerequisite for building accurate R_S breakdowns of solar cells.

Multilayers development

Thirdly, multilayer developments demonstrated their potential to decouple the various contributions to the electrical losses by modifying the coupling properties at different shell levels. The individual components constituting the shell, which are the thin hydrogenated silicon layers and the TCO, were developed and characterized. This allowed us to figure out the material properties which are required to reach high electrical performance by improving the passivation quality and minimizing the resistive effects. It also allowed us to consider the transversal and lateral resistive losses contribution of each solar cell architecture. In particular, chapter 5 demonstrated that an important trade-off is often present between high passivation quality and low resistive effects but that it can be mitigated by in-depth development, working on the optimization of the coupling properties between doped thin silicon layers and TCO. In addition, chapters 5 and 6 demonstrated the promising potential of multilayers to optimize the material properties coupling at different levels inside the shell. Indeed, n-type amorphous/nanocrystalline multilayers demonstrated a clear potential for improving the contact resistance while keeping high passivation quality when coupled with AZO and ITO layers. Furthermore, AZO multilayers demonstrated their ability to optimize the material properties coupling with the doped thin silicon layer while independently reducing the AZO R_{sh} . A low R_{sh} is required to reach an optimal lateral transport of carriers to the finger grid and

Chapter 7. Conclusion and prospects

to reduce the R_s of the solar cell. Finally, in chapter 5, boron microdoping was demonstrated to be a promising means of reducing the resistive losses thanks to a-Si:H(i)/ μD multilayers. However, it was found that the trade-off between passivation quality and R_s obtained with these $i/\mu D$ multilayers is challenging to optimize. This trade-off may be mitigated by adapting the a-Si:H(i) layer properties and by building an adapted gradient of boron quantity in the top μD layer. This solution is expected to allow for the required R_s reduction while allowing for not jeopardizing the passivation quality. Overall, multilayers are demonstrated to be a very promising means of improving the electrical transport in SHJ solar cells. Additional developments would be interesting to perform by using various layer combinations to build optimized multilayers featuring more than two layers. In addition, their compatibility for implementation in the production line while keeping high production yield needs to be assessed.

High solar cell performance

Finally, thanks to this methodology, it became possible to build a global understanding of the shell properties which, combined with extensive characterization methods, allowed us to process high FF and efficiency solar cells. High quality shell characteristics were obtained and their integration in actual devices allowed us to reach a FF up to 83.20% along with an efficiency of 24.38% for full area 6 inch solar cells. In addition, it allowed us to reach a FF of 82.27% along an efficiency of 24.32% for 2 cm \times 2 cm screen-printed SHJ monofacial solar cells, as well as a FF of 82.50% with an efficiency of 25.45% for IBC devices presenting a size of 5 cm \times 5 cm. Finally, the necessity of optimizing the electrical properties without jeopardizing the optical ones was demonstrated. In this context, a high J_{SC} of 40.81 mA cm⁻² was obtained for 2 cm \times 2 cm screen-printed SHJ monofacial solar cells and, combining optimal electrical and optical properties, an impressive efficiency of 24.24% was demonstrated with AZO layer. This also demonstrated the potential of indium-free TCOs to replace the rear ITO layer in SHJ solar cells. These data are gathered in Table 7.1.

An overview summarizing the different outcomes of this thesis is given by a schematic description in Figure 7.1.

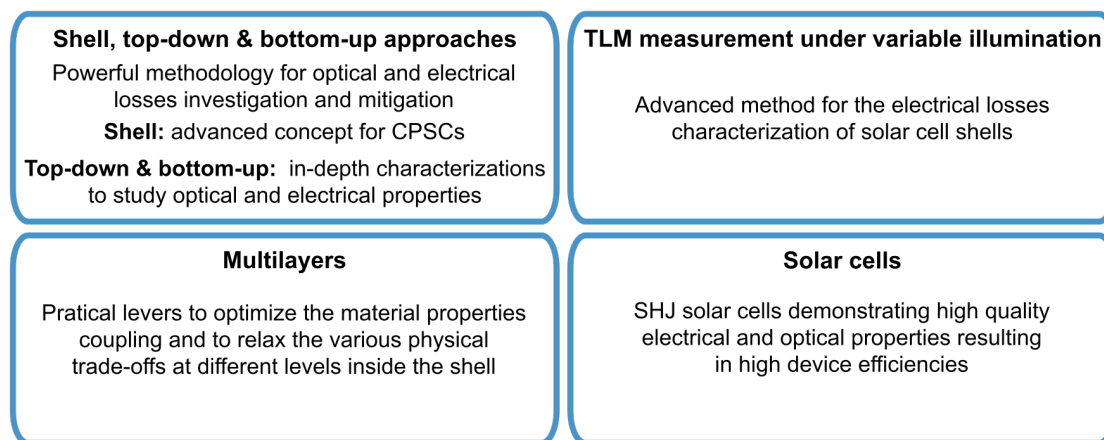


Figure 7.1 – Schematic summary of the four main aspects of this work.

7.2 Prospects

During the years of this thesis, the development of new methods such as the ones presented in this work and various project objectives and deliverables allowed for the continuous improvement of our three SHJ solar cell architectures of interest, which are 2 cm × 2 cm monofacial, 6 inch bifacial, and 5 cm × 5 cm IBC. The efficiency evolution as a function of the year for these three architectures are presented in Figure 7.2. It is observed that an efficiency improvement from 23% to above 24% was achieved between 2016 and 2018 for both our 2 cm × 2 cm monofacial and 5 cm × 5 cm IBC solar cells. Then, the upscaling to 6 inch bifacial solar cells occurred starting at the end of 2017 up to now, passing from below 23% to almost 24.5%. This last technology improvement was conducted in parallel to industrialisation projects which required the development of processes compatible with production lines. Concurrently, the continuous IBC efficiency improvement allowed us to reach up to 25.45% efficiency in 2020. The record CSEM devices were achieved thanks to a careful application of the methodology summarized in the previous section 7.1.

Table 7.1 presents an overview of the CSEM best SHJ solar cells along with the best in-class SHJ solar cells reported in the literature for two side-contacted and IBC architectures. Comparing the performance of two side-contacted CSEM solar cells with the Hanergy cell [Ru 2020], it is observed that mainly significant V_{OC} and FF improvements are required to catch up with the record efficiency. Regarding the IBC technology, it is observed that, comparing to the record device of [Yoshikawa 2017], our V_{OC} is similar, however, significant light collection and FF improvement are required to reach above 26% efficiency. These will be the next focus for our internal developments using the methodology presented in this work.

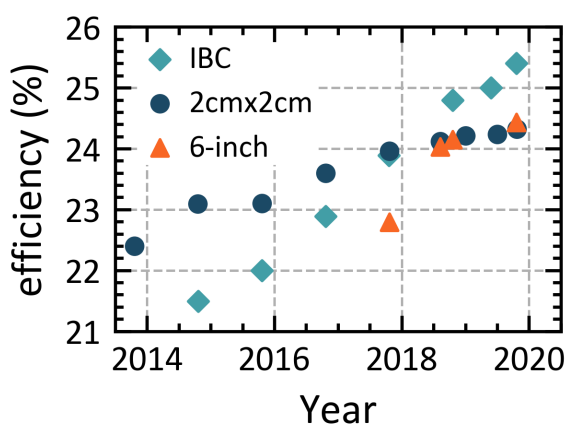


Figure 7.2 – CSEM solar cell efficiencies evolution as a function of the year for the three SHJ solar cell architectures under study which are 2 cm × 2 cm monofacial, 6 inch bifacial and 5 cm × 5 cm IBC.

Chapter 7. Conclusion and prospects

Architecture	Type	Area (cm^2)	J_{sc} (mA/cm^2)	V_{oc} (mV)	FF (%)	eff. (%)	Reference
two sides contacted	Lab-scale	151.9 (ap)	40.80	738	83.5	25.10	[Adachi 2015]
two sides contacted	Pilot	244.45 (t)	39.55	747	85.0	25.11	[Ru 2020]
IBC	Lab-scale	79.0 (da)	42.65	738	84.9	26.7	[Yoshikawa 2017]
two sides contacted	Lab-scale	244.33 (t)	39.72	738	83.2	24.38	CSEM in-house
two sides contacted	Lab-scale	244.33 (t)	38.99	742	83.06	24.03	CSEM certified
IBC	Lab-scale	25.0 (da)	41.80	738	82.50	25.45	CSEM in-house
IBC	Lab-scale	25.035 (da)	41.48	736	81.87	25.00	CSEM certified
two sides contacted	Lab-scale	4.0 (da)	40.52	729.6	82.27	24.32	CSEM in-house
two sides contacted	Lab-scale	4.0 (da)	40.32	729.9	82.28	24.21	CSEM certified

Table 7.1 – Overview of the performance of best-in class single junction c-Si based SHJ solar cell technologies and the best CSEM devices.

Importantly, the development of CSEM solar cells strongly contributed to the industrialization of advanced SHJ devices, through technology transfer and collaboration with numerous institutes and companies. SHJ is now a mature technology demonstrating high efficiency and which is, as stated in chapter 1, ready for a large deployment in the coming years. Nowadays, record efficiencies for SHJ solar cells and modules are achieved by PV mass-production companies rather than by lab-scale research centres, such as CSEM. This results mainly from the fact that bringing about further efficiency improvements requires a stable and reproducible device performance, i.e., a small variance of the results for a given process, in addition to a high number of devices to establish relevant statistics. In mass production, these conditions are made possible by the full automation of the production lines and the large quantities of devices produced. In contrast, at CSEM, only manual handling methods and lab-scale systems with limited throughput are used, and many different technologies are developed in parallel. Consequently, the batch-to-batch variance is large and the throughput is low, making it challenging to reach the highest device performance. In this regard, PV companies now have the resources to achieve the remaining efficiency improvements thanks to large scale production but lab-scale research centres still have the cumulative knowledge to continue to leverage their in-depth understanding of the physics behind SHJ devices to support PV companies. This is why research and development will remain important assets to provide PV

industries in the future with a continuously updated understanding of material properties and shell performance. In this regard, the whole methodology developed in this work is expected to be of particular relevance. Overall, thanks to continued industrial improvements such as advanced tools, process and takt time optimisation, integrated masking methods, reduction of defectivity thanks to full automation, strict selection of incoming c-Si wafers, advances in edge defect mitigation and post-treatments (light soaking, forward bias and temperature recovery), PV companies are expected to produce SHJ solar cells in bifacial configuration with efficiencies higher than 25%, and in IBC configuration with efficiencies above 26% in mass-production.

As a broader prospect, the time when single junction c-Si-based solar cells will reach their practical efficiency limit is in sight. Silicon-on-perovskite tandems, whose efficiency limit is above 45%, have been identified as the most promising technology to take over single junction, c-Si-based solar cells. Consequently, for all PV companies, mastering the processing of this next generation of PV devices with improved performances is a must to keep their competitive edge. This calls for a shift of the research efforts from single junction c-Si-based solar cells to tandem solar cells, in order to anticipate the future needs of industry. The methodology combining the shell concept with the *top-down* and the *bottom-up* approaches which include advanced characterization methods, such as TLM under variable illumination, are foreseen to provide relevant insights to drive the understanding and optimization of tandem solar cells toward higher efficiencies.

A Appendix

A.1 TLM under variable illumination and non-ohmic behavior

In this appendix section, the appearance of the non-ohmic regime due to the drift of the free carriers induced by the voltage applied between two consecutive TLM pads is explained in more detail. This phenomenon leads to a non-homogeneous carrier density and thus a variation of the wafer R_{sh} below the TLM pads and the gap in-between. Consequently, one of the fundamental hypotheses of TLM measurement, which states that the R_{sh} must be homogeneous inside the conductive layer, i.e., inside the c-Si bulk here, is no longer fulfilled. Our simple calculations reveal that the higher the voltage bias applied between two TLM pads, the higher the global resistance seen by the TLM current when flowing through the conductive layer, leading then to a non-ohmic I-V behaviour. Under illumination, free holes and electrons are generated inside the c-Si bulk. First, considering zero applied TLM voltage between two pads, i.e., $\Delta U = 0V$ voltage bias, and an n-type c-Si bulk, the electrons are homogeneously distributed inside the bulk along the distance L , and their total density n equals to $n_0 + \Delta n$ everywhere within the sample bulk, with n_0 the bulk doping density and Δn the injected carrier density (see Figure A.1). We then have:

$$R_{sh} = \frac{\rho}{t} \tag{A.1}$$

$$\sigma = q \cdot \mu \cdot n \tag{A.2}$$

$$\rho = \frac{1}{q \cdot \mu \cdot n} \tag{A.3}$$

$$\tag{A.4}$$

with t the wafer thickness, σ the conductivity, q equal to the elementary charge, ρ the resistivity, and μ the mobility. These three parameters are homogeneous inside the wafer and thus the resistive contribution R of the wafer to the total resistance measured between two TLM pads

Appendix A. Appendix

is also homogeneous and is given by:

$$U = R \cdot I \quad (\text{A.5})$$

$$I = \frac{U}{R} = U \cdot \Sigma \quad (\text{A.6})$$

$$\Sigma = \frac{1}{R} = \frac{\sigma}{L} = \frac{q\mu n}{L} \quad (\text{A.7})$$

$$(\text{A.8})$$

with U the voltage and I the current between two TLM pads, Σ the conductance (the inverse of R) and L the total distance as depicted in Figure A.1. Under an applied TLM bias $\Delta U = \alpha V$ (with $\alpha > 0$), the free generated electrons (and holes) will drift because of the applied external field. This drift will depend on the intensity of the bias. As a simple case study, we now assume, for this given non-zero TLM bias, these electrons to be distributed following a simple non-homogeneous distribution: in the sample region $0 < x < L/2$, the electron density is now n_0 , whereas in the region $L/2 < x < L$, the electron density is $n_0 + 2\Delta n$. Note that the total number of electrons (and hence holes) is chosen to be constant inside the whole volume of the sample in both the 0V and the αV cases. This is equivalent to assuming the same total recombination rate in both cases. Considering these two different c-Si(n) parts as connected in series, we thus have (with the hypothesis $q\mu = \text{cst}$):

$$\Sigma_{0V} \propto \frac{n_0 + \Delta n}{L} \quad (\text{A.9})$$

$$\Sigma_{\alpha V} \propto \left(\frac{\frac{L}{2}}{n_0} + \frac{\frac{L}{2}}{n_0 + 2\Delta n} \right)^{-1} = \frac{n_0(n_0 + 2\Delta n)}{L(n_0 + \Delta n)} \quad (\text{A.10})$$

$$(\text{A.11})$$

and comparing both parameters, we get:

$$\frac{\Sigma_{\alpha V}}{\Sigma_{0V}} = \frac{n_0^2 + 2\Delta n n_0}{n_0^2 + 2\Delta n n_0 + \Delta n^2} < 1 \quad (\text{A.12})$$

$$\frac{R_{0V}}{R_{\alpha V}} = \frac{n_0^2 + 2\Delta n n_0}{n_0^2 + 2\Delta n n_0 + \Delta n^2} < 1 \quad (\text{A.13})$$

$$(\text{A.14})$$

Thus, from the computed equivalent resistance of the c-Si bulk seen by the electrons in the 0V

A.1. TLM under variable illumination and non-ohmic behavior

and the αV cases (R_{0V} and $R_{\alpha V}$, respectively), it turns out that $R_{0V} < R_{\alpha V}$. In other words, the wafer resistance is depending on the applied bias ΔU , i.e., $R = R(\Delta U)$. Hence, the higher the TLM applied bias, the higher the total resistance seen by the TLM current between two TLM pads ($R_{\alpha V}$ gets larger and larger compared to R_{0V}). This explains the non-ohmic shape of the IV curve obtained between two TLM pads under illumination. Therefore, at low voltages, a linear I-V regime is still present because the drift effect is small, but as soon as the voltage increases, the non-ohmic I-V behaviour appears, then stabilises at high voltages to a second linear I-V regime. This second linear regime features a higher slope than the first linear one, evidencing the increase of the c-Si global resistance with the voltage (see Figure A.2). In addition, it is also observed that with the increase of the illumination, and thus of Δn , the applied voltage required to reach a given current is smaller, i.e., the global resistance is smaller, as the R_{sh} of the c-Si(n) bulk decreases with Δn increase (see Figure A.2). Importantly, due to the fact that, for a given high TLM bias, both TLM pads feature two different R_{sh} below them, the ρ_c is not equal between the two pads, making it impossible to perform TLM computation, as the hypothesis of a symmetric system is no longer fulfilled. In addition, the resulting resistance between two TLM pads varies with the TLM bias voltage, but this resistive effect is negligible compared to the wafer R_{sh} variation with the TLM bias voltage.

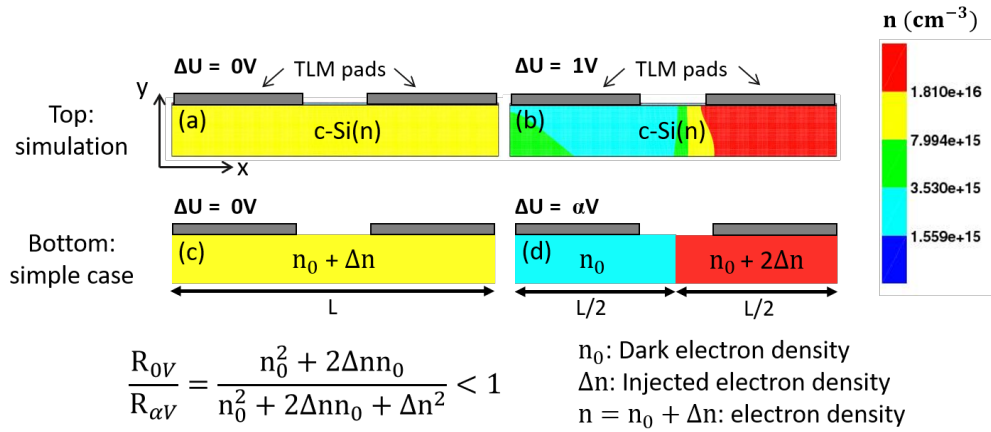


Figure A.1 – Top: electron density for 1 sun illuminated TLM sample, under (a) 0 and (b) 1 V TLM voltage; Bottom: simplified case study with at (c) 0V the total number of electrons homogeneously distributed inside the c-Si bulk along the distance L, and at (d) αV , a particular non-homogeneous distribution. This simple case study illustrates that the higher the TLM applied bias, the higher the total resistance seen by the TLM current between two TLM pads ($R_{0V} < R_{\alpha V}$).

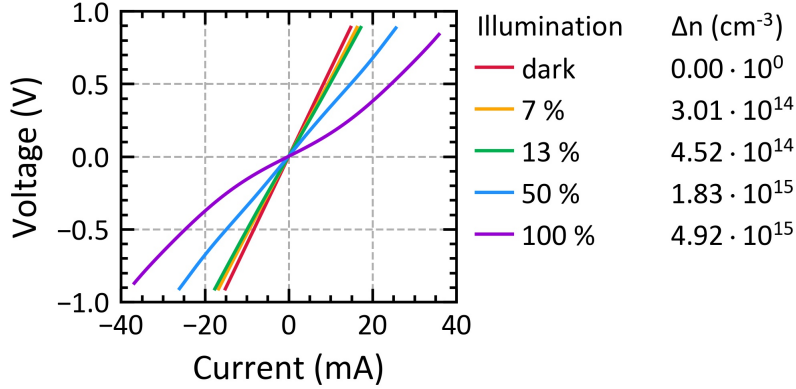


Figure A.2 – I-V characteristics of the shell #2 as a function of the illumination, for the TLM gap of 2.5 mm. The injected electron densities (Δn) are also reported along with the corresponding illuminations.

A.2 TLM under variable illumination - injected carrier density computation

This appendix section details the computation steps required to extract the injected carrier density reached inside the c-Si bulk knowing its resulting R_{sh} induced by variable illumination and measured by TLM. This R_{sh} is directly linked to the carrier type of the TLM current which is defined by the type of the shell part under investigation, i.e., electrons (n-type) or holes (p-type). In the case of c-Si wafers of the same doping type than the shell parts under investigation, the injected carrier density can be calculated as follows. First, the initial doping density n_{0i} of the wafer is extracted from the dark measured R_{sh} . Then, knowing the wafer thickness (t), the c-Si wafer resistivity, which is related to the R_{sh} extracted from TLM (ρ_{TLM}), is calculated using the relation $\rho_{\text{TLM}} = R_{\text{sh}} \cdot t$. From there, the corresponding conductivity is expressed as:

$$\sigma_{\text{TLM}} = \frac{1}{\rho_{\text{TLM}}} = q \cdot \mu_i \cdot n_{0i} \quad (\text{A.15})$$

with q equal to the elementary charge, μ the carrier mobility and i standing for electron (e) or hole (h) associated with the c-Si bulk type. σ_{TLM} is then defined by one type of carriers only which are, in this case, the majority carriers inside the c-Si bulk during TLM measurement. Then, knowing the relation of the c-Si bulk resistivity (ρ) as a function of the doping density, it is possible to extract the value of n_{0i} . For this study, we used the relation given by the PVLighthouse tables [McIntosh 2011] and which are given in Figure A.3 for the case of c-Si(n) and c-Si(p) wafers. The c-Si ρ value given by PVLighthouse (named here ρ_{PVLH}) is calculated considering the contribution of both majority and minority carriers present inside the c-Si

A.2. TLM under variable illumination - injected carrier density computation

bulk in dark condition. In our case studies, the wafers used are either n or p-type, and thus the ρ_{PVLH} is considered equal to ρ_{TLM} as the minority carriers contribution is negligible in dark conditions. From there, for each given ρ_{TLM} value, it is possible to extract the corresponding doping density from the PVLighthouse data, referred to as $n_{0i, \text{PVLH}}$ and related to the given ρ_{PVLH} . Then, the final dark mobility of majority carrier inside the c-Si bulk is computed using equation A.15 and considering the measured ρ_{TLM} in dark condition and the related $n_{0i, \text{PVLH}}$.

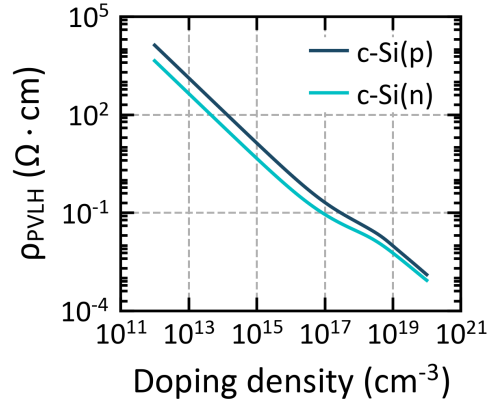


Figure A.3 – Bulk resistivity as a function of the doping density for n-type (turquoise) and p-type (dark blue) c-Si wafers given by PVLighthouse tables [McIntosh 2011].

Thus, knowing n_{0i} , it is possible to find the value of the injected carrier density (Δn_i) obtained for the different illuminations under study with the relation:

$$\sigma_{\text{TLM}} = \frac{1}{\rho_{\text{TLM}}} = q \cdot \mu_i(n_{0i}, \Delta n_i) \cdot (n_{0i} + \Delta n_i) \quad (\text{A.16})$$

$$\Delta n_i = \frac{1}{q \cdot \mu_i(n_{0i}, \Delta n_i) \cdot \rho_{\text{TLM}}} - n_{0i} \quad (\text{A.17})$$

Here equation A.17 expresses Δn_i as a function of the majority carriers mobility which depends on Δn_i in addition to n_{0i} . Thus, to find the value of Δn_i for a given ρ_{TLM} , the PVLighthouse tables giving the majority carriers mobility as a function of the injected carrier density for a fixed c-Si bulk n_{0i} were used. To illustrate this parameter, the electron mobility (turquoise curve) as a function of the injected carrier density is presented in Figure A.4 for the case of an n-type c-Si wafer featuring an n_{0e} of $1.65 \times 10^{15} \text{ cm}^{-3}$. Then, the equation A.17 is solved using the fixed point method to extract a unique value of $\Delta n_{i, \text{PVLH}}$ considering the dependence of the majority carrier mobility to Δn_i . Finally, as in the case of dark conditions, the mobility of majority carriers inside the c-Si bulk is computed using equation A.17 by combining the extracted value of $\Delta n_{i, \text{PVLH}}$ and the measured value of ρ_{TLM} .

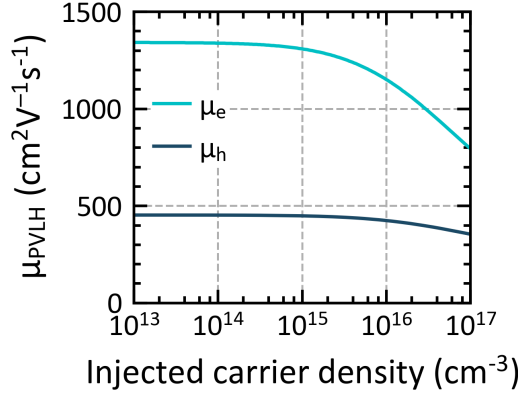


Figure A.4 – Electron (turquoise) and hole (dark blue) mobilities as a function of the injected carrier density given by PVLighthouse for an n-type c-Si wafer with $n_{0e} = 1.65 \times 10^{15} \text{ cm}^{-3}$.

In the case of c-Si wafers with the inverse doping type than the shell parts under investigation, the injected carrier density can be calculated following a similar procedure. However, in that case the measured R_{sh} from TLM under variable illumination is assumed to be related to the minority carrier inside the c-Si bulk of type j (with j equal to e for electron or equal to h for hole). In addition, the value of n_{0j} can not be extracted from TLM measurement performed in dark condition. Indeed in that case, the TLM measurement probes the R_{sh} of the inversion layer and not the one of the c-Si bulk under study. Thus, to compute a value of n_{0j} another measurement technique, here PCD measurement, is used. Thus, considering minority carriers, hereafter related to the symbol i standing for electron (e) or hole (h), and a given injection level we get $n_{0i} \ll \Delta n_i$ and equations A.16 and A.17 become:

$$\sigma_{\text{TLM}} = \frac{1}{\rho_{\text{TLM}}} = q \cdot \mu_i(n_{0j}, \Delta n_i) \cdot \Delta n_i \quad (\text{A.18})$$

$$\Delta n_i = \frac{1}{q \cdot \mu_i(n_{0j}, \Delta n_i) \cdot \rho_{\text{TLM}}} \quad (\text{A.19})$$

with i standing for minority carrier equal to e if the c-Si bulk is hole-type, i.e., if $j = h$, and equal to h if the c-Si bulk is electron-type, i.e., if $j = e$. Here again equation A.19 expresses Δn_i as a function of the minority carrier mobility which depends on Δn_i in addition to n_{0j} . Thus, as was done previously, to find the value of Δn_i for a given ρ_{TLM} , the PVLighthouse tables giving the minority carrier mobility as a function of the injected carrier density for a fixed c-Si bulk n_{0j} were used. To illustrate this parameter, hole mobility (yellow curve) as a function of the injected carrier density is presented in Figure A.4 for the case of an n-type c-Si wafer featuring an n_{0e} of $1.65 \times 10^{15} \text{ cm}^{-3}$. Then, the equation A.19 is solved using the fixed point method to extract a unique value of $\Delta n_{i, \text{PVLH}}$ considering the dependence of the minority carrier mobility to Δn_i .

A.3 Transparent conductive oxide and thickness properties

This appendix section presents the dependence of the TCO properties on their thickness for given process flow parameters. While performing TCO layer developments, it is important to consider that the final electrical properties measured by Hall measurements, which are the carrier density, the mobility, the resistivity, as well as the sheet resistance (R_{sh}), will depend on the thickness of the TCO layer. Indeed, for fixed deposition parameters, the variation of the deposition time, in the case of the Clusterline PVD tool, or of the scan speed, in the case of Octopus II PVD system, result in different TCO thicknesses as well as in different electrical properties. This thickness dependence on the electrical properties must be considered when developing TCO layers, as presented here for three different TCO processes. Figures A.5 and A.6 present (a) the carrier density, (b) the mobility, (c) the resistivity and (d) the R_{sh} obtained by Hall measurements as a function of the TCO thickness for two different ITO deposition processes with either 1.21% or 4.09% of O_2 content in the deposition gas flow, and for an AZO deposition process with 0.15% of O_2 content in the deposition gas flow. It is observed that a strong dependence of the Hall parameters is present with the TCO thickness. Indeed, for the ITO deposition with 4.09% of O_2 and the AZO one, the carrier densities are found to decrease with the thickness increase. In addition, in both cases, the mobility is found to slightly decrease while the resistivity is found to significantly increase. This results in a corresponding R_{sh} behaviour. Indeed, the R_{sh} is related to the resistivity (ρ) with $R_{sh} = \rho / t$, with t the TCO thickness and ρ which depends on the carrier density and mobility as presented in section 3.2.1. In contrast, the ITO layer with 1.21% of O_2 in the deposition gas flow presents different trends with the thickness. Here, the carrier density is found to first increase then to decrease with the thickness increase. The resistivity, mobility and R_{sh} present also different trends with the thickness increase than the ITO with 4.09% of O_2 in the deposition gas flow. This demonstrates that for given deposition parameters, i.e., given O_2 contents here, the electrical parameters will present different values with the thickness. Moreover, the thickness dependence is present for the three deposition parameters. Interestingly, here, for the two ITO layers, the thinnest ones show similar carrier density and resistivity values but different mobilities. Overall, this dependence on the TCO thickness may be due to a higher defect density near the substrate interface induced by the nucleation layer of the TCO. Such defects, like oxygen vacancies, can act as donor levels hence increasing the carrier concentration. Such a dependence of the carrier concentration to the thickness has already been observed in [Holman 2013c] for the case of ITO layers, and further material analysis are proposed in [Look 2013].

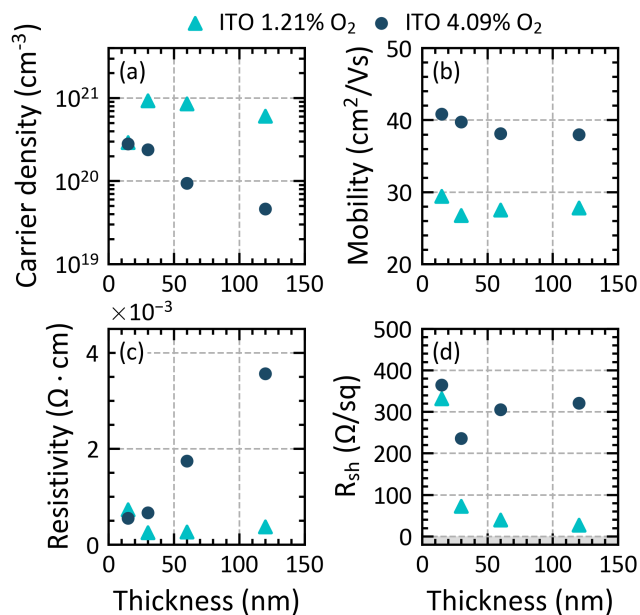


Figure A.5 – (a) Carrier density, (b) mobility, (c) resistivity and (d) sheet resistance obtained by Hall measurement as a function of the ITO thickness for two different ITO deposition processes with either 1.21% or 4.09% of O₂ content in the deposition gas flow.

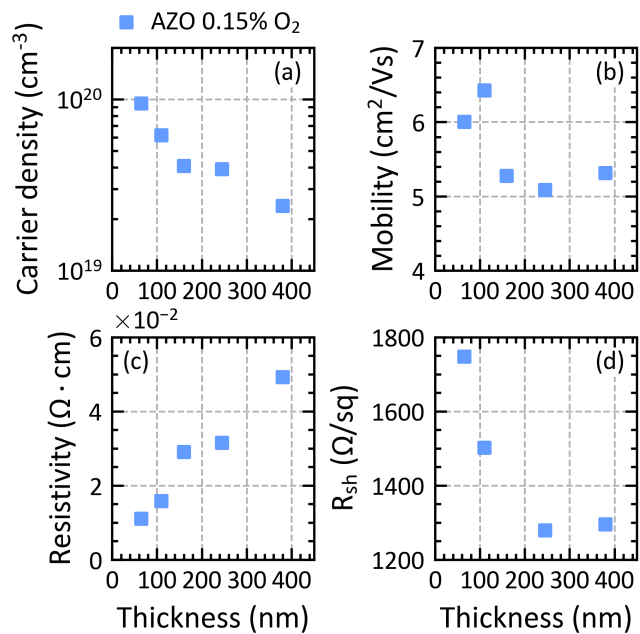


Figure A.6 – (a) Carrier density, (b) mobility, (c) resistivity and (d) sheet resistance obtained by Hall measurement as a function of the AZO thickness for an AZO deposition process with 0.15% of O₂ content in the deposition gas flow.

Bibliography

- [Aberle 2000] Armin G. Aberle. *Surface passivation of crystalline silicon solar cells: a review*. Progress in Photovoltaics: Research and Applications, vol. 8, no. 5, pages 473–487, 2000.
- [Adachi 2015] Daisuke Adachi, José Luis Hernández and Kenji Yamamoto. *Impact of carrier recombination on fill factor for large area heterojunction crystalline silicon solar cell with 25.1% efficiency*. Applied Physics Letters, vol. 107, no. 23, pages 2013–2016, 2015.
- [Altermatt 2018] Pietro P. Altermatt, Zhen Xiong, Qiu Xiang He, Wei Wei Deng, Feng Ye, Yang Yang, Yifeng Chen, Zhi Qiang Feng, Pierre J. Verlinden, Anyao Liu, Daniel H. Macdonald, Tabea Luka, Dominik Lausch, Marko Turek, Christian Hagendorf, Hannes Wagner-Mohnsen, Jonas Schön, Wolfram Kwapil, Felix Frühauf, Otwin Breitenstein, Erin E. Looney, Tonio Buonassisi, David B. Needleman, Christine M. Jackson, Aaron R. Arehart, Steven A. Ringel, Keith R. McIntosh, Malcolm D. Abbott, Ben A. Sudbury, Anika Zuschlag, Clemens Winter, Daniel Skorka, Giso Hahn, Daniel Chung, Bernhard Mitchell, Peter Geelan-Small and Thorsten Trupke. *High-performance p-type multicrystalline silicon (mc-Si): Its characterization and projected performance in PERC solar cells*. Solar Energy, vol. 175, no. January, pages 68–74, 2018.
- [Ashcroft 1976] Neil W Ashcroft and N David Mermin. Solid state physics. Harcourt College, 1976.
- [Barraud 2013] L. Barraud, Z. C. Holman, N. Badel, P. Reiss, A. Descoedres, C. Battaglia, S. De Wolf and C. Ballif. *Hydrogen-doped indium oxide/indium tin oxide bilayers for high-efficiency silicon heterojunction solar cells*. Solar Energy Materials and Solar Cells, vol. 115, pages 151–156, 2013.
- [Battaglia 2016] Corsin Battaglia, Andres Cuevas and Stefaan De Wolf. *High-efficiency crystalline silicon solar cells: Status and perspectives*. Energy and Environmental Science, vol. 9, no. 5, pages 1552–1576, 2016.
- [Berger 1972a] H. H. Berger. *Contact Resistance and Contact Resistivity*. Journal of The Electrochemical Society, vol. 119, no. 4, page 507, 1972.
- [Berger 1972b] H. H. Berger. *Models for contacts to planar devices*. Solid State Electronics, vol. 15, no. 2, pages 145–158, 1972.

Bibliography

- [Bivour 2014a] M Bivour, M Reusch, F Feldmann, M Hermle and S Glunz. *Requirements for Carrier Selective Silicon Heterojunctions*. In Proceedings of the 24th Workshop on Crystalline Silicon Solar Cells & Modules, pages 1–9, 2014.
- [Bivour 2014b] M Bivour, M Reusch, S Schroder, F Feldmann, J Temmler, H Steinkemper and M Hermle. *Doped Layer Optimization for Silicon Heterojunctions by Injection-Level-Dependent Open-Circuit Voltage Measurements*. vol. 4, no. 2, pages 566–574, 2014.
- [Bivour 2014c] Martin Bivour, Heiko Steinkemper, Jan Jeurink, Sebastian Schroer and Martin Hermle. *Rear emitter silicon heterojunction solar cells: Fewer restrictions on the optoelectrical properties of front side TCOs*. Energy Procedia, vol. 55, pages 229–234, 2014.
- [Blakers 1989] Andrew W. Blakers, Aihua Wang, Adele M. Milne, Jianhua Zhao and Martin A. Green. *22.8% Efficient Silicon Solar Cell*. Applied Physics Letters, vol. 55, no. 13, pages 1363–1365, 1989.
- [Bouhafs 1998] D. Bouhafs, A. Moussi, A. Chikouche and J. M. Ruiz. *Design and simulation of antireflection coating systems for optoelectronic devices: Application to silicon solar cells*. Solar Energy Materials and Solar Cells, vol. 52, no. 1-2, pages 79–93, 1998.
- [Boussey 1998] Jumana Boussey. *Stripping Hall effect, sheet and spreading resistance techniques for electrical evaluation of implanted silicon layers*. Microelectronic Engineering, vol. 40, no. 3-4, pages 275–284, 1998.
- [Bowden 2001] S. Bowden and A. Rohatgi. *Rapid and accurate determination of series resistance and fill factor losses in industrial silicon solar cells*. 17th European Photovoltaic Solar Energy Conference, 2001.
- [Brendel 2016] Rolf Brendel and Robby Peibst. *Contact Selectivity and Efficiency in Crystalline Silicon Photovoltaics*. IEEE Journal of Photovoltaics, vol. 6, no. 6, pages 1413–1420, 2016.
- [Brodsky 1977] M. H. Brodsky, Manuel Cardona and J. J. Cuomo. *Infrared and Raman spectra of the silicon-hydrogen bonds in amorphous silicon prepared by glow discharge and sputtering*. Physical Review B, vol. 16, no. 8, pages 3556–3571, oct 1977.
- [Bustarret 1988] E. Bustarret, M. A. Hachicha and M. Brunel. *Experimental determination of the nanocrystalline volume fraction in silicon thin films from Raman spectroscopy*. Applied Physics Letters, vol. 52, no. 20, pages 1675–1677, may 1988.
- [Carpenter 2017] Joe V. Carpenter, Mark Bailly, Allison Boley, Jianwei Shi, Michael Minjares, David J. Smith, Stuart Bowden and Zachary C. Holman. *Substrate-independent analysis of microcrystalline silicon thin films using UV Raman spectroscopy*. Physica Status Solidi (B) Basic Research, vol. 254, no. 9, 2017.

- [Cattin 2020a] Jean Cattin. *Characterisation of Silicon Heterojunction Solar Cells Beyond Standard Test Conditions*. PhD thesis, École Polytechnique Fédérale de Lausanne (EPFL), 2020.
- [Cattin 2020b] Jean Cattin, Jan Haschke, Christophe Ballif and Mathieu Boccard. *Influence of local surface defects on the minority-carrier lifetime of passivating-contact solar cells*. *Influence of local surface defects on the minority-carrier lifetime of passivating-contact solar cells*. Applied Physics Letters, vol. 113901, no. February, 2020.
- [Chavali 2018] Raghu V. K. Chavali, Stefaan De Wolf and Muhammad A. Alam. *Device physics underlying silicon heterojunction and passivating-contact solar cells: A topical review*. Progress in Photovoltaics: Research and Applications, vol. 26, no. 4, pages 241–260, apr 2018.
- [Chopra 1983] K.L. Chopra, S. Major and D.K. Pandya. *Transparent conductors—A status review*. Thin Solid Films, vol. 102, no. 1, pages 1–46, apr 1983.
- [Clugston 1997] Donald A. Clugston and Paul A. Basore. *PC1D version 5: 32-bit solar cell modeling on personal computers*. Conference Record of the IEEE Photovoltaic Specialists Conference, pages 207–210, 1997.
- [Cox 1967] R. H. Cox and H. Strack. *Ohmic contacts for GaAs devices*. Solid State Electronics, vol. 10, no. 12, pages 1213–1218, 1967.
- [Cruz 2020] Alexandros Cruz, Florian Ruske, Alberto Eljarrat, Pawel P. Michalowski, Anna B. Morales-Vilches, Sebastian Neubert, Er-Chien Wang, Christoph T. Koch, Bernd Szyszka, Rutger Schlatmann and Bernd Stannowski. *Influence of Silicon Layers on the Growth of ITO and AZO in Silicon Heterojunction Solar Cells*. IEEE Journal of Photovoltaics, vol. 10, no. 2, pages 703–709, mar 2020.
- [Cuevas 1996] Andrés Cuevas, Paul A. Basore, Gaëlle Giroult-Matlakowski and Christiane Dubois. *Surface recombination velocity of highly doped n-type silicon*. Journal of Applied Physics, vol. 80, no. 6, 1996.
- [Cuevas 2015] Andres Cuevas, Thomas Allen, James Bullock, Yimao Wan, Di Yan and Xinyu Zhang. *Skin care for healthy silicon solar cells*. 2015 IEEE 42nd Photovoltaic Specialist Conference, PVSC 2015, no. 1, 2015.
- [Cuevas 2018] Andres Cuevas, Yimao Wan, Di Yan, Christian Samundsett, Thomas Allen, Xinyu Zhang, Jie Cui and James Bullock. *Carrier population control and surface passivation in solar cells*. Solar Energy Materials and Solar Cells, vol. 184, no. April, pages 38–47, 2018.
- [Demaurex 2012] Bénédicte Demaurex, Stefaan De Wolf, Antoine Descoeur, Zachary Charles Holman and Christophe Ballif. *Damage at hydrogenated amorphous/crystalline silicon interfaces by indium tin oxide overlayer sputtering*. Applied Physics Letters, vol. 101, no. 17, pages 1–4, 2012.

Bibliography

- [Demaurex 2014a] Bénédicte Demaurex. *Passivating contacts for homojunction solar cells using a-Si:H/c-Si hetero-interfaces*. PhD thesis, Ecole Polytechnique fédérale de Lausanne (EPFL), 2014.
- [Demaurex 2014b] Bénédicte Demaurex, Johannes P Seif, Sjoerd Smit, Bart Macco, W M Erwin Kessels, Jonas Geissbühler, Stefaan DeWolf and Christophe Ballif. *Atomic-Layer-Deposited Transparent Electrodes for Silicon Heterojunction Solar Cells*. IEEE Journal of Photovoltaics, vol. 4, no. 6, pages 1387–1396, 2014.
- [Descoedres 2011] A. Descoedres, L. Barraud, Stefaan De Wolf, B. Strahm, D. Lachenal, C. Guérin, Z. C. Holman, F. Zicarelli, B. Demaurex, J. Seif, J. Holovsky and C. Ballif. *Improved amorphous/crystalline silicon interface passivation by hydrogen plasma treatment*. Applied Physics Letters, vol. 99, no. 12, pages 2009–2012, 2011.
- [Descoedres 2017] A. Descoedres, J. Geissbühler, J. Horzel, A. Lachowicz, J. Levrat, S. Martin de Nicolas, S. Nicolay, B. Paviet-Salomon, L.-L. Senaud, A. Tomasi, C. Ballif, C. Allebe, M. Despeisse, N. Badel, L. Barraud, J. Champlaud, G. Christmann, L. Curvat, F. Debrot and A. Faes. *Advanced silicon thin films for high-efficiency silicon heterojunction-based solar cells*. 2017 IEEE 44th Photovoltaic Specialist Conference (PVSC), Washington, DC, pages 50–55, 2017.
- [DeWolf 2007] Stefaan DeWolf and Michio Kondo. *Boron-doped a-Si:H/c-Si interface passivation: Degradation mechanism*. Applied Physics Letters, vol. 91, no. 11, pages 1–4, 2007.
- [DeWolf 2012] Stefaan DeWolf, Antoine Descoedres, Zachary C. Holman and Christophe Ballif. *High-efficiency Silicon Heterojunction Solar Cells: A Review*. Green, vol. 2, pages 1–18, 2012.
- [Droz 2003] Corinne Droz. *Thin Film Microcrystalline Silicon Layers and Solar Cells : Microstructure and Electrical Performances*. PhD thesis, Université de Neuchâtel, 2003.
- [Droz 2004] C Droz, J Bailat, L Feitknecht, J Meier and A Shah. *Relationship between Raman crystallinity and open-circuit voltage in microcrystalline silicon solar cells*. Solar Energy Materials and Solar Cells, vol. 81, pages 61–71, 2004.
- [Eidelloth 2014] Stefan Eidelloth and Rolf Brendel. *Analytical theory for extracting specific contact resistances of thick samples from the transmission line method*. IEEE Electron Device Letters, vol. 35, no. 1, pages 9–11, 2014.
- [Ellmer 2001] K. Ellmer. *Resistivity of polycrystalline zinc oxide films: Current status and physical limit*. Journal of Physics D: Applied Physics, vol. 34, no. 21, pages 3097–3108, 2001.
- [European Commission 2019] European Commission. *The European Green Deal*, 2019.

- [Feldmann 2014] Frank Feldmann, Martin Bivour, Christian Reichel, Martin Hermle and Stefan W. Glunz. *Passivated rear contacts for high-efficiency n-type Si solar cells providing high interface passivation quality and excellent transport characteristics*. Solar Energy Materials and Solar Cells, vol. 120, no. PART A, pages 270–274, 2014.
- [Fell 2015] Andreas Fell, Keith R. McIntosh, Pietro P. Altermatt, Gaby J.M. Janssen, Rolf Stangl, Anita Ho-Baillie, Heiko Steinkemper, Johannes Greulich, Matthias Muller, Byungsul Min, Kean C. Fong, Martin Hermle, Ingrid G. Romijn and Malcolm D. Abbott. *Input parameters for the simulation of silicon solar cells in 2014*. IEEE Journal of Photovoltaics, vol. 5, no. 4, pages 1250–1263, 2015.
- [Fell 2017] Andreas Fell, Jonas Schön, Martin C. Schubert and Stefan W. Glunz. *The concept of skins for silicon solar cell modeling*. Solar Energy Materials and Solar Cells, vol. 173, no. March, pages 128–133, 2017.
- [Filipič 2013] Miha Filipič, Zachary C. Holman, Franc Smole, Stefaan De Wolf, Christophe Ballif and Marko Topič. *Analysis of lateral transport through the inversion layer in amorphous silicon/crystalline silicon heterojunction solar cells*. Journal of Applied Physics, vol. 114, no. 7, 2013.
- [Fraunhofer ISE 2020] Fraunhofer ISE. *Photovoltaics Report - Fraunhofer ISE*. Rapport technique September, 2020.
- [Fujiwara 2007] Hiroyuki Fujiwara. Spectroscopic ellipsometry: principles and applications. John Wiley and Sons, Ltd, 2007.
- [Ginley 2011] David S. Ginley, Hideo Hosono and David C. Paine. Handbook of Transparent Conductors. Springer, Boston, MA, 2011.
- [Gogolin 2014] Ralf Gogolin, Mircea Turcu, Rafel Ferre, Juliane Clemens, Nils Peter Harder, Rolf Brendel and Jan Schmidt. *Analysis of series resistance losses in a-Si:H/c-Si heterojunction solar cells*. IEEE Journal of Photovoltaics, vol. 4, no. 5, pages 1169–1176, 2014.
- [Green 1981] Martin A. Green. *Solar cell fill factors: General graph and empirical expressions*. Solid State Electronics, vol. 24, no. 8, pages 788–789, 1981.
- [Green 1982] Martin A. Green. Solar cells: operating principles, technology, and system applications. University of NSW, 1982.
- [Green 2008] Martin A. Green. *Self-consistent optical parameters of intrinsic silicon at 300 K including temperature coefficients*. Solar Energy Materials and Solar Cells, vol. 92, no. 11, pages 1305–1310, 2008.
- [Green 2021] Martin Green, Ewan Dunlop, Jochen Hohl-Ebinger, Masahiro Yoshita, Nikos Kopidakis and Xiaojing Hao. *Solar cell efficiency tables (version 57)*. Progress in Photovoltaics: Research and Applications, vol. 29, no. 1, pages 3–15, 2021.

Bibliography

- [Guo 2017] Siyu Guo, Geoffrey Gregory, Andrew M. Gabor, Winston V. Schoenfeld and Christopher O. Davis. *Detailed investigation of TLM contact resistance measurements on crystalline silicon solar cells*. Solar Energy, vol. 151, pages 163–172, 2017.
- [Haase 2018] Felix Haase, Christina Hollemann, Sören Schäfer, Agnes Merkle, Michael Rienäcker, Jan Krügener, Rolf Brendel and Robby Peibst. *Laser contact openings for local poly-Si-metal contacts enabling 26.1%-efficient POLO-IBC solar cells*. Solar Energy Materials and Solar Cells, vol. 186, no. June, pages 184–193, 2018.
- [Hahn 2010] G. Hahn. *Status of Selective Emitter Technology*. 25th European Photovoltaic Solar Energy Conference and Exhibition, no. September, pages 1091–1096, 2010.
- [Halevy 2011] Ran Halevy. *A Method for measuring the specific interface resistivity between two semiconductor layers and its application to a heavily doped n-type InP / GaInAs heterostructure* Ran Halevy. PhD thesis, Technion - Israel Institute of Technology Sivan, 2011.
- [Hall 1952] R. N. Hall. *Electron-hole recombination in Germanium*. Physical Review, vol. 87, no. 2, page 387, 1952.
- [Han 2003] Daxing Han, Keda Wang, Jessica M. Owens, Lynn Gedvilas, Brent Nelson, Hitoe Habuchi and Masako Tanaka. *Hydrogen structures and the optoelectronic properties in transition films from amorphous to microcrystalline silicon prepared by hot-wire chemical vapor deposition*. Journal of Applied Physics, vol. 93, no. 7, pages 3776–3783, apr 2003.
- [Haschke 2020] Jan Haschke, Gabriel Christmann, Christoph Messmer, Martin Bivour, Mathieu Boccard and Christophe Ballif. *Lateral transport in silicon solar cells*. Journal of Applied Physics, vol. 127, no. 11, 2020.
- [Hezel 1981] R. Hezel and R. Schörner. *Plasma Si nitride - A promising dielectric to achieve high-quality silicon MIS/IL solar cells*. Journal of Applied Physics, vol. 52, no. 4, pages 3076–3079, 1981.
- [Higashi 1990] G. S. Higashi, Y. J. Chabal, G. W. Trucks and Krishnan Raghavachari. *Ideal hydrogen termination of the Si (111) surface*. Applied Physics Letters, vol. 56, no. 7, pages 656–658, 1990.
- [Hoex 2008] B. Hoex, J. J.H. Gielis, M. C.M. Van De Sanden and W. M.M. Kessels. *On the c-Si surface passivation mechanism by the negative-charge-dielectric Al₂O₃*. Journal of Applied Physics, vol. 104, no. 11, 2008.
- [Hofmann 2008] M. Hofmann. *Rear surface conditioning and passivation for locally contacted crystalline silicon solar cells*. PhD thesis, Fraunhofer ISE, Germany, 2008.
- [Holman 2013a] Zachary C. Holman, Stefaan De Wolf and Christophe Ballif. *Improving metal reflectors by suppressing surface plasmon polaritons: A priori calculation of the internal*

- reflectance of a solar cell*. Light: Science and Applications, vol. 2, no. OCTOBER, page 0, 2013.
- [Holman 2013b] Zachary C. Holman, Antoine Descoeurdes, Stefaan De Wolf and Christophe Ballif. *Record infrared internal quantum efficiency in silicon heterojunction solar cells with dielectric/metal rear reflectors*. IEEE Journal of Photovoltaics, vol. 3, no. 4, pages 1243–1249, 2013.
- [Holman 2013c] Zachary C. Holman, Miha Filipič, Antoine Descoeurdes, Stefaan De Wolf, Franc Smole, Marko Topič and Christophe Ballif. *Infrared light management in high-efficiency silicon heterojunction and rear-passivated solar cells*. Journal of Applied Physics, vol. 113, no. 1, pages 1–13, 2013.
- [IEA 2014] IEA. *Technology Roadmap - Solar Photovoltaic Energy*. Rapport technique, 2014.
- [IEA 2017] IEA. *World Energy Outlook 2017*. Rapport technique, 2017.
- [IEA 2020a] IEA. *Key World Energy Statistics 2020*. Rapport technique, IEA, Paris, 2020.
- [IEA 2020b] IEA. *Renewables 2020 - Analysis and forecast to 2025*. Rapport technique, 2020.
- [IEA 2020c] IEA. *World Energy Outlook 2020*. Rapport technique, 2020.
- [Jeong 1998] MeiKei Jeong, P.-M. Solomon, S. E. Laux, H.-S. P. Wong and D. Chidambarrao. *Comparison of raised and Schottky source/drain MOSFETs using a novel tunneling contact model*. International Electron Devices Meeting 1998 Technical Digest (Cat. No.98CH36217), pages 733–736, 1998.
- [IPCC 2013] IPCC. *Climate Change 2013: The Physical Science Basis. Contribution of Working Group I to the Fifth Assessment Report of the Intergovernmental Panel on Climate Change*. Rapport technique, IPCC, 2013.
- [IPCC 2014] IPCC. *Climate Change 2014: Impacts, Adaptation, and Vulnerability. Part A: Global and Sectoral Aspects. Contribution of Working Group II to the Fifth Assessment Report of the Intergovernmental Panel on Climate Change*. Rapport technique, 2014.
- [IPCC 2018] IPCC. *Global Warming of 1.5 °C*. Rapport technique, 2018.
- [Islam 2001] Md N. Islam and Satyendra Kumar. *Influence of crystallite size distribution on the micro-Raman analysis of porous Si*. Applied Physics Letters, vol. 78, no. 6, pages 715–717, 2001.
- [ITRPV 2020] ITRPV. *International Technology Roadmap for Photovoltaic*. Rapport technique April, 2020.
- [Jellison 1996] G. E. Jellison and F. A. Modine. *Parameterization of the optical functions of amorphous materials in the interband region*. Applied Physics Letters, vol. 69, no. 3, pages 371–373, 1996.

Bibliography

- [Jiménez-Molinos 2002] F. Jiménez-Molinos, F. Gámiz, A. Palma, P. Cartujo and J. A. López-Villanueva. *Direct and trap-assisted elastic tunneling through ultrathin gate oxides*. Journal of Applied Physics, vol. 91, no. 8, pages 5116–5124, 2002.
- [Jin 2007] Hao Jin, K. J. Weber, N. C. Dang and W. E. Jellett. *Defect generation at the Si-SiO₂ interface following corona charging*. Applied Physics Letters, vol. 90, no. 262109, pages 1–3, 2007.
- [JinkoSolar 2017] JinkoSolar. *JinkoSolar sets new mono-PERC cell efficiency record*, 2017.
- [Kamioka 2021] Takefumi Kamioka, Yutaka Hayashi, Kazuhiro Gotoh, Tomohiko Hara, Ryo Ozaki, Motoo Morimura, Ayako Shimizu, Kyotaro Nakamura, Noritaka Usami, Atsushi Ogura and Yoshio Ohshita. *Simulation study on lateral minority carrier transport in the surface inversion layer of the p-aSi : H / i-aSi : H / cSi heterojunction solar cell*. Japanese Journal of Applied Physics, vol. 60, no. 2, page 026503, 2021.
- [Kane 1961] Evan O. Kane. *Theory of tunneling*. Journal of Applied Physics, vol. 32, pages 83–91, 1961.
- [Kerr 2002] Mark J Kerr, Andres Cuevas and Ronald A Sinton. *Generalized analysis of quasi-steady-state and transient decay open circuit voltage measurements*. Journal of Applied Physics, vol. 91, no. 1, pages 399–404, 2002.
- [Kim 2011] Sun Kyung Kim, Ho Seok Ee, Woonkyung Choi, Soon Hong Kwon, Ju Hyung Kang, Yoon Ho Kim, Hoki Kwon and Hong Gyu Park. *Surface-plasmon-induced light absorption on a rough silver surface*. Applied Physics Letters, vol. 98, no. 1, pages 1–4, 2011.
- [Kim 2017] Ki Hyung Kim, Chang Sub Park, Jae Doo Lee, Jong Youb Lim, Je Min Yeon, Il Hwan Kim, Eun Joo Lee and Young Hyun Cho. *Record high efficiency of screen-printed silicon aluminum back surface field solar cell: 20.29%*. Japanese Journal of Applied Physics, vol. 56, no. 8, 2017.
- [Klaassen 1992a] D. B. M. Klaassen. *A Unified Mobility Model for Device Simulation - I. Model Equation and Concentration Dependence*. Solid State Electronics, vol. 35, no. 7, pages 953–959, 1992.
- [Klaassen 1992b] D. B.M. Klaassen. *A unified mobility model for device simulation-II. Temperature dependence of carrier mobility and lifetime*. Solid State Electronics, vol. 35, no. 7, pages 961–967, 1992.
- [Klein 2009] A Klein, C Körber, A Wachau, F Säuberlich, Y Gassenbauer, R Schafranek, S P Harvey and T O Mason. *Surface potentials of magnetron sputtered transparent conducting oxides*. Thin Solid Films, vol. 518, no. 4, pages 1197–1203, 2009.
- [Klein 2010] Andreas Klein, Christoph Körber, André Wachau, Frank Säuberlich, Yvonne Gassenbauer, Steven P. Harvey, Diana E. Proffit and Thomas O. Mason. *Transparent*

- conducting oxides for photovoltaics: Manipulation of fermi level, work function and energy band alignment*. Materials, vol. 3, no. 11, pages 4892–4914, 2010.
- [Kobliska 1973] R. J. Kobliska and S. A. Solin. *Raman spectrum of wurtzite silicon*. Physical Review B, vol. 8, no. 8, pages 3799–3802, 1973.
- [Kondo 1996] Michio Kondo, Yasutake Toyoshima, Akihisa Matsuda and Kazuyuki Ikuta. *Substrate dependence of initial growth of microcrystalline silicon in plasma-enhanced chemical vapor deposition*. Journal of Applied Physics, vol. 80, no. 10, pages 6061–6063, nov 1996.
- [Koswatta 2015] Priyaranga Koswatta, Mathieu Boccard and Zachary Holman. *Carrier-selective contacts in silicon solar cells*. 2015 IEEE 42nd Photovoltaic Specialist Conference, PVSC 2015, no. 2, pages 13–16, 2015.
- [Lachenal 2016] Damien Lachenal, Derk Baetzner, Walter Frammelsberger, Boris Legradic, Jérôme Meixenberger, Pierre Papet, Benjamin Strahm and Guillaume Wahli. *Heterojunction and Passivated Contacts: A Simple Method to Extract Both n/tco and p/tco Contacts Resistivity*. Energy Procedia, vol. 92, pages 932–938, 2016.
- [Lachenal 2019] D. Lachenal, P. Papet, B. Legradic, R. Kramer, T. Kössler, L. Andreetta, N. Holm, W. Frammelsberger, D. L. Baetzner, B. Strahm, L. L. Senaud, J. W. Schüttauf, A. Descoeurdes, G. Christmann, S. Nicolay, M. Despeisse, B. Paviet-Salomon and C. Ballif. *Optimization of tunnel-junction IBC solar cells based on a series resistance model*. Solar Energy Materials and Solar Cells, vol. 200, no. March, page 110036, 2019.
- [Lazard 2020] Lazard. *Lazard's Levelized Cost of Energy - Version 14.0*. Rapport technique October, 2020.
- [Ledinský 2006] M. Ledinský, L. Fekete, J. Stuchlík, T. Mates, A. Fejfar and J. Kočka. *Characterization of mixed phase silicon by Raman spectroscopy*. Journal of Non-Crystalline Solids, vol. 352, no. 9-20, pages 1209–1212, jun 2006.
- [Ledinský 2008] M. Ledinský, A. Vetushka, J. Stuchlík, T. Mates, A. Fejfar, J. Kočka and J. Štěpánek. *Crystallinity of the mixed phase silicon thin films by Raman spectroscopy*. Journal of Non-Crystalline Solids, vol. 354, no. 19-25, pages 2253–2257, may 2008.
- [Ledinský 2016] Martin Ledinský, Bertrand Paviet-Salomon, Aliaksei Vetushka, Jonas Geissbühler, Andrea Tomasi, Matthieu Despeisse, Stefaan De Wolf, Christophe Ballif and Antonín Fejfar. *Profilometry of thin films on rough substrates by Raman spectroscopy*. Scientific Reports, vol. 6, no. 1, page 37859, dec 2016.
- [Lee 2000] S. E. Lee, S. W. Choi and J. Yi. *Double-layer anti-reflection coating using MgF₂ and CeO₂ films on a crystalline silicon substrate*. Thin Solid Films, vol. 376, no. 1-2, pages 208–213, 2000.

Bibliography

- [Lee 2014] Seung-Yoon Lee, Hongsik Choi, Hongmei Li, Kwangsun Ji, Seunghoon Nam, Junghoon Choi, Seh-Won Ahn, Heon-Min Lee and Byungwoo Park. *Analysis of a-Si:H/TCO contact resistance for the Si heterojunction back-contact solar cell*. Solar Energy Materials and Solar Cells, vol. 120, no. PART A, pages 412–416, jan 2014.
- [Leilaeioun 2016] Mehdi Leilaeioun and Zachary C. Holman. *Accuracy of expressions for the fill factor of a solar cell in terms of open-circuit voltage and ideality factor*. Journal of Applied Physics, vol. 120, no. 12, 2016.
- [Lewis 2000] Brian G Lewis and David C Paine. *Applications and Processing of Transparent*. MRS bulletin, vol. 8, no. August, pages 22–27, 2000.
- [Lieberman 1994] M. A. Lieberman and A. J. Lichtenberg. Principles of plasma discharges and materials processing. John Wiley and Sons, 2nd édition, 1994.
- [Look 2013] David C. Look, Kevin D. Leedy, Arnold Kiefer, Bruce Clafflin, Naho Itagaki, Koichi Matsushima and Iping Suhariadi. *Model for thickness dependence of mobility and concentration in highly conductive zinc oxide*. Optical Engineering, vol. 52, no. 3, pages 1–5, 2013.
- [Luderer 2020] Christoph Luderer, Christoph Messmer, Martin Hermle and Martin Bivour. *Transport Losses at the TCO/a-Si:H/c-Si Heterojunction: Influence of Different Layers and Annealing*. IEEE Journal of Photovoltaics, vol. 10, no. 4, pages 952–958, 2020.
- [Madou 2002] M. Madou. Fundamentals of microfabrication: The science of miniaturization. second édition, 2002.
- [Maslova 2013] O. Maslova, A. Brézard-Oudot, M. E. Gueunier-Farret, J. Alvarez, W. Favre, D. Muñoz and J. P. Kleider. *Understanding inversion layers and band discontinuities in hydrogenated amorphous silicon/crystalline silicon heterojunctions from the temperature dependence of the capacitance*. Applied Physics Letters, vol. 103, no. 18, 2013.
- [McIntosh 2011] Keith McIntosh, Malcolm Abbott and Ben Sudbury. *PVLighthouse - web site*. PV Lighthouse Pty. Ltd. (ACN 160 420 477), 2011.
- [Nagel 1999] Henning Nagel, Christopher Berge and Armin G. Aberle. *Generalized analysis of quasi-steady-state and quasi-transient measurements of carrier lifetimes in semiconductors*. Journal of Applied Physics, vol. 86, no. 11, pages 6218–6221, 1999.
- [Nogay 2016] Gizem Nogay, Johannes Peter Seif, Yannick Riesen, Andrea Tomasi, Quentin Jeangros, Nicolas Wyrsh, Franz-Josef Haug, Stefaan De Wolf and Christophe Ballif. *Nanocrystalline Silicon Carrier Collectors for Silicon Heterojunction Solar Cells and Impact on Low-Temperature Device Characteristics*. IEEE Journal of Photovoltaics, vol. 6, no. 6, pages 1654–1662, nov 2016.
- [Olibet 2007a] S Olibet, E Vallat-Sauvain, C Ballif, L Korte and L Fesquet. *Silicon Solar Cell Passivation using Heterostructures*. Proceedings of NREL's 17th Workshop on Crystalline Silicon Solar Cells & Modules: Materials and Processes, pages 1–8, 2007.

- [Olibet 2007b] Sara Olibet, Evelyne Vallat-sauvain and Christophe Ballif. *Model for a-Si:H/c-Si interface recombination based on the amphoteric nature of silicon dangling bonds*. PHYSICAL REVIEW B, vol. 76, no. 035326, pages 1–14, 2007.
- [Olibet 2009] Sara Olibet. *Properties of interfaces in amorphous / crystalline silicon heterojunctions*. PhD thesis, 2009.
- [Onno 2019] Arthur Onno, Christopher Chen, Priyaranga Koswatta, Mathieu Boccard and Zachary C. Holman. *Passivation, conductivity, and selectivity in solar cell contacts: Concepts and simulations based on a unified partial-resistances framework*. Journal of Applied Physics, vol. 126, no. 18, 2019.
- [Pankove 1979] J. I. Pankove and M. L. Tarng. *Amorphous silicon as a passivant for crystalline silicon*. Applied Physics Letters, vol. 34, no. 2, pages 156–157, 1979.
- [Papet 2006] P. Papet, O. Nichiporuk, A. Kaminski, Y. Rozier, J. Kraiem, J. F. Lelievre, A. Chaurmartin, A. Fave and M. Lemiti. *Pyramidal texturing of silicon solar cell with TMAH chemical anisotropic etching*. Solar Energy Materials and Solar Cells, vol. 90, no. 15, pages 2319–2328, 2006.
- [Procel 2018] Paul Procel, Guangtao Yang, Olindo Isabella and Miro Zeman. *Theoretical evaluation of contact stack for high efficiency IBC-SHJ solar cells*. Solar Energy Materials and Solar Cells, vol. 186, no. April, pages 66–77, 2018.
- [Procel 2019] Paul Procel, H. Xu, L. Mazzarella, Laurie-Lou Senaud, Bertrand Paviet-Salomon, H. Radhakrishna, M. Filipic, M. Xu, Mathieu Boccard, Angela Fioretti, Raphaël Monnard, J. Stang, P. Wagner, D. Meza, Damien Lachenal, Benjamin Strahm, W. Duan, A. Lambertz, A. Fejfar, Kaining Ding, Mattiheu Despeisse, I. Gordon, Lars Korte, Christophe Ballif, Olindo Isabella and Miro Zeman. *On the Correlation between Contact Resistivity and High Efficiency in (IBC-) SHJ Solar Cells*. In Proceedings of the 36th European Photovoltaic Solar Energy Conference and Exhibition (2019) 2CO.12.6, pages 251–254, 2019.
- [Procel 2020] Paul Procel, Haiyuan Xu, Aurora Saez, Carlos Ruiz-Tobon, Luana Mazzarella, Yifeng Zhao, Can Han, Guangtao Yang, Miro Zeman and Olindo Isabella. *The role of heterointerfaces and subgap energy states on transport mechanisms in silicon heterojunction solar cells*. Progress in Photovoltaics: Research and Applications, no. March, pages 1–11, 2020.
- [Pysch 2007] D. Pysch, A. Mette and S. W. Glunz. *A review and comparison of different methods to determine the series resistance of solar cells*. Solar Energy Materials and Solar Cells, vol. 91, no. 18, pages 1698–1706, 2007.
- [Raman 1928] C. V. Raman and K. S. Krishnan. *A new type of secondary radiation*. Nature, vol. 121, no. 3048, pages 501–502, 1928.

Bibliography

- [Richter 2012] Armin Richter, Stefan W Glunz, Florian Werner, Jan Schmidt and Andres Cuevas. *Improved quantitative description of Auger recombination in crystalline silicon*. Physicall review B, vol. 165202, no. 86, pages 1–14, 2012.
- [Richter 2013] Armin Richter, Martin Hermle and Stefan W. Glunz. *Reassessment of the limiting efficiency for crystalline silicon solar cells*. IEEE Journal of Photovoltaics, vol. 3, no. 4, pages 1184–1191, 2013.
- [Richter 2019] A. Richter, J. Benick, F. Feldmann, A. Fell, B. Steinhauser, J.-I. Polzin, N. Tucher, J. N. Murthy, M. Hermle and S. W. Glunz. *Both sides contacted silicon solar cells: option for approaching 26% efficiency*. 36th European Photovoltaic Solar Energy Conference and Exhibition, pages 90–95, 2019.
- [Richter 2021] Armin Richter, Ralph Müller, Jan Benick, Frank Feldmann, Bernd Steinhauser, Christian Reichel, Andreas Fell, Martin Bivour, Martin Hermle and Stefan W. Glunz. *Design rules for high-efficiency both-sides-contacted silicon solar cells with balanced charge carrier transport and recombination losses*. Nature Energy, 2021.
- [Ritzau 2014] Kurt Ulrich Ritzau, Martin Bivour, Sebastian Schröer, Heiko Steinkemper, Patrick Reinecke, Florian Wagner and Martin Hermle. *TCO work function related transport losses at the a-Si:H/TCO-contact in SHJ solar cells*. Solar Energy Materials and Solar Cells, vol. 131, pages 9–13, 2014.
- [Roe 2019] Ellis T. Roe, Kira E. Egelhofer and Mark C. Lonergan. *Exchange current density model for the contact-determined current-voltage behavior of solar cells*. Journal of Applied Physics, vol. 125, no. 22, 2019.
- [Römer 2014] Udo Römer, Robby Peibst, Tobias Ohrdes, Bianca Lim, Jan Krügener, Eberhard Bugiel, Tobias Wietler and Rolf Brendel. *Recombination behavior and contact resistance of n+ and p+ poly-crystalline Si/mono-crystalline Si junctions*. Solar Energy Materials and Solar Cells, vol. 131, pages 85–91, 2014.
- [Ru 2020] Xiaoning Ru, Minghao Qu, Jianqiang Wang, Tianyu Ruan, Miao Yang, Fuguo Peng, Wei Long, Kun Zheng, Hui Yan and Xixiang Xu. *25.11 % efficiency silicon heterojunction solar cell with low deposition rate intrinsic amorphous silicon buffer layers*. Solar Energy Materials and Solar Cells, vol. 215, no. Septembre, page 110643, 2020.
- [Schroder 1984] Dieter K. Schroder and Daniel L. Meier. *Solar Cell Contact Resistance—A Review*. IEEE Transactions on Electron Devices, vol. 31, no. 5, pages 637–647, 1984.
- [Schroder 2006] Dieter K. Schroder. *Semiconductor Material and Device Characterization*. John Wiley & Sons, third edit édition, 2006.
- [Schulze 2010] T. F. Schulze, L. Korte, E. Conrad, M. Schmidt and B. Rech. *Electrical transport mechanisms in a-Si:H/c-Si heterojunction solar cells*. Journal of Applied Physics, vol. 107, no. 2, pages 1–13, 2010.

- [Seidel 1990] H. Seidel, L. Csepregi, A. Heuberger and H. Baumgärtel. *Anisotropic Etching of Crystalline Silicon in Alkaline Solutions: II. Influence of Dopants*. Journal of The Electrochemical Society, vol. 137, no. 11, pages 3626–3632, nov 1990.
- [Seif 2015] Johannes Peter Seif. *Window Layers for Silicon Heterojunction Solar Cells: Properties and Impact on Device Performance*. PhD thesis, EPFL, 2015.
- [Senaud 2019] Laurie-Lou Senaud, Gabriel Christmann, Antoine Descoedres, Jonas Geissbuhler, Loris Barraud, Nicolas Badel, Christophe Allebe, Sylvain Nicolay, Matthieu Despeisse, Bertrand Paviet-Salomon and Christophe Ballif. *Aluminium-Doped Zinc Oxide Rear Reflectors for High-Efficiency Silicon Heterojunction Solar Cells*. IEEE Journal of Photovoltaics, vol. 9, no. 5, pages 1217–1224, 2019.
- [Sentauros 2015] Sentauros. *Sentauros Device User Guide*. Rapport technique, 2015.
- [Shah 2010] Arvind Shah, Christophe Ballif, Wolfhard Beyer, Friedhelm Finger and Horst Schade. *Thin-Film Silicon Solar Cells*. EPFL press, 2010.
- [Shockley 1952] W. Shockley and W. T. Read. *Statistics of the recombinations of holes and electrons*. Physical Review, vol. 87, no. 5, pages 835–842, 1952.
- [Sinton 1996] Ronald A Sinton, Andres Cuevas and Michael Stuckings. *Quasi-stead-state photoconductance, a new method for solar cell material and device characterization*. Conference Record of the Twenty Fifth IEEE Photovoltaic Specialists Conference, pages 457–460, 1996.
- [Sinton 2000] R. A. Sinton and A. Cuevas. *A Quasi-Steady-State Open-Circuit Voltage Method for Solar Cell Characterization*. 16th European Photovoltaic Solar Energy Conference, Glasgow, UK, no. May, pages 1–4, 2000.
- [Sinton 2013] R A Sinton, A L Blum and J S Swirhun. *Overview and Latest Developments in Photoconductance Lifetime Measurements in Silicon*. Solid State Phenomena, vol. 205–206, pages 103–109, 2013.
- [Smith 1995] D. Smith. *Thin-filmdeposition: Principles and practice*. McGraw-Hill Education, 1995.
- [Smith 2014] David D. Smith, Peter Cousins, Staffan Westerberg, Russelle De Jesus-Tabajonda, Gerly Aniero and Yu Chen Shen. *Toward the practical limits of silicon solar cells*. IEEE Journal of Photovoltaics, vol. 4, no. 6, pages 1465–1469, 2014.
- [Smits 1958] F. M. Smits. *Measurement of sheet resistivities with the four-point probe*. Bell System Technical Journal, vol. 37, no. 3, pages 711–718, 1958.
- [Sobkowicz 2014] Igor Paul Sobkowicz. *Study and optimization of the growth of a-Si:H on wetchemically textured c-Si substrates for the enhancement of a-Si:H/c-Si heterojunction solar cells*. PhD thesis, Ecole Polytechnique Paris, 2014.

Bibliography

- [SolarPower Europe & LUT University 2020] SolarPower Europe & LUT University. *100% Renewable Europe - How to make Europe's energy system climate-neutral before 2050*. page 64, 2020.
- [Steinhauser 2007] J. Steinhauser, S. Faÿ, N. Oliveira, E. Vallat-Sauvain and C. Ballif. *Transition between grain boundary and intragrain scattering transport mechanisms in boron-doped zinc oxide thin films*. Applied Physics Letters, vol. 9, no. 142107, pages 1–3, 2007.
- [Stückelberger 2014] Michael Elias Stückelberger. *Hydrogenated amorphous silicon : Impact of process conditions on material properties and solar cell efficiency*. PhD thesis, Ecole polytechnique fédérale de Lausanne (EPFL), 2014.
- [Suckow 2014] Stephan Suckow, Tobias M. Pletzer and Heinrich Kurz. *Fast and reliable calculation of the two-diode model without simplifications*. Progress in Photovoltaics: Research and Applications, vol. 22, no. 4, pages 494–501, apr 2014.
- [Sze 2006] S.M. Sze and Kwok K. Ng. Physics of Semiconductor Devices. 2006.
- [Sze 2012] S. M. Sze and Kwok K. Ng. Physics of Semiconductor Devices: Third Edition. third édition, 2012.
- [’T Hooft 1981] G. W. ’T Hooft. *The radiative recombination coefficient of GaAs from laser delay measurements and effective nonradiative carrier lifetimes*. Applied Physics Letters, vol. 39, no. 5, pages 389–390, 1981.
- [Tanaka 1992] Makoto Tanaka, Mikio Taguchi, Takao Matsuyama, Toru Sawada, Shinya Tsuda, Shoichi Nakano, Hiroshi Hanafusa and Yukinori Kumano. *Development of new a-si/c-si heterojunction solar cells: Acj-hit (artificially constructed junction- heterojunction with intrinsic thin-layer)*. Japanese Journal of Applied Physics, vol. 31, no. 11 R, pages 3518–3522, 1992.
- [Tiedje 1984] Tom Tiedje, Eli Yablonovitch, G.D. Cody and B.G. Brooks. *Limiting efficiency of silicon solar cells*. IEEE Transactions on Electron Devices, vol. 31, no. 5, pages 711–716, may 1984.
- [Tomasi 2016] Andrea Tomasi, Florent Sahli, Johannes Peter Seif, Lorenzo Fanni, Silvia Martin, De Nicolas Agut and Jonas Geissb. *Transparent Electrodes in Silicon Heterojunction Solar Cells : Influence on Contact Passivation*. IEEE Journal of Photovoltaics, vol. 6, no. 1, pages 17–27, 2016.
- [Tomasi 2017] Andrea Tomasi, Bertrand Paviet-Salomon, Quentin Jeangros, Jan Haschke, Gabriel Christmann, Loris Barraud, Antoine Descoedres, Johannes PeterSeif, Sylvain Nicolay, Matthieu Despeisse, Stefaan De Wolf and Christophe Ballif. *Simple processing of back-contacted silicon heterojunction solar cells using selective-area crystalline growth*. Nature Energy, vol. 2, no. 5, pages 1–8, 2017.

- [Trupke 2006] T. Trupke, R. A. Bardos, M. C. Schubert and W. Warta. *Photoluminescence imaging of silicon wafers*. Applied Physics Letters, vol. 89, no. 4, pages 1–4, 2006.
- [Tsu 1982] R. Tsu, J. Gonzalez-Hernandez, S. S. Chao, S. C. Lee and K. Tanaka. *Critical volume fraction of crystallinity for conductivity percolation in phosphorus-doped Si:F:H alloys*. Applied Physics Letters, vol. 40, no. 6, pages 534–535, mar 1982.
- [Turrell 1996] G. Turrell and J. Corset. Raman Microscopy. 1996.
- [TWG 2017] TWG. *SET-Plan TWP - PV Implementation Plan Final Draft Approved by TWG members*. Rapport technique, 2017.
- [Valdes 1954] L.B. Valdes. *Resistivity Measurements on Germanium for Transistors*. Proceedings of the IRE, vol. 42, no. 2, pages 420–427, 1954.
- [Vallat-Sauvain 2000] E. Vallat-Sauvain, U. Kroll, J. Meier, A. Shah and J. Pohl. *Evolution of the microstructure in microcrystalline silicon prepared by very high frequency glow-discharge using hydrogen dilution*. Journal of Applied Physics, vol. 87, no. 6, pages 3137–3142, mar 2000.
- [Vallat-Sauvain 2005] E. Vallat-Sauvain, J. Bailat, J. Meier, X. Niquille, U. Kroll and A. Shah. *Influence of the substrate's surface morphology and chemical nature on the nucleation and growth of microcrystalline silicon*. Thin Solid Films, vol. 485, no. 1-2, pages 77–81, aug 2005.
- [Varache 2012] R. Varache, J. P. Kleider, W. Favre and L. Korte. *Band bending and determination of band offsets in amorphous/crystalline silicon heterostructures from planar conductance measurements*. Journal of Applied Physics, vol. 112, no. 12, 2012.
- [Vossier 2010] Alexis Vossier, Baruch Hirsch and Jeffrey M Gordon. *Is Auger recombination the ultimate performance limiter in concentrator solar cells?* Journal of Applied Physics, vol. 32, no. 3, pages 1–4, 2010.
- [Wang 2011] Xiaoting Wang, Lado Kurdgelashvili, John Byrne and Allen Barnett. *The value of module efficiency in lowering the levelized cost of energy of photovoltaic systems*. Renewable and Sustainable Energy Reviews, vol. 15, no. 9, pages 4248–4254, 2011.
- [Wang 2018] Yichun Wang. *Mono Wafer Requirements for Advanced HE Cell*. In Silicon PV, Lausanne, Switzerland, 2018.
- [Weber 2000] W. H. Weber and R. Merlin. Raman scattering in materials science, volume 214. Springer, 2000.
- [Weber 2018] J. Weber, S. Gutscher, S. Lohmüller, E. Lohmüller and A.A. Brand. *Laser-Doped Selective Emitter - Process Development and Speed-Up*. European Photovoltaic Solar Energy Conference and Exhibition, no. September, pages 379 – 384, 2018.

Bibliography

- [Wolf 1963] Martin Wolf and Hans Rauschenbach. *Series resistance effects on solar cell measurements*. Advanced Energy Conversion, vol. 3, no. 2, pages 455–479, 1963.
- [World Energy Council 2010] World Energy Council. *2010 Survey of Energy Resources*. Rapport technique, 2010.
- [WorldBank 2012] WorldBank. *Turn down the heat : why a 4°C warmer world must be avoided*. Rapport technique, 2012.
- [Würfel 2005] Peter Würfel. *Physics of Solar Cells: From Principles to New Concepts*. 2005.
- [Wurfel 2015] Uli Würfel, Andres Cuevas and Peter Würfel. *Charge carrier separation in solar cells*. IEEE Journal of Photovoltaics, vol. 5, no. 1, pages 461–469, 2015.
- [Xia 1995] Hua Xia, Y. L. He, L. C. Wang, W. Zhang, X. N. Liu, X. K. Zhang, D. Feng and Howard E. Jackson. *Phonon mode study of Si nanocrystals using micro-Raman spectroscopy*. Journal of Applied Physics, vol. 78, no. 11, pages 6705–6708, 1995.
- [Yablonovitch 1985] E. Yablonovitch, T. Gmitter, R. M. Swanson and Y. H. Kwark. *A 720 mV open circuit voltage SiO_x:c-Si:SiO_x double heterostructure solar cell*. Applied Physics Letters, vol. 47, no. 11, pages 1211–1213, 1985.
- [Yablonovitch 1986] E. Yablonovitch, D. L. Allara, C. C. Chang, T. Gmitter and T. B. Bright. *Unusually low surface-recombination velocity on silicon and germanium surfaces*. Physical Review Letters, vol. 57, no. 2, pages 249–252, 1986.
- [Yoshikawa 2017] Kunta Yoshikawa, Hayato Kawasaki, Wataru Yoshida, Toru Irie, Katsunori Konishi, Kunihiro Nakano, Toshihiko Uto, Daisuke Adachi, Masanori Kanematsu, Hisashi Uzu and Kenji Yamamoto. *Silicon heterojunction solar cell with interdigitated back contacts for a photoconversion efficiency over 26%*. Nature Energy, vol. 2, no. 5, 2017.
- [Zhao 1996] Jianhua Zhao, Aihua Wang, Pietro P. Altermatt, Stuart R. Wenham and Martin A. Green. *24% Efficient per silicon solar cell: Recent improvements in high efficiency silicon cell research*. Solar Energy Materials and Solar Cells, vol. 41-42, pages 87–99, 1996.
- [Zhao 1999] Jianhua Zhao, Aihua Wang and Martin A. Green. *24.5% efficiency silicon PERT cells on MCZ substrates and 24.7% efficiency PERL cells on FZ substrates*. Progress in Photovoltaics: Research and Applications, vol. 7, no. 6, pages 471–474, 1999.

Remerciements

Je tiens premièrement à remercier chaleureusement mon directeur de thèse, Christophe Ballif, d'avoir dirigé ma thèse et de m'avoir offert la possibilité de réaliser ce travail de doctorat au sein de la division V du CSEM et au PVLab – EPFL, et de m'avoir ainsi permis d'intégrer une équipe exceptionnelle et très stimulante. Merci pour l'intérêt que tu as montré pour ce travail et pour tes précieux retours et conseils que tu m'as apporté durant ces quatre années. Je remercie par-dessus tout Bertrand Paviet-Salomon pour avoir codirigé cette thèse et pour son énorme soutien au quotidien. Merci d'avoir toujours été présent et prêt à m'aider à relever toutes les difficultés et les défis liés à la thèse. Merci beaucoup pour ton engagement, ta confiance, ton intérêt, et ton immense aide tout au long de cette thèse. La générosité et la motivation avec laquelle tu as partagé ton temps, ta force, tes conseils, tes connaissances et tes intérêts ont été un pilier important pour l'accomplissement de cette thèse. Merci du fond du cœur aussi pour tous les super moments partagés et pour cette super équipe co-directeur & doctorante. Je souhaite adresser un grand merci à la Prof. Anna Fontcuberta, au Dr. Damien Lachenal, au Prof. Olindo Isabella et au Prof. Nicolas Grandjean d'avoir accepté de prendre part à mon jury de thèse et pour leur lecture de ma thèse. Un immense et chaleureux merci à Matthieu Despeisse pour son important soutien et ses encouragements qui ont été présents depuis le début de mon projet de master jusqu'à la fin de ma thèse, ainsi que de m'avoir permis et encouragée à faire plein de riches expériences dans divers projets européens, réunions clients, voyages professionnels et conférences. Merci beaucoup pour ton encadrement en tant que chef de secteur, pour tous tes précieux conseils, pour ton soutien, pour ton énergie positive et ta motivation ainsi que pour tous les bons moments partagés.

Je souhaite aussi remercier très sincèrement Jonas Geissbühler et Gabriel Christmann pour leur soutien scientifique et leur chaleureuse présence durant ces quatre années. Un grand merci à Jonas qui, depuis le projet de master, m'a beaucoup appris sur le photovoltaïque et la physique des semiconducteurs ainsi que sur les systèmes de déposition et de mesure. Merci aussi de m'avoir toujours partagé ta grande motivation dans le domaine, cela a eu un impact important sur ma décision d'entreprendre cette thèse. Merci aussi d'avoir été mon mentor de thèse et de m'avoir apporté ton soutien, ton écoute, tes conseils et toujours beaucoup d'optimisme. Un immense merci à Gabriel également qui a toujours été là pour m'aider dans la compréhension des phénomènes physiques et qui a toujours été prêt à prendre du temps pour en discuter. Merci infiniment d'avoir partagé ton savoir, de m'avoir aidé à

Remerciements

résoudre des problèmes physiques et d'avoir toujours été intéressé par mes sujets. Merci beaucoup pour ta patience et tes sages conseils. Merci beaucoup à tous les deux pour tous les bons moments partagés en votre compagnie. Un grand et chaleureux merci aussi à Antoine Descoedres, Mathieu Boccard, Christophe Allebé et Sylvain Nicolay pour leur grande aide et leur apport scientifique qui ont été très importants pour moi. Un immense merci pour toutes les discussions partagées et pour tout le savoir que vous m'avez transmis, ainsi que votre intérêt pour ce travail de thèse. Merci aussi beaucoup pour vos soutiens respectifs qui étaient importants dans plein d'aspects différents de ce travail de thèse. Je tiens à remercier également chaleureusement Paul Procel pour notre précieuse et enrichissante collaboration. Merci infiniment pour tes encouragements et ton précieux partage de connaissances, ça a vraiment été un immense plaisir de travailler ensemble. Un grand et chaleureux merci aussi à Apolline Puaud et à Delfina Muñoz pour leur collaboration et pour les projets que nous avons partagés dans le cadre de nos thèses respectives. C'était vraiment super et aussi un immense plaisir de travailler avec vous deux.

Je remercie chaleureusement tous mes collègues de la division V au CSEM et du PVLab. Ces années avec vous ont été une belle opportunité d'intégrer une équipe exceptionnelle de chercheurs, de scientifiques, d'ingénieurs, de collaborateurs, de techniciens et de doctorants. Merci à tous pour votre aide et votre enthousiasme ainsi que pour m'avoir tant appris sur les cellules solaires et dans le domaine du PV en général. Merci aussi pour tous les bons moments partagés avec vous autour d'un apéro, au ski, à l'apéro saumon ainsi qu'aux fêtes de l'été et de Noël. Je tiens particulièrement à remercier Adriana, Andrea, Antoine, Antonin, Arnaud, Céline, Christophe A., Bertrand, Brett, Delphine, Elisa, Gabriel, Gizem, Jacques, Jean, Jonas, Jonathan, Joyce, Juan, Julie, Jun, Laura, Loris, Luca, Matthieu, Mathieu, Marion, Nelson, Nicolas, Patrick, Quentin, Sophie, Sophie W., Sylvain, Sylvia, pour m'avoir offert votre aide toujours si spontanément et pour la magnifique ambiance de travail. Un immense merci tout particulier à mes collègues doctorants en hétérojonctions Jean, Julie et Luca avec qui il a toujours été si bon de se retrouver, de discuter, de partager et de s'entre aider. Merci pour votre aide et pour votre soutien, c'était vraiment chouette de faire équipe avec vous. Merci aussi à Julie d'avoir pris le train avec moi jusqu'à Catane en Sicile, c'était vraiment une super expérience. Merci à Jean d'avoir toujours été là pour nous coacher et à Luca pour notre super collaboration dans nos expériences et recherches communes. Merci à toute l'équipe de grimpeurs (Christophe A., Delphine, Elisa, Gabriel, Gizem, Julie, Luca, Marion, Nicolas, Raphaël, William) pour nos chouettes moments passés ensemble. Merci aussi beaucoup à Gabriel et Christophe A. pour les soirées « souper & science » passées à refaire le monde et à parler de science avec des bon gins. Merci aussi beaucoup à Gizem et Ana pour leurs présences et leurs conseils ainsi que pour les chouettes moments partagés toutes les trois. Je remercie chaleureusement Sophie, Sophie W., Joyce, Mary-Claude et Karin pour leur aide précieuse dans toutes les tâches administratives, un grand merci particulièrement à Sophie d'être toujours si souriante et à l'écoute, et aussi merci à Claudio pour son soutien en informatique. Je remercie aussi infiniment tout le groupe technique (Aymeric, Cédric, Lionel, Nathanaël, Sylvain D., Thierry) pour le grand travail fourni afin d'entretenir et de développer toutes les machines

qui ont été nécessaires au quotidien de cette thèse. Tout particulièrement, un grand merci à Aymeric pour toute son aide apporté pour réparer et améliorer le système du sigma dark.

Je remercie infiniment et de tout mon cœur tous mes amis pour leur amitié si douce et incroyable partagée au quotidien et pour tous les bons moments passés ensemble. Merci à Elisa, William et Yara d'être toujours présent pour se retrouver, même tard après les longues journées de travail, et pour discuter de tout sans tabou et pour votre soutien si important. Merci à Yara et Elisa pour leurs discussions si précieuses et marrantes et à William d'être "quand tu veux". Merci aussi du fond du cœur à toute la Bame and Geer family (Alexia, André, Eva, Gabriel, Jérôme, Luca, Magali, Marie, Maxime, Michele, Mylène, Olivia, Paul, PO, Raphaël, Simon, Sofia) d'être toujours là pour partager plein de moments si précieux dans la vie et pour apprendre à devenir de plus belles personnes ensemble. Merci pour toutes les magnifiques aventures passées ensemble et pour toutes celles à venir. Merci beaucoup à Maxime, PO et Michele de m'avoir aidé en relisant des parties de ma thèse pour l'anglais, un immense merci à Paul pour toute ton aide si importante avec Python, merci beaucoup à Raphaël pour nos discussions sur les courbes IV et pour ton intérêt pour mon sujet de thèse, c'était toujours chouette de pouvoir en discuter ensemble et de partager nos sujets respectifs, et finalement merci beaucoup à Luca pour notre précieuse entre-aide sans faille qui est toujours présente au labo comme dans la vie. Merci beaucoup aussi à Elise, Pauline et Marie d'être mes amies depuis si longtemps et pour leur doux soutien et encouragements depuis tout ce temps. Un grand merci et des douces pensées à Thomas et Tunvez qui sont aussi en train d'écrire leur thèse en ce moment et pour leur soutien importants de doctorants en fin de thèse.

Je remercie du fond du cœur ma famille pour leur soutien tout au long de ces années. Merci à ma mère, Claudine, pour son doux soutien si fort et toujours si présent, à mon père Patrick et ma belle-mère Géraldine, d'avoir toujours été à l'écoute, de bons conseils et d'un grand soutien, merci beaucoup à mon grand frère Yann, à ma belle belle-sœur Crystel et à ma toute jolie nièce Alice ainsi qu'à mon petit frère Alex. Enfin, je remercie de tout cœur mon Maxime d'avoir été là pour moi, de m'avoir encouragée et soutenue avec sa jolie énergie, de m'offrir tous les jours son joli sourire et de m'avoir redonné du courage et de la force dans les moments les plus difficiles. Merci d'être dans ma vie et de la rendre tous les jours un peu plus belle.

Neuchâtel, le 17 avril 2021

Laurie-Lou

Rue des Fahys 59
CH - 2000 Neuchâtel
☎ 079 748 78 40
✉ lauriesno@gmail.com
🇨🇭 Swiss citizenship
👤 14 March 1991



Laurie-Lou Senaud

Professional experiences

- March 2017 - **PhD candidate**, *CSEM - PV Center/ EPFL - PV-lab*, Neuchâtel, Switzerland.
 - May 2021 Electrical losses mitigation in silicon heterojunction solar cells.
- Nov. 2016 - **Internship**, *CSEM - PV Center*, Neuchâtel, Switzerland.
 - Fev. 2017 Continuation and extension of the architectures developed during the Master Thesis.
- March - Aug. **Master Thesis**, *CSEM - PV Center*, Lausanne, Switzerland.
 - 2016 Development of new advanced architectures for high performance silicon photovoltaics solar cells.
- 2012 - 2015 **Teaching assistant in physics**, *EPFL*, Lausanne, Switzerland.
 - 4h per week Students supervision during exercise sessions.
- Nov. 2015 **Scientastic 2015 – Festival des sciences**, *EPFL*, Lausanne, Switzerland.
 - Animation stand on the theme of the energy for the public.

Education

- 2014 - 2016 **Master in engineering physics**, *EPFL*, Lausanne, Switzerland.
 - Focus on theoretical physics - particles and cosmology - and on solid state physics - semiconductors.
- 2015 - 2016 **Minor in Energy**, *EPFL*, Lausanne, Switzerland.
 - Focus on renewable energy technologies - photovoltaics.
- 2010 - 2014 **Bachelor in Physics**, *EPFL*, Lausanne, Switzerland.
- 2007 - 2010 **Swiss Maturity Diploma**, *Auguste Piccard High School*, Lausanne, Switzerland.
 - Scientific section, bilingual German–French. Physics and chemistry prize.

Technical competencies and Languages

Technical competencies

- Experimental Solar cell and thin-film developments and characterizations : PECVD and PVD thin-film depositions, advanced characterization methods, data analysis
- Computer skills Python, C++, Matlab, VBA, \LaTeX , GitHub, Draftsight, Clewin, Inkscape, GIMP, Microsoft Office, Origin, LabVIEW, R, Root.
- Pension fund CSEM employee representative in the CSEM pension fund.
- Other Driving license (class B)

Languages

- English B2-C1, professional working proficiency
- German B1-B2, 3-months stay in Germany (2008)
- Japanese A1-A2
- French Native

Personal Interests

- Discoveries Hiking, travelling, foreign cultures.
- Activities Climbing, juggling, fencing, reading.

List of scientific contributions

Publications in peer-reviewed journals

- L.-L. Senaud, P. Procel, G. Christmann, A. Descoedres, J. Geissbühler, C. Allebé, N. Badel, P. Wyss, M. Boccard, O. Isabella, M. Zeman, S. Nicolay, M. Despeisse, C. Ballif and B. Paviet-Salomon, "*Advanced Method for Electrical Characterization of Carrier-Selective Passivating Contacts using Transfer-Length-Method Measurements under Variable Illumination*", Journal of Applied Physics, Featured Article, 2021
- L.-L. Senaud, G. Christmann, A. Descoedres, J. Geissbühler, L. Barraud, N. Badel, C. Allebé, S. Nicolay, M. Despeisse, B. Paviet-Salomon and C. Ballif, "*Aluminium-Doped Zinc Oxide Rear Reflectors for High-Efficiency Silicon Heterojunction Solar Cells*", IEEE Journal of Photovoltaic, 2019
- J. Cattin, L.-L. Senaud, J. Haschke, C. Ballif and M. Boccard, "*Influence Of Light Soaking On Silicon Heterojunction Solar Cells With Various Architectures*", IEEE Journal of Photovoltaics, 2021
- L. Antognini, L.-L. Senaud, D. Türkay, L. Marthey, J. Dréon, B. Paviet-Salomon, M. Despeisse, M. Boccard and C. Ballif, "*Contact Resistivity Measurements and their Applicability for Accurate Series Resistance Breakdown in Heterojunction Solar Cell*", AIP Proceeding SiliconPV, 2021
- L. Antognini, V. Paratte, J. Haschke, L.-L. Senaud, J. Dréon, J. Cattin, M. Lehmann, Q. Jeangros, C. Ballif and M. Boccard, "*Influence of the Dopant Gas Precursor in p-type Nanocrystalline Silicon Layers on the performance of front junction Heterojunction Solar Cells*", IEEE Journal of Photovoltaics, 2021
- M. Boccard, L. Antognini, V. Paratte, J. Haschke, M. Truong, J. Cattin, J. Dréon, W. Lin, L.-L. Senaud, B. Paviet-Salomon, S. Nicolay, M. Despeisse and C. Ballif, "*Hole-Selective Front Contact Stack Enabling 24.1%-Efficient Silicon Heterojunction Solar Cells*", IEEE Journal of Photovoltaics, 2021

Appendix A. List of scientific contributions

- A. Puaud, A.-S. Ozanne, L.-L. Senaud, D. Muñoz and C. Roux, "*Microcrystalline Silicon Tunnel Junction for Monolithic Tandem Solar Cells using Silicon Heterojunction Technology*", IEEE Journal of Photovoltaics, 2020
- A. Descoedres, J. Horzel, B. Paviet-Salomon, L.-L. Senaud, G. Christmann, J. Geissbühler, P. Wyss, N. Badel, J.-W. Schüttauf, J. Zhao, C. Allebé, A. Faes, S. Nicolay, C. Ballif and M. Despeisse, "*The versatility of passivating carrier-selective silicon thin films for diverse high-efficiency screen-printed heterojunction-based solar cells*", Progress in Photovoltaics: Research and Applications, 2020
- P. Procel, H. Xu, L. Mazzarella, L.-L. Senaud, B. Paviet-Salomon, H. Sivaramakrishnan Radhakrishnan, M. Filipič, M. Xu, M. Boccard, A. Fioretti, R. Monnard, J.-C. Stang, P. Wagner, D. Meza, D. Lachenal, B. Strahm, W. Duan, A. Lambertz, A. Fejfar, K. Ding, M. Despeisse, I. Gordon, L. Korte, C. Ballif, O. Isabella and M. Zeman, "*On the correlation between contact resistivity and high efficiency in (IBC-) SHJ solar cells*", IEEE 36th European Photovoltaic Solar Energy Conference and Exhibition EUPVSEC, 2019
- D. Lachenal, P. Papet, B. Legradic, R. Kramer, T. Kössler, L. Andretta, N. Holm, W. Frammelsberger, D.L. Baetzner, B. Strahm, L.-L. Senaud, J.-W. Schüttauf, A. Descoedres, G. Christmann, S. Nicolay, M. Despeisse, B. Paviet-Salomon and C. Ballif, "*Optimization of tunnel-junction IBC solar cells based on a series resistance model*", Solar Energy Materials and Solar Cells, 2019
- M. Boccard, L. Antognini, J. Cattin, J. Dréon, O. Dupré, A. Fioretti, J. Haschke, R. Monnard, M. Morales-Masis, V. Paratte, E. Rucavado, L.-L. Senaud, S. Zhong, B. Paviet-Salomon, M. Despeisse and C. Ballif, "*Paths for maximal light incoupling and excellent electrical performances in silicon heterojunction solar cells*", IEEE 46th Photovoltaic Specialists Conference (PVSC), 2019
- M. Despeisse, L. Barraud, B. Paviet-Salomon, A. Descoedres, L.-L. Senaud, C. Allebe, J. Levrat, J. Horzel, A. Lachowicz, F. Debrot, J. Champliaud, A. Faes, N. Badel, J. Geissbühler, S. Martin de Nicolas, G. Christmann, J. Diaz, L. Ding, S. Nicolay and C. Ballif, "*Engineering of Thin Film Silicon Material for High Efficiency Crystalline Silicon Solar Cells*", IEEE 7th World Conference on Photovoltaic Energy Conversion (WCPEC), 2018
- A. Faes, L. Curvat, H. Li, J. Levrat, J. Champliaud, K. Thomas, J. Escarré, N. Badel, B. Paviet-Salomon, J. Geissbühler, C. Allebé, L. Barraud, F. Debrot, A. Descoedres, A. Lachowicz, J. Horzel, L.-L. Senaud, L.-E. Perret-Aebi, C. Ballif and M. Despeisse, "*Direct Contact to TCO with SmartWire Connection Technology*", IEEE 7th World Conference on Photovoltaic Energy Conversion (WCPEC), 2018

-
- A. Descoeurdes, C. Allebé, N. Badel, L. Barraud, J. Champiaud, G. Christmann, F. Debrot, A. Faes, J. Geissbühler, J. Horzel, A. Lachowicz, J. Levrat, S. Martin de Nicolas, S. Nicolay, B. Paviet-Salomon, L.-L. Senaud, C. Ballif and M. Despeisse, "*Low-temperature processes for passivation and metallization of high efficiency crystalline silicon solar cells*", Solar energy, 2018
 - A. Descoeurdes, C. Allebé, N. Badel, L. Barraud, J. Champiaud, G. Christmann, L. Curvat, F. Debrot, A. Faes, J. Geissbühler, J. Horzel, A. Lachowicz, J. Levrat, S. Martin de Nicolas, S. Nicolay, B. Paviet-Salomon, L.-L. Senaud, A. Tomasi, C. Ballif, M. Despeisse, "*Advanced Silicon Thin Films for High-Efficiency Silicon Heterojunction-Based Solar Cells*", IEEE 44th Photovoltaic Specialist Conference (PVSC), 2017

Conference presentations - major contributions

- L.-L. Senaud, P. Procel, G. Christmann, A. Descoeurdes, J. Geissbühler, C. Allebé, N. Badel, P. Wyss, M. Boccard, O. Isabella, M. Zeman, S. Nicolay, M. Despeisse, C. Ballif and B. Paviet-Salomon, "*Illuminated Contact Resistivity Measurements to Investigate the Electrical Properties of Contact Stacks in Silicon Heterojunction Solar Cells*", Oral presentation, European PV Solar Energy Conference and Exhibition (EUPVSEC), Online, 2020
- L.-L. Senaud, G. Christmann, A. Descoeurdes, P. Procel, C. Allebé, J. Geissbühler, N. Badel, P. Wyss, J.-W. Schüttauf, L. Antognini, M. Boccard, S. Nicolay, O. Isabella, M. Despeisse, B. Paviet-Salomon and C. Ballif, "*Bottom-up vs. Top-down Approaches for Identifying and Mitigating the Electrical Losses in High-Efficiency Silicon Heterojunction Solar Cells*", Oral presentation, European PV Solar Energy Conference and Exhibition (EUPVSEC), Marseille - France, 2019
- L.-L. Senaud, A. Descoeurdes, G. Christmann, J. Geissbühler, N. Badel, C. Allebé, L. Antognini, M. Boccard, S. Nicolay, M. Despeisse, B. Paviet-Salomon and C. Ballif, "*Transport Losses Mitigation for > 24% 2x2 screen-printed Silicon Heterojunction Solar Cells*", Oral presentation, European Materials Research Society Conference (EMRS) spring meeting, Nice - France, 2019
- L.-L. Senaud, A. Descoeurdes, G. Christmann, J. Geissbühler, N. Badel, C. Allebé, L. Antognini, M. Boccard, S. Nicolay, M. Despeisse, B. Paviet-Salomon and C. Ballif, "*Decoupling Bulk and Interface Properties in the Shells of Silicon Heterojunction Solar Cells*", Oral presentation, International Conference on Crystalline Silicon Photovoltaics (Silicon PV), Leuven - Belgium, 2019

Appendix A. List of scientific contributions

- L.-L. Senaud, L. Barraud, G. Christmann, L. Antognini, J. Cattin, J. Dréon, M. Boccard, A. Descoeurdes, S. Nicolay, M. Despeisse, B. Paviet-Salomon and C. Ballif, "*Transport-Loss Mitigation in the Shells of Silicon Heterojunction Solar Cells*", Visual presentation, International Conference on Crystalline Silicon Photovoltaics (Silicon PV), Lausanne - Switzerland, 2018
- L.-L. Senaud, G. Christmann, N. Badel, C. Allebé, L. Barraud, A. Descoeurdes, S. Martin de Nicolas, J. Geissbühler, S. Nicolay, B. Paviet-Salomon, C. Ballif and M. Despeisse, "*High efficiency silicon heterojunction solar cells with improved IR response*", Oral presentation at the European PV Solar Energy Conference and Exhibition (EUPVSEC), Amsterdam - Netherlands, 2017
- L. Antognini, L.-L. Senaud, L. Marthey, D. Türkay, J. Dréon, B. Paviet-Salomon, M. Despeisse, M. Boccard, and C. Ballif, "*Contact Resistance Measurements and their Applicability for Various Contact Types in Heterojunction Solar Cell*", Visual presentation, International Conference on Crystalline Silicon Photovoltaics (Silicon PV), Online, 2021
- A. Puaud, L.-L. Senaud, B. Paviet-Salomon and D. Muñoz, "*Deep Insight of Nanocrystalline Silicon Tunnel Junctions for High Efficiency Solar Cells*", Visual presentation, International Conference on Crystalline Silicon Photovoltaics (Silicon PV), Online, 2021